NUCLEAR MAGNETIC RESONANCE AND THE BROADBAND ACOUSTIC RESPONSE OF POROUS ROCKS

A DISSERTATION

SUBMITTED TO THE DEPARTMENT OF GEOPHYSICS

AND THE COMMITTEE ON GRADUATE STUDIES

OF STANFORD UNIVERSITY

IN PARTIAL FULFILLMENT OF THE REQUIREMENTS

FOR THE DEGREE OF

DOCTOR OF PHILOSOPHY

By

Ehud J. Schmidt

February, 1987.

NUCLEAR MAGNETIC RESONANCE AND THE BROADBAND ACOUSTIC RESPONSE OF POROUS ROCKS

Ehud J. Schmidt

Stanford Rock Physics Project, Geophysics Department, Stanford University,
Stanford, California, 94025

Abstract

The thesis involves a study of the pore structure and interfacial properties of porous rocks utilizing proton nuclear magnetic resonance (NMR) and a broadband acoustic study of the frequency dependence of the elastic properties of porous rocks. The underlying philosophy behind this study is that in order to understand the physical properties of porous rocks, it is important to initially characterize their microstructure. The characterization of the pore space, whose importance is large due to the great variation of its properies from that of the solid rock matrix, is carried out utilizing NMR, which provides a measure of the surface area to volume probability distribution of the pore space when the rocks' pores are fully water saturated, and the physical state of the water when the pore space contains air-water mixtures. The physical state of the water is shown by NMR to vary greatly as the water volume fraction decreases, going from a connected pore space to an isolated pore response, and finally to isolated water films on the pore surfaces at low saturations. Effects of variation of the chemical composition of the pore saturating fluid on rock interfacial properties are also examined. Broadband acoustic studies of the shear and compressional elastic moduli of porous rocks and artificial porous materials have been initiated in order to study the dominant mechanisms responsible for wave-rock interaction over several frequency intervals, corresponding to greatly varying spatial and temporal intervals. These studies have required the solution of the complex elastic wave equations in waveguided systems to obtain dispersion relations governing the propagation of two orthogonal elastic wave modes in cylindrical samples, the construction of a new experimental apparatus to measure these dispersion curves in rock samples, as well as the inversion of the experimental dispersion curves for the frequency dependent complex elastic moduli.

The results of this study are the clear identification of frequency dependent phenomena in the elastic response of rocks, with a large change in behavior occuring at approximately 100 kHz, below which interfacial and viscous processes dominate, and above which scattering effects dominate. A general conclusion of this work is the strong role of interfacial forces in influencing the static and dynamic physical properties of porous rocks and other porous materials. A measure of the extent of this influence, for appropriate physical conditions and pore geometry, is in the ratio of the interfacial energy to the other relevant energies, such as elastic energy for pressure variations and thermal work for temperature variations. For quartz-based water saturated porous rocks at atmospheric conditions with pore sizes below $2 \cdot 10^{-2} cm$, this ratio is greater than one and the importance of interfacial effects is clear.

TABLE OF CONTENTS

QUANTIFYING SOLID-FLUID INTERFACIAL PHENOMENA IN POROUS ROCKS WITH PROTON NUCLEAR MAGNETIC RESONANCE *

Ehud J. Schmidt, Katherine K. Velasco and Amos M. Nur
Rock Physics Project, Geophysics Department, Stanford University,
Stanford, California 94305

Abstract

The three order of magnitude variation in the proton nuclear magnetic resonance (NMR) longitudinal relaxation time T_1 of water adsorbed on silica surfaces versus that of bulk water makes proton NMR studies of porous materials powerful tools to study the effects of adsorption. Recent theory permits the utilization of this different response to obtain pore space surface to volume ($\frac{S}{V}$) distribution functions by inverting the decay of the z component of magnetization of fully saturated porous rocks; information can likewise be obtained on the fluid distribution at partially saturated conditions. A computer program has been developed to invert the NMR relaxation curves for the $\frac{S}{V}$ distribution function, assuming an isolated pore regime, the ramifications of which are examined. The program has been applied to experimental results from water, porous sandstones and tight gas sands at various pore fluid saturations and varying electrolyte content. For the fully saturated case, the results show promise in the application of NMR to describing pore space geometries in rock samples with widely varying surface to volume ratios. For partially saturated rocks, the results reflect the preferential early draining of the large pores at high water saturations, connectivity percolation phenomena at intermediate saturations and the dominating role of adsorbed water films at low water saturations. Experiments on rocks saturated with saline solutions disclose the importance of the effects of alteration of the active sites on the rock surfaces as well as the role of electrolytes in modifying the structural properties of bulk solution.

* appeared in J. Appl. Phys. 59 (8), 2788 (1986)

Theory of Nuclear Magnetic Resonance in Porous Rocks

The nuclear magnetic resonance (NMR) response of rocks requires the solution of the Bloch equations of magnetization [1] with the appropriate magnetic boundary conditions at the rock-solution interface taken into account [2,3]. The complicated internal geometry of granular rocks' pores which consists of various shapes, sizes and interpore connections makes exact analysis very difficult.

The treatment of the NMR response of rocks by Cohen and Mendelson [3] forms the basis for the interpretation of our experimental results. Each pore is assumed to possess two types of water: a layer of thickness l of surface adsorbed water with relaxation time T_{1surf} and water further away from the surface with relaxation time T_{1bulk}, which behaves as bulk water. The relaxation time of surface adsorbed water is shorter due to hindered rotation of the water molecules in the presence of a potential field applied from the surface, contributing to a longer correlation time for molecular motion [4] and via the Bloembergen-Purcell-Pound equation [5,6] to a shorter T_1. The ratio of the relaxation times between surface adsorbed water and bulk water depends highly on the nature of the adsorbent and somewhat on surface geometry. Values used in the results section, $T_{1surf} = 10^{-3}$ sec and $T_{1bulk} = 2$ sec are approximate figures for silica-water interfaces obtained by other authors [4,7,8] and supported by our own findings.

The condition $\frac{\Delta E_{NMR}}{KT} << 1$,where ΔE_{NMR} is the splitting of the spin energy levels due to a DC magnetic field and KT the thermal energy, is true at room temperature conditions, and forces us to take into account the coupling of the NMR relaxation with diffusion processes in the pore space. These processes act to smooth spatial gradients in the magnetization which exist between the adsorbed water component and bulk component within each pore and between adjacent pores. Mathematically, this requires the addition of a diffusion term to the right side of the Bloch equations [2,3] which for the z component becomes

$$\frac{\partial M_z}{\partial t} = \gamma \cdot (M \; X \; H)_z - \frac{(M_z - M_\infty)}{T_1} + D \cdot \frac{\partial^2 M}{\partial z^2} \qquad [1]$$

where H is the magnetic field, M the magnetization, γ the proton gyromagnetic ratio and D the diffusion constant. M_∞, the equilibrium magnetization is mainly due to paramagnetic minerals whereas $(M_z \; (t) - M_\infty)$, the dispersion component, is due to the excited spins.

Two cases of diffusion interest us: that which exists between the adsorbed water and free water in a single pore and that which exists between neighboring pores.

Within a pore of radius r, gradients in magnetic field between the surface magnetization and bulk magnetization are smoothed by diffusion in a time [2,3]

$$T = \frac{r^2}{6D} \cdot (\frac{Sl}{V}) \qquad [2]$$

where $\frac{S}{V}$ is the pore surface to volume ratio. If T is smaller than the relaxation time for that pore T_{1i}, we will observe an averaged signal for that pore. If T_{1i} is greater than T we will observe a multicomponent signal from that pore, since spatial inhomogeneities persist during the decay process. l, which is the thickness of the adsorbed layer will be taken in the analysis as $10^{-7}\ cm$, which corresponds to approximately 5 monolayers of water. $\frac{S}{V} = \frac{3}{r}$ for a spherical pore and taking the shortest T_{1surf} to be $10^{-3}\ s$, and $D = 3 \cdot 10^{-5}\ cm/s$ at room temperature, we obtain a critical pore radius r_c which distinguishes between pores of radius

$$r < r_c = 6 \cdot 10^{-1} cm \qquad [3]$$

for which we will always observe an averaged signal and larger pores for which we will observe a multicomponent signal.

The average relaxation time, T_{1aver}, obtained for pores of radius $r < r_c$ is given by [3]

$$(T_{1aver})^{-1} = (1 - \frac{Sl}{V}) \cdot (T_{1bulk})^{-1} + \frac{Sl}{V} \cdot (T_{1surf})^{-1} \qquad [4]$$

By measuring T_{1aver} for a given pore we can get the surface to volume ratio of the particular pore.

For pores of $r > r_c$ we obtain a multicomponent decay signal [3,4]

$$M_z(t) = M_\infty + (M_o - M_\infty) \cdot \left[\frac{Sl}{V} \cdot e^{\frac{-t}{T_{1surf}}} + \left(1 - \frac{Sl}{V}\right) \cdot e^{\frac{-t}{T_{1bulk}}} \right] \quad [5]$$

For pores of $r > r_c$, $\frac{Sl}{V} < 10^{-6}$ so the amplitude of the surface adsorbed water is small and we observe a pore response close to that of free water.

Interpore diffusion depends on the mean distance between neighboring pores, L, which for a rock of uniform spherical pores is given by approximately [3]

$$L = 2 \cdot r \cdot \phi^{-1/3} \quad [6]$$

where ϕ is the rock porosity. Diffusion also depends on the size of the pore throats, since narrow pore throats decrease the diffusion flux between pores. Finally, it depends on the presence of a large gradient in magnetization between neighboring pores. As it is difficult to predict all these variables, interpore diffusion will present an increasing problem the higher the rock porosity, the higher its permeability and the higher the variability in size of its pores. In the extreme case of interpore diffusion dominating the rock response, we will see one relaxation time T_{1aver} for the whole rock. Equation [4] will then hold for the entire rock, and the rock's average surface to volume ratio could be retrieved from it.

In situations where interpore diffusion is negligible the rock behaves as a collection of isolated pores. Each pore will relax with its own characteristic relaxation time, a function of its surface to volume ratio. Grouping pores of the same size together we obtain the integral equation governing the z component of magnetization in this regime [3]:

$$M_z(t) = M_\infty + (M_o - M_\infty) \cdot \int_{\omega_{min}}^{\omega_{max}} e^{-\omega \cdot t} \cdot P(\omega)\, d(\omega) \quad [7]$$

where $\omega = (T_1)^{-1}$ is the angular frequency of relaxation and where $P(\omega)$ is the fraction of water which resides in pores of this particular relaxation angular frequency . This probability distribution is normalized

$$1 = \int_{\omega_{min}}^{\omega_{max}} P(\omega)\, d(\omega) \quad [8]$$

Both integrals range from ω_{min}, which is that of the slow relaxing free water, to ω_{max}, which is that of the fastest relaxation in the system. In practice ω_{max} is limited by the shortest relaxation time observable with the particular time spacing used in the measurement sequence. For each instrument the absolute limiting time step is the machine's "dead time".

Experiment

The NMR experiments were performed with an IBM (Bruker produced) PC-20 spectrometer. The magnetic field source was a 4.7 $\pm$ 0.01 Kgauss fixed magnet with an air gap of 0.2 cm. The oscillating field is 20 Mhz for protons with an acceptance band width of $\pm$ .15 Mhz. The magnet is held at 40 $\pm$ 0.01 Celsius. The probe used was a 10 mm solid/liquid probe with $<$10 μs dead time, which determines the minimum relaxation time observable with the instrument.

All measurements made were of T_1 by the spin recovery method (π , τ , $\frac{\pi}{2}$) in which an RF pulse is applied in the -z direction and the spins thus excited to the upper energy level are allowed to recover back to their equilbrium states in the +z direction. They are observed by applying a fast (12 μs) secondary pulse which allows observation of the spins in the xy plane after successive delay times τ. The spectrometer was operated with a phase sensitive detector which assured the fastest detector response.

The PC-20 is a time domain spectrometer. Signal averaging for higher signal to noise ratios was performed within the instrument by averaging the results of many measurements for the same τ value, commonly, 100 measurements per τ for τ' s below 2 milliseconds and 64 for those greater than 2 milliseconds. The number of measurements was increased for rocks of small porosities and at low water saturations. Between pulses the samples were allowed to equilibrate for times greater than the longest relaxations found in the sample (commonly 2 to 4 seconds for rocks, 20 seconds or more for liquids).

The rock samples were cored in 1 cm by 4 cm cylinders, parallel or perpendicular to any discernable layering, cleaned of surface cuttings ultrasonically, dried in a vacuum oven and weighed. The samples were then placed in a pressure vessel, evacuated under $< 23\ mm\ Hg$ vacuum and later saturated under 180 *bars* pressure with deionized, deaired water for periods of two days or more, depending on the rock permeability. Following saturation the rock samples were stored in jars of water until the time of the experiment. In preparation for experimentation, the rocks were removed from storage, surface dried and then weighed to determine their fully saturated weight, to be referred to as 100% saturation weights. The difference between the fully saturated weights and the dry weight being the pore fluid weight, the weight of required partial water saturations could then be determined. After weighing, the rocks were placed in thin-walled quartz test tubes. To minimize evaporation during the experiments pure quartz rods were added so as to entirely fill the test tube volume, which was then hermetically capped. These quartz rods were pretested and found to be transparent to the NMR signal.

The test tubes were then inserted into the spectrometer, allowed to equilibrate to the probe ambient temperature and then measured. Measurements were conducted in two linear sequences, a sub millisecond span of 10 to 20 points using the instrument microsecond time scale (from 0.1 - 50 milliseconds) and a second linear sequence in the millisecond time scale (2 to 10000 milliseconds). These two measurements were then combined for the full relaxation spectra of each rock.

To achieve partial saturations the rocks were dried in an anhydrous $CaSO_4$ desiccator to the required weight and allowed to equilibrate for at least 6 hours in the test tubes before the experiment was performed. Accuracy of the saturation levels was determined by a comparison between the sample weights before and after the experiment and were found to be better than 0.1% saturation. Measurements at partial saturations involved tuning the probe and the measurement pulses slightly because the Larmor frequency and the relaxation times varied (as will later be shown) as the water saturation changed.

The NMR spectrometer was run remotely via an RS-232 interface by an IBM/XT computer. The computer set the experiment parameters and received the instrument's averaged results following each τ value. Experiments at high water saturations commonly took about 8 hours and those at extremely low water saturations up to 14 hours. These long measurement times were required in order to obtain high signal to noise ratios necessary in order to invert the data for detailed $P(\omega)$ distributions.

Data Inversion Program

In the isolated pore regime, which was taken to hold in our experiments, the NMR response is given by equation [7] where equation [4] relates the relaxation time of each pore group to its surface to volume ratio. We have developed an algorithm to invert the full integral equation, without any prior assumptions.

Equation [7] is rewritten

$$M_z\ (t) = M_\infty - \int_{\omega_{min}}^{\omega_{max}} e^{-\omega t}\ P(\omega)'\ d(\omega) \qquad [9]$$

where $P(\omega)' = (M_\infty - M_o) \cdot P(\omega)$. The quantity $(M_\infty - M_o)$, the extent of the NMR dispersion can later be determined because of the normalizing condition, equation [8].

Since we sample $M_z\ (t)$ at various discrete τ_j $(j = 1,2,...N)$ we require the digitised form of equation [9], which after writing $P(\omega)'\ d(\omega)$ as $P_i\ (\omega_i)'$ becomes

$$M_z\ (\tau_j) = M_\infty - \sum_{\omega_i = \omega_{min}}^{\omega_i = \omega_{max}} e^{-\omega_i \tau_j}\ P_i\ (\omega_i)' \qquad [10]$$

with the normalizing condition

$$1 = \sum_{\omega_i = \omega_{min}}^{\omega_i = \omega_{max}} P_i\ (\omega_i) \qquad [11]$$

If we measure $M_z\ (\tau_j)$ at N points then

$$w_{max} = \frac{\pi}{(\tau_j - \tau_{j-1})_{min}} \quad \text{and} \quad w_{min} = \frac{\pi}{(\tau_N - \tau_1)} \qquad [12]$$

We divide ($\omega_{max} - \omega_{min}$) into M intervals where

$$\Delta\omega = \frac{\omega_{max} - \omega_{min}}{M} \qquad [13]$$

and numbering the values of ω_i by

$$\omega_i = \omega_{min} + \Delta\omega \cdot (i - 1) \qquad [14]$$

($i = 1,2,.....M+1$) we get M+2 unknowns ($M+1$ P_i (ω_i)$'$ and M_∞) with N equations. These can be solved by least squares if $N \geq M+2$.

In our inversion program equation [10] is solved in the linear least squares sense with the constraint

$$P_i\ (\omega_i\ )' \geq 0 \qquad [15]$$

which follows from the P_i (ω_i) being probabilities.

Since $\Delta\omega$ may be a large sector over which P_i (ω_i)$'$ is averaged even in cases where the largest allowable M's for a given N have been picked, the program is run in an iterative fashion. After the first iteration the program looks for the maximum ω_i for which P_i (ω_i)$'$ ≥ 0. It takes one more $\Delta\omega$ and makes this the new ω_{max}. The intervals $\Delta\omega$ are now redefined between ω_{min} and the new ω_{max}. As these runs are repeated we can expect to see further detail among the nonzero P_i (ω_i)$'$.

The iterative process ends when a nonzero P_i (ω_i)$'$ appears at ω_{max}, or alternatively if there is no further improvement in the computed error. At this point the program divides out ($M_\infty - M_o$) to recreate the normalized $P_i(\omega_i)$. The program calculates the $\frac{S}{V}$ ratios of the nonzero ω_i using equation [4]. An average surface to volume ratio for the rock is obtained by averaging over the distribution function using the equation

$$[\frac{S}{V}]_{rock} = \sum_{\omega_i = \omega_{min}}^{\omega_i = \omega_{max}} P(\omega_i) \cdot (\frac{S}{V})_i \qquad [16]$$

where $(\frac{S}{V})_i$ is the surface to volume ratio of the pores with angular frequency ω_i which contain $P_i(\omega_i)$ volume fraction of the total water in the rock.

With the assumption of spherical pores ($(\frac{S}{V})_i = \frac{3}{r_i}$) we can obtain an estimate of the pore size distribution of the rocks.

The interpretation we give to the data assumes non-interacting pores. The validity of this assumption has been treated theoretically [3], where it is found that by examining the y^{th} moment of $P(\omega)$

$$< \omega^y > = \int_{\omega_{min}}^{\omega_{max}} P(\omega) \cdot \omega^y \, d(\omega) \qquad [17]$$

where y is some integer, diffusion effects do not affect the mean $y = 1$, so that equation [16] for the average surface to volume ratio of the rock is not affected. They also do not affect $y = 2$, the variance of $P(\omega)$. They affect $y = 3$ and add positively to $y = 4$. Neglecting the constant M_∞ our equation is

$$M_z(t) = (M_o - M_\infty) \cdot \int_{\omega_{min}}^{\omega_{max}} P(\omega) \, e^{-\omega t} \, d(\omega) \qquad [18]$$

expanding $e^{-\omega t}$ in (ωt)

$$e^{-\omega t} = 1 - (\omega t) + \frac{(\omega t)^2}{2} - \frac{(\omega t)^3}{6} + \frac{(\omega t)^4}{24} + ..+ \qquad [19]$$

we observe that powers of ω appear only with the same power of t. It is therefore obvious that the higher moments are important only when we can observe the decay for long times, unobstructed by thermal noise. This requires relatively large amplitudes $P(\omega)$, for even when $(\omega t) = 1$ the fourth moment is only 13% of the amplitude. Interpore diffusion is therefore expected to be more effective for long relaxation times. The effect of interpore diffusion on the fourth moment is to narrow the distribution function $P(\omega)$ around the mean ω. In a recent paper Mendelson [9] has examined the effects of interpore diffusion to first order in the intersection of a pore's surface area with that of adjacent pores and found that equation [7] is still valid in this case, although the $P(\omega)$ now are not merely the volume fractions of water in a particular pore size but rather this value minus the sum of the surfaces that connect

each pore to its neighbours.

Results

a. Deionized De-aerated Water

The NMR response of deionized de-aerated water has been measured in order to establish the T_{1bulk} necessary for the inversion of porous rock results and to test the inversion algorithm in situations where there is no microstructure and therefore only one relaxation time.

The NMR relaxation of bulk water is sensitive to the presence of small fractions of paramagnetic O^{17} so measurements were conducted under vacuum. Figures 1(a) and 1(b) show the experimental results for deionized water. Figure 1(a) shows $M_z\ (t)$ as a function of time, the points being the experimental data and the line passing through the points the fitted relaxation curve produced by the inversion program. The decay of the amplitude to M_∞ is extremely slow and required sampling for 24 seconds in order to observe the entire relaxation.

The result of the inversion program, $P(\omega)$, is shown in figure 1(b) as a function of the relaxation angular frequency, ω(units are sec^{-1}). 61.7% of the water relaxes with $\omega = 0.260$ and 38.3% with $\omega = 0.258$. The relaxation time for the deionized degassed water is 3.84 ± 0.02 seconds, which varies by about 10% from that observed by other authors [10,11] for this temperature. The narrowness of the peak in the distribution function observed for water is a result of the rapid diffusion of the water molecules, so that only local maxima in the distribution function can be observed.

The low noise level of the data and the quality of the fit, variance$<.4\%$, may also be seen in figure 1(a).

b. Fully saturated rocks

Figures 2(a) and 2(b) show the experimental results for a 100% saturated sample of Beaver sandstone, a clean quartz sandstone with very low clay content. Figure 2(a) shows the

magnetization, M_z (t), as a function of time, with the points being the experimental data and the line passing through them the results of the inversion. It can be seen that Beaver sandstone has a relatively low $\frac{S}{V}$ ratio, since its relaxation continues to approximately 2.5 seconds, approaching the relaxation time for bulk water. This is shown quantitatively by the results of the inversion, figure 2(b). The average $\frac{S}{V}$ for the rock is approximately $2 \cdot 10^4\ cm^{-1}$, corresponding to an average pore size in the micron ($10^{-4}\ cm$) range. The exact ω distribution function for this rock is plotted in figure 2(b). This rock has a surface to volume spectrum ranging from $7 \cdot 10^3\ cm^{-1}$ to $3 \cdot 10^4\ cm^{-1}$, all representing fairly large pores. The low noise level in the data and the quality of the fit to it, $<7\%$ variance, can also be seen in figure 2(a).

The resolved $\left(\frac{S}{V}\right)_i$ are used , with the assumption of spherical pores, to obtain the pore radius distribution for this rock, shown in figure 2(c). Half of the pores are of effective radius between 4 and 4.3 microns while there is a narrower distribution of smaller pores of 0.8-0.9 micron radius. Computing the $\frac{volume}{pore}$, consistent with the spherical pore assumption, and knowing the sample porosity it is possible to compute the $\frac{\#\ pores}{cc\ rock\ sample}$. The numbers obtained range from 10^8, for the larger pores, to 10^{10}, for the smaller pores, which suggests the extreme importance of the pore space and the solid-fluid interface in influencing physical processes in porous rocks.

Figures 3(a) and 3(b) show the results for 100% saturated Tight Gas sand 4558, a rock of small pores and therefore high surface to volume ratio. The high surface to volume ratio is evident from figure 3(a) since the relaxation for this rock ends by 250 milliseconds, in contrast with that of the low surface area Beaver (figure 2(a)) whose relaxation curve extends to 2.5 seconds. The results of the inversion program, figure 3(b), bear this out, the average $\frac{S}{V}$ ratio being $3 \cdot 10^6\ cm^{-1}$, two orders of magnitude higher than Beaver sandstone. This can also be

seen in the angular frequency spectrum, in that the spectrum extends to an angular frequency of 1200 sec^{-1} which corresponds to pores on the scale of tens of angstroms. Pores of such size correspond to the spacing between the layers of clay sheets, so it is probable that the high ω component is due to interclay water. The largest pores of this sample are one order of magnitude smaller than those of Beaver sandstone, which is why the angular frequency spectrum begins at 12 sec^{-1}, whereas it is concentrated in the 1 to 4 sec^{-1} range for the Beaver sample.

NMR characterization of rock microgeometry is compared with that of mercury porisimetry (provided courtesy of T. Plona, Schlumberger-Doll Research) in figure 4(a). The spectras shown are of QF10, an artificial fused quartz sand sample, and the NMR pore size distribution is derived from the $\frac{S}{V}$ distribution with the assumption of spherical pores. The width of the pore spectra obtained by both methods is similar. Figure 4(b) is a scanning electron microscope photograph of QF10. It is possible to see that the pore sizes are indeed of the order which the NMR measurement predicts. The bimodal distribution observed by the NMR may be due to the variation in surface area between the circular and ellipsoidal pores in this sample [12]. The sensitivity of mercury porisimetry to the pore throats , which can be seen to be generally narrower than the pores themselves, may explain the smaller pore sizes returned by this method. The large pores found in this rock approach the upper limits of the usefullness of the NMR technique, since the surface water component is extremely small, tending to increase the relative error in the inferred results.

c. Partially saturated rocks

Study of rocks with air-water mixtures in their pores is important since it is one of the methods of varying a rock property independently of others. As the NMR response of the air phase may be ignored at ambient vapour pressures, it is possible to observe the state of the water remaining following the evacuation of a given fraction of the total water content.

Without regard to rock microgeometry it is expected that the magnetization dispersion ($M_0 - M_\infty$) decrease as water molecules are removed from the sample since [13]

$$(M_0 - M_\infty) = \frac{N \gamma \hbar}{2} \tanh \left(\frac{\gamma \hbar H}{2 KT} \right) \qquad [20]$$
$$= \frac{N (\gamma \hbar)^2 H}{4 KT} \quad \text{for} \quad \left(\frac{\gamma \hbar H}{2 KT} \right) << 1$$

where $\hbar$ is Planck's contant divided by 2π and N, the number of nuclear spins per unit volume, decreases during the drying process.

Taking into account the variability in pore sizes found in rocks, it is expected that the evaporation process will not be homogenous in all the pores. The vapour pressure in a pore of radius r, V_P (r), relative to the atmospheric value $V_{P\,\infty}$ is given by the Kelvin equation

$$\frac{V_P (r)}{V_{P\,\infty}} = e^{\frac{-2 g_{lv} V_m \cos (\theta)}{r RT}} \qquad [21]$$

where g_{lv} is the water-vapor interfacial tension coefficent, V_m the fluid molecular volume and θ the contact angle the film interface makes with the surface. For water ($cos (\theta) > 0$) the vapour pressure in small pores is greatly reduced from its atmospheric value. It is harder to evacuate these small pores since the driving force for evaporation, which is equilibration with the external vapor pressure, is very weak. The evaporation process therefore treats preferentially the largest pores. Within each pore the bulk fluid component should be drained first, since removal of the adsorbed molecules requires a greater expenditure of energy.

Figures 5(a) and 5(b) show the inversion results for Berea 100 sandstone, a high porosity rock with 6% clay (most of which is found coating grains), at water saturations ranging from 100% to 4%. Figure 5(a) is an expansion of the low ω, low $\frac{S}{V}$, region in which the high water saturation (100% through 70%) results are concentrated. The dashed line in each plot represents the water saturation axis, with decreasing saturations into the page.

At 100% saturation, as seen in figure 5(a), 14% of the water resides in the largest pores, $\omega = 1.53$, 72% in smaller pores, $\omega = 4.4$ to $\omega = 4.9$, and 12% in the smallest pores $\omega = 29$.

By 90% saturation the component with $\omega = 1.53$ has dissappeared and the component with $\omega = 4.4$ is reduced to 14%, having been partially evacuated and the remainder of the water in these pores now behaving as tighter adsorbed water. This causes 16% of the water found in the rock at 90% saturation to appear at $\omega = 6.2$, with 61% now in a higher adsorbed state at $\omega = 14.1$ to $\omega = 15.7$. A percent appears at a higher adsorbed state, $\omega = 53.7$, with 8% moving to a much higher adsorbed state, $\omega = 161$. This shows that the water in the pores is becoming increasingly skewed towards the adsorbed component within each pore. Along with the relative shift to higher adsorption the non-zero distributions are clearly separating from each other. This suggests a decrease in the interaction between adjacent pores of different size.

At 80% saturation we see a continuation of this behavior, with only 8% remaining at $\omega = 6.1$ while 86% of the water is at $\omega = 24.46$ to $\omega = 25.9$. 6% of the water now appears at a new higher adsorbed state, $\omega = 99$. It is clear that the influence of the adsorbed components is growing at the expense of the low $\frac{S}{V}$ components.

At 70% saturation in Berea 100 sandstone we have an extreme variation in behavior, which can be seen in the 70% saturation spectra in figure 5(b). There is a rapid shift of 52% of the remaining water to a much tighter adsorbed state, $\omega = 7012$ to 7085, with 45% clearly separated and lying in the low ω region (figure 5(a)) in which all the higher saturation results were contained.

At saturations below 70% the behavior remains essentially like that at 70%, with two well separated P (ω) distributions, one at low ω and the other at very high ω's. The high ω distribution gradually grows in size at the expense of the low ω component. Below 30% saturation there are strong oscillations in the resolved distributions, suggesting a change in behavior tied to the removal of the final fluid monolayers from the rock surface.

Accompanying the change in the spectra at 70% water saturation there is a large increase in the magnetization, the size of the NMR dispersion, as can be seen in figure 5(c), a

plot of the magnetization (in relative units, for conversion to Gauss the result must be divided by $2.3 \cdot 10^{12}$) versus water saturation. As the magnetization is the sum of the magnetic moments of the spins in the sample, it is expected to decrease with water saturation (equation [20]). This behavior is observed below 70% saturation, but the peaked behavior above this saturation level clearly indicates the presence of another, more powerful, physical process. The strong peak in the magnetization at 70% saturation suggests a collective motion of the water molecules, which would tend to enhance the contribution of each spin to the total magnetization. The critical phenomena may be the result of connectivity percolation of the bulk fluid in the pore space. This hypothesis is supported by the DC conductivity of this rock (provided courtesy of R. Knight, Stanford Geophysics), also plotted in figure 5(c). The variation of rock conductivity with water saturation shifts at the same saturations as the peak in magnetization, suggesting a change in the nature of the ionic conduction mechanism, from bulk water controlled to surface adsorbed water controlled.

Figure 5(d) shows the effective average surface to volume ratio of the pore space of Berea 100 sandstone as a function of water saturation. This result is obtained by averaging over the distribution function using equation [16] and is free of the effects of diffusion, as it could be obtained by fitting a single relaxation time to the rock's relaxation curve at each water saturation level. This effective average $\frac{S}{V}$ is the average surface to volume ratio at full saturation, while at partial saturation it represents the average surface to volume ratio of the fluid filler. It can be seen that the average $\frac{S}{V}$ ratio climbs strongly from 100% to 70% saturation, going from $7 \cdot 10^4\ cm^{-1}$ at 100% to $4 \cdot 10^7\ cm^{-1}$ at 70% saturation, an increase of three orders of magnitude. It drops somewhat below 70% saturation, increasing again at 10% saturation, perhaps due to the increasing role of interfacial processes at extremely low saturations, where the drying process requires the stripping of the last liquid monolayers from the grain surfaces.

Assuming a model of the drying process as a removal of the bulk water from the pores, while leaving the surface layers intact, it is expected that there be a slow increase in the effective average surface to volume ratio, which is observed from 100% to 80% saturation, but the sharp increase from 80% to 70% is clearly due to critical behavior.

The strong increase of the surface to volume ratio, or the mean ω, mirrors the increase in the magnetization (figure 5(c)) and strongly suggests critical behavior tied to an insulator-conductor transition. Similar behavior of the mean ω was observed by Boyce and Huberman [14] in the NMR spectra of CuI, a superionic conductor, through its phase transitions to insulating phases, in which a structural change was induced in the conducting sublattice.

The possibility that these strong changes in the NMR response at partial saturation, with emphasis on the peak in magnetization, may have originated from experimental problems (such as signal saturation, probe tuning, paramagnetic influence) has been thoroughly investigated, and we are now satisfied that these effects are both repeatable and physical in nature.

Among the rock samples we have explored, we have been able to separate between rocks that have the "percolation" response and those that do not. Massillon Light sandstone affords insight into the mechanisms behind this phenomena. Massillon Light and Berea 100 are similar in their total fluid content but differ in their clay and hematite content, Massillon Light containing 3% clay and 1% hematite.

Figures 6(a) and 6(b) show the inversion results for Massillon Light sandstone at saturations ranging from 100 to 30%. Figure 6(a) is a magnification of the low ω range in which all the 100 to 65% results are confined.

The 100% saturation distribution, figure 6(a), contains some high ω components at $\omega = 130$, so that the initial $\frac{S}{V}$ ratio for this rock is higher than that of Berea 100, figure 5(a). These high ω populations are gradually decreased as the water saturation drops until they disappear at 80% saturation. Over this water saturation interval the low ω components are

shifting to somewhat higher states, but the separation between the components and their relative proportions remain unchanged.

Below 80% saturation there is a shift to higher adsorbed states, but the pace is slow enough so that by 30% saturation only states of the same size as those seen at 100% saturation are seen. From this point on the spectra change drastically, with the appearance of very high ω's.

Figure 6(c) shows the magnetization of Massillon Light as a function of water saturation. The magnetization drops linearly with water saturation, as the continuum equation [20] predicts.

Figure 6(d) shows the effective average surface to volume ratio for Massillon Light sandstone as a function of water saturation. There is a slight minimum at 70% saturation, when the high ω components disappear from the resolved spectra (figure 6(a)), followed by a gradual increase of the average $\frac{S}{V}$ expected through the evacuation of the bulk water from the sample. At 30% saturation there is the onset of a strong increase in $\frac{S}{V}$, tied to the onset of criticality associated with the removal of the surface monolayers.

It appears that the combination of an ability to withdraw the initial high $\frac{S}{V}$ components and to keep the various ω distributions close to each other has enabled this rock to remain subcritical to low water saturations. The critical ω for the onset of criticality is of the order of 200. This suggests that rocks containing water films which during the evacuation process reach a $\frac{S}{V}$ ratio of $2 \cdot 10^{-6}\ cm$, or a thickness of 50 angstroms, will reach criticality and their behavoir will become effectively surface dominated.

d. Effects of pore fluid salinity

As diffusion between the surface and bulk fluid components of each pore produces an

average relaxation time for that pore (equation [4]), it should be possible to observe a shift in the NMR $P(\omega)$ by changing the chemical environment in the pore.

Electrolytes influence the pore fluid in two ways. The salt ions within the pore are hydrated by water molecules and therefore compete with the surface in attracting water molecules. Other salt ions exchange with hydrogen ions (and other ions) on the active sites on the surface. Electrolytes are commonly divided into "structure making" and "structure breaking", according to their ability to respectively increase or decrease the viscosity, the associated rotational correlation time and other structural properties of water [10].

Approximate formulas for the effect of ions on the properties of bulk water are [10];

$$\frac{\eta}{\eta_o} = 1 + B \cdot c \quad \text{and} \quad \frac{\omega_{bulk}}{\omega_{bulko}} = 1 + B' \cdot c \qquad [22]$$

where η_o and ω_{bulko} are the values of the viscosity and relaxation angular frequency at infinite dilution, c is the ion concentration and B, B' empirical factors measuring the strength of the ion in altering these properties. If B, B'>0 the ions are considered to be "structure making", otherwise they are "structure breaking".

The results of Engel and Hertz [10] on water at 25 degrees celsius show that NaCl is a "structure maker" with B'=0.05 $molal^{-1}$ (Na^+ is strongly "structure making", B'=0.06 $molal^{-1}$, while Cl^- is weakly "structure breaking", B'=-0.01 $molal^{-1}$).

Boise sandstone samples were saturated with 0.01 and 0.1 Molar NaCl solutions and left for several days in hermetic jars to allow for equilibration of the exchange interactions at the pore-matrix interfaces. Figure 7 shows the Boise sandstone results for two saturating fluid salinities.The two spectra are similar but displaced slightly , which is clearly seen in the inset magnification of the low ω region. The 0.1 Molar solution is displaced towards lower ω's but the population of each peak in the distribution is kept. This may be interpreted as different averaging within each of the pore groupings, with higher salinity reducing the role of the adsorbed water component. The fact that the relative populations of the various groupings of

pores is kept despite the salinity changes attests to the validity of the assumed correspondence between the relative intensity at a given relaxation angular frequency and a given fraction of the total water residing in particular size pores.

Using equation [22], with 1 $molal = 1\ Molar$, we can calculate the expected ω_{bulk}'s at the two salinities and the ratio between them;

$$\frac{\omega_{bulk}\ (0.1\ Molar\ )}{\omega_{bulk}\ (0.01\ Molar\ )} = 1.004\ . \qquad [23]$$

This computation accounts for the effect of only the ions in bulk solution but not for the effects of the ions on the adsorbed layers at the interface, and would predict $\omega\ (0.1 Molar\ )$ is 0.4% larger than $\omega\ (0.01\ Molar\ )$ within each pore. The observed shift in our spectra is -7.8%, which shows an opposite trend to what equation [22] predicts.

As the disparity could be a result of surface layer modification, we can obtain an estimate of the extent of the changes in surface properties by assuming that equation [4] holds for both, equation [22] holds for the bulk fluid components in each pore and that the $\frac{S}{V}$ ratio of the pore is unchanged. With these assumptions we have

$$\frac{\omega_{aver}\ (0.1\ Molar\ ) - \omega_{bulk}\ (0.1\ Molar\ )}{\omega_{aver}\ (0.01\ Molar\ ) - \omega_{bulk}\ (0.01\ Molar\ )} = \frac{\omega_{surf}\ (0.1\ Molar\ ) \cdot l\,(0.1\ Molar\ )}{\omega_{surf}\ (0.01\ Molar\ ) \cdot l\,(0.01\ Molar\ )} \qquad [24]$$

where $\omega_{aver} = (\ T_{1aver}\ )^{-1}$ and the ratio on the right hand side of the equation measures the effective strength of the adsorbed layer at 0.1 $Molar$ relative to its strength at 0.01 $Molar$. Using the Boise sandstone experimental results we find the effective influence at 0.1 $Molar$ to be 91.6% of the effective influence at 0.01 $Molar$. The variation in surface properties is quite small for the one order increase in pore fluid salinity, and may be due to surface species exchanging with the Na^+ or Cl^- ions.

The extent of the effect of the saline solutions agrees well with the results of Morariu and Mills [7] on 1 $Molar$ solutions of KCl, at coverages of 1.5 monolayers, on silica gels, in which, at the same temperature, an approximately -20% shift in the relaxation angular frequencies

was observed. This suggests a similarity in the behavior of porous silica-based rocks and silica gel, as well as the dominating role of surface property modification due to the effect of the various ions, since KCl, as opposed to NaCl, is a "structure breaker" [10], and thus modifies the bulk properties of water in the inverse direction.

Conclusions

The application of proton NMR to fully saturated porous rocks permits the retrieval of important geometric information on the pore space in silica-based rocks with $\frac{S}{V}$ ratios from $10^3\ cm^{-1}$ to $10^8\ cm^{-1}$. It is expected that for lower $\frac{S}{V}$ ratios the surface effect would be so weak that the NMR response would be indistinguishable from that of bulk water. NMR can be used for porous rocks of $CaCO_3$ composition but the different fluid-solid interfacial properties need to be understood in advance.

In partially saturated rocks NMR allows for a better understanding of the position and state of the remaining water; this has implications for the electromagnetic and elastic response of rocks saturated with air-water mixtures. The percolation process seen at intermediate saturations has strong implications on the fluid dynamical and electrical transport properties of the pore space. The dominating role of adsorbed water at low saturations could be associated with the increase of kHz elastic and electromagnetic dissipation factors in rocks at these saturations.

Changes in the NMR spectra of rocks with pore fluid salinity reflect the role of both structural changes in the bulk fluid as well as a possible rearrangement of the active sites on the pore surfaces. These changes may be important in the effective elastic properties of the wetted solid grains.

Acknowledgements

The authors thank Dale Morgan and Rosemary Knight of Stanford Geophysics, George Parks and Gordon Brown of Stanford Appl. Earth Sci., Kenneth Mendelson of Marquette University, and R. Pearson of Kaiser Aluminum Research, Pleasanton, CA, for helpful critical discussions.

The study was supported by the Office of Naval Research contract # N00014- 84-K-0560

References

[1]F. Bloch, Nuclear induction, *Phys. Rev. 70, 460 (1946)*

[2]K. Brownstein and C. Tarr, Importance of classical diffusion in NMR studies of water in biological cells, *Phys. Rev. A 19 (6), 2446 (1979)*

[3]M. Cohen and K. Mendelsohn, Nuclear magnetic resonance and the internal geometry of porous rocks, *J. Appl. Phy. 53 (27), 1127 (1982)*

[4]H. Resing, NMR relaxation of adsorbed molecules with emphasis on adsorbed water, *Adv. Mol. Relaxation Processes 3, 199 (1972)*

[5]N. Bloembergen, E. Purcell, and R. Pound, Relaxation effects in NMR absorption, *Phys. Rev. 73 (7), 679 (1948)*

[6]R. Kubo and K. Tomita, A general theory of NMR absorption, *J. Phys. Soc. Jap. 9, 818 (1954)*

[7]V. Morariu and R. Mills, An NMR study of water adsorbed on silica, the influence of cations exchanged on the surface 2, *Zeit. Physik. Chem. Neue. Folge 85, 98 (1972)*

[8]A. Timur, Velocity of compressional waves in porous media at permafrost temperatures, *Geophysics 33 (4), 584 (1968)*

[9]K. Mendelson, Nuclear magnetic relaxation in porous media, *In Proc. Symposium on chemistry and physics of composite media (Edit. by* M. Tomkiewitz and P.N. Sen), Electrochemical Society Press, Pennington, New Jersey, 282 (1985)

[10]G. Engel and H. Hertz, On the negative hydration , A nuclear magnetic resonance study, *Ber. Bunsenges Physik. Chem. 72, 808 (1968)*

[11]J. Jonas, T. Defries, and D. Wilbur, Molecular motions in compressed liquid water, *J. Chem. Phy. 65 (2), 582 (1976)*

[12]K. Mendelson, private communication

[13]J. Emsley, J. Feaney, and L. Sutcliffe, High resolution NMR spectroscopy, *Vol. 1, Pergammon, New York (1965)*

[14]J. Boyce and B. Huberman, Sublattice melting in a superionic conductor, *Solid State Comm. 21, 91 (1977)*

[15]F. Etzler, A statistical thermodynamic model for water near solid interfaces, *J. of Coll. and Int. Sci. 92, 43 (1983)*

[16]J. Fripiat and J. Cases, Thermodynamic and microdynamic behavior of water in clay suspensions and gels, *J. of Coll. and Int. Sci. 89 (2), 378 (1982)*

[17]K. Kadi-Hanafi, Proton NMR studies of one layer hydrates of oriented hectorites, *Clays and Clay Min. 28 (1), 65 (1970)*

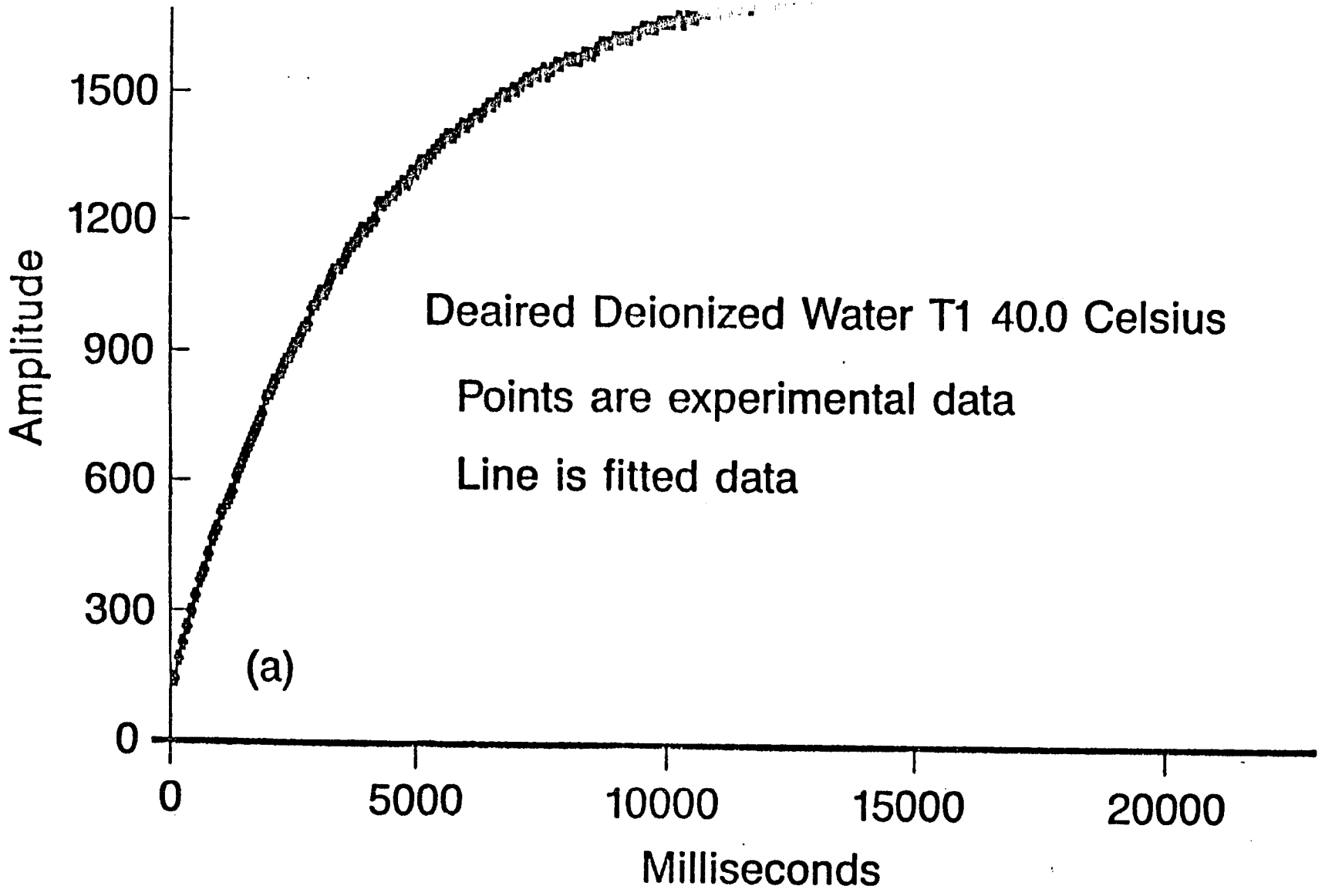

FIG. 1(a). Deionized Water experimental and inversion results.

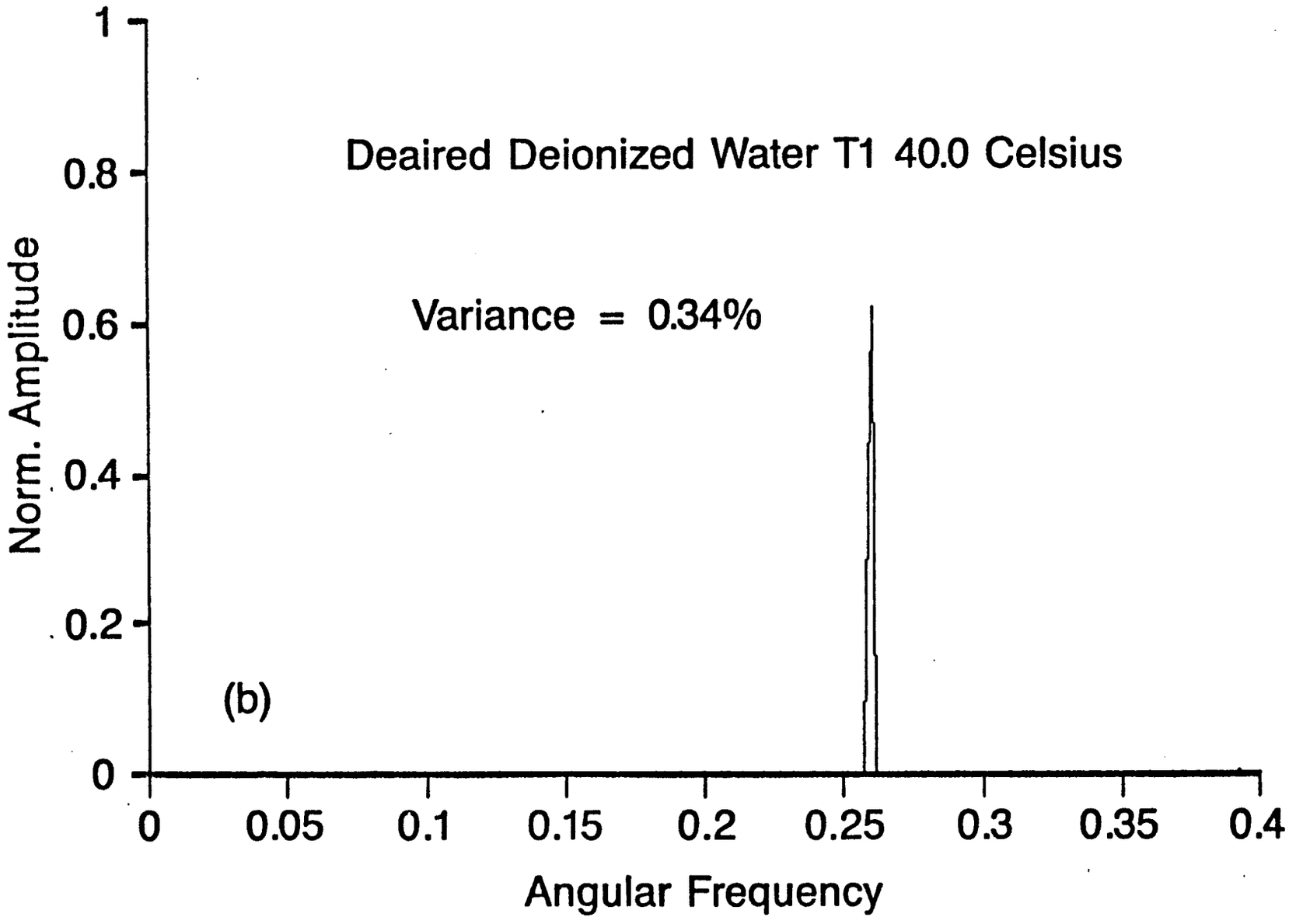

FIG. 1(b). Deionized Water P (ω).

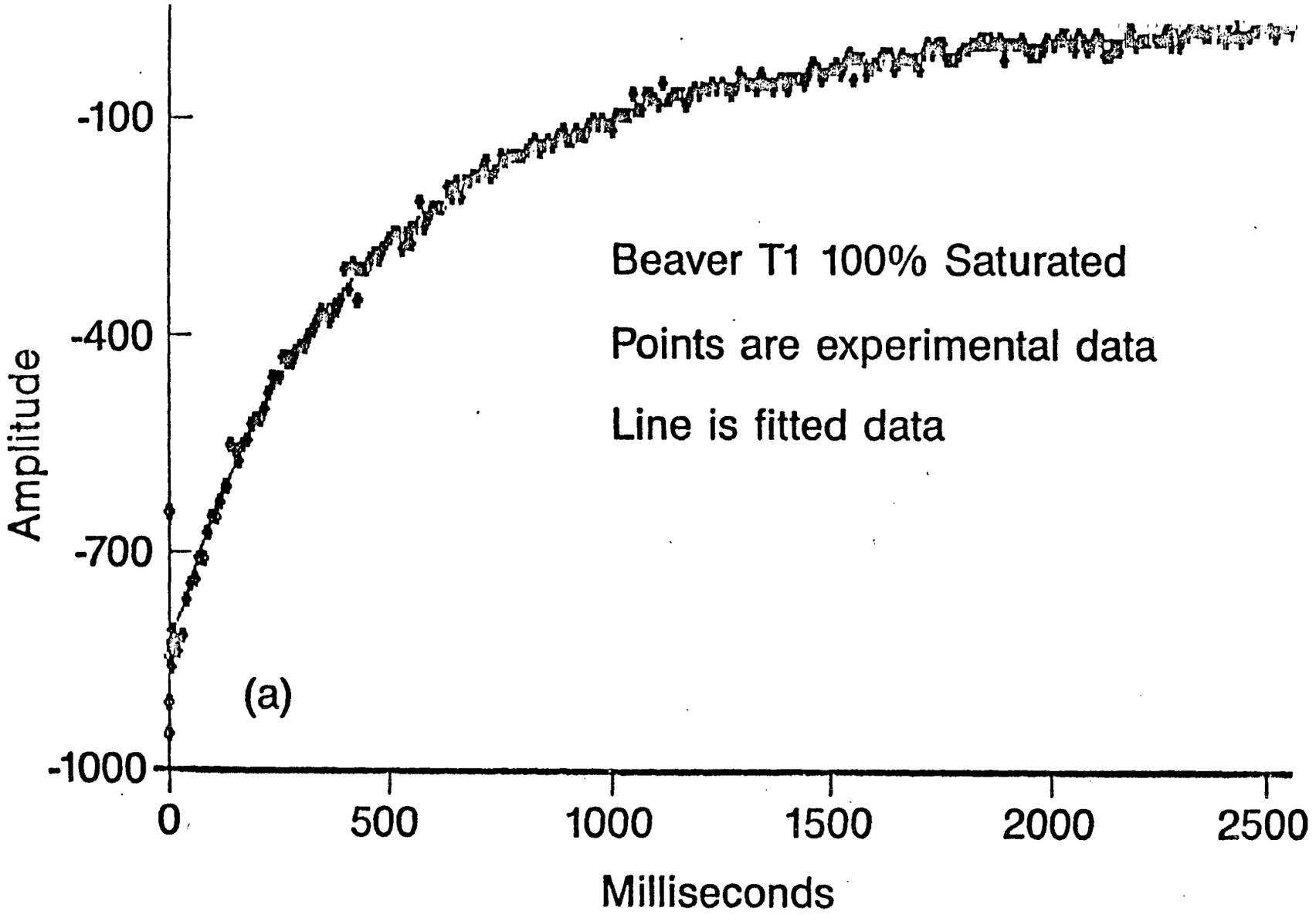

FIG. 2(a). 100% saturated Beaver sandstone experimental and inversion results.

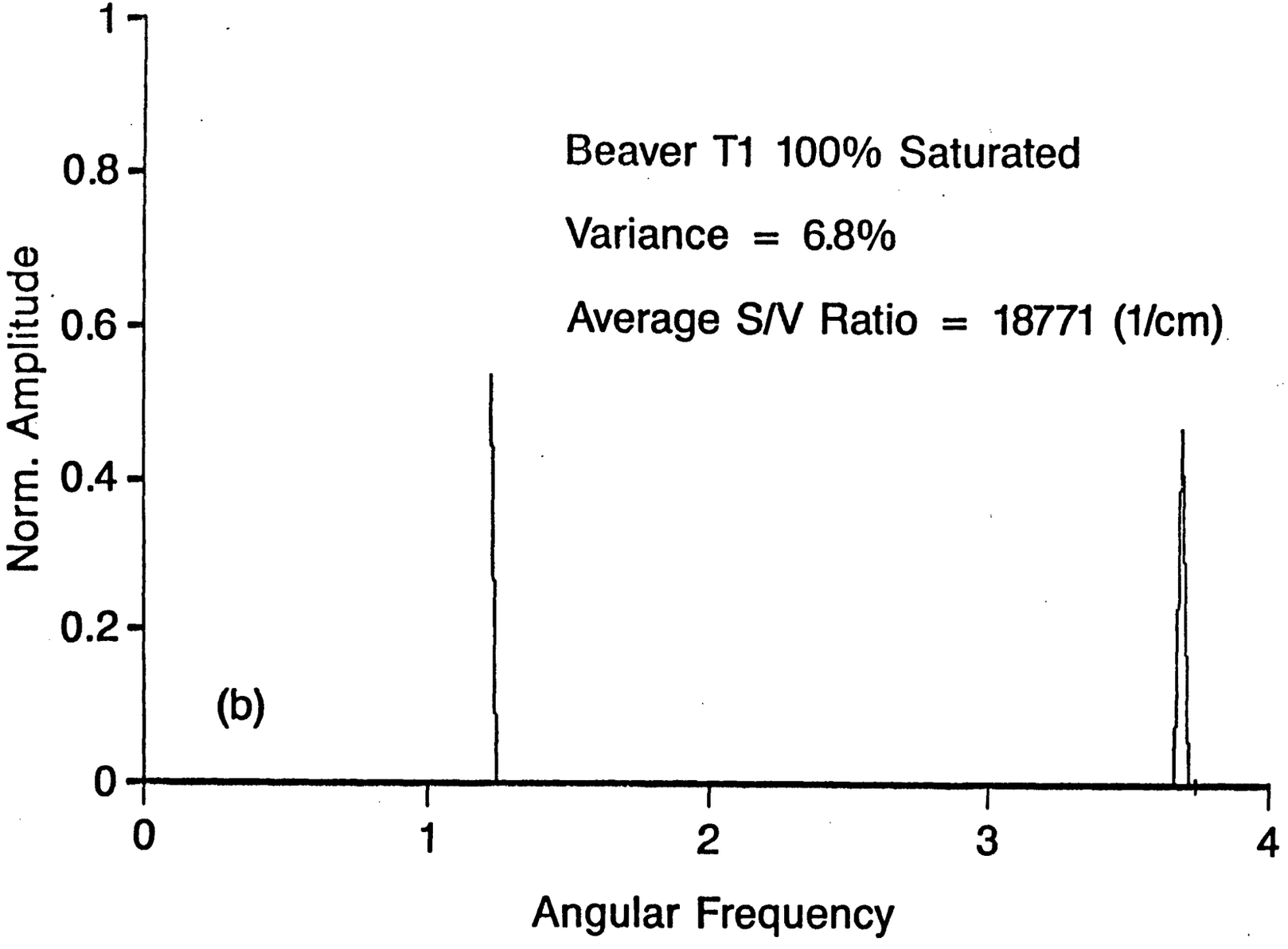

FIG. 2(b). 100% saturated Beaver sandstone P (ω).

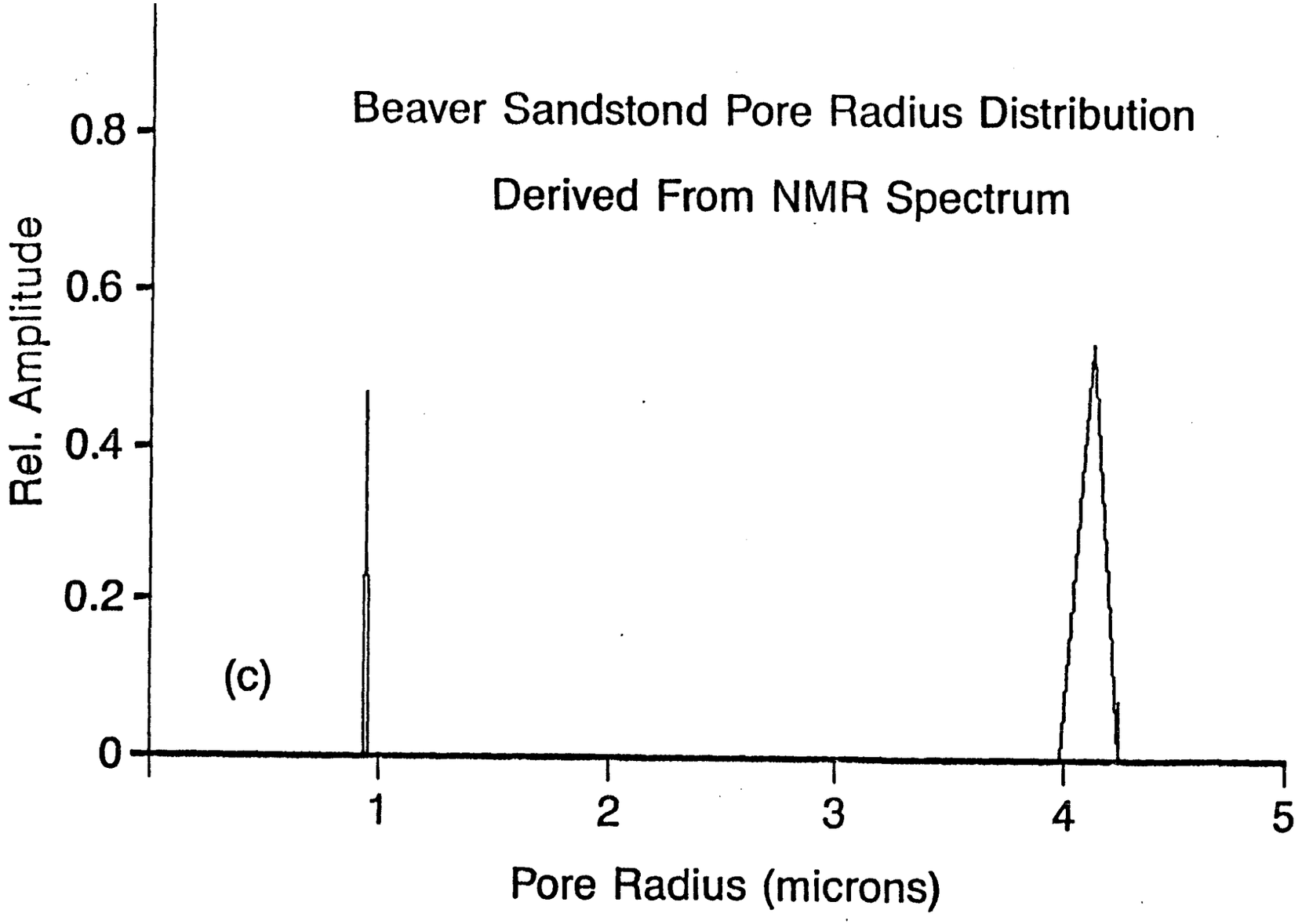

FIG. 2(c). 100% saturated Beaver sandstone NMR inferred pore radius distribution.

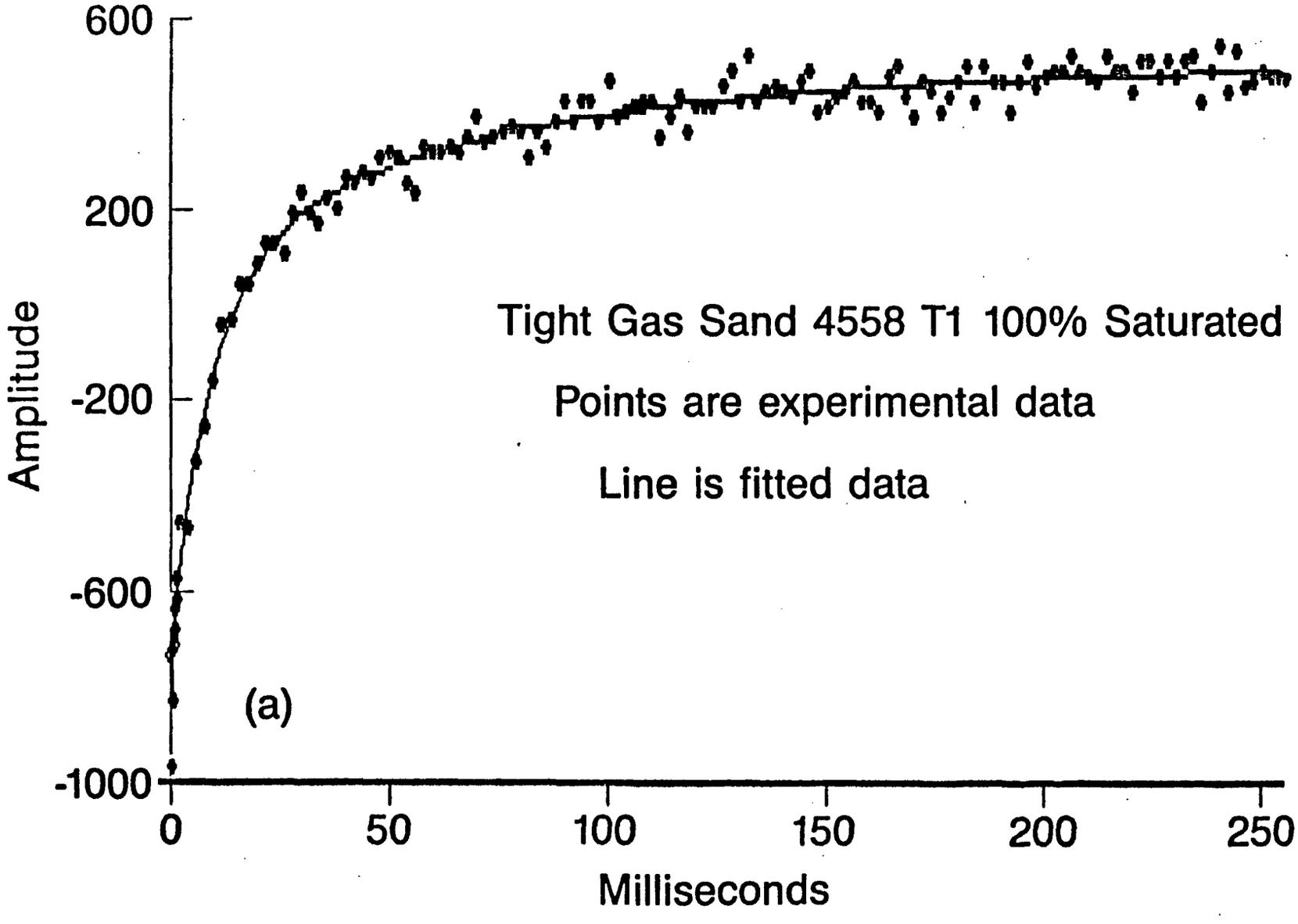

FIG. 3(a). 100% saturated Tight Gas sand 4558 experimental and inversion results.

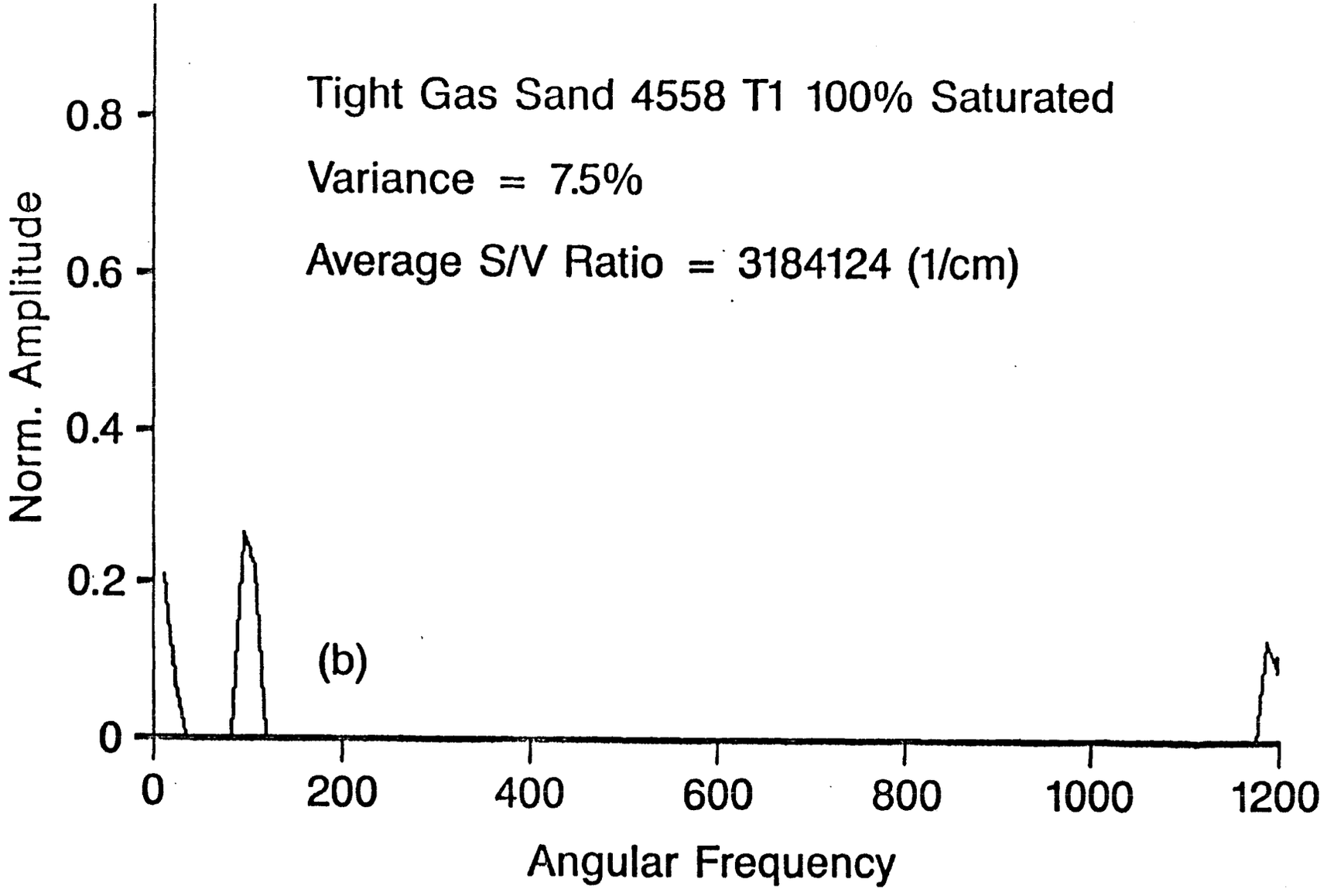

FIG. 3(b). 100% saturated Tight Gas sand 4558 P (ω).

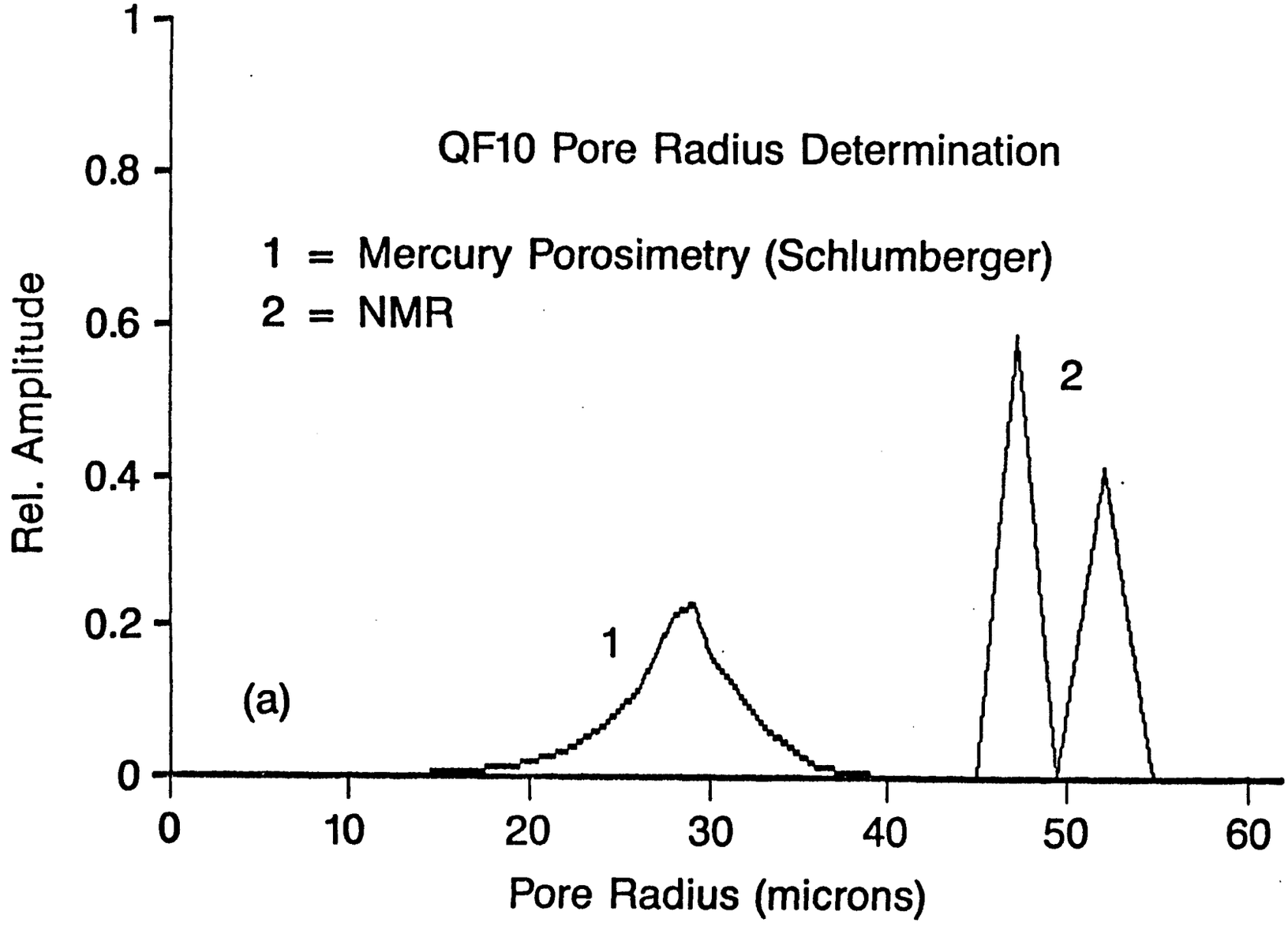

FIG. 4(a). QF10 NMR and mercury porisimetry derived pore radius distributions.

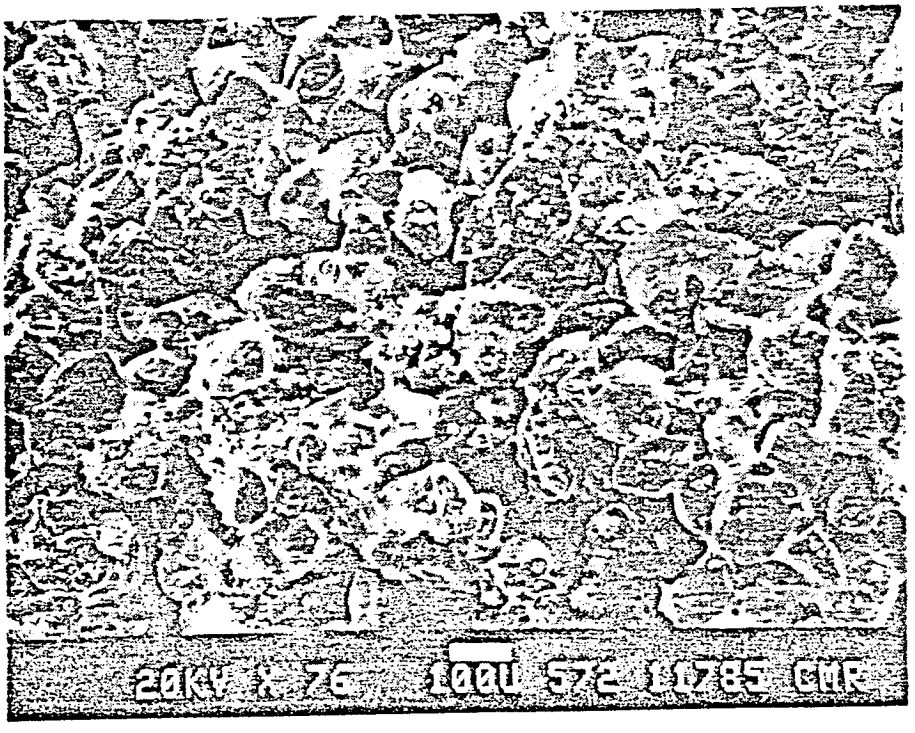

(b)

FIG. 4(b). Scanning electron micrograph of QF10. 100 micron scale is shown on lower right.

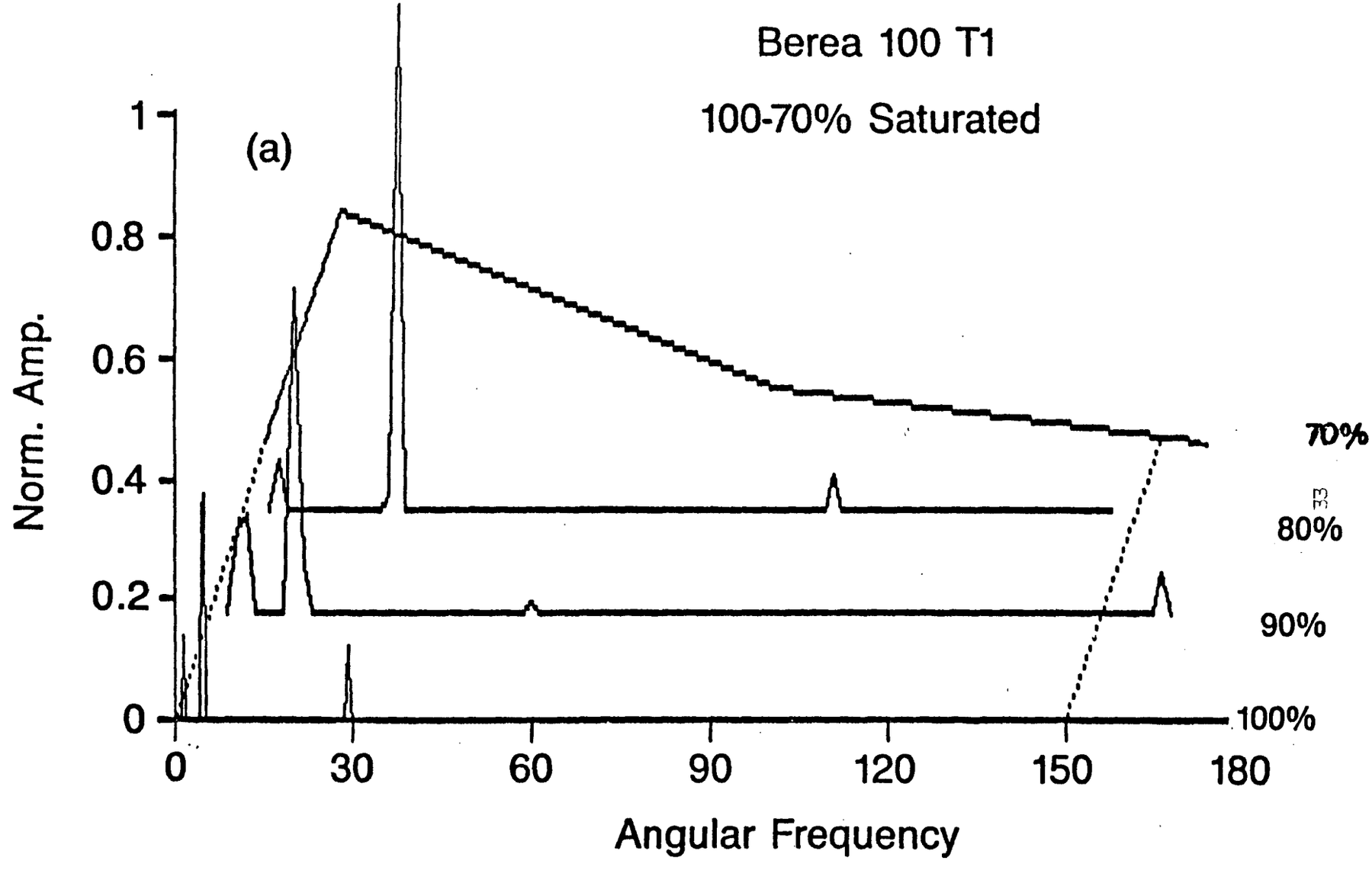

FIG. 5(a). Berea 100 sandstone $P(\omega)$ at 100% through 70% water saturation.

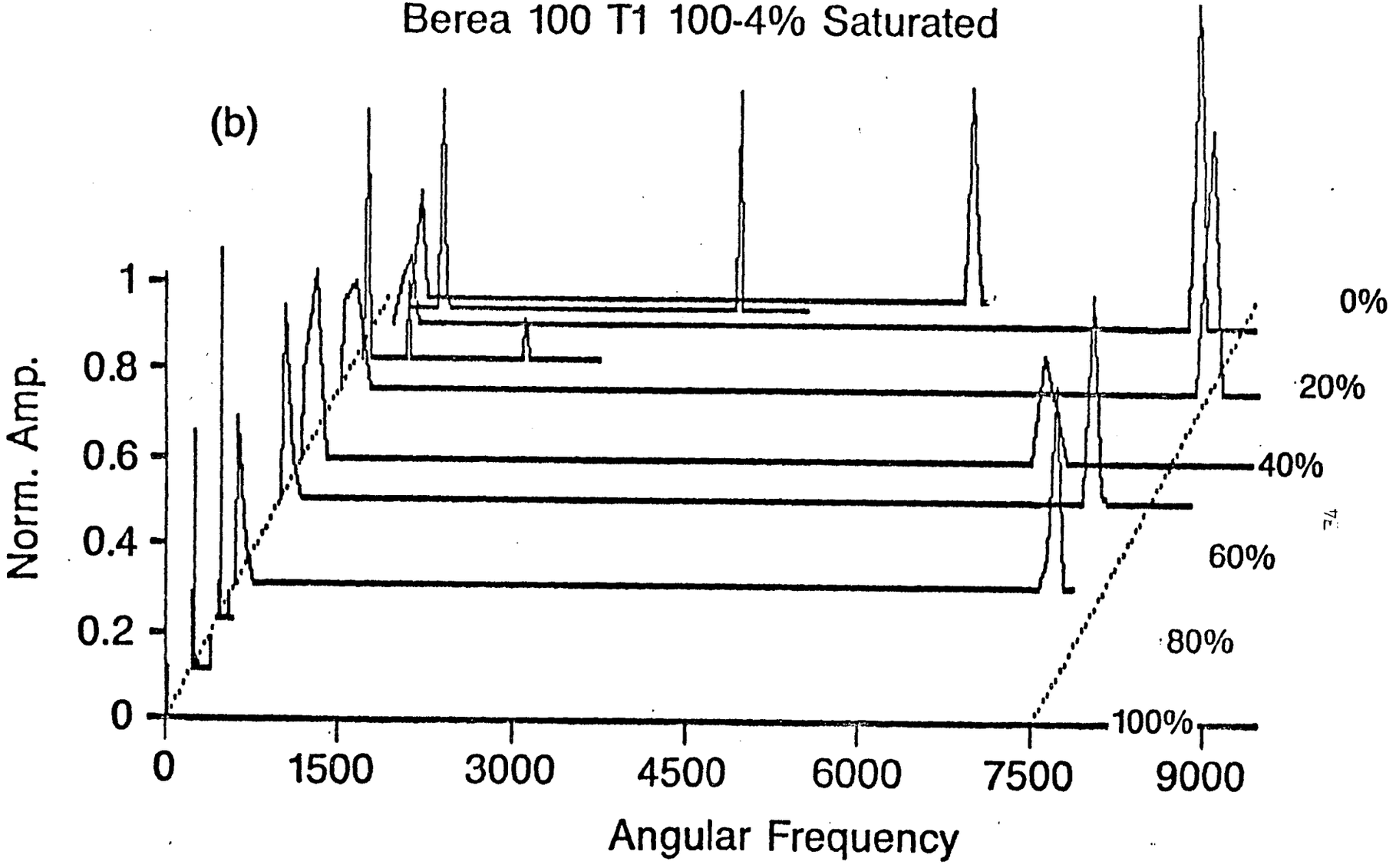

FIG. 5(b). Berea 100 sandstone $P\ (\omega)$ at 100% through 4% water saturation.

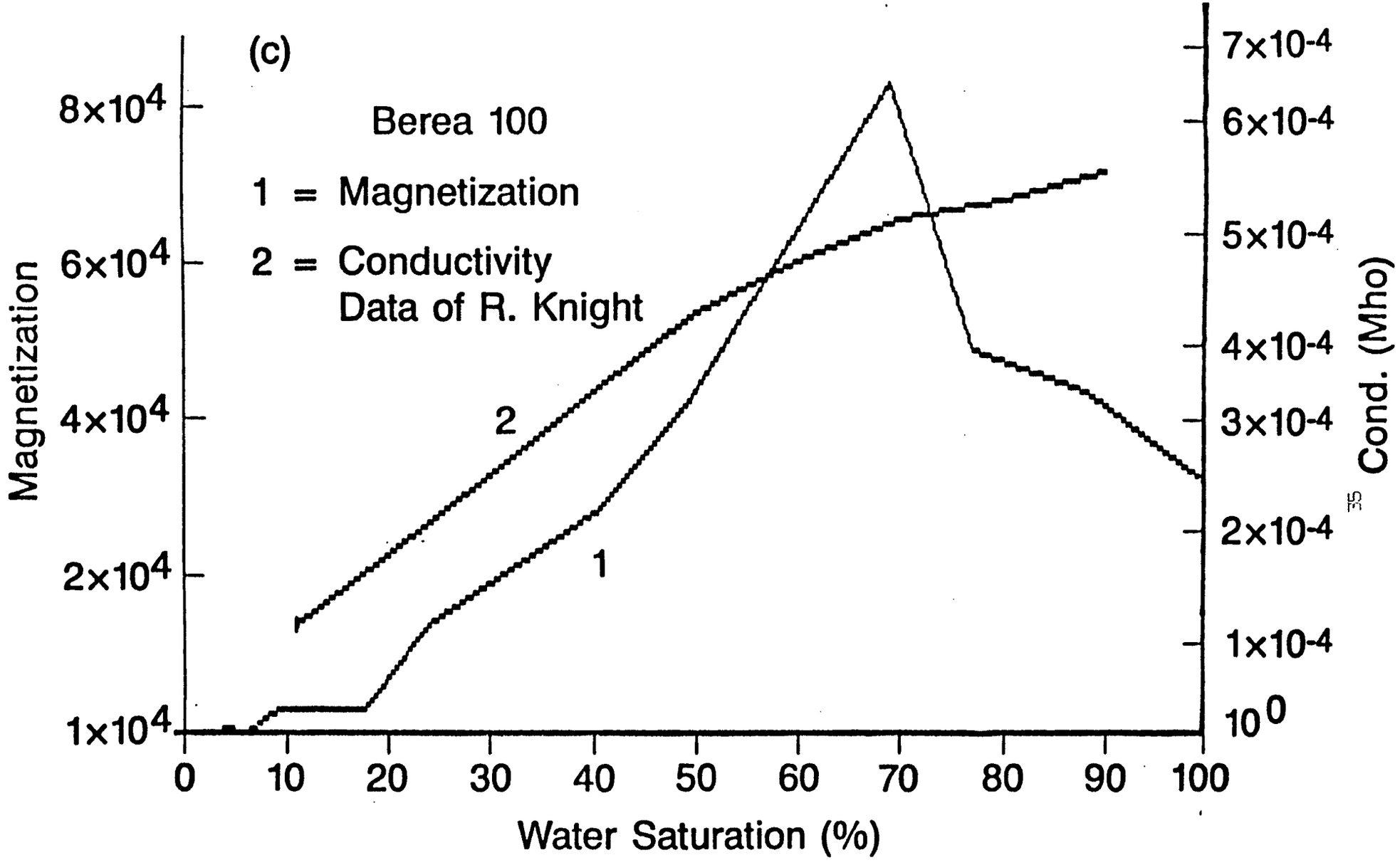

FIG. 5(c). Berea 100 sandstone magnetization and DC conductivity versus water saturation.

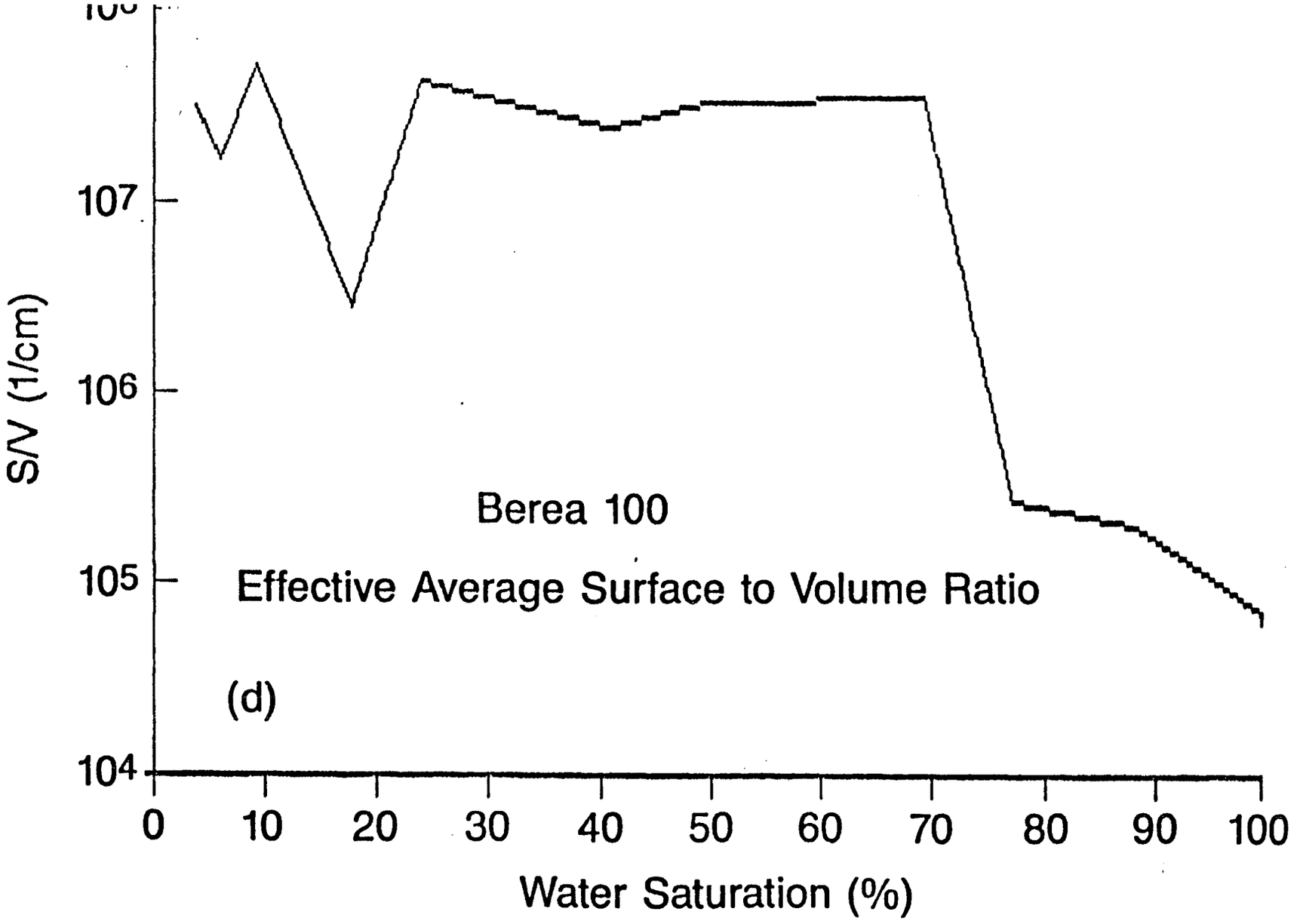

FIG. 5(d). Berea 100 sandstone effective average $\frac{S}{V}$ ratio versus water saturation.

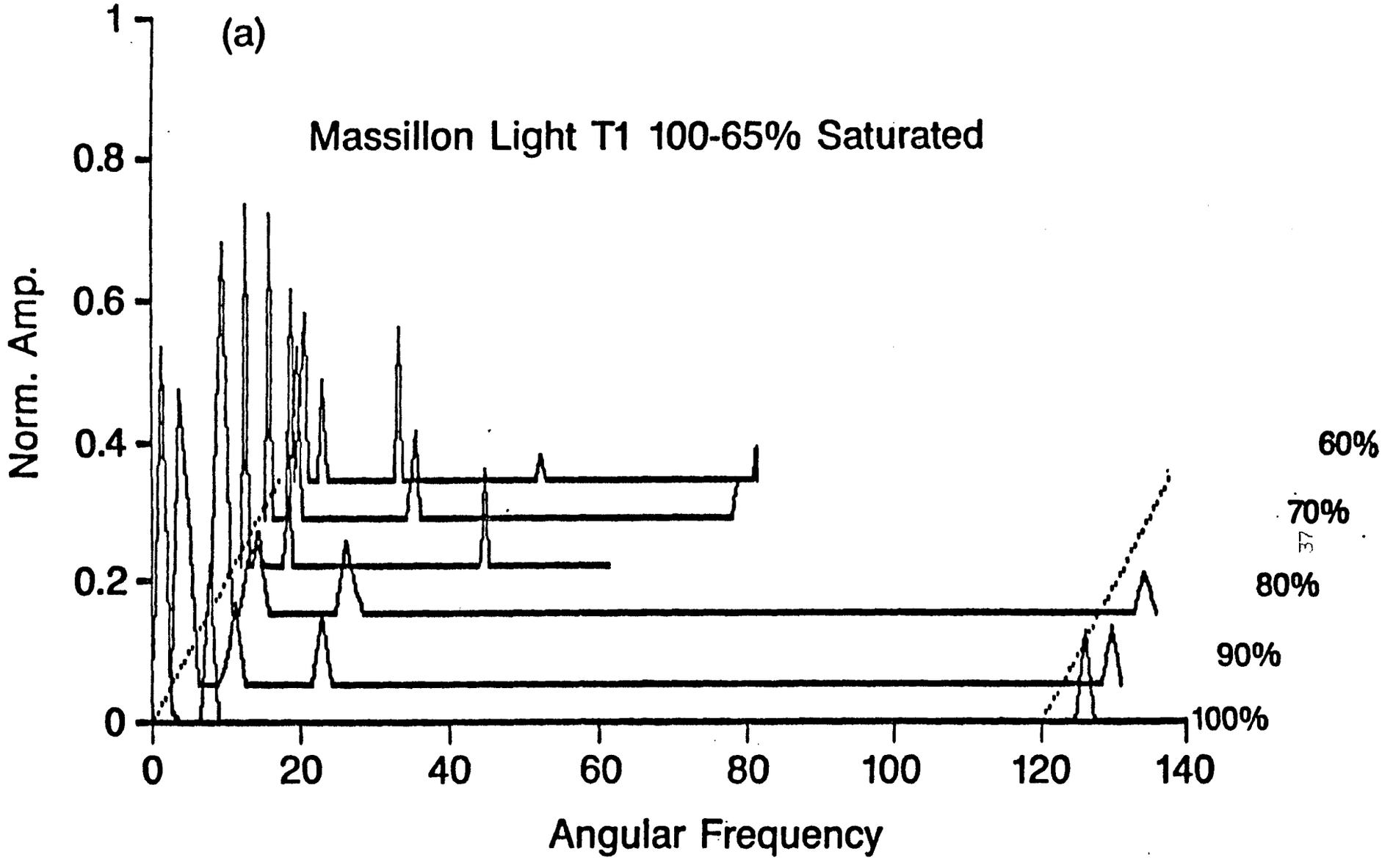

FIG. 6(a). Massillon Light sandstone $P\ (\omega)$ at 100% through 65% water saturation.

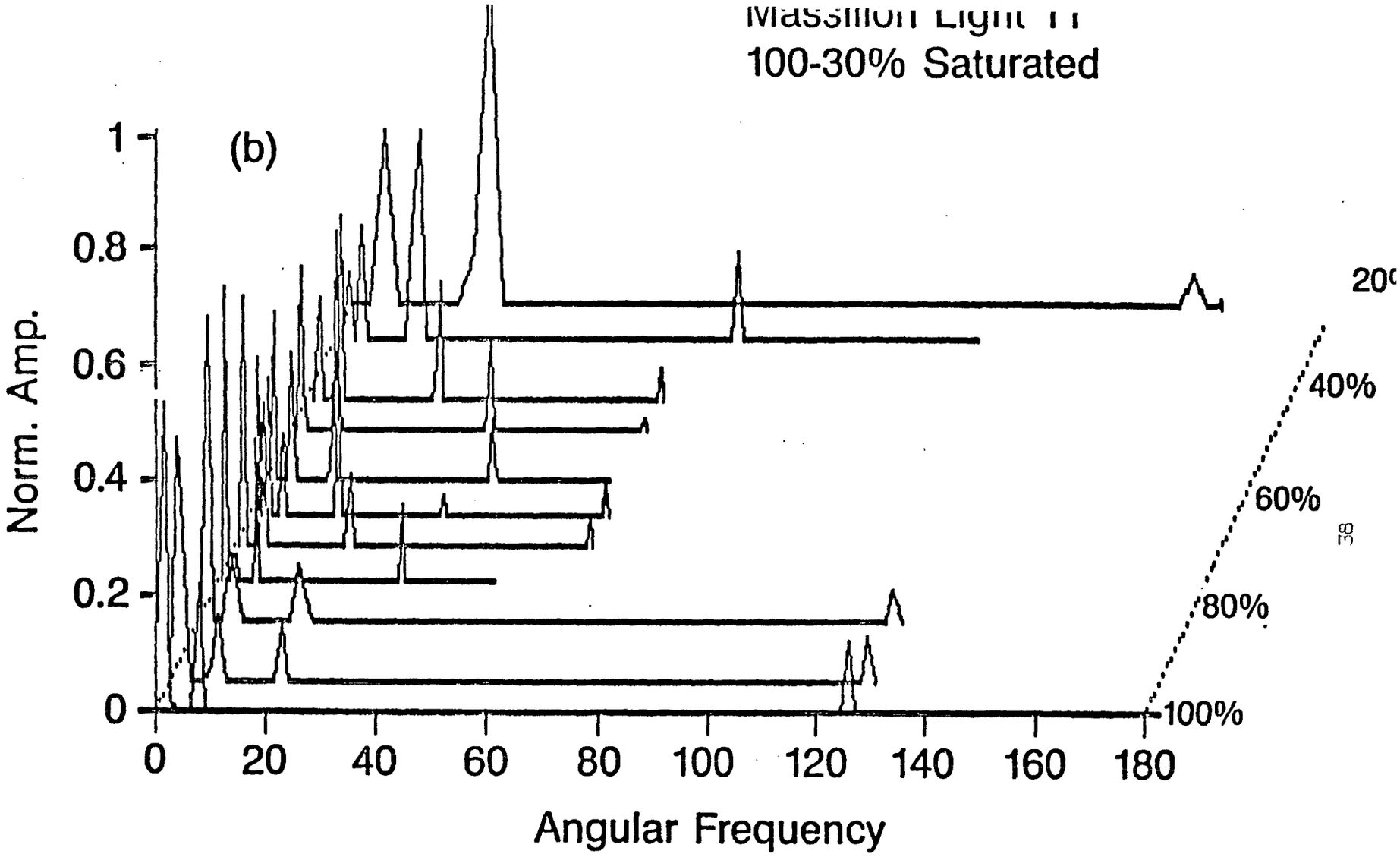

FIG 6(b). Massillon Light sandstone $P\ (\omega)$ at 100% through 30% water saturation.

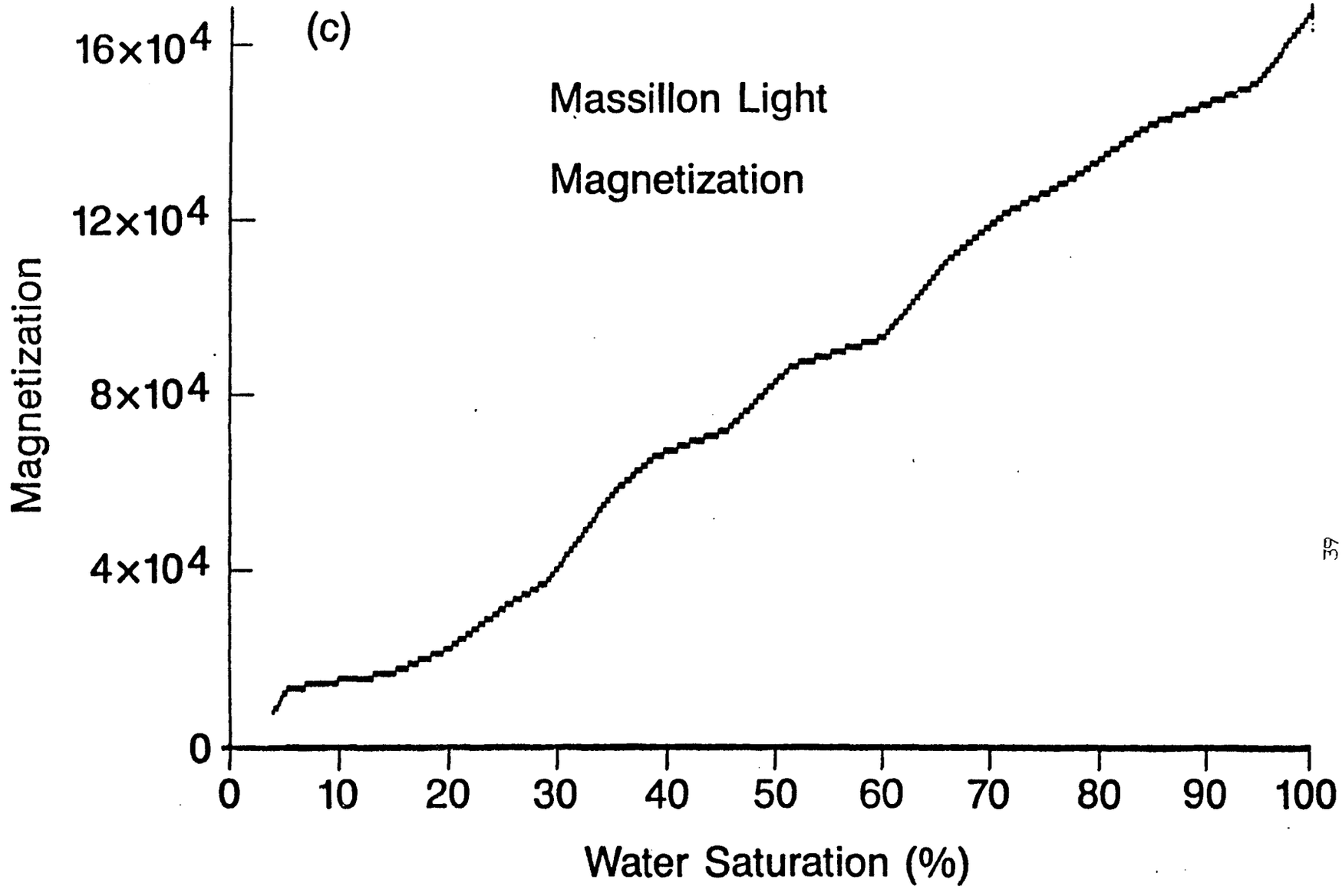

FIG 6(c). Massillon Light sandstone magnetization versus water saturation.

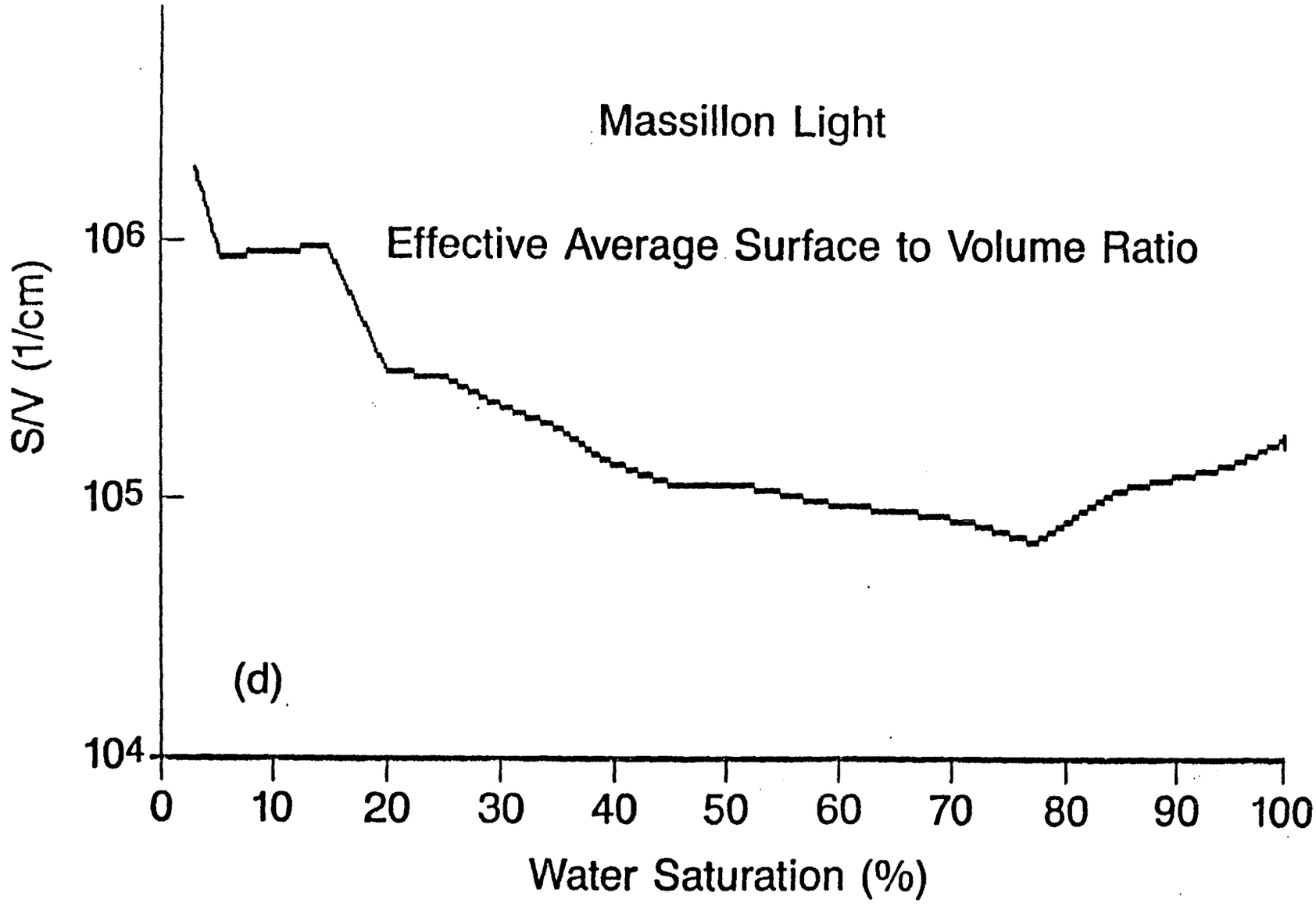

FIG 6(d). Massillon Light sandstone effective average $\frac{S}{V}$ ratio versus water saturation.

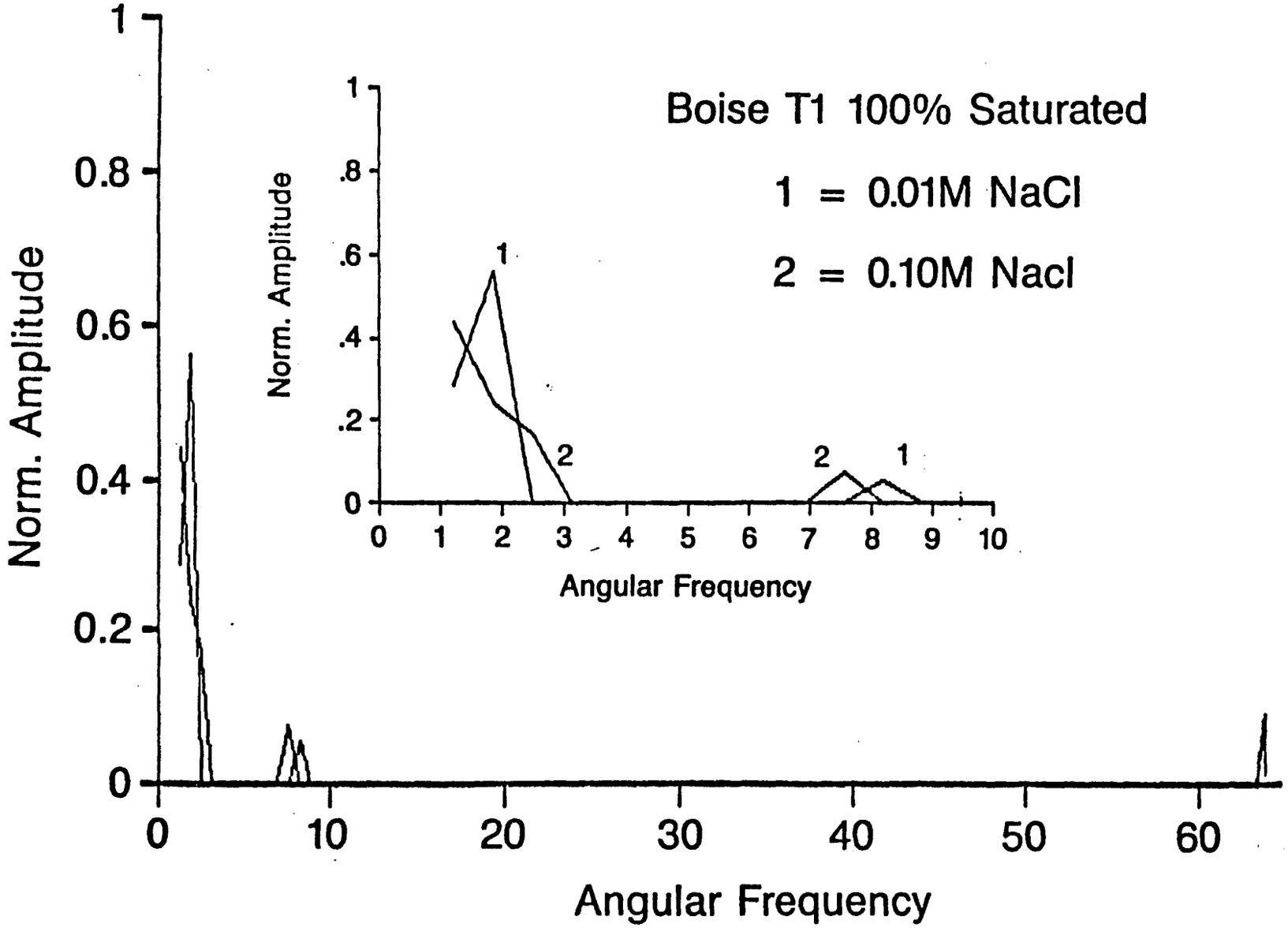

FIG. 7. 100% saturated Boise sandstone $P\ (\omega)$ at 0.01 and 0.1 *Molar* NaCl solutions.

Appendix A - TRY265.FOR NMR inversion program

This program is written in Microsoft FORTRAN 77 which is compatible with mainframe IBM and DIGITAL computers. A limitation of Microsoft FORTRAN is it's inability to accept nondimensionalized arrays. For this purpose a separate program must be written for each combination of N data points and (M + 2) unknowns. The version given here is for 265 data points and 101 unknowns, these being 100 P_i (ω_i)' and M_∞. The places where changes should be made for different combinations of data points and inverted results are denoted in the program comments. The current size of the arrays requires a computer with approximately 256 *Kilobytes* of memory. Since the mainframe FORTRAN implimentations support nondimensionalized arrays a mainframe version may be designed to read the appropriate dimensions so that only one version would be needed.

The current configuration of the program reads in an unformatted data file (BASIC language data file) with the following arrangement of data:

Line 1: XMAX,YMAX,YMIN

Line 2: N

Lines 3 through (N+2): τ_j ,$M(\tau_j)$ $\quad j = 1,2,...N$

where $XMAX$ is the maximum value of τ_j, $YMAX$,$YMIN$ are the maximum and minimum values of $M(\tau_j)$, and N is the number of data points. Note that the τ_j in the data file are in milliseconds, which the program converts to the second scale.

The program is configured in an interactive fashion. It requests the data file name. It prints on the user's screen the procedures through which it goes through. Results of every iteration are printed both on the user's screen and to a printer (refered to as "LPT1"). After concluding the iterative process the program prints both the data $M(\tau_j)$ and the fitted $M(\tau_j)$ to the screen and to a user determined data file. Another user determined datafile will contain the resolved ω_i ,P_i (ω_i) pairs.

The amount of change in ω_{max} and ω_{min} between successive iterations may be adjusted differently than the format in this program. Programing a smaller shrinkage of the ω range can lead to the program terminating with a slightly more detailed distribution of relaxation frequencies, but will cause a longer running time, which is currently about 5 minutes for three iterations using the IBM/XT math coprocesser.

There are numereous examples of relaxation processes which occur in physical systems as a whole and rock physics in particular. Some notable cases are electromagnetic dipolar relaxations, mechanical viscoelastic relaxations, classical geometrical resonances with relaxations. If these are studied in the time domain, an analysis of the rate constants may be made with this program. A version of the program has been applied to neutron spectra from rocks and yielded good results.

```
C       FORTRAN FILE TO INVERT DATA USING CONSTRAINED LEAST SQUARES
C       FOR A USER PICKED AMOUNT OF RELAXATIONS
C        FUNCTION USED IS
C                  <
C       M(t)=MINF- ! A(I)*EXP(-W(I)*t)
C                  <
C       WITH THE CONSTRAINT THAT A(I)>=0.E0
C       W(I) ARE CONSTRAINED BY SAMPLING THEOREM TO LIE BETWEEN
C       WMIN AND WMAX, WHERE WMIN=PI/(t(N)-t(1))
C       AND WMAX=PI/(t(2)-t(1))
c       variable declaration section starts here
        REAL*4 T,M,WMAX,WMIN,W,SUM
        REAL*4 MINF,MAXX,MAXY,MINY,CON,MA,MS
        REAL*4 NORMA,RESW,SV,SVA,RESA,CC,WLCUT,CCM,RNORMO
        REAL*4 WS,Z,AA,RNORM,WCUT,CON1,MAXMA,MINMA,MDIF
        INTEGER*4 INDEX,FLAG,COUNT,WFLAG
        INTEGER*4 I,J,N,NN,I7
        CHARACTER*64 FNAME,FNAME2,FNAME3
$LARGE  MD
        REAL*4 MD
C       DIMENSIONS OF ARRAYS ON NEXT 6 LINES MUST BE
C       CONFIGURED ACCORDING TO
C       NUMBER OF DATA POINTS->HERE SET AT 265
C       NUMBER OF RELAXATIONS->HERE SET AT 100
C       TOTAL NUMBER OF UNKNOWNS->HERE SET AT 100+MINF=101
        DIMENSION T(265),W(100)
        DIMENSION RESW(100),RESA(100),SV(100)
        DIMENSION INDEX(101),WS(101),Z(265)
        COMMON/LION/M(265),MA(265),MS(265)
        COMMON/JACK/MD(265,101)
        COMMON/LIORA/AA(101)
C       M=VECTOR OF MAGNETIZATION=M(T(I))
C       MS=SAME AS M BUT SAVED AFTER GOING TO NNLS
C       MA=PROGRAM PRODUCED VECTOR OF MAGNETIZATION
C       MD=MATRIX OF DIFFERENTIAL VALUES
C       W=VECTOR OF POINTS IN W SPACE WHERE RELAXATIONS ARE
C       AA=VECTOR OF RESOLVED AMPLITUDES AT THESE W
        N=265
C       NOTE THAT NN HERE IS ONLY NUMBER OF RELAXATIONS
C       LATER THE MINF TERM WILL MAKE THIS NN+1
        NN=100
C       FLAG IS FOR NUMBER OF ITERATION, ZERO IS FOR FIRST
        FLAG=0
        DO 30 I=1,N
        DO 30 J=1,NN+1
 30     MD(I,J)=0.0E0
C       INPUTING REAL DATA
C       PROMPTING FOR INPUT FILE
        WRITE (*,6) '        LAP265 INVERSION PROGRAM'
        WRITE (*,6) ' (C) COPYRIGHT STANFORD ROCK PHYSICS PROJECT 1984'
        WRITE (*,6) ' FULL LAPLACE TRANSFORM T1 INVERSION PROGRAM'
        WRITE (*,'(A\)') ' INPUT FILE NAME FOR INVERSION?'
        READ (*,'(A)') FNAME
        OPEN(7,FILE=FNAME,STATUS='OLD',ACCESS='SEQUENTIAL')
        REWIND 7
        WRITE(*,6) ' READING DATA FILE'
  6     FORMAT(A)
C       FORMAT OF DATA FILES USED HERE IS AS FOLLOWS
C       ALL DATA ARE IN UNFORMATTED FORM (BASIC LANGUAGE DATA FILE)
C       FIRST LINE:   MAXX,MAXY,MINY
C       MAXX=MAXIMUM VALUE OF X FOUND IN FILE
C       MAXY=MAXIMUM VALUE OF Y FOUND IN FILE
C       SECOND LINE:   N
C       N=NUMBER OF t,M(t) PAIRS THERE ARE (NUMBER OF DATA POINTS)
C       THIRD THROUGH (N+3) LINES: t,M(t) PAIRS
```

```
      READ (7,*) MAXX,MAXY,MINY
      READ(7,*) N
      DO 16 I=1,N
      READ(7,*) T(I),M(I)
C     TIME VALUES ARE IN MILLISECONDS-CONVERT TO SECONDS
      T(I)=T(I)*1.0E-03
C     CHECK TO SEE IF SOME OF M(I) ARE POSITIVE ELSE
C     ADD A CONSTANT TO MAKE SOME POSITIVE (GET MINF>0)
      CON1=M(I)
   16 CONTINUE
      CLOSE (7)
C     LINEARIZING FIRST TWO POINTS
      M(1)=(M(1)+M(2))/2.0E0
C     REGION TO WRITE INPUT FILE NAME TO PRINTER
      OPEN(6,FILE='LPT1',STATUS='NEW',ACCESS='SEQUENTIAL')
      WRITE(6,*) ' DATAFILE USED FOR INVERSION IS ',FNAME
      CLOSE (6)
      RNORMO=1.E0
      IF (CON1.GT.0.E0) GOTO 76
C     NEXT FOUR LINES ARE FOR CASE OF ALL M(I).LT.0.E0
      CON1=ABS(CON1)+100.0E0
      DO 31 I=1,N
   31 M(I)=M(I)+CON1
      GOTO 125
C     NEXT TWO LINES ARE FOR CASE OF SOME M(I).GT.0.E0
   76 CON1=0.E0
      GOTO 125
c     START ENTERING INVERSION VARIABLES
  125 WMIN=3.140E0/T(N)
      WMAX=3.140E0/(T(2)-T(1))
      IF (FLAG.EQ.1) WMAX=WCUT
      IF (FLAG.EQ.1) WMIN=WLCUT
      CON=(LOG10(WMAX/WMIN))/NN
c     NUMBER OF REQUIRED W POINTS-NN-ALWAYS LESS THAN N
c     HAVE HERE A LOOP TO CHECK THAT NN<N ELSE PROMPT AGAIN
      DW=(WMAX-WMIN)/FLOAT(NN-1)
c     WE NOW FILL UP MATRIX OF EXP(-W*T) WHICH IS MODEL
      WRITE (*,82) ' FILLING MD'
      IF (FLAG.EQ.1) GOTO 378
      NN=NN+1
  378 CC=36.8E0
C     CC IS CUT OFF POINT ,CCM IS CUTOFF VALUE (DAMPING)
      CCM=-1.0E-16
      DO 40 I=2,NN
C     W(I-1)=WMIN*10.E0**((I-2)*CON)
      W(I-1)=WMIN+DW*FLOAT(I-2)
      DO 50 J=1,N
      MD(J,I)=-1.0E0*EXP(-W(I-1)*T(J))
C     CONDITION TO PREVENT INVERSE BLOWING UP
      IF  (W(I-1)*T(J).GE.CC) MD(J,I)=CCM
C     WRITE (6,66) I,J,W(I-1),MD(J,I)
C     FORMAT(2X,I4,2X,I4,2X,F10.4,2X,E20.4)
   50 CONTINUE
   40 CONTINUE
      DO 41 J=1,N
   41 MD(J,1)=1.0E0
      SUM=0.E0
      DO 42 I=1,N
      SUM=SUM+M(I)*M(I)
   42 MS(I)=M(I)
      SUM=SQRT(SUM)
      WRITE (*,82) ' CALLING NNLS'
      RNORM=0.0E0
```

```
C       NOW CALL NNLS=THE NONNEGATIVE LEAST SQUARES SUBROUTINE
        CALL NNLS(MD,N,N,NN,M,AA,RNORM,WS,Z,INDEX,MODE)
C       ************************THE ANSWER FOR THIS ITERATION
C       ********************** HAS BEEN OBTAINED
        GOTO 159
 159    WRITE (*,82) ' ANSWER FOLLOWS'
        OPEN (6,FILE='LPT1',STATUS='OLD',ACCESS='SEQUENTIAL')
        IF (FLAG.EQ.1) WRITE (6,82) ' BANDNARROWED ITERATION'
        WRITE (6,82) ' ANSWER FOLLOWS'
        WRITE (6,179) ' WMIN= ',WMIN,'WMAX= ',WMAX
 179    FORMAT (A,2X,E10.3,2X,A,2X,E10.3)
        AA(1)=AA(1)-CON1
        WRITE (6,69) ' MINF=',AA(1)
  69    FORMAT(A,2X,E10.3)
        WRITE (6,177) ' W=','A(W)='
 177    FORMAT(5X,A,16X,A)
        MDIF=0.0E0
        DO 200 I=2,NN
        MDIF=MDIF+AA(I)
        IF (AA(I).GT.0.0E0) WRITE(6,67) W(I-1),AA(I)
 67     FORMAT(5X,F14.7,5X,E10.3)
 200    CONTINUE
        WRITE(6,192) ' MO-MINF=',MDIF
        WRITE(6,192) ' RNORM=',RNORM
        RNORM=RNORM/SUM
        WRITE(6,192) ' RELATIVE ERROR=',RNORM
 192    FORMAT(A,2X,E10.4)
        WRITE(6,345) ' NUMBERS DIVIDED BY MINF FOLLOW'
 345    FORMAT(A)
        COUNT=0
        NORMA=0.E0
        WRITE (6,177) ' W=','A(W)='
        DO 346 I=2,NN
        NORMA=NORMA+AA(I)
        IF (AA(I).GT.0.0E0) COUNT=COUNT+1
        IF (AA(I).GT.0.0E0) RESW(COUNT)=W(I-1)
        IF (AA(I).GT.0.0E0) RESA(COUNT)=AA(I)
 346    IF (AA(I).GT.0.0E0) WRITE(6,347) W(I-1),AA(I)/ABS(AA(1))
 347    FORMAT(5X,F14.7,5X,E10.3)
 82     FORMAT(A)
        WRITE (6,82) '                    '
C       ***********************************
C       PUTTING IN CONDITION TO LOOP BACK WITH EXPANDED
C       FREQUENCY SCALE
C       PROGRAM WILL FIND NEW HIGH W CUTOFF=WCUT
C       AND LOW W CUTOFF=WLCUT
C       CRITERIA ARE ---WCUT IS THE LARGER OF
C                        ((LAST NON-ZERO W VALUE)+ DW)
C                           (1.5 * (LAST NON-ZERO W VALUE))
C       WLCUT IS THE GREATER OF
C                       ((FIRST NON-ZERO W VALUE) - DW)
C                          (WMIN)
        WFLAG=0
 169    DO  292 I=2,NN
        IF (WFLAG.EQ.1) GOTO 292
        IF (AA(I).GT.0.E0) WLCUT=W(I-1)
        IF (AA(I).GT.0.E0) WFLAG=1
 292    IF (AA(I).GT.0.E0) WCUT=W(I-1)
        IF (FLAG.EQ.0) WCUT=WCUT+DW
        WLCUT=WLCUT-DW
        IF (WLCUT.LE.WMIN) WLCUT=WMIN
        IF (FLAG.EQ.1.AND.WCUT+DW.GT.1.5E0*WCUT) WCUT=WCUT+DW
        IF (FLAG.EQ.1.AND.WCUT+DW.LT.1.5E0*WCUT) WCUT=1.5E0*WCUT
        IF (FLAG.EQ.1) FLAG=0
```

```
      IF (WCUT.LT.WMAX) FLAG=1
C     CONDITIONING A NEW ITERATION ON THE IMPROVEMENT IN
C     THE ERROR WHICH THIS ITERATION HAS GIVEN
C     CHECK FIRST THAT RNORM<RNORMO*.99
      IF (RNORM.GT.RNORMO*.99) GOTO 175
      RNORMO=RNORM
      IF (FLAG.EQ.0) GOTO 175
      DO 293 I=1,N
 293  M(I)=MS(I)
      CLOSE (6)
      GOTO 125
C     ************************************************************
C     FINAL PRINTOUT SECTION FOLLOWS
C     CHECKING TO SEE THE CLOSENESS BETWEEN REAL RESULTS
C     AND PROGRAM PRODUCED RESULTS
 175  WRITE (6,345) ' STATISTICS OF RELAXATIONS FOLLOW'
C     CALCULATE TAUS,SURFACE TO VOLUME RATIOS,AVERAGE SURFACE
C     TO VOLUME FOR ROCK ,PERCENTAGES ETCETRA
      DO 333 I=1,COUNT
 333  SV(I)=(RESW(I)-0.2595E0)*1.0E4
      SVA=0.E0
      DO 334 I=1,COUNT
      WRITE (6,335) ' A(W)=',RESA(I),'PERCENT=',RESA(I)*100.E0/NORMA
 335  FORMAT(A,2X,E10.4,2X,A,2X,F14.5)
      WRITE (6,336) ' W=',RESW(I),'TAU=',1.0E0/RESW(I)
 336  FORMAT(A,2X,F14.5,2X,A,2X,E10.4)
      WRITE (6,337) ' SUR/VOL=',SV(I)
 337  FORMAT(A,2X,E15.4)
      SVA=SVA+SV(I)*RESA(I)/NORMA
 334  CONTINUE
      WRITE (6,338) ' AVERAGE SUR/VOL=',SVA
 338  FORMAT(A,2X,E15.4)
      DO 321 I=1,N
      MA(I)=AA(1)
      DO 321 J=2,NN
      IF (W(J-1)*T(I).GE.36.8) GOTO 321
      MA(I)=MA(I)-AA(J)*EXP(-W(J-1)*T(I))
 321  CONTINUE
C     NOW PRINT THEM TOGETHER
      WRITE (6,345) ' REAL AND PROGRAM PRODUCED M(I) FOLLOW'
      WRITE (6,349) 'TIME(MS)','REAL M(t)','FITTED M(t)'
      MAXMA=-1.0E-13
      MINMA=1.0E13
 349  FORMAT(8X,A,11X,A,12X,A)
      DO 322 I=1,N
      IF (MA(I).GT.MAXMA) MAXMA=MA(I)
      IF (MA(I).LT.MINMA) MINMA=MA(I)
      WRITE (6,323) T(I)*1.E03,MS(I)-CON1,MA(I)
 323  FORMAT(2X,E15.4,2X,E15.4,2X,E15.4)
 322  CONTINUE
      WRITE (6,456)
 456  FORMAT(1H1)
      CLOSE (6)
C     ********************END OF PRINTING ****************************
C     DATA STORAGE SECTION FOLLOWS
C     PROMPT FOR STORAGE FILE
      WRITE(*,'(A\)') ' INPUT W,A(W) STORAGE FILE NAME?'
      READ(*,'(A)') FNAME2
      WRITE(*,'(A\)') ' T(I),MA(I) STORAGE FILE NAME?'
      READ(*,'(A)') FNAME3
      OPEN(8,FILE=FNAME2,STATUS='NEW',ACCESS='SEQUENTIAL')
      REWIND 8
      MAXX=W(NN-1)
```

```
      MAXY=-1.E-13
      MINY=1.0E+13
      DO 562 I=2,NN
      AA(I)=ABS(AA(I))
      IF (AA(I).GT.MAXY) MAXY=AA(I)
  562 IF (AA(I).LT.MINY) MINY=AA(I)
      WRITE (8,*) MAXX,MAXY/NORMA,MINY/NORMA
      WRITE (8,*) NN-1
      DO 563 I=2,NN
  563 WRITE (8,*) W(I-1),AA(I)/NORMA
      CLOSE (8)
C     NOW SEND T(I),MA(I) TO FILE
      OPEN(8,FILE=FNAME3,STATUS='NEW',ACCESS='SEQUENTIAL')
      MAXX=T(N)*1.0E03
      WRITE (8,*) MAXX,MAXMA,MINMA
      WRITE (8,*) N
      DO 568 I=1,N
  568 WRITE (8,*) T(I)*1.0E03,MA(I)
      CLOSE (8)
      STOP
      END
C     ************************************************************
C     ************************************************
C     ******************************************
C     ********************************************
C     SUBROUTINE NNLS-NONNEGATIVE LEAST SQUARES FOLLOWS
C     WRITTEN BY LAWSON AND HANSON IN "SOLVING LEAST SQUARES
C     PROBLEMS",PRENTICE HALL,1974
C     PARAMETERS OF SUBROUTINE FOLLOW
C     A(M,N)=DIFFERENTIAL MATRIX
C     X(N)=UNKNOWN VECTOR OF VARIABLES
C     B(M)=RESULT VECTOR
C     SUCH THAT A * X = B
C     RNORM=EUCLIDEAN NORM OF THE RESIDUAL VECTOR
C     W(N)=ARRAY OF WORKING SPACE-DUAL SOLUTION VECTOR
C     ZZ(M)=ARRAY OF WORKING SPACE
C     INDEX(N)=INTEGER WORKING ARRAY
C     ON EXIT THE CONTENTS OF THE ARRAY DEFINE SETS P AND Z
C     AS FOLLOWS
C     INDEX(1) THRU INDEX(NSETP) = SET P
C     INDEX(IZ1) THRU INDEX(IZ2) = SET Z
C     IZ1=NSETP+1 =NPP1
C     IZ2=N
C     MODE IS A SUCCESS-FAILURE FLAG WITH THE FOLLOWING MEANING
C     1 THE SOLUTION HAS BEEN SUCCESSIVELY COMPUTED
C     2 THE DIMENSIONS OF THE PROBLEM ARE BAD(M<0 OR N<0)
C     3 ITERATION COUNT EXCEEDED. MORE THEN 3*N ITERATIONS
      SUBROUTINE NNLS (A,MDA,M,N,B,X,RNORM,W,ZZ,INDEX,MODE)
      DIMENSION A(MDA,N),B(M),X(N),W(N),ZZ(M)
      INTEGER INDEX(N)
      ZERO=0.E0
      ONE=1.E0
      TWO=2.E0
      FACTOR=0.01E0
C
      MODE=1
      IF (M.GT.0.AND.N.GT.0) GOTO 10
      MODE=2
      RETURN
   10 ITER=0
      ITMAX=3*N
C     INITIALIZE THE ARRAYS INDEX AND X
      DO 20 I=1,N
```

```
      X(I)=ZERO
   20 INDEX(I)=I
C
      IZ2=N
      IZ1=1
      NSETP=0
      NPP1=1
C
C     MAIN LOOP BEGINS HERE **********************************
   30 CONTINUE
C     QUIT IF ALL COEFFICIENTS ARE ALREADY IN THE SOLUTION
C     OR IF M COLS OF A HAVE BEEN TRIANGULARIZED
      IF (IZ1.GT.IZ2.OR.NSETP.GE.M) GOTO 350
C     COMPUTE COMPONENTS OF THE DUAL (NEGATIVE GRADIENT) VECTOR
C     W
      DO 50 IZ=IZ1,IZ2
      J=INDEX(IZ)
      SM=ZERO
      DO 40 L=NPP1,M
   40 SM=SM+A(L,J)*B(L)
   50 W(J)=SM
C     FIND LARGEST POSITIVE W(J)
   60 WMAX=ZERO
      DO 70 IZ=IZ1,IZ2
      J=INDEX(IZ)
      IF(W(J).LE.WMAX) GOTO 70
      WMAX=W(J)
      IZMAX=IZ
   70 CONTINUE
C
C     IF WMAX.LE.0 GO TO TERMINATION
C     THIS INDICATES SATISFACTION OF THE KUHN-TUCKLER CONDITIONS
      IF (WMAX) 350,350,80
   80 IZ=IZMAX
      J=INDEX(IZ)
C
C     THE SIGN OF W(J) IS OK FOR J TO BE MOVED TO SET P
C     BEGIN THE TRANSFORMATION AND CHECK NEW DIAGONAL ELEMENT
C     TO AVOID NEAR LINEAR DEPENDENCE
C
      ASAVE=A(NPP1,J)
      CALL H12(1,NPP1,NPP1+1,M,A(1,J),1,UP,DUMMY,1,1,0)
      UNORM=ZERO
      IF (NSETP.EQ.0) GOTO 100
      DO 90 L=1,NSETP
   90 UNORM=UNORM+A(L,J)**2
  100 UNORM=SQRT(UNORM)
      IF (DIFF(UNORM+ABS(A(NPP1,J))*FACTOR,UNORM)) 130,130,110
C
C     COL J IS SUFFICIENTLY INDEPENDENT COPY B INTO ZZ,UPDATE ZZ
C     AND SOLVE FOR ZTEST(=PROPOSED NEW VALUE FOR X(J))
  110 DO 120 L=1,M
  120 ZZ(L)=B(L)
      CALL H12(2,NPP1,NPP1+1,M,A(1,J),1,UP,ZZ,1,1,1)
      ZTEST=ZZ(NPP1)/A(NPP1,J)
C
C     SEE IF ZTEST IS POSITIVE
      IF (ZTEST) 130,130,140
C
C     REJECT J AS A CANDIDATE TO BE MOVED FROM SET Z TO SET P
C     RESTORE A(NPP1,J),SET W(J)=0., AND LOOP BACK TO TEST DUAL
C     COEFFS AGAIN
  130 A(NPP1,J)=ASAVE
```

```
      W(J)=ZERO
      GOTO 60
C
C     THE INDEX J=INDEX(IZ) HAS BEEN SELECTED TO BE MOVED FROM SET Z
C     TO SET P. UPDATE B,UPDATE INDICES, APLLY HOUSEHOLDER
C     TRANSFORMATIONS TO COLS IN NEW SET Z, ZERO SUBDIAGONAL
C     ELTS IN COL J, SET W(J)=0.
 140  DO 150 L=1,M
 150  B(L)=ZZ(L)
C
      INDEX(IZ)=INDEX(IZ1)
      INDEX(IZ1)=J
      IZ1=IZ1+1
      NSETP=NPP1
      NPP1=NPP1+1
C
      IF (IZ1.GT.IZ2) GOTO 170
      DO 160 JZ=IZ1,IZ2
      JJ=INDEX(JZ)
 160  CALL H12(2,NSETP,NPP1,M,A(1,J),1,UP,A(1,JJ),1,MDA.1)
 170  CONTINUE
C
      IF (NSETP.EQ.M) GOTO 190
      DO 180 L=NPP1,M
 180  A(L,J)=ZERO
 190  CONTINUE
C
      W(J)=ZERO
C     SOLVE THE TRIANGULAR SYSTEM
C     STORE THE SOLUTION TEMPORARILY IN ZZ
      ASSIGN 200 TO NEXT
      GOTO 400
 200  CONTINUE
C     SECONDARY LOOP BEGINS HERE**************************
C
C     ITERATION COUNTER
 210  ITER=ITER+1
      WRITE(*,600) ' ITER=',ITER
 600  FORMAT(A,2X,I4)
      IF (ITER.LE.ITMAX) GOTO 220
      MODE=3
      WRITE (6,440) ' NNLS QUITING ON ITERATION COUNT'
      GOTO 350
 220  CONTINUE
C
C     SEE IF ALL NEW CONSTRAINED COEFFS ARE FEASIBLE
C     IF NOT COMPUTE ALPHA
      ALPHA=TWO
      DO 240 IP=1,NSETP
      L=INDEX(IP)
      IF (ZZ(IP)) 230,230,240
C
 230  T=-X(L)/(ZZ(IP)-X(L))
      IF (ALPHA.LE.T) GOTO 240
      ALPHA=T
      JJ=IP
 240  CONTINUE
C
C     IF ALL NEW CONSTRIANED COEFFS ARE FEASIBLE THEN ALPHA WILL
C     STILL=2. IF SO EXIT FROM SECONDARY LOOP TO MAIN LOOP
      IF (ALPHA.EQ.TWO) GOTO 330
C
```

```
C
C       OTHERWISE USE ALPHA WHICH WILL BE BETWEEN 0. AND 1. TO
C       INTERPOLATE BETWEEN THE OLD X AND THE NEW ZZ
        DO 250 IP=1,NSETP
        L=INDEX(IP)
 250    X(L)=X(L)+ALPHA*(ZZ(IP)-X(L))
C
C       MODIFY A AND B AND THE INDEX ARRAYS TO MOVE COEFF I FROM SET P
C       TO SET Z
C
        I=INDEX(JJ)
 260    X(I)=ZERO
C
        IF (JJ.EQ.NSETP) GOTO 290
        JJ=JJ+1
        DO 280 J=JJ,NSETP
        II=INDEX(J)
        INDEX(J-1)=II
        CALL G1 (A(J-1,II),A(J,II),CC,SS,A(J-1,II))
        A(J,II)=ZERO
        DO 270 L=1,N
        IF (L.NE.II) CALL G2 (CC,SS,A(J-1,L),A(J,L))
 270    CONTINUE
 280    CALL G2 (CC,SS,B(J-1),B(J))
 290    NPP1=NSETP
        NSETP=NSETP-1
        IZ1=IZ1-1
        INDEX(IZ1)=I
C
C       SEE IF THE REMAINING COEFFS IN SET P ARE FEASIBLE
C       THEY SHOULD BE BECAUSE OF THE WAY ALPHA WAS DETERMINED.
C       IF ANY ARE INFEASIBLE IT IS DUE TO ROUND OFF ERROR.
C       ANY THAT ARE NONPOSITIVE WILL BE SET TO ZERO AND MOVED
C       FROM SET P TO SET Z
C
        DO 300 JJ=1,NSETP
        I=INDEX(JJ)
        IF (X(I)) 260,260,300
 300    CONTINUE
C
C       COPY B INTO ZZ. THEN SOLVE AGAIN AND LOOP BACK
C
        DO 310 I=1,M
 310    ZZ(I)=B(I)
        ASSIGN 320 TO NEXT
        GOTO 400
 320    CONTINUE
        GOTO 210
C       END OF SECONDARY LOOP**********************************
C
 330    DO 340 IP=1,NSETP
        I=INDEX(IP)
 340    X(I)=ZZ(IP)
C       ALL NEW COEFFS ARE POSITIVE. LOOP BACK TO BEGINNING
        GOTO 30
C
C       END OF MAIN LOOP
C
C       COME HERE FOR TERMINATION. COMPUTE NORM OF THE
C       FINAL RESIDUAL VECTOR
 350    SM=ZERO
        IF (NPP1.GT.M) GOTO 370
```

```
      DO 360 I=NPP1,M
 360  SM=SM+B(I)**2
      GOTO 390
 370  DO 380 J=1,N
 380  W(J)=ZERO
 390  RNORM=SQRT(SM)
      RETURN
C
C
C     THE FOLLOWING BLOCK OF CODE IS USED AS AN INTERNAL SUBROUTINE
C     TO SOLVE THE TRIANGULAR SYSTEM, PUTTING THE SOLUTION IN
C     ZZ(I)
 400  DO 430 L=1,NSETP
      IP=NSETP+1-L
      IF (L.EQ.1) GOTO 420
      DO 410 II=1,IP
 410  ZZ(II)=ZZ(II)-A(II,JJ)*ZZ(IP+1)
 420  JJ=INDEX(IP)
 430  ZZ(IP)=ZZ(IP)/A(IP,JJ)
      GOTO NEXT, (200,320)
 440  FORMAT(A)
      END
C
C     DIFF FUNCTION FOLOWS*****************************
      FUNCTION DIFF(X,Y)
C     LAWSON AND HANSON
      DIFF=X-Y
      RETURN
      END
C     ************************************************
C     ************************************************
C     SUBROUTINE H12 FOLLOWS
C     BY LAWSON AND HANSON
C     CONSTRUCTION AND/OR APPLICATION OF A SINGLE
C     HOUSEHOLDER TRANSFORMATION
C     Q = I+U*(U**T)/B
C     PARAMETERS FOLLOW
C     MODE=1 ALGORITHM H1
C     MODE=2 ALGORITHM H2
C     LPIVOT=THE INDEX OF THE PIVOT ELEMENT
C     L1,M IF L1.LE.M TRANSFORMATION WILL BE CONSTRUCTED
C     WITH ZERO ELEMENTS FROM L1 THRU M.
C     IF L1.GT.M THE SUBROUTINE DOES AN IDENTITY TRANSF.
C     U= PIVOT VECTOR
C     IUE=STORAGE INCREMENT BETWEEN ELEMENTS
C     UP=VECTOR WITH ELEMENTS OF U
C     C=MATRIX TO WHICH HOUSEHOLDER TRANSFORMATION
C     IS APPLIED
C     ICE=STORAGE INCREMENT BETWEEN ELEMENTS OF VECTORS IN C
C     ICV=STORAGE INCREMENT BTWEEN VECTORS IN C
C     NCV=NUMBER OF VECTORS IN C TO BE TRANSFORMED
C
      SUBROUTINE H12 (MODE,LPIVOT,L1,M,U,IUE,UP,C,ICE,ICV,NCV)
      DIMENSION U(IUE,M),C(1)
      DOUBLE PRECISION SM,B
      ONE=1.E0
C
      IF (0.GE.LPIVOT.OR.LPIVOT.GE.L1.OR.L1.GT.M) RETURN
      CL=ABS(U(1,LPIVOT))
      IF (MODE.EQ.2) GOTO 60
C     CONSTRUCT THE TRANSFORMATION ************************
      DO 10 J=L1,M
 10   CL=AMAX1(ABS(U(1,J)),CL)
```

```
      IF (CL) 130,130,20
 20   CLINV=ONE/CL
      SM=(DBLE(U(1,LPIVOT))*CLINV)**2
      DO 30 J=L1,M
 30   SM=SM+(DBLE(U(1,J))*CLINV)**2
C     CONVERT DBLE. PREC. SM TO SNGLE. PREC. SM1
C
      SM1=SM
      CL=CL*SQRT(SM1)
      IF (U(1,LPIVOT)) 50,50,40
 40   CL=-CL
 50   UP=U(1,LPIVOT)-CL
      U(1,LPIVOT)=CL
      GOTO 70
C
C     APPLY THE TRANSFORMATION I+U*(U**T)/B TO C ********
 60   IF (CL) 130,130,70
 70   IF (NCV.LE.0) RETURN
      B=DBLE(UP)*U(1,LPIVOT)
C     B MUST BE NONPOSITIVE HERE IF B=0. RETURN
C
      IF (B) 80,130,130
 80   B=ONE/B
      I2=1-ICV+ICE*(LPIVOT-1)
      INCR=ICE*(L1-LPIVOT)
      DO 120 J=1,NCV
      I2=I2+ICV
      I3=I2+INCR
      I4=I3
      SM=C(I2)*DBLE(UP)
      DO 90 I=L1,M
      SM=SM+C(I3)*DBLE(U(1,I))
 90   I3=I3+ICE
      IF (SM) 100,120,100
 100  SM=SM*B
      C(I2)=C(I2)+SM*DBLE(UP)
      DO 110 I=L1,M
      C(I4)=C(I4)+SM*DBLE(U(1,I))
 110  I4=I4+ICE
 120  CONTINUE
 130  RETURN
      END
C     ************************************************
C     ************************************************
      SUBROUTINE G1 (A,B,COS,SIN,SIG)
C     LAWSON AND HANSON
C     COMPUTE ORTHOGONAL ROTATION MATRIX
C     COMPUTE MATRIX  (C, S) SO THAT (C, S)(A) =(SQRT(A**2+B**2))
C                     (-S,C)         (-S,C)(B)   (0               )
C     COMPUTE SIG=SQRT(A**2+B**2)
C     SIG IS COMPUTED LAST TO ALLOW FOR POSSIBILITY THAT
C     SIG MAY BE IN THE SAME LOCATION AS A OR B
C
      ZERO=0.E0
      ONE=1.E0
      IF (ABS(A).LE.ABS(B)) GOTO 10
      XR=B/A
      YR=SQRT(ONE+XR**2)
      COS=SIGN(ONE/YR,A)
      SIN=COS*XR
      SIG=ABS(A)*YR
      RETURN
```

```
 10      IF (B) 20,30,20
 20      XR=A/B
         YR=SQRT(ONE+XR**2)
         SIN=SIGN(ONE/YR,B)
         COS=SIN*XR
         SIG=ABS(B)*YR
         RETURN
 30      SIG=ZERO
         COS=ZERO
         SIN=ONE
         RETURN
         END
C        ***********************************************
C        ***********************************************
         SUBROUTINE G2 (COS,SIN,X,Y)
C        LAWSON AND HANSON
C        APPLY THE ROTATION COMPUTED BY G1 TO (X,Y)
         XR=COS*X+SIN*Y
         Y=-SIN*X+COS*Y
         X=XR
         RETURN
         END
C        ***********************************************
C        ***********************************************
```

Appendix B- Near Orthogonality Relations

Any inversion algorithm utilized has limits of resolution of the desired unknowns. Some of these, based upon the Heisenberg uncertainty relations, have been included in the program itself. Other limits are dependent on the signal to noise ratio of the data vis-a-vis the amount of desired unknowns (the ratio of well resolved data points to number of equations). Beyond these two questions there remains the issue of the interaction terms between resolved unknowns.

The inversion scheme utilized here has the advantage of a near orthogonality of it's eigenvalues, as can be seen from it's relation to the generalized Laplace series. The following will show the interaction terms between two resolved relaxation frequencies ω_l and ω_k over the time interval of the experiment $\tau_{\min}$ through $\tau_{\max}$.

The Kernel of the relaxation operator is $e^{-\omega_i t}$ whose inverse is $e^{\omega_i t}$. We wish to show then what is

$$A_{kl} = \sum_{\tau_j = \tau_{\min}}^{\tau_j = \tau_{\max}} e^{-\omega_k \tau_j} e^{\omega_l \tau_j} \qquad \text{[B1]}$$

for $(\omega_k - \omega_l) \geq 0$.

This is the discrete form of the integral

$$\int_{\tau_{\min}}^{\tau_{\max}} e^{-\omega_k t} e^{\omega_l t} \, dt \qquad \text{[B2]}$$

which for $\tau_{\min} = 0$ and $\tau_{\max} = \infty$ is given by

$$\frac{1}{\omega_l - \omega_k} . \qquad \text{[B3]}$$

For the linear time sampling used here

$\tau_j = \tau_{\min} + (j - 1) \cdot \Delta\tau \quad (j = 1,2,...N)$, where $\Delta\tau = \dfrac{(\tau_{\max} - \tau_{\min})}{N - 1}$.

Therefore A_{kl} becomes:

$$A_{kl} = e^{-(\omega_k - \omega_l)\tau_{\min}} \cdot \sum_{j=1}^{j=N} \left[e^{-(\omega_k - \omega_l)\Delta\tau} \right]^{(j-1)} \qquad \{B4\}$$

and using the relation

$$\sum_{j=1}^{j=N} X^{(j-1)} = \frac{X^N - 1}{X - 1}$$

this becomes

$$A_{kl} = e^{-(\omega_k - \omega_l)\tau_{\min}} \cdot \left[\frac{e^{-(\omega_k - \omega_l)\Delta\tau N} - 1}{e^{-(\omega_k - \omega_l)\Delta\tau} - 1} \right] \quad . \qquad [B5]$$

We can further simplify this expression since $\omega_k - \omega_l = \Delta\omega \cdot (k - l)$, obtaining

$$A_{kl} = e^{-\Delta\omega(k-l)\tau_{\min}} \cdot \left[\frac{e^{-\Delta\omega(k-l)\Delta\tau N} - 1}{e^{-\Delta\omega(k-l)\Delta\tau} - 1} \right] \quad . \qquad [B6]$$

This is a general result which shows the explicit dependence of the interaction terms on $\Delta\tau$,$\Delta\omega$, and on N. Implicit in the result is the dependence on M, since this determines the size of $\Delta\omega$ (equation [13]). When $k = l$ we have $A_{kl} = 1$, and for $K > l$ A_{kl} quickly decays, giving us near orthogonality between eigenvalues $P_k\ (\omega_k\ )'$ and $P_l\ (\omega_l\ )'$.

For the special case $\tau_{\min} = \Delta\tau$, the expression simplifies greatly to become

$$A_{kl} = e^{-\frac{\pi}{M}(1 - \frac{1}{N})(k-l)} \cdot \left[\frac{e^{-\frac{\pi}{M}(1 - \frac{1}{N})(k-l)N} - 1}{e^{-\frac{\pi}{M}(1 - \frac{1}{N})(k-l)} - 1} \right] \qquad [B7]$$

which shows explicitly the dependence both on N and on M. The smaller M, the faster the decay of the interaction terms. An increase in N leads to a greater approach to $\tau = \infty$, increasing the orthogonality. This has lead us to sample in time to times where the change in magnetization is below the signal to noise level. In terms of the inverse we have found that the ratio of $\frac{100}{265}$ in $\frac{M}{N}$, with the acheived signal to noise ratio due to signal averaging (below 5% variance), gives the same results as do smaller M's.

Appendix C- Artificial Relaxation Spectra

Following the near orthogonality relations submitted in Apppendix B, an example of the inversion of artificial relaxation distributions is forthcoming. This is important since in the case of the materials studied here we do not know the real pore size or $\frac{S}{V}$ distributions.

An artificial $T1$ relaxation curve was produced using two gaussian relaxation distributions. The two distributions shown in figure C(b) as lines have means at $\omega = 1.23$ and $\omega = 3.50$ with variances of 0.025 and 0.05, respectively. After a 265 point relaxation curve was produced using these distributions, 5% gaussianly distributed random noise was added to the artificial data, producing the relaxation curve shown as points in figure C(a). This noisy data was then used as input to our inversion. The inverted fit to the data is seen in figure C(a) as a line, and the resolved rate distribution is shown as the dashed line (with points being the actual points in the inversion) in figure C(b). The good agreement of the resolved distribution with the original distribution can be seen.

Experimenting with various configurations of artificial distributions at varying noise levels has lead to the following conclusions with respect to the the current inversion algorithm. The shape and position of the artificial distributions is relatively maintained with noise levels up to 10% variance. Beyond this noise level the distributions inverted are displaced in terms of their center and changed in their shape from the original distributions. The distributions which are first distorted are the broadest ones (largest variance for gaussian distributions) followed by narrower ones. In the case of several well seperated distributions, the smaller the number of these, the larger the noise level required to distort them. This may lead to the use of only three distributions in inverted field NMR studies, where magnetic field inhomogenuity and a need for rapid sampling leads to a low signal to noise level.

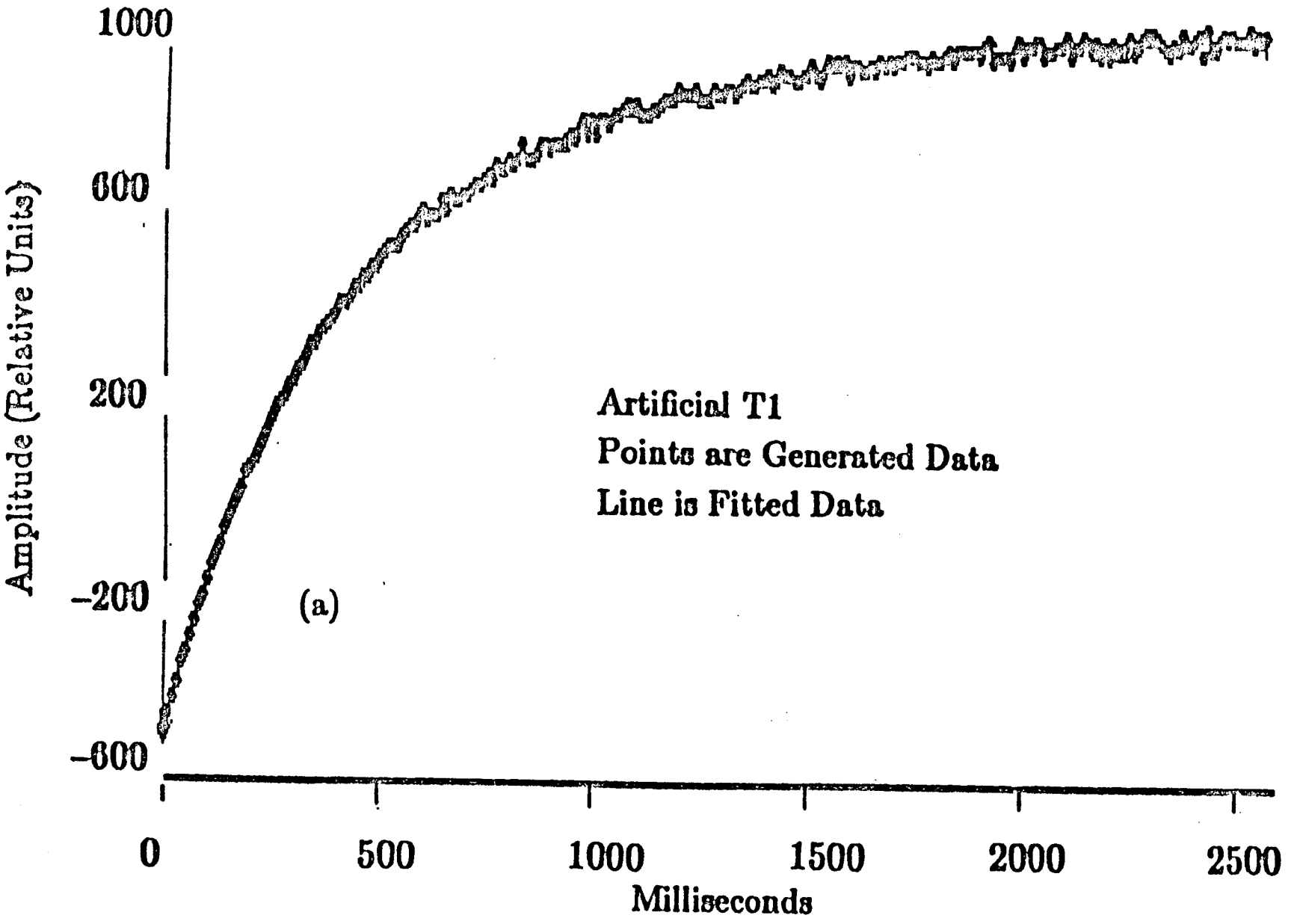

FIG. C(a). Artificial generated and inverted NMR $T1$ relaxations.

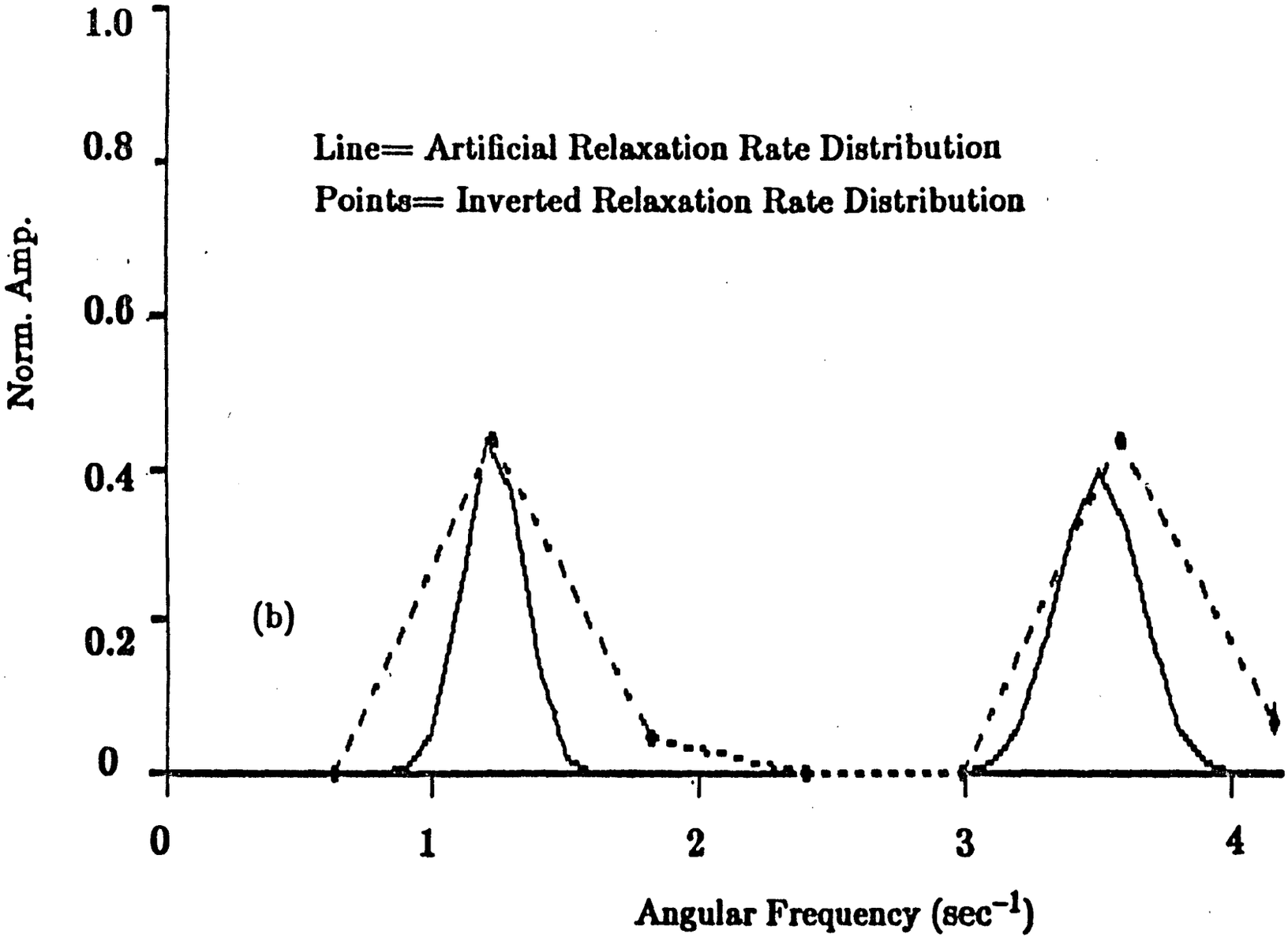

FIG. C(b). Artificial generated and inverted relaxation rate distributions.

THE STATE OF FLUIDS IN POROUS ROCKS AT PARTIAL SATURATIONS: A PROTON NUCLEAR MAGNETIC RESONANCE STUDY

Ehud J. Schmidt, Katherine K. Velasco, and Charles West

Stanford Rock Physics Project, Geophysics Department, Stanford University, Stanford, California, 94025

Abstract

Nuclear magnetic resonance (NMR) studies of porous rocks saturated with air-water mixtures have disclosed drastic changes in the distribution of relaxation rates as well as a peak in the magnetization which occurs between 80 and 60% water saturation. The peak in magnetization is extremely interesting in that it violates the mean field result. Further study has disclosed that these phenomena are not seen in all rocks but do exist in many rocks as well as in artificial porous materials. Existing theoretical treatment of the NMR response of coupled pores suggests that the changes in the distribution of relaxation rates may be associated with a breakup in the pore space connectivity, seen through NMR as a transition from a coupled pore to an isolated pore regime. Two types of connectivety percolation are suggested. A fluid mechanical approach to the stability of flow in porous media predicts a breakup of hydraulic connectivity at 66% saturation, when air-water surface tension effects begin to be important ($r_{pore} \leq 170\ micron$, where r_{pore} is the pore radius, for atmospheric pressure gradients) and at increasingly larger water saturations as pore size decreases and surface tension effects become more pronounced. Solution of the equilibrium configuration of water fillers in pores with negative external radii of curvature predicts a retreat of the water films into disconnected annular pockets. The finding of this transition in the NMR response has practical importance in establishing a connection between the NMR response and the connectivety of the porous media, thus forming a physical basis for the application of NMR results to the prediction of transport phenomena in porous rocks.

Introduction

In an earlier paper [1] the techniques of data acquisition, relevant theory and a data inversion algorithim were discussed for nuclear magnetic resonance (NMR) measurements of the longitudinal relaxation time T_1 distribution function and the fluid nuclear spin magnetization. Experimental results from porous rocks fully saturated with deionized water were inverted to obtain their surface to volume $(\frac{S}{V})$ probability distributions, assuming that the rock magnetization was governed by the equation [2]

$$M_z\ (t) = M_\infty + (\ M_0 - M_\infty\ ) \cdot \sum_{i=1}^{i=I} P_i\ e^{-\omega_{av\,i}\ t} \tag{A1}$$

where

$$\omega_{av\,i} = \omega_b + (\ \frac{Sl}{V}\ )_i \cdot \omega_{surf} \tag{A2}$$

is the average relaxation angular frequency $(\frac{1}{T_{avi}})$ of the $i^{\ th}$ pore, P_i is the volume percent of water residing in pores of this size, M_∞ is the equilibrium magnetization and $M_0 - M_\infty$ is the magnetization dispersion, the magnetization which relaxes following the NMR excitation. $\omega_b = \frac{1}{T_{1b}}$ is the relaxation angular frequency of bulk water and ω_{surf} that of a water layer of thickness l adsorbed on the silica surface.

The magnetization dispersion measured during the experiments was assumed to be proportional to rock porosity via the mean field result

$$(\ M_0 - M_\infty\ ) = \frac{(\ \gamma_{pr}\ \hbar\ )^2\ N_0\ \phi\ H}{4\ KT} \tag{A3}$$

where $\hbar$ is Planck's constant over 2π, γ_{pr} is the proton nuclear spin susceptibility, KT the thermal energy, N_0 is the nuclear spin density, and ϕ the sample porosity.

Experiments were later initiated on rock samples dried to various degrees of water saturation S_w, in order to study the process of pore fluid evacuation and the changing balance between the effect of the bulk water and the surface adsorbed water. As the rock dried from

full saturation there was an increase in the relaxation angular frequency for each of the P_i observed at 100% saturation. This gradual increase in the importance of the surface adsorbed water was followed by a drastic jump in ω_{ei} at saturations which ranged from 80% to 60% for most of the rocks studied. Concurrent with this increase in the relaxation angular frequency we found a substantial increase in the magnetization dispersion, sometimes as much as a doubling of the full saturation value, which is contrary to the mean field result, equation (A3).

An investigation was undertaken to study the causes of this effect with carefully controlled measurements at small water saturation intervals. The following sections will exhibit some of our recent results concerning this percolation phenomena, followed by a theoretical investigation of the expected results of the breakup of pore space connectivity on the NMR response. Later sections attempt to determine the position of the breakup point from a fluid mechanical criterion. The concluding section will discuss the question of the equilibrium configuration of the water and air fillers in pores with boundaries with negative radii of curvature from the point of view of surface energy minimization, and the possibility of a physical decoupling of the water films within these pores.

The chief motivation for this study is in the existence of possibilities of understanding from a physical point of view the connection between NMR results and transport properties of porous rocks. Previous work has shown an empirical link between NMR and hydraulic permiability, based upon the utilization of NMR results, assumed to provide only static rocks properties, as parameters in empirical relations [3] for hydraulic permeability. This past approach has been successful at times, but failed in many instances. Possibilities exist now for the existence of a rigid physical basis for the connection, as well as for the future formulation of predictive equations based upon this connection.

Experimental Results

Figure 1(a) shows the magnetization of Massillon Dark (ϕ=17.4%) and Massillon Light (ϕ=22.2%) sandstones as a function of water saturation. The magnetization (in Gauss) shown has been normalized by division by the respective rock porosity so that a comparison may be made without the effect of the different volume of water in the two samples. Massillon Dark differs from Massillon Light in that it has a higher clay and Ferrous oxide concentration. The normalized magnetization of both samples is identical at full saturations, but shows large differences at lower water saturations. The magnetization of Massillon Light drops monotonically as water saturation decreases, in agreement with equation (A3), with the porosity term ϕ at full saturation, going to the product of porosity times water saturation $\phi\ S_w$ at partial saturation, while that of Massillon Dark, although identical at full saturation, increases sharply to a peak at approximately 80% saturation, thereafter dropping monotonically with a possible second peak of smaller intensity at 30% saturation.

The differences between the rocks are better seen in figure 1(b), where the magnetization has been divided by the product of sample porosity and the water saturation, and plotted versus water saturation. The mean field result, equation (A3), would predict that this value be independent of water saturation. The results for Massillon Light sandstone show that the predictions of mean field theory are valid, except for saturations below 20%. For Massillon Dark, we find an increase in this value from 100 to 80%, in disagreement with theory, then a region of agreement up to 45% (a straight line), followed by the low saturation region where clear disagreement is seen. We can thus see that Massillon Dark and Massillon Light display entirely different behavior in the course of the drying process.

Figure 2 shows the average effective $\frac{S}{V}$ ratio of (a) Massillon Dark sandstone, and (b) Massillon Light sandstone as a function of water saturation. This average is computed by averaging over the relaxation angular frequency distribution function [1] and is thus insensitive to the details of the distribution. At full saturation this average represents the true average

surface to volume ratio of the rock, whereas at partial saturation it reflects the effective surface to volume ratio of the water filler. The average $\frac{S}{V}$ of Massilon dark, figure 2(a), exhibits a series of large increases, the first between 90 and 80% saturation, then at 30% saturation and at 10% saturation, with gradual increases in intermediate areas. The $\frac{S}{V}$ increases mirror the magnetization increases for this rock (figure 1(b)). The average effective $\frac{S}{V}$ ratio is approximately $10^6\ cm^{-1}$ at 90% saturation, which corresponds to the rock behaving as if a layer of 100 A^o thick water were covering its surface, this coverage being an extremely low value for such a high saturation.

Figure 2(a) shows the average $\frac{S}{V}$ ratio of Massillon Light sandstone as a function of water saturation. The $\frac{S}{V}$ ratio of this rock is about $2 \cdot 10^5\ cm^{-1}$ at 100% saturation and rises gradually until it has a discontinuous jump at 20% saturation. The effective $\frac{S}{V}$ ratio is 5 times smaller than in Massillon Dark, and displays a very different variation of behavior with water saturation.

To better understand these differences in terms of the actual changes occurring in the rock it is useful to consider the relaxation angular frequency distribution function $P\ (\omega)$. Such distribution functions can show how the individual pore components are behaving, as opposed to the magnetization and average surface to volume ratio which are whole rock averages. Figure 3(a) shows the normalized angular frequency probability distribution function of Massillon Dark sandstone at water saturations ranging from 100 to 60%. The water saturation axis is perpendicular to the page. At 100% saturation the probability distribution shows 4 discrete peaks, with the largest magnitude one being at the lowest angular frequency. This corresponds to most of the water in the rock residing in the largest pores (those with smallest $\frac{S}{V}$). The highest angular frequency component is at $\omega \approx 180$. As the water saturation decreases, the

peaks all shift to higher angular frequencies, indicating the increasing role of the adsorbed water component. The peaks are seen to move apart from each other, and the relative magnitude of each component changes.

At 80% saturation we have the sudden appearance of a component with three times higher angular frequency, corresponding to a much more adsorbed state. The low angular frequency components continue to separate, with the relative magnitudes shifting so as to decrease the low angular frequency (low adsorption) components while the higher angular frequency (high adsorption) components increase. Below 80% saturation the high ω component does not change appreciably until approximately 30% saturation where a second increase (not shown here) occurs.

Figure 3(b) shows the relaxation angular frequency probability distribution of Massillon Light sandstone over approximately the same water saturation interval. At 100% saturation the distribution is composed of three clear peaks, the largest being at the low ω end. There is here, as in the Massillon Dark case, a non-zero component at $\omega \approx 130$. As the water saturation is decreased we observe a gradual shift of the low angular frequency components to higher values, but a dramatic effect is the gradual disappearance of the high ω component, which is not observed below 75% saturation. Below this point a gradual increase in the angular frequencies occurs, but no discontinuous jumps as occurred in the case of Massillon Dark, figure 3(a).

Following the clear confirmation of this effect in several rocks, we have studied artificial materials, where the material composition and pore sizes are better controlled. QF10 is a fused quartz grain sample of 42.5% porosity and a very narrow pore size distribution composed of large 50 *micron* radius pores [1].

Figure 4(a) shows as a line the porosity normalized magnetization of QF10 as a function of water saturation. The dashed line in the figure shows the mean field prediction. The mag-

netization does not change with fluid withdrawal from 100 to 80% saturation, in clear disagreement with theory. It then drops suddenly at 77% saturation, with strong fluctations thereafter. By 55% saturation the magnetization seems to have leveled off again. At 30% saturation there is a second decrease in magnetization followed by a rapid decrease at yet lower saturations. The magnetization is larger than mean field predictions from 100 to 80%, then drops at 77% to the mean field value, while below 55% saturation the magnetization is again above mean field predictions.

Figure 4(b) shows the normalized angular frequency probability distribution of QF10 at water saturations from 100% to 77%, where the first magnetization drop is observed. The distribution shows a narrowly separated bimodal distribution at very low angular frequency, indicating the existance of ellipsoidal and spherical pores in this sample (which is also confirmed in the electronmicrograph of QF10 shown in reference 1). These peaks shift gradually to higher ω's, until at 77% saturation a sudden breakup of the primary peak occurs with the appearance of new, higher angular frequency components. The behavior here is similar to that observed in Massillon Dark at high saturations, and its observance in artificial materials suggests that the phenomena we observe are more universal in nature.

The origins of this magnetization peak has at least two plausible explanations, which are to some extent related through the geometric transition of the water films in the pore space which they require.

The first explanation is a transition in dimensionality of the water films. The theory for this response was introduced by Richards [4,5] and proven experimentally by Dietz [6]. In cases where the NMR relaxation is produced by diffusional exchange between excited and non-excited spins, the diffusion rate in the various directions determines the relaxation time (and thus the relaxation angular frequencies). When the system is isotropic in three dimensions $\omega_{ss} = K\ \tau_c$ for the motionaly narrowed regime $\omega_L\ \tau_c << 1$, where ω_L is the Larmor excitation frequency and τ_c is the proton rotational correlation function, the time span over which

molecular motion is correlated. The constant K is the strength of spin-spin interactions. For a system where diffusion in one of the directions is cut off or strongly inhibited, that is a two dimensional system, the relaxation angular frequency is given as [5] $\omega_{av} = K\ \tau_c \cdot ln(\ \omega_L\ \tau_c{}^{-1}\ )$. For a one dimensional system the relaxation angular frequency is $\omega_{av} = K\ \tau_c \cdot (\ \omega_L\ \tau_c\ )^{-1/2}$.

Applying these theoretical results to our experimental results, with the instrument excitation frequency of 20 MHz ($\omega_L = 1.2 \cdot 10^8\ s^{-1}$) and $\tau_c \approx 10^{-10}\ s$, we would be a multiplication by a factor of 4.4 for a three dimensional to two dimensional transition, and by a factor of 8.9 for a transition from three dimensions to one dimension. The change in magnetization as a results of these transitions has not been addressed, in part as a result of the fact that in most high resolution NMR experiments the absolute signal amplitude is not used for quantitative purposes.

The second explanation for the observed phenomena is a breakup of water phase connectivity in the pore space which occurs at this point. It is suggested by the changes in the angular frequency probability distribution at these points. This second explanation will be addressed in the remainder of this paper because of its link with the first possible explanation, namely that lower dimensionality would appear only if water films of A° thickness scales appear at some points in the pore space, which would tend to cut off diffusive communication between the thicker films on either side of this layer. Some of the higher ω's which appear at the transition point, as in the case of QF10, do not seem to be high enough to be valid for A° thickness films, assuming that the wetting properties of QF10 are similar to those found in rocks. The first possibility can readily be tested by the use of NMR spectrometers of differing Larmor excitation frequencies, since the theoretical results perdict a dependence of the relaxation time on the Larmor frequency.

Nuclear Magnetic Resonance in Porous Rocks at Partial Fluid Saturation

We will discuss in this section the theoretical nuclear magnetic resonance response of a pore space partially filled with air in order to examine the agreement of our experimental results with available theory.

a. Effect of partial saturation on the NMR relaxation in a single pore

The Nuclear Magnetic Resonance (NMR) response of porous rocks is governed by diffusion and relaxation via the modified Bloch equation [2,7,8]

$$\frac{\partial M_z}{\partial t} = -\frac{(M_z - M_\infty)}{T_{1b}} + D \cdot \nabla^2 M_z \tag{1}$$

where M_z is the $\hat{z}$ component of the magnetization, M_∞ the equilibrium magnetization, T_{1b} the relaxation time of bulk water and D the diffusion constant.

Consider the case of a pore partially filled with air. It will be assumed that this air, due to the greater affinity of water for the silica surface, forms a continuous bubble in the center of the pore. A pore of cylindrical geometry will be chosen of radius R_2 which contains a cylindrical air filler of radius R_1. The water saturation of this pore is $S_w = 1 - \left(\frac{R_1}{R_2}\right)^2$.

Due to the cylindrical symmetry, we will pick a solution to equation (1) of the form

$$M_z = M_\infty + A_n\ J_n\ (k_t\ r) \begin{matrix}\cos n\,\phi \\ \sin n\,\phi\end{matrix} e^{-i\beta_n z}\ e^{-(\omega_n + \omega_b)t} + \tag{2}$$
$$B_n\ N_n\ (k_t\ r) \begin{matrix}\cos n\,\phi \\ \sin n\,\phi\end{matrix} e^{-i\beta_n z}\ e^{-(\omega_n + \omega_b)t}$$

where J_n and N_n are Bessel functions of the first and second kind of order n, k_t is the transverse ($\hat{r}$) component of the wavenumber, β is the $\hat{z}$ component of the wavenumber, $\omega_b = (T_{1b})^{-1}$ is the angular frequency of relaxation of the bulk water and $\omega_n = (T_{1n})^{-1}$ is the angular frequency of relaxation of the diffusive modes.

When this solution is inserted into equation (1) we obtain

$$k_t^2 + \beta_n^2 = \frac{\omega_n}{D} \tag{3}$$

which is the dispersion relation which links the wavenumbers to the relaxation angular frequency of each mode. If the k_t , β_n are determined, as they will be from the boundary conditions, it will be possible to determine ω_n and later the average relaxation angular frequency

$$\omega_{av} = \omega_b + \omega_n \tag{4}$$

which is analogous to the general equation (A2) used for fully water saturated pores

$$\omega_{av} = \omega_b + \frac{Sl}{V} \cdot \omega_{surf} \quad . \tag{5}$$

Specializing to the lowest order mode n =0, which does not have angular dependence, the solution must satisfy boundary conditions on the two surfaces, the air-water and the water-silica interfaces. The boundary condition for the magnetization on an active surface, a surface with a given density of spin relaxation sites, is

$$\hat{n} \cdot D \vec{\nabla} M_z + \mu M_z = 0 \tag{6}$$

where $\hat{n}$ is the normal to the surface and μ is the average surface site (sink) density, defined as

$$\mu = \frac{1}{S} \int \mu (r) \, dS \tag{7}$$

$\mu (r)$ being the local site density at each point on the surface S.

At both interfaces, $r = R_1$ and $r = R_2$,

$$\hat{n} \cdot \vec{\nabla} M_z = \hat{r} \frac{\partial M_z}{\partial r} .$$

It will be assumed that the air-water interface is devoid of relaxation sites, neglecting the small concentration of paramagnetic O^{17} found in air, so that after utilizing some relations among Bessel functions

$$-k_t D [A_0 J_1 (k_t R_1) + B_0 N_1 (k_t R_1)] = 0 \tag{8}$$

or

$$B_0 = -A_0 \cdot \frac{J_1 (k_t R_1)}{N_1 (k_t R_1)}$$

At $r = R_2$, the interface with silica, we have active relaxation sites, so that equation (6) for this interface is, after inserting the results of equation (8)

$$-J_1(k_t\ R_2) + \frac{\mu}{k_t\ D} \cdot J_0(k_t\ R_2) \tag{9}$$

$$+ \frac{J_1(k_t\ R_1)}{N_1(k_t\ R_1)} \cdot [N_1(k_t\ R_2) - \frac{\mu}{k_t\ D} \cdot N_0(k_t\ R_2)\ ] = 0\ .$$

The top line of this equation contains terms which exist even in the absence of an air filler (fully saturated pore, $R_1 = 0$) while the lower line shows the additional terms introduced due to the new air-water interface, producing changes in the relaxation angular frequency with water saturation, since R_1 continuously varies as the water saturation changes.

μ, the remaining free parameter in this model, is determined by comparing equations (4) and (5), for the case of a fully saturated pore, which gives $\omega_0 = \frac{Sl}{V} \cdot \omega_{surf} = \frac{2l}{R_2} \cdot \omega_{surf}$ for a cylinder. In our analysis [1] the value of $(\ l\ \omega_{surf}\ ) = 10^{-4}\ cm/s$ has been assumed for quartz based rocks so that $\omega_0 = 2 \cdot 10^{-4}/R_2\ s^{-1}$.

Using a diffusion constant $D = 3 \cdot 10^{-5}\ cm^2/s$, and using previous [8] theoretical results which show that for the case of $(\mu \cdot R_2)/D \ll 1$, which is valid for the cases of rocks, the relaxation rate is given by $\omega_0 = \mu/R_2$ so that one finally obtains that $\mu_{rock} = 2 \cdot 10^{-4}\ cm/s$.

This surface site density is surprisingly small compared with biological cells where Brownstein [8] finds $\mu = 3 \cdot 10^{-2}\ cm/s$, two orders of magnitude higher surface activity.

For the isolated cylindrical pore β may be set to zero and equation (9) solved numerically. The resulting relaxation angular frequency ω_0 is plotted in figure 5 as a function of water saturation for a 100 *micron* (1 *micron* $= 10^{-4}\ cm$) radius pore. The average relaxation angular frequency for this pore is $\omega_b + \omega_0$. Since $\omega_b = 0.35$ the diffusive mode is weak for this large pore compared to the bulk relaxation angular frequency until low water saturation (approximately 20%) when it dominates. This variation of ω with S_w will be observed for the single isolated pore as the drying process progresses.

In figure 6 the results for the diffusive relaxation angular frequency of a 1 *micron* radius pore are plotted (line) versus water saturation. The resolved angular frequencies are 100 times greater than those in figure 5, showing the scaling of the relaxation angular frequency with pore size. The variation with water saturation also is identical to that for the 100 *micron* pore. Cohen [9] suggested the use of an approximate equation for the average relaxation angular frequency in the partially saturated case

$$\omega_{av} = \omega_b + \frac{Sl}{V \cdot S_w} \omega_{surf} \quad . \tag{10}$$

The results of this equation (minus the bulk relaxation angular frequency ω_b) are plotted as points on the figure and confirm the validity of this equation. For the parameters of this model it is therefore possible to predict the relaxation angular frequency at any partial saturation from knowledge of the results at full saturation. The shortening of the relaxation time (increase in relaxation angular frequency) is here solely the result of a decrease in the fluid volume and should not be confused with the effect of additional relaxation sites added at the fluid-air interface, as these have been neglected here.

The normalized intensity of the 0th order mode can be studied to determine if it is indeed the dominant mode here and what is the contribution of the higher order modes. The volume normalized intensity of this mode is [8]

$$I_0 = \frac{1}{V} \cdot \frac{\left[\int F_0(r)\, dV\right]^2}{\int F_0(r)^2\, dV} \tag{11}$$

where $F_0(r)$ is the magnetization solution (equation (2)) without the equilibrium magnetization M_∞, with $n = 0$. The evaluated intensity for this case is

$$I_0 = \frac{4}{(R_2^2 - R_1^2) \cdot k_t^2} \cdot \tag{12}$$

$$\left[[J_1(X_2)\, R_2 - J_1(X_1)\, R_1] + \frac{J_1(X_1)}{N_1(X_1)} \cdot [N_1(X_1)\, R_1 - N_1(X2)\, R_2] \right]^2 \cdot$$

$$[\ [R_2^2\,(J_0(X_2)^2 + J_1(X_2)^2) - R_1^2\,(J_0(X_1)^2 + J_1(X_1)^2)\ ] +$$

$$\left(\frac{J_1(X_1)}{N_1(X_1)}\right)^2 [\ R_2^2\,(N_0(X_2)^2 + N_1(X_2)^2) - R_1^2\,(N_0(X_1)^2 + N_1(X_1)^2)\ ]^{-1}$$

where $X2 = k_t\ R_2$, $X1 = k_t\ R_1$.

The results obtained for the intensity of the lowest order mode for a 1 *micron* radius pore are 1.00 at full water saturation, dropping to 0.97 at 20% saturation. This shows that ignoring the higher order modes contributes at most to a 3% error.

b. Effect of partial saturation on the NMR response of coupled pores

In cases where the rock porosity is sufficiently large so that the mean distance between pores is of order of the pore diameters, there is an exchange of fluid between adjacent pores due to the differing relaxation rates in them. The smaller pores serve as alternate relaxation sites to intrapore surface sites available to adjacent larger pores.

In this case the NMR response of the i^{th} pore is given by [10]

$$\frac{\partial M_i}{\partial t} = -\frac{M_i - M_\infty}{T_{1i}} + \sum_{j=1}^{j=N} \frac{D}{V_j} \int \hat{n} \cdot \vec{\nabla} M_b \ dS_{ij} \tag{13}$$

where $T_{1i}^{-1} = \omega_{sv\,i}$ is the average relaxation time for the i^{th} pore. A sum is taken over the N nearest neighbours of this pore, each of which have an intersecting surface area S_{ij} in common with this pore. Mendelsohn [10] has shown that for the weakly coupled case where $S_{ij} << S_i\ , S_j$, S_i and S_j being the surface areas of the two neighbouring pores, these equations have the following solution

$$M_i = M_\infty + (M_0 - M_\infty) \cdot \left[1 - \sum_{j=1}^{j=N} \frac{S_{ij}}{V_i\ \Delta_{ij}} \right) e^{-\omega_{sv\,i}\ t} + \sum_{j=1}^{j=N} \frac{S_{ij}}{V_i\ \Delta_{ij}}\ e^{-\omega_{sv\,j}\ t} \Bigg] \tag{14}$$

where $\Delta_{ij} = \left(\frac{S}{V}\right)_i - \left(\frac{S}{V}\right)_j$ is the difference in surface areas between these pores. This solution states that in every coupled pore there is a fraction of the pore volume which relaxes with its own characteristic relaxation time while a remaining fraction relaxes with a neighbour's relaxation time.

The total sample magnetization can be obtained by summing over all pores, resulting in the following expression [10]

$$M\ (t) = M_\infty + (\ M_0 - M_\infty\ ) \cdot \sum_{i=1}^{i=I} \left(P_i - \frac{2}{V} \sum_{j=1}^{j=N} \frac{S_{ij}}{\Delta_{ij}} \right) e^{-\omega_{sv\,i}\ t} \tag{15}$$

P_i being the probability of occurance of the i^{th} pore.

Comparing this result to the result valid for the isolated pore regime [2]

$$M(t) = M_\infty + (M_0 - M_\infty) \cdot \sum_{i=1}^{i=I} P_i \; e^{-\omega_{av_i} \cdot t} \tag{16}$$

we find that there is a shift in the probability distribution, which is a measure of the pore space connectivity. For large pores (small S/V) bordered by smaller pores (larger S/V) Δ_{ij} is negative, so that the amplitude of the large pores is intensified at the expense of their neighbours. We would thus expect to see , while in this regime of weak coupling, a larger probability of large pores (with small relaxation angular frequencies) than are actually found in the rock.

In the strongly coupled case $S_{ij} \approx S_i \; , S_j$, regions whose size is much greater than the single pore will relax together. The limiting effect is the whole rock relaxing in cohesion with a relaxation angular frequency

$$\omega_{av\ rock} = w_b + \left(\frac{Sl}{V}\right)_{rock} \cdot \omega_{surf}$$

The predictions of the coupled pore models may be seen in our experimental results in terms of the broadening and of the appearance of new features in the angular frequency distribution functions (see figure 4(b) at 77%). This may coincide with a transition from the strongly coupled regime to the weakly coupled regime.

The theoretical results do not explain two important features seen in the experimental results, the increase of magnetization which is observed at the transition S_w , and the actual water saturation at which the phenomenon occurs. The theoretical results cannot predict these features because they do not concern themselves with the actual mechanisms of the transition between the various connectivity regimes, but rather with the end members created by this process. Above the transition water saturation we are in a well connected pore space, where the resolved NMR probability distribution will show only variations of the $\frac{S}{V}$ which exist over

length scales much greater than typical interpore distances. Below the transition we will see a loosely connected or totally unconnected pore space, where many more features of the pore space will be observable.

To predict the critical water saturation and the magnetization peak observed at this saturation it is essential to understand the topology of the fluid-air mixtures in the pore space, and as these are governed mainly by mechanical forces, a mechanical model must be examined.

Fluid Flow in Partially Saturated Porous Media

We will examine initially water flow through a pore partially saturated with air and following that look at the connectivity percolation on the larger, whole rock scale. The motivation for this division is that fluid percolation can occur on various length scales in rocks, but with similar features. In essence, there can be either pockets of isolated films of water in the pores, or flow over macroscopic multi-pore distances can be cut off.

a. Water flow through a partially saturated pore

The geometry considered is the same geometry discussed previously in connection with relaxation in a partially saturated pore, that of a cylindrical pore with a central air filler of radius R_1 surrounded by water that fills the remaining distance to the pore wall, $R = R_2$. Implicit in this geometry is the greater affinity of the water for the silica surface, that is that the silica-water surface tension is much lower than the silica-water vapor surface tension. A later section will look at more complicated pore geometries where this geometry may not be maintained at all water saturations.

The equation that governs fluid flow is the Navier-Stokes equation, which for flow down the cylinder axis may be written as [11]

$$\eta \nabla^2 v_z = - \frac{\Delta P}{L} \tag{17}$$

where η is the water viscosity, v_z is the fluid velocity along the cylinder and $\frac{\Delta P}{L}$ is the pressure gradient per unit length which drives the flow. This equation can be written as

$$\frac{1}{r}\frac{d}{dr}\left(r\,\frac{d\,v_z\,(r)}{dr}\right) = -\frac{\Delta P}{\eta\,L}$$

which can be integrated to provide the general solution to this problem

$$v_z\,(r) = -\frac{\Delta P}{4\,\eta\,L}\,r^2 + a\;ln\,(r) + b \tag{18}$$

where a and b are constants to be determined from the boundary conditions.

Two boundary conditions must be satisfied. At the interface of the water with air, there cannot exist any normal stresses, except those due to the air-water surface tension. Therefore we have

$$\sigma_{rz} = \eta\,\frac{\partial v_z}{\partial r} = \frac{\gamma_{lv}}{r} \tag{19}$$

at $r = R_1$, where γ_{lv} is the air-water surface tension coefficent. Using the general solution, equation (18), we determine that

$$a = \frac{\gamma_{lv}}{\eta} + \frac{\Delta P}{2\,\eta\,L}\,R_1^{\,2}\ .$$

The second boundary condition requires flow velocity continuity at the water-solid interface, requiring that the flow velocity vanish on this surface. Using equation (18) with the value of a inserted gives

$$b = \frac{\Delta P}{4\,\eta\,L}\,R_2^{\,2} - \left(\frac{\gamma_{lv}}{\eta} + \frac{\Delta P}{2\,\eta\,L}\,R_1^{\,2}\right)\ln R_2\ .$$

The solution thus obtained is

$$v_z\,(r) = \frac{\Delta P}{4\,\eta\,L}\left(R_2^{\,2} - r^2\right) + \frac{\Delta P}{2\,\eta\,L}\,R_1^{\,2}\ln\!\left(\frac{r}{R_2}\right) + \frac{\gamma_{lv}}{\eta}\ln\!\left(\frac{r}{R_2}\right)\ . \tag{20}$$

The first term in the velocity is the familiar Poiseiville flow term. The next terms do not exist in the absence of the air filler. The second term, always negative, is the adverse contribution of the air-water boundary condition, which since it cannot support the large shear stresses imposed by fast flow, forces a reduction in the flow rate at the boundary. The last term is the ad-

verse contribution of the surface tension, since fluid motion at the surface will have to perform work to deform the air-water meniscus.

The volume flux of water passing through a cross-sectional area of the cylinder per unit time may now be computed. This quantity is given by

$$Q = \int_{r=R_1}^{r=R_2} \rho \, v_z \, (r) \, dS \tag{21}$$

where ρ is the fluid density and the integration is over the cross-sectional area. For a cylinder $dS = 2 \pi r \, dr$ so

$$Q = 2 \pi \rho \int_{r=R_1}^{r=R_2} v_z \, (r) \, r \, dr \tag{22}$$

which after using the relation between the radii and the water saturation S_w can be written as

$$Q = \frac{\pi \rho \Delta P \, R_2^4}{8 \eta L} \left[(3 \, S_w - 2) (S_w) - 2 (1 - S_w)^2 \, ln (1 - S_w) \right] + \frac{\pi \gamma_{lv} \rho R_2^2}{2\eta} \left[(- S_w) - (1 - S_w) \, ln (1 - S_w) \right] \tag{23}$$

This solution is quite different from the parabolic solution which is obtained in the absence of the air filler. The top line is the solution in the absence of the air-water surface tension effect. The terms preceding the brackets in this line are those found in flow thorough a full pipe. New features of this line are the dependence on $(3 \, S_w - 2)$, and a logarithmic boundary layer flow term. For $S_w \leq S_{wc} = 0.66$, the first term of this line goes negative and the logarithmic term in the flux dominates, maintaining a small positive flux at all saturations. The bottom line in the expression for the flux, equation (23), is related to the air-water surface tension effects. This line contains two terms, a first term which is always negative, and a second logarithmic positive term. The negative term in this line will lead to a flow percolation at S_{wc} if its effect becomes significant. In order to study the importance of the surface tension term vis-a-vis the first term we introduce a dimensionless constant

$$B_{pore} = \frac{R_2^2 \, \Delta P}{4 \, L \, \gamma_{lv}} \tag{24}$$

which measures the relative size of the pressure forces versus the surface tension forces. If $B_{pore} > 1$ viscous forces dominate, if $B_{pore} < 1$ surface tension forces dominate.

Taking $\gamma_{lv} = 72.5\ erg/cm^2$ and the pressure drop $\Delta P/L$ at $1\ Bar/cm = 10^6 Dyne/cm^3$, as in gravity drainage, we find that the transitional $B_{pore} = 1$ is achieved if $R_2 = 170\ micron$, which is of the order of the largest pores found in a typical sandstone. All pores smaller than that size are completely dominated by capillary effects for this pressure gradient. For example, for a pore of radius 1 *micron* we obtain $B_{pore} = 3 \cdot 10^{-5}$.

Figure 7 shows the theoretical flux , equation (23), for a pore of radius 500 *micron* as a function of water saturation. The flux shown $Q' = Q \cdot \eta/\rho$ is normalized for the effects of viscosity and density (units are $g\ cm^2/s^2$). This pore size has $B_{pore} > 1$, so that air-water surface tension forces are expected to play a secondary role. The upper curve shows the results without surface tension effects, that is neglecting the second line of equation (23). This would be a valid approximation in a physical situation if the system were heated or if some surfactant were introduced. The lower line shows the flux with the surface tension term included. Following the upper curve from full saturation, close to full saturation there is a square dependence on the water saturation, which is the parabolic dependence on effective radius typical of Poiseiville flow. From approximately 80% saturation the slope changes dramatically as the effects of the air inclusion become greater, so the dominant term becomes the logarithmic term. At yet lower fluid saturation the flux remains positive but small. The lower plot in the figure shows the flux with the surface effects included. It is possible to observe that the effect of creating the bubble, which occurs just below full saturation, immediately decreases the flux by a substantial amount. This is due to the drag forces exerted by the bubble. The flux including the surface tension effects tracks at lower saturations the upper curve from below. The adverse effect of surface tension can clearly be seen.

Figure 8 shows the flux for a 200 *micron* radius pore as a function of water saturation. The size of this pore indicates that it is just within the regime where surface effects become

important($B_{pore} \approx 1$), so it affords a view of the surface dominating regime of equation (23). From the flux obtained at full saturation ignoring the effects of surface tension, the upper curve, the effect of the small size of this pore may be seen, for the flux is one order of magnitude smaller than the 500 *micron* radius pore. The upper plot, where air-water surface tension effects are ignored, shows essentially the same behavior as in figure 5. Comparing the lower plot with the upper plot, the increased importance of surface tension on the flux for this pore size may be seen, since a large drop in the flux appears immediately with the nucleation of the bubble, just below full saturation, with further decreases as the saturation decreases, leading to a percolation threshold at 62% saturation. The effect of surface tension in leading to a flow percolation threshold as pore size decreases may thus be clearly seen. For yet smaller pore sizes the asymptotic percolation threshold is at 66%. Equation (23) predicts an negative flux below the percolation threshold which is physically impossible. It may be that the large surface tensions below the threshold will lead to changes in the form of the water-air interface so that the equation (23) is no longer valid.

Experiments with capillaries filled with air-water mixtures were performed by Taylor [12], Goldsmith and Mason [13] and Cox [14]. Goldsmith [13] arrived at equations identical to equation (20), but without the surface tension term. He showed experimentally the negative velocity terms, predicted by this equation, which are greatest near the air-water contact. His experimental results for increasing bubble size showed the percolation of flow predicted by equation (23). Taylor [12] and Cox [14] arrived experimentally and theoretically at the percolation point. Experimental results lie between $S_{wc} = 0.63$ and 0.68, in good agreement with theory. Saffmann [15] studied the dependence of this percolation point in geometries other than cylinders and for incompressible non-wetting fluids, where stress and velocity continuity must be imposed on the nonwetting phase, wetting phase interface. He arrived at $S_{wc} = 0.6 + 0.4\ m_t$ as the critical saturation, m_t being a geometry dependent constant.

b. Fluid flow at partial saturation through coupled pores

The phenomena of fluid flow through coupled pores at partial saturations has been dealt with by Saffmann [15] and Wilkinson [16] . The much more complicated case of the coupled pore system, representative of the pore space, involves other length scales than those in the single pore case, where the relevant scales are the bubble size and the pore size. In multipore percolation the issue addressed is whether air will enter the pore, as opposed to flow localization within the pore, considered earlier. The governing length scales in the multipore case are the grain radius of curvature and the distances over which the pressure gradients are exerted. It is possible to define a second scaling term [16]

$$B_{cp} = \frac{\Delta P \ R_{grain}{}^2}{L \ \gamma_{lv}} \tag{25}$$

where R_{grain} is the grain size. For low values of B_{cp} simulations performed by Wilkinson [16] showed the percolation $S_{wc} = 0.659$. Here S_w refers to the volume fraction of water with respect to the total pore volume, as opposed to the earlier use of S_{wc} with respect to the volume of an individual pore.

Percolation on the multipore scale will lead to isolated clusters of pores fully saturated with fluid but disconnected to the neighbouring clusters. This effect may also expressed as a transition from a single peak in the NMR relaxation angular frequency probability distribution to multiple peaks. Since $R_{grain} \geq R_{pore}$ the individual pore percolation mechanism is expected to exist even in situations where the the coupled pore mechanism is no longer valid.

Equilibrium Shape of the Air Filler

The cylindrical pore examples examined in the previous sections have been simple geometries where the shape of the air filler is always spherical and the assumption of a totally water wet solid surface is valid at all fluid saturations. Knowledge of the phases geometry in the pore space is nessecary in order to solve the relevant differential equations of classical physics on the particular geometry. In this section an examination will be made of a realistic pore shape where the assumption of total wetting of the solid surface is not generally valid at all

partial saturations.

The pore shape examined here is the grain boundary pore. This pore is created by a number of grains in contact. The specific case examined here is that of four spherical grains of radius R in contact and is typical of a cubic packed system. A unit cell of this geometry is shown in figure 9. The system will be taken to be a two dimensional system, so that the grains are infinite cylinders extending into the plane of the figure. The porosity of such a system is $(4 - \pi)/\pi = 0.215$, and the pore surface to volume ratio is $(2\pi)/((4 - \pi)R)$. Figure 9(a) shows the geometry of the air filler at high saturations, when the air filler radius, r, is smaller than the equivalent spherical cell radius, r_e, the radius of the largest circle which could be fit into the void, given by $r_e = (\sqrt{2} - 1) \cdot R$. At greater levels of fluid saturation (for this geometry $S_w = 0.374$), the air filler is cylindrical with a positive radius of curvature, as in the case of the cylindrical pore examined previously, which does not follow the grain surface. Such an air filler shape will be termed an *incommensurate* filler. At saturations close to the saturation where the air filler radius reaches the equivalent radius, the filler must change it's geometry. The two end members geometries it may adopt are shown in figures 9(b) and 9(c). Figure 9(b) shows a filler which has adopted the grain boundary geometry. This filler, which we term a *commensurate* filler, leaves the grain surfaces totally liquid wet and the fluid film connected. It is fully charectarized by the thickness of the liquid film ΔR. A distinctive feature of this geometry is the negative radius of curvature of the air filler. Figure 9(c) is the case of the *incommensurate* air filler at low fluid saturations. Here the solid surface of each grain is not water wet over an angular region $\Delta\theta$, and the water films are concentrated in annular pockets on the pore corners, each with positive air-water radii of curvature. It is expected that the differences of the equilibrium shapes of the air fillers, for a given water saturation S_w, will be extremely important in determining some of the physical properties of these air-water mixtures. The water film of the incommensurate shape behaves as a connected body for most transport properties, whereas the commensurate shape is disconnected (except for possi-

ble surface diffusion).

The equilibrium shape of the air filler may be determined from requiring that the configuration which the system adopts be that which has the minimum total interfacial energy [17]. The interfacial energy is given by

$$W = \sum_{k=1}^{k=K} \gamma_k \cdot A_k \tag{26}$$

where the summation is over the K interfaces betwen the phases, each interface being charectarized by a surface tension γ_k and and an area A_k. In this case there are three relevant surface tensions; γ_{sl}, γ_{lv}, and γ_{sv}, the solid-liquid, liquid-vapor, and solid-vapor surface tensions, respectively.

The incommensurate filler geometry of figure 9(a) has the following interfacial energy per unit cell;

$$W_a = \gamma_{lv} \cdot 2\pi rL + \gamma_{sl} \cdot 2\pi RL \quad , \tag{27a}$$

where L is the pore length perpendicular to the plain of the paper, at a water saturation of

$$S_w = 1 - (\frac{\pi}{4-\pi}) \cdot (\frac{r}{R})^2 \qquad \text{for } S_w \geq 0.374 \quad .$$

The commensurate filler geometry of figure 9(b) has an interfacial energy per unit cell;

$$W_b = \gamma_{lv} \cdot 2\pi(R + \Delta R)\,(1 - 8\,\frac{g}{360})L + \gamma_{sl} \cdot 2\pi RL \tag{27b}$$

where g is an angle given (in degrees) by $g = \cos^{-1}(\frac{R}{R + \Delta R})$ at a water saturation given by

$$S_w = (\frac{\pi}{4-\pi}) \cdot \frac{(2\,R\,\Delta R + \Delta R^2)}{R^2} \quad .$$

The incommensurate filler geometry of figure 9(c) has an interfacial energy per unit cell given by

$$W_c = \gamma_{lv} \cdot 2\pi r' \,(\frac{2\beta}{90})L + \gamma_{sl} \cdot 2\pi R\,(1 - \frac{\Delta\theta}{90})L + \gamma_{sv} \cdot 2\pi R\,(\frac{\Delta\theta}{90})L \quad , \tag{27c}$$

where $\beta = 90 - \alpha$ is the half apperature angle of the circular water-air interface, r' is the radius of this interface, and α is the half apperature angle of the corner. From geometric argu-

ments $\alpha = 45 - \frac{\Delta\theta}{2}$, $r' = \tan(\alpha) \cdot (\sqrt{2} - 1)R\ (1 - \frac{\Delta\theta}{90})$. The water saturation of this configuration is

$$S_w = 0.613 \cdot (\frac{\pi^2}{4\,(4-\pi)})\,(1 - \frac{\Delta\theta}{90})^2 \tan(\alpha) \cdot [1 - \pi\tan(\alpha) \cdot (\frac{1}{2} - \frac{\alpha}{180})\,] \quad \text{for } S_w \leq 0.374\ .$$

The solutions for r and S_w in the case of W_c utilize an assumption of zero contact angle for the liquid-vapor interface at the triple contact of air, liquid, and solid. The solution for higher contact angles may therefore be slightly different.

Solutions for the minimum energy configuration are aided by the application of Young's equation [18]

$$\gamma_{sv} = \gamma_{sl} + \gamma_{lv}\cos(\phi) \tag{28}$$

where ϕ is the triple point contact angle, which we assumed was zero for the calculations of W_c.

Inserting realistic values for the quartz-water system [19]; $\gamma_{sl} = 334\ erg/cm^2$ and $\gamma_{sv} = 406\ erg/cm^2$ the three energies W_a, W_b and W_c are plotted in figure 10 as a function of water saturation for a one micron grain radius. The surface energy per unit cell shown is normalized by division by the length L, the values being in erg/cm. It can be seen that at saturations above 0.374, where only solutions W_a and W_c exist, the lowest energy solution is the incommensurate circular filler W_a. At $S_w = 0.374$ solution W_a becomes impossible to maintain geometrically and the system merges smoothly into solution W_c, the incomensurate disconnected configuration. The connected configuration W_b is much higher energetically for the given values of surface tension. The significance of the difference among the various configurations becomes apparent when compared to the unit cell thermal energy of the water, which at standard temperature and pressure is given by

$$W_{th} = 1.27 \cdot 10^9\ S_w\ (4 - \pi)R^2\ L \tag{29}$$

Comparing the expression for the thermal energy to equations (27a) through (27c), it may be seen that since the interfacial energy scales as R, while the thermal energy as R^2, the relative

importance of the differences among the interfacial energy configurations increases as the grain radius decreases (for $R << 1\ cm$). Also important is the linear decrease of the thermal energy, W_{th} , with water saturation, whereas the interfacial energies vary inversely to the water saturation (see figure 10), so that at low water saturations the interfacial energetic differences become more important. Assuming that only states W_b and W_c exist at saturations below 0.374, and using Boltzmann statistics for the relative populations of the two, it is found that for the 1 micron grain of figure 10, there are at $S_w = 0.37$ already 0.2% more cells with the incommensurate geometry whose energy is W_c than those with energy W_b .

Detailed examination of equations (27a) through (27c) reveals that for the zero contact angle ϕ case, only γ_{lv} influences the results so that the relative ordering of the three energy states at a given S_w may not be changed. If a non-zero contact angle is allowed, as would be the case for a higher γ_{sv} [18], the relative configuration could be changed, bringing the commensurate solution W_b below W_c at some saturation. This would allow the system to remain connected to low water saturations.

A conclusion of this energetic treatment of the grain boundary pore interfacial energy is the discovery of a transition from a connected pore to disjointed water films at $S_w = 0.374$. For a three dimensional simple cubic system the same transition would occur at $S_w = 0.57$ ($r_c = (\sqrt{3} - 1)R$), and at slightly higher saturations for denser packed systems (where a unit porous cell consists of more than a single pore). This suggests that the effect which is seen by NMR may also be due to a physical disjointing of the water in pores with negative radii of curvature. Rocks which do not display this behavior may correspond to those with pores having mainly positive radii of curvature, or low solid-vapor interfacial tensions.

Conclusions

A study of the behavior of water in porous rocks at partial fluid saturations suggests the presence of connectivity percolation phenomena in some rocks, which is seen by NMR as a

change in the relaxation angular frequency probability distribution function and in the sample magnetization. In the relaxation rate distribution, it is seen with the appearance of much higher relaxation rates (adsorbed states). In the magnetization, it is seen in a magnetization much greater than mean field predictions.

Available NMR theory predicts these changes in the relaxation rate distribution at the transition from the strongly diffusionally coupled to the weakly coupled, or decoupled, regimes of pore space. Satisfactory explanation of the anamolously high magnetization awaits further theoretical work.

Fluid mechanical considerations of flow stability predict flow percolation at 66% water saturation for rocks with pore sizes which are within the surface tension dominated regime. Two possibilities of percolation exist, those on the individual pore scale and those on the multiple pore scale.

For pores with negative radii of curvature boundaries surface tension minimization arguments predict that the lowest energy state, for typical values of the quartz-water-vapor interfacial tensions, which is therefore the most stable, at low fluid saturation is that which requires the retreat of the water into disjointed annular pockets at the grain contacts. This argument predicts physical disjointing of the fluid films at saturations ranging from 37% to 66%, depending upon the packing arangement of the pore space, denser packed systems having a higher water saturation percolation threshold.

Several explanations may be provided for rocks which do not seem to display this phenomena. The first option is that they are effectively decoupled very close to full saturation as would be the case for high S/V rocks. The second possibility is that they remain connected to very low saturations, which requires a combination of low S/V, low wettability and specific pore size and geometry distributions. A third option is the existence of very large scale heterogeneities, which could smear out these phenomena.

Acknowledgements

The authors thank Rosemary Knight of Stanford Geophysics, George Parks and Gordon Brown of Stanford Applied Earth Science, Aharon Kapitolnik of Stanford Applied Physics, Kenneth Mendelson of Marquette University, and Morrel Cohen of Exxon Research for helpful critical discussions. The interest and comments of our fellow student in the Stanford Rock Physics Project, Diane Jizba, has been an important stimulus for this work.

References

[1] E. J. Schmidt, K. K. Velasco, and A. M. Nur, Quantifying solid-fluid interfacial phenomena in porous rocks with proton nuclear magnetic resonance, *J. Appl. Phy. 59 (8), 2788 (1986)*

[2] M. Cohen and K. Mendelsohn, Nuclear magnetic resonance and the internal geometry of porous rocks, *J. Appl. Phy. 53 (27), 1127 (1982)*

[3]W. E. Kenyon, P. I. Day, C. Straley, and J. F. Willemsen, Compact and consistent representation of rock NMR data for permeability estimation, *Soc. Petrol. Eng. paper #15643, presented at the 61th Annual Tech. Conf.*, New Orleans (1986)

[4]P. Richards, Effect of low dimensionality on prefactor anomalies in superionic conductors, *Sol. St. Comm., 25, 1019 (1978)*

[5]P. Richards, Magnetic resonance in superionic conductors, *In Physics of superionic conductors (Edit. M. Salamon)*, Springer Verlag 15, Berlin (1979)

[6]R. Dietz, F. Meritt, and R. Dingle, Exchange narrowing in one dimensional systems, *Phy. Rev. Let. 26 (19), 1186 (1971)*

[7]K. Mendelsohn, Nuclear magnetic resonance in sedimentary rocks: effect of proton desorption rate *J. Appl. Phy. 53 (9), 6465 (1982)*

[8]K. Brownstein, and C. Tarr, Importance of classical diffusion in NMR studies of water in biological cells, *Phys. Rev. A 19 (6), 2446 (1979)*

[9]M. Cohen, Nuclear magnetic resonance in random porous materials, *Proc. Conf. on transport and relaxation in random media,* Nat. Bur. of Stands., Gaithersburg, Maryland (1986)

[10]K. Mendelsohn, Nuclear magnetic relaxation in porous media, *Proc. Symposium on Chemistry and physics of composite media (Edit. by* M. Tomkiewitz and P.N. Sen), Electrochemical Society Press, Pennington, New Jersey, 282, (1985)

[11]L. D. Landau, and E. M. Lifshitz, Fluid mechanics, *Course of Theor. Physics Vol. 6, 55, Pergamon, New York, (1959)*

[12]G. I. Taylor, Deposition of a viscous fluid on the wall of a tube, *J. Fluid Mech. 10, 161 (1961)*

[13]H. L. Goldsmith, and S. G. Mason, The movement of single large bubbles in closed vertical tubes, *J. Fluid Mech. 14, 42 (1962)*

[14]B. G. Cox, On driving a viscous fluid out of a tube, *J. Fluid Mech. 14, 81 (1962)*

[15]P. G. Saffman, Fingering in porous media, *In Macroscopic properties of porous media (Edit R. Burridge, S. Childress* and G. Papanicolaou), Springer Verlag 154, Berlin, 208 (1982)

[16]D. Wilkinson, Percolation model of immiscible displacement in the presence of buoyancy forces, *Phy. Rev. A 30 (1), 520 (1984)*

[17]R. E. Johnson, J. R., and R. H. Dettre, Contact angle hysteresis, *In Advances in Chemistry (Edit. R. F. Gould), Vol. 43, 112,* American Chemical Society Press, Washington (1964)

[18]C. A. Miller and P. Neogi, Interfacial phenomena, *Surfactant Science Series (Edit. M. J. Schick and F. M. Fowkes),* Vol. 17, Marcel Dekker, New York (1985)

[19]G. A. Parks, Surface and interfacial energies of quartz, *J. Geophys. Res. 89 (B6), 3997 (1984)*

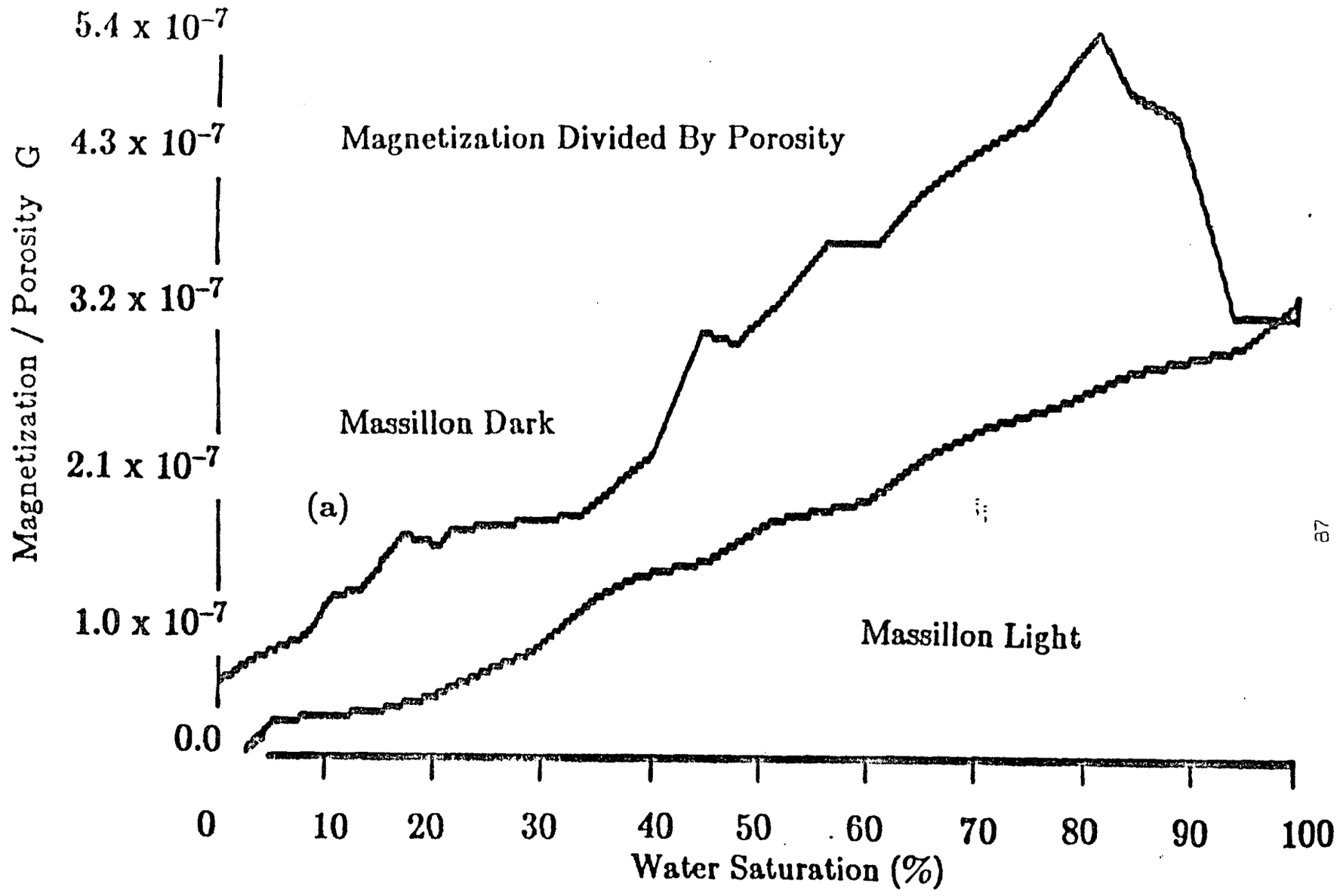

FIG. 1(a). Massillon Dark and Massillon Light sandstone porosity normalized magnetization as a function of water saturation.

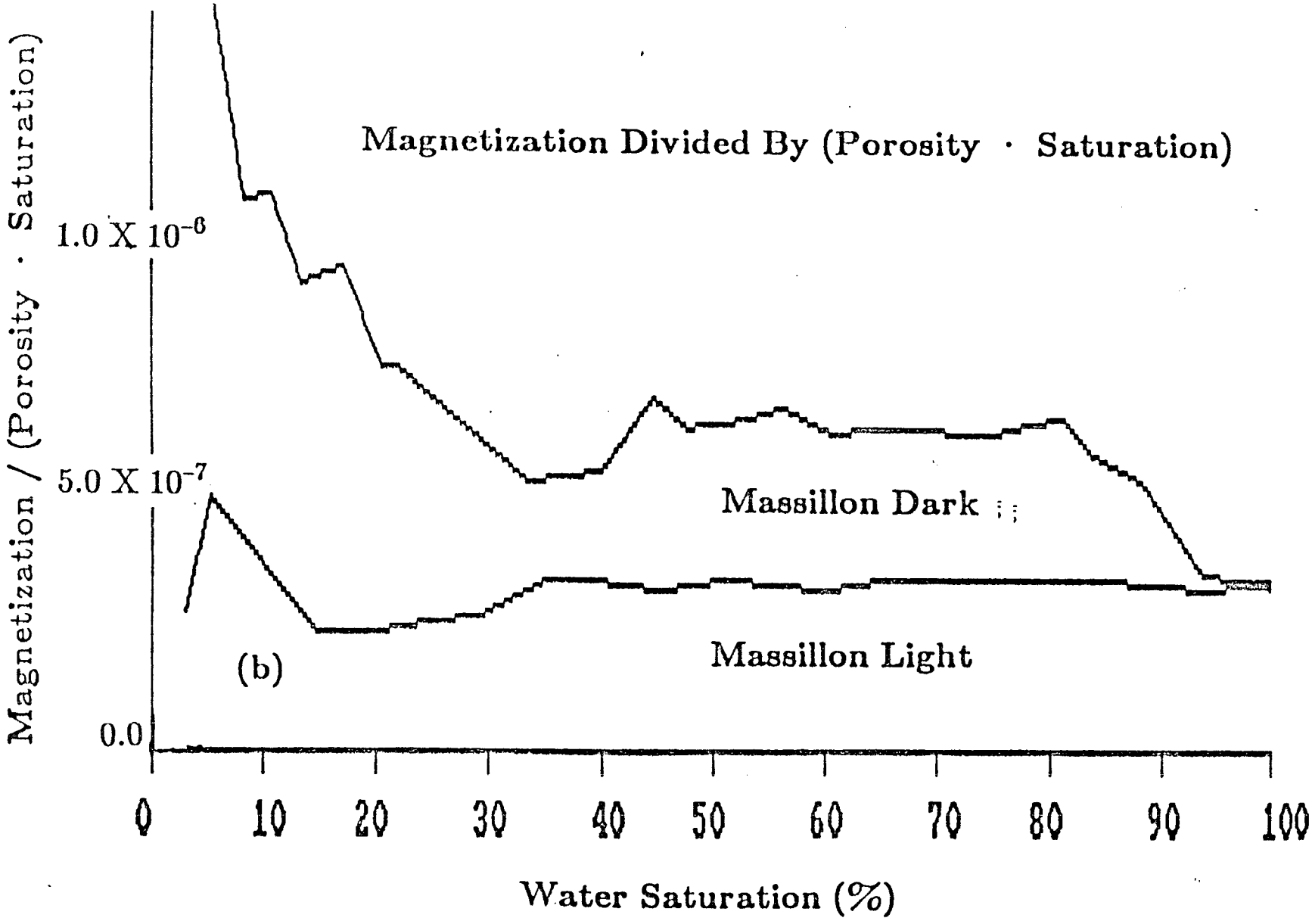

FIG. 1(b). Massillon Dark and Massillon Light sandstone magnetization normalized to the product of porosity and water saturation as a function of water saturation.

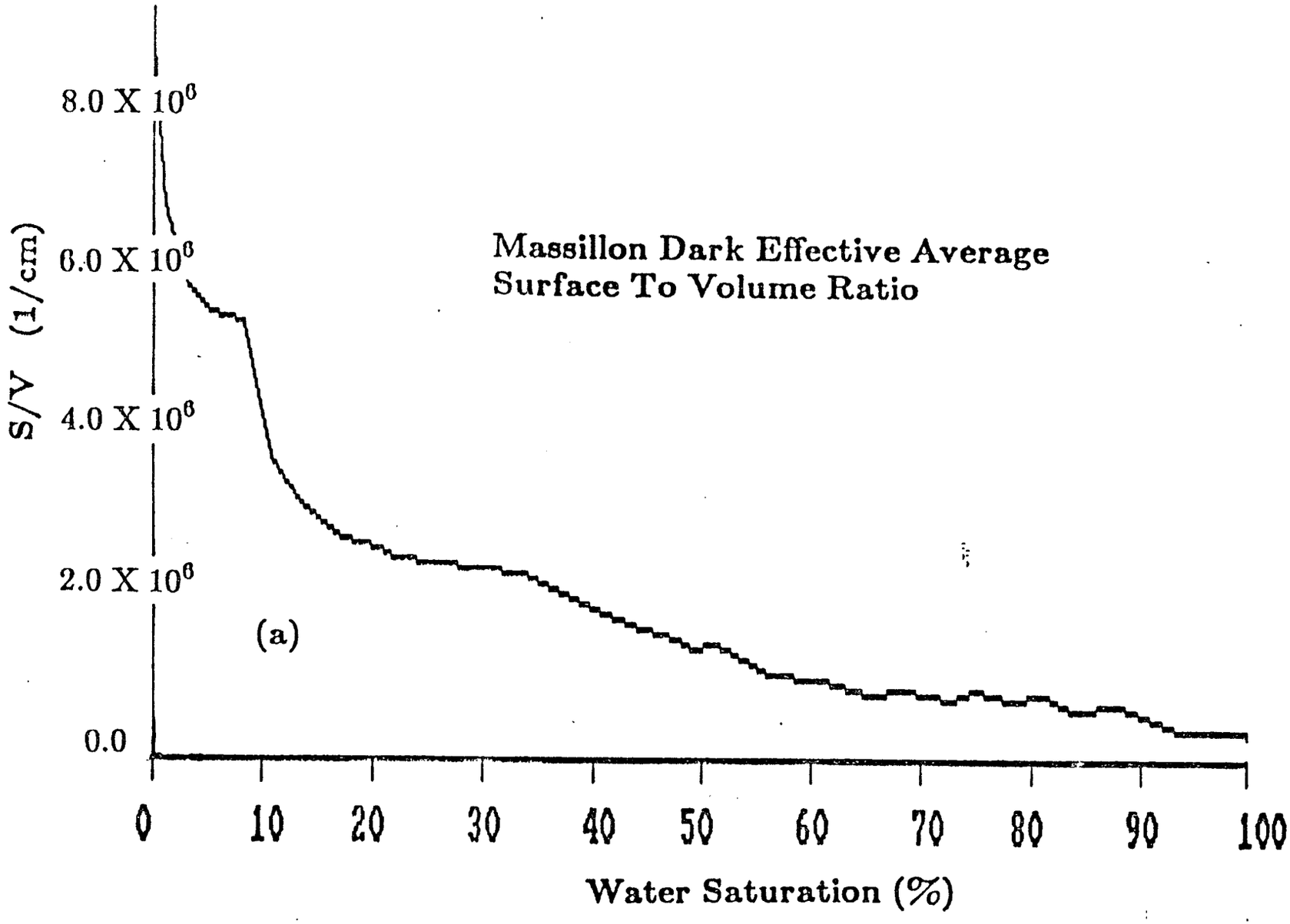

FIG. 2(a). Massillon Dark sandstone average effective $\frac{S}{V}$ ratio as a function of water saturation.

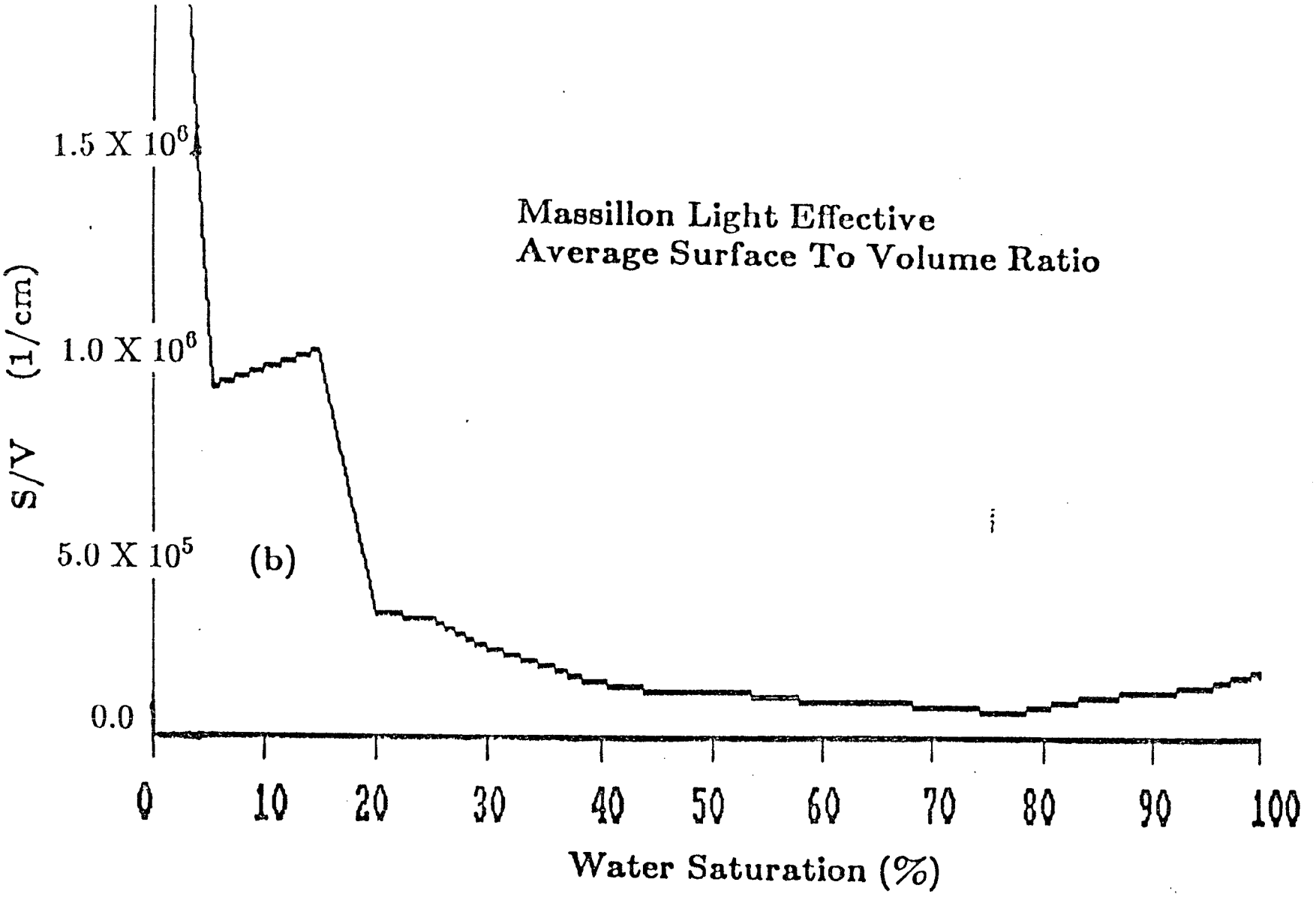

FIG. 2(b). Massillon Light sandstone average effective $\frac{S}{V}$ ratio as a function of water saturation.

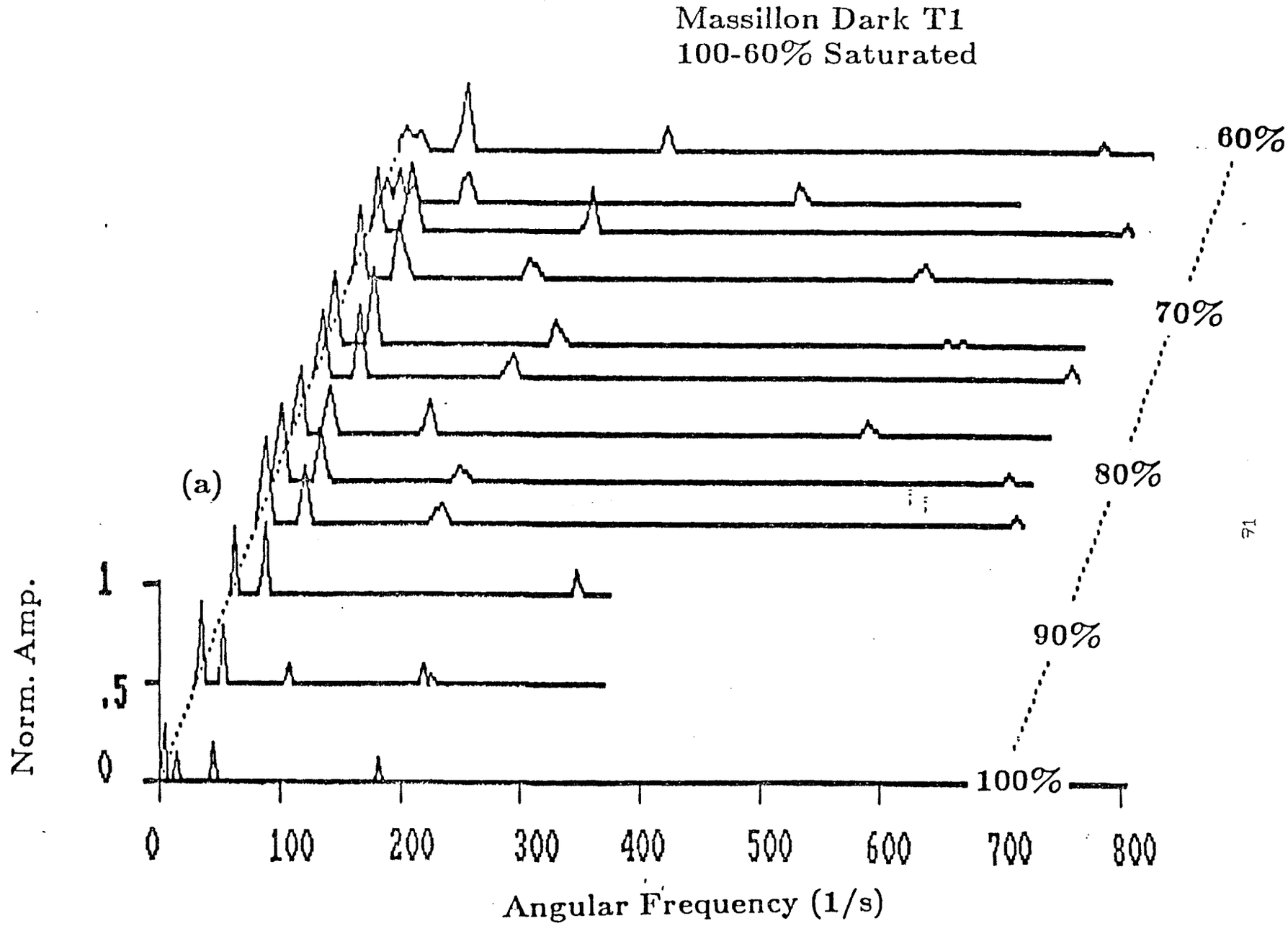

FIG. 3(a). Normalized relaxation angular frequency probability distribution, $P(\omega)$, as function of water saturation, for Massillon Dark at 100% to 60% water saturation.

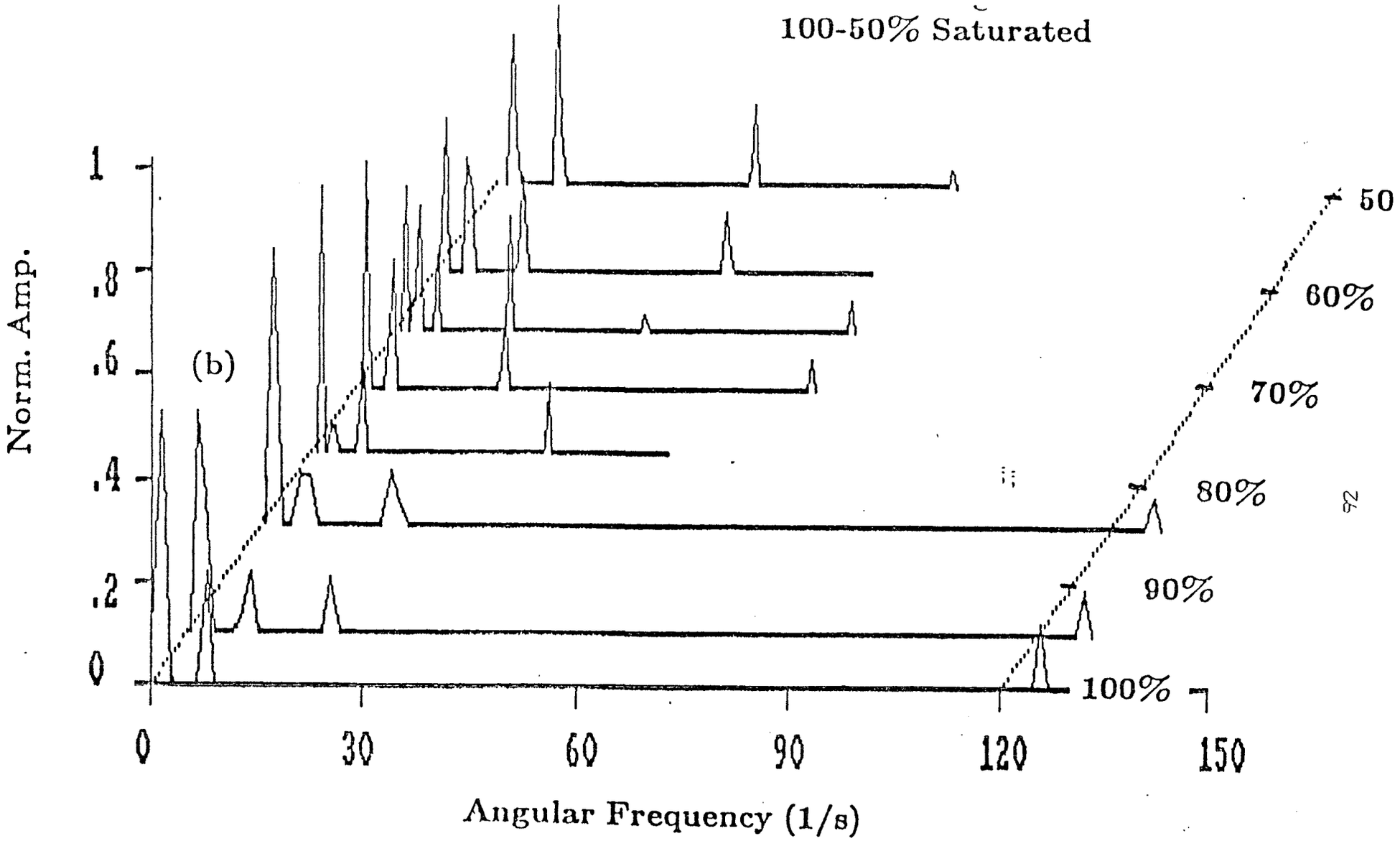

FIG. 3(b) Normalized relaxation angular frequency probability distribution, $P(\omega)$, as a function of water saturation, for Massillon Light at 100% to 50% water saturation.

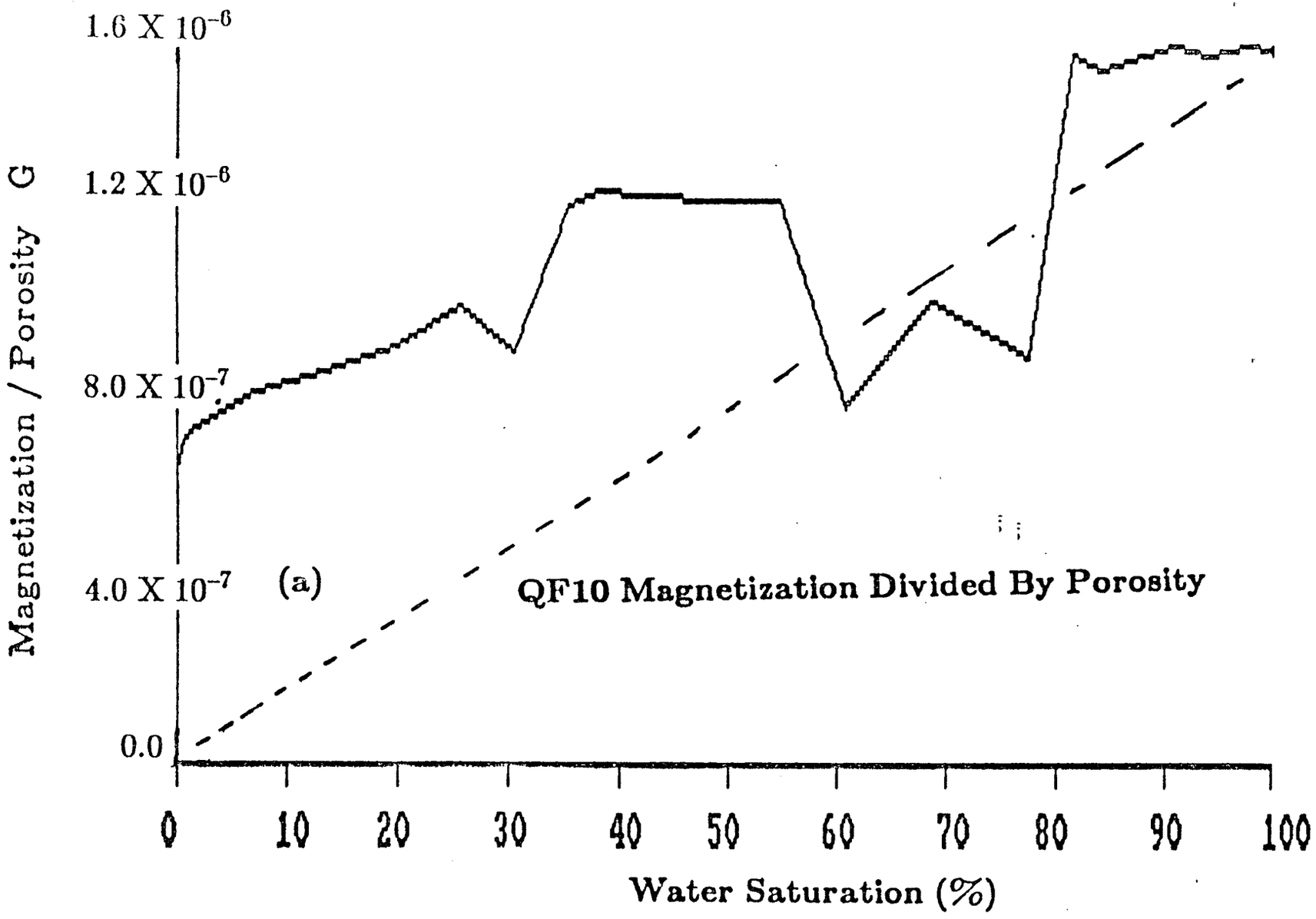

FIG. 4(a). QF10 magnetization as a function of water saturation.

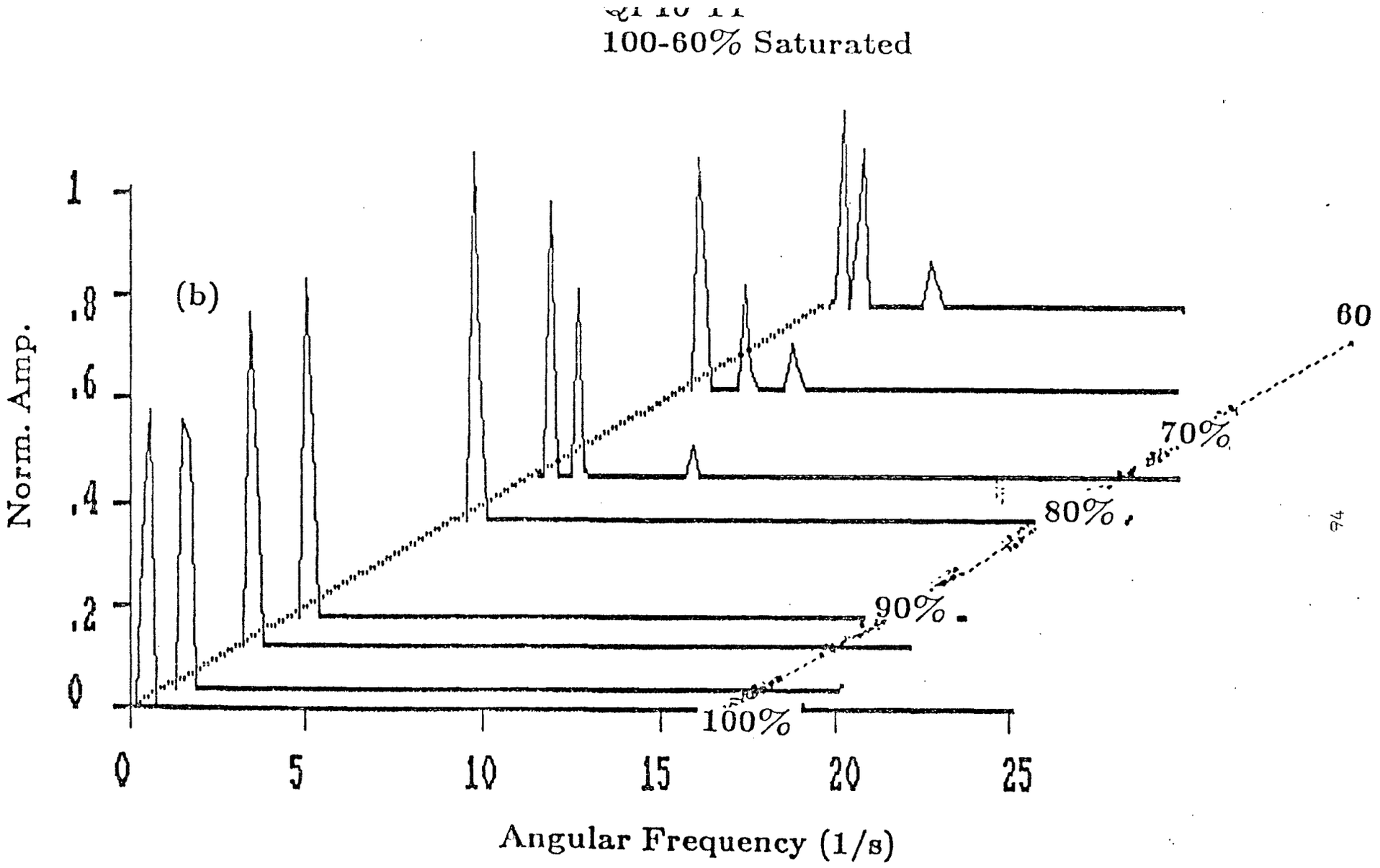

FIG. 4(b). QF10 normalized relaxation angular frequency probability distribution, $P(\omega)$, as a function of water saturation.

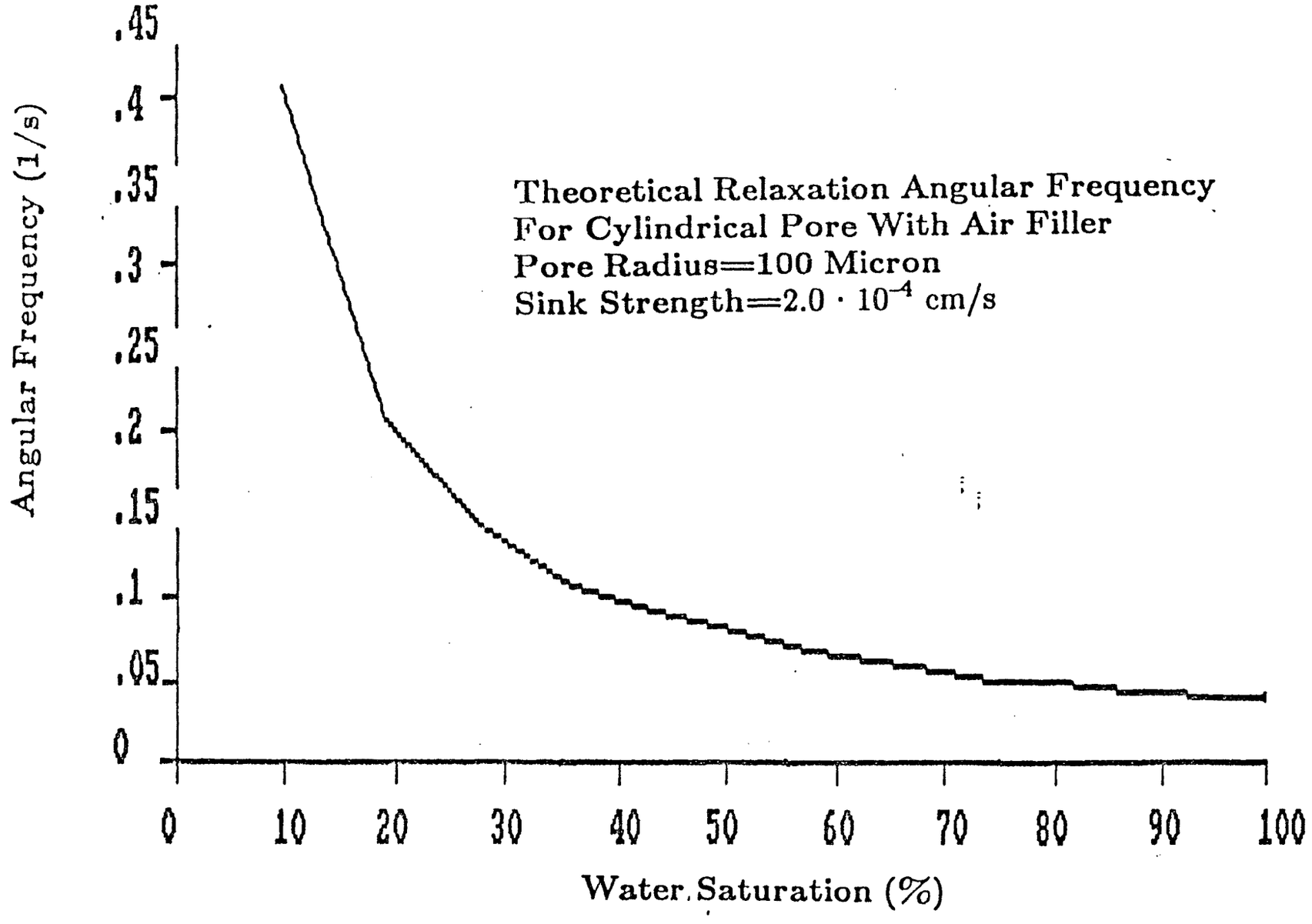

FIG. 5. Theoretical diffusional relaxational angular frequency, ω_0, for a 100 *micron* radius cylindrical pore as a function of water saturation.

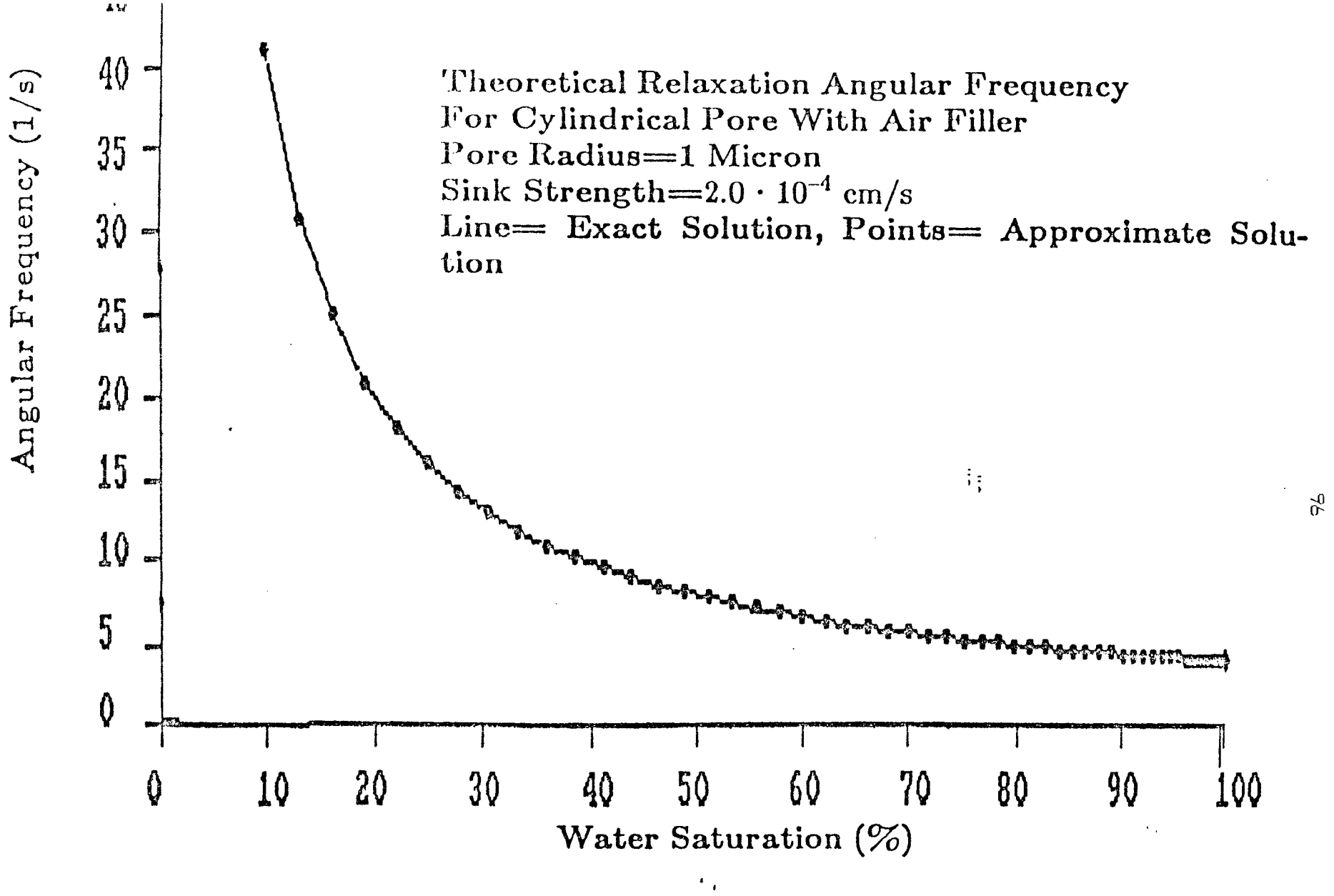

FIG. 6. Theoretical diffusional relaxational angular frequency, ω_0, for a 1 *micron* radius cylindrical pore as a function of water saturation. Line is exact theory, points are approximate theory of Cohen [9].

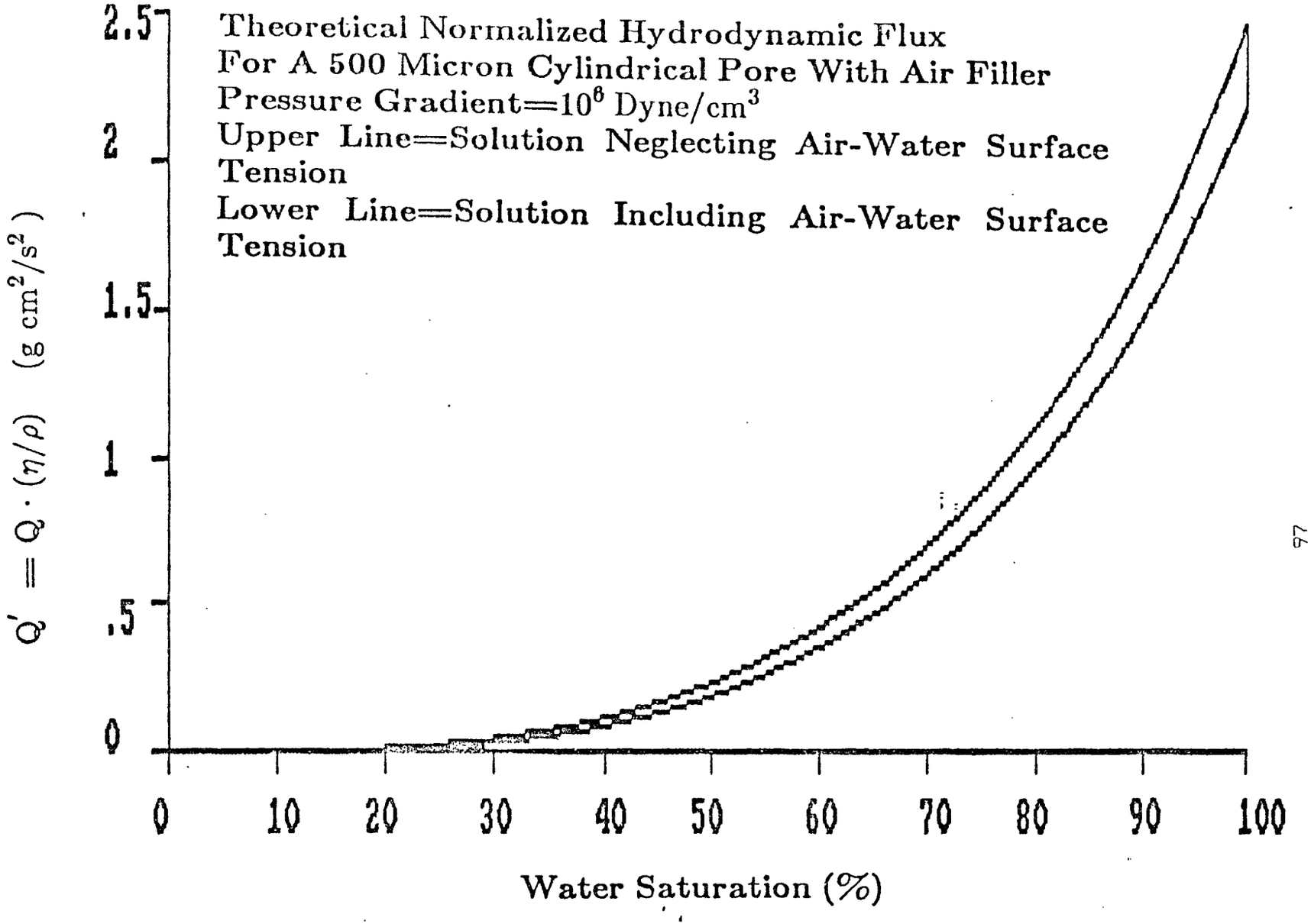

FIG. 7. Theoretical normalized hydrodynamic flux for a 500 *micron* radius cylindrical pore as a function of water saturation. Upper curve are results of equation (23) neglecting air-water surface tension. Lower curve are results including surface tension.

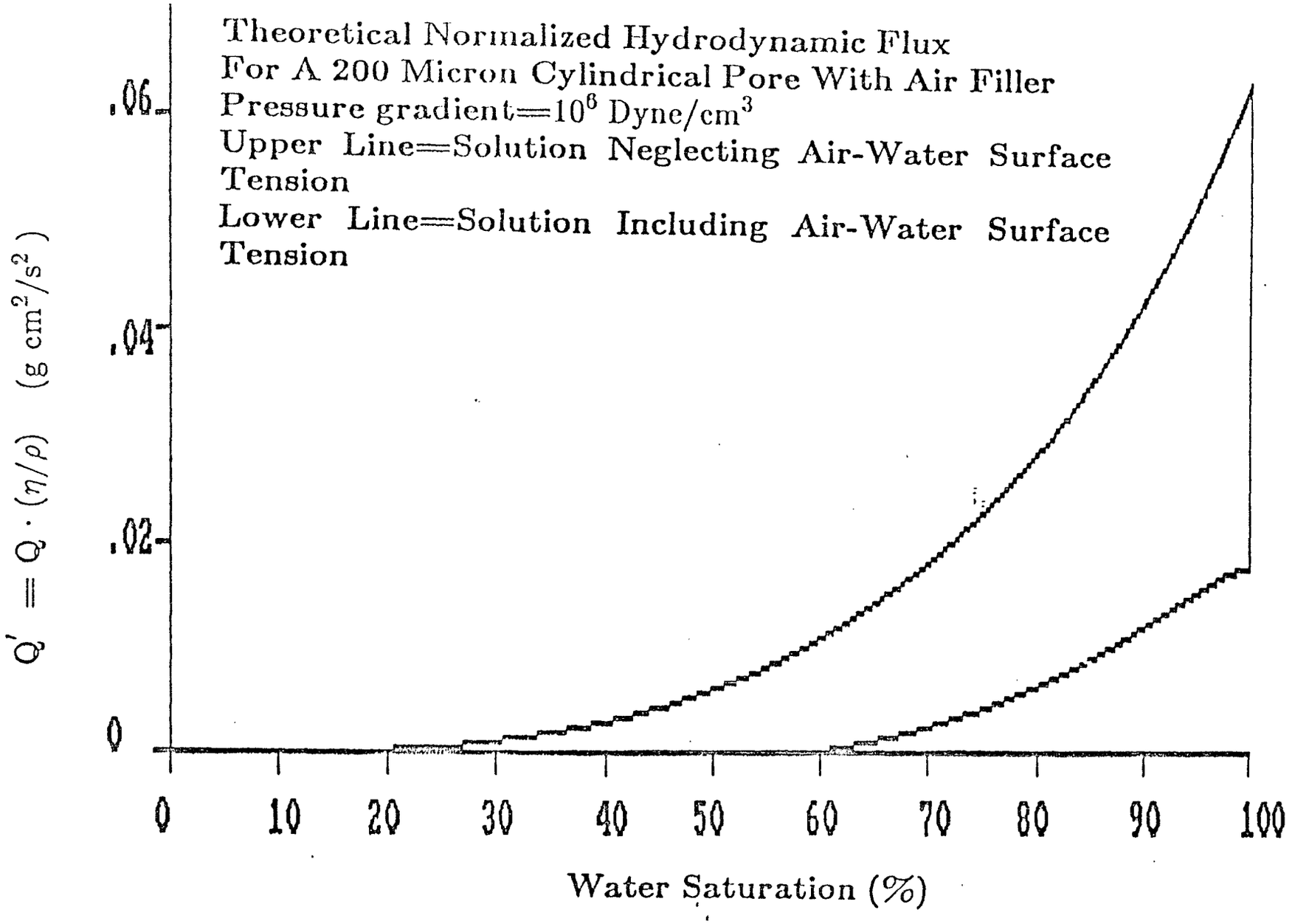

FIG. 8. Theoretical normalized hydrodynamic flux for a 200 *micron* radius cylindrical pore as a function of water saturation. Upper curve are results of equation (23) neglecting air-water surface tension. Lower curve are results including surface tension.

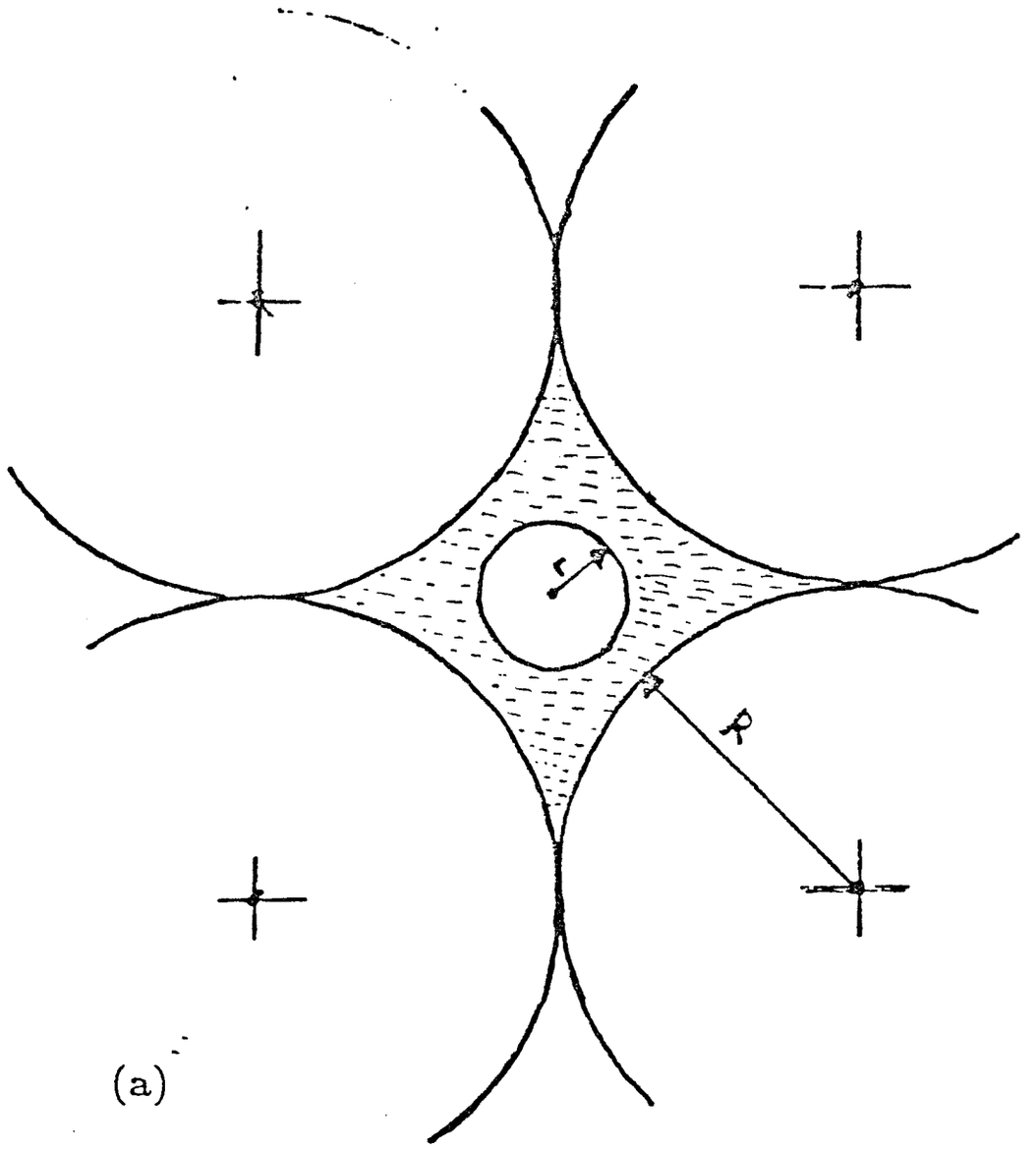

Grain Boundary Pore With Incommensurate Air Filler
At High Water Saturation

FIG. 9(a). Spherical grain pack pore *incommensurate* air filler at high water saturation. All angles and lengths shown are defined in the text.

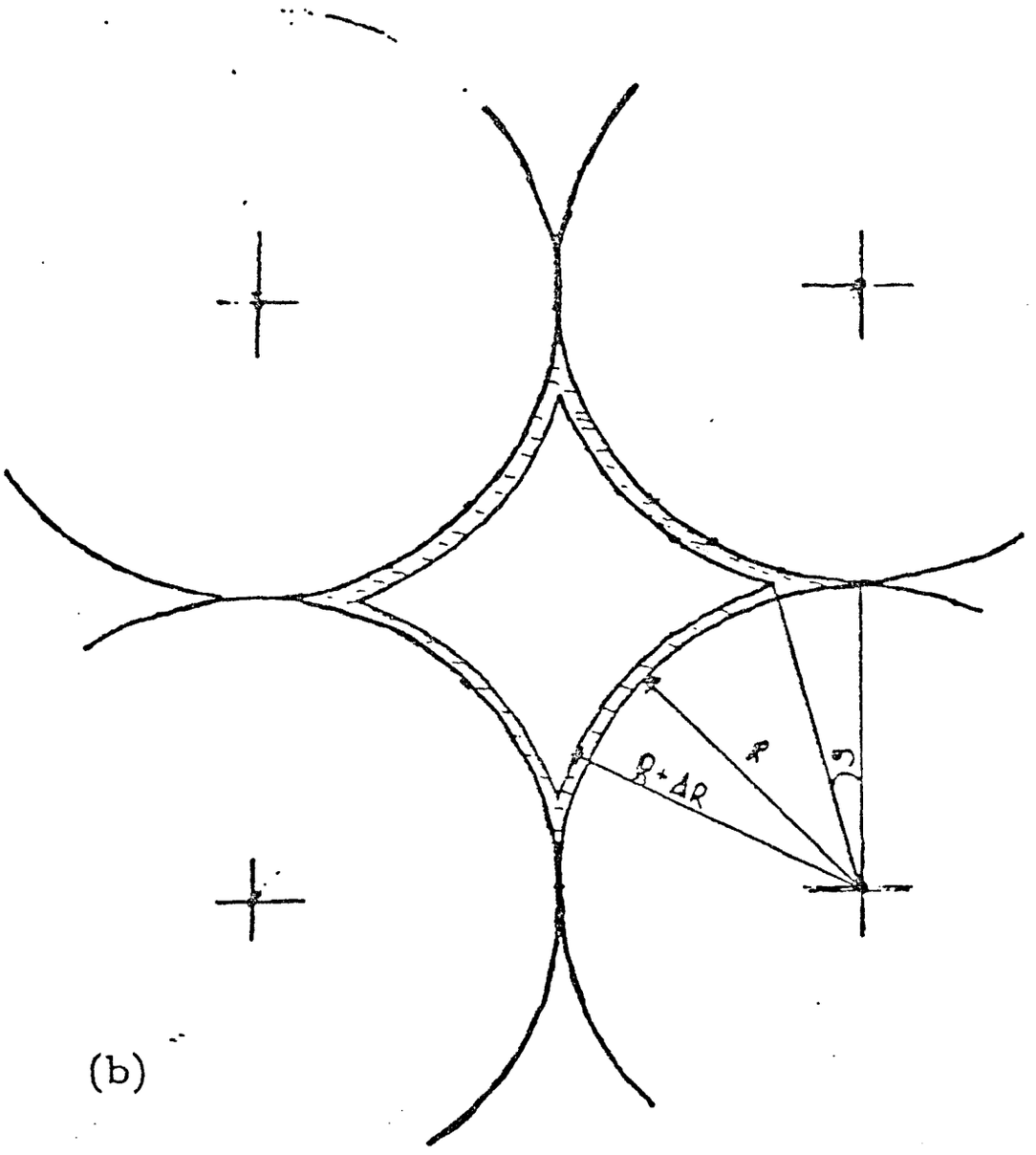

Grain Boundary Pore With Commensurate Air Filler

FIG. 9(b). Spherical grain pack pore *commensurate* air filler at low water saturation. All angles and lengths shown are defined in the text.

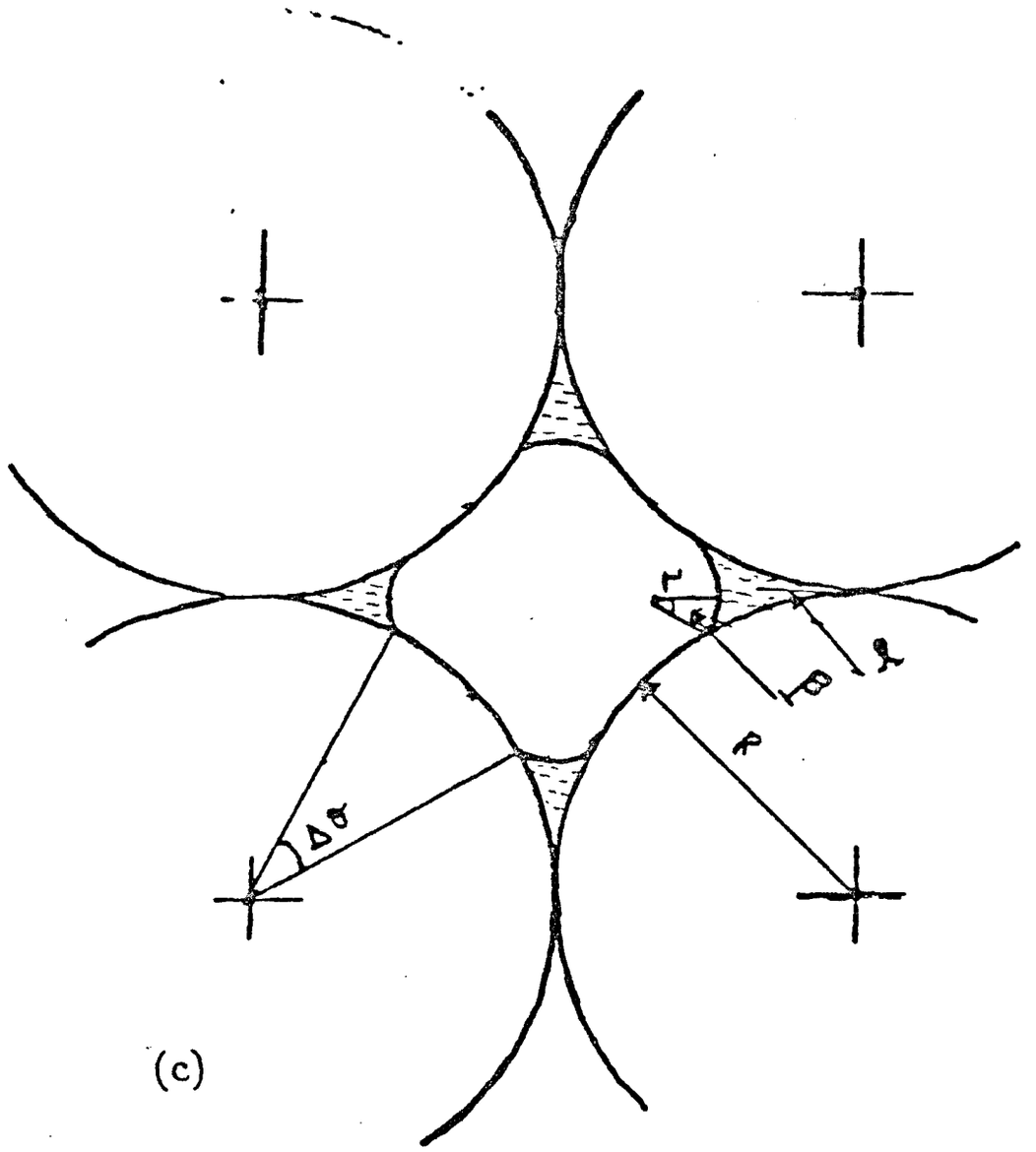

**Grain Boundary Pore With Incommensurate Air Filler
At Low Water Saturation**

FIG. 9(c). Spherical grain pack pore *incommensurate* air filler at low water saturation. All angles and lengths shown are defined in the text.

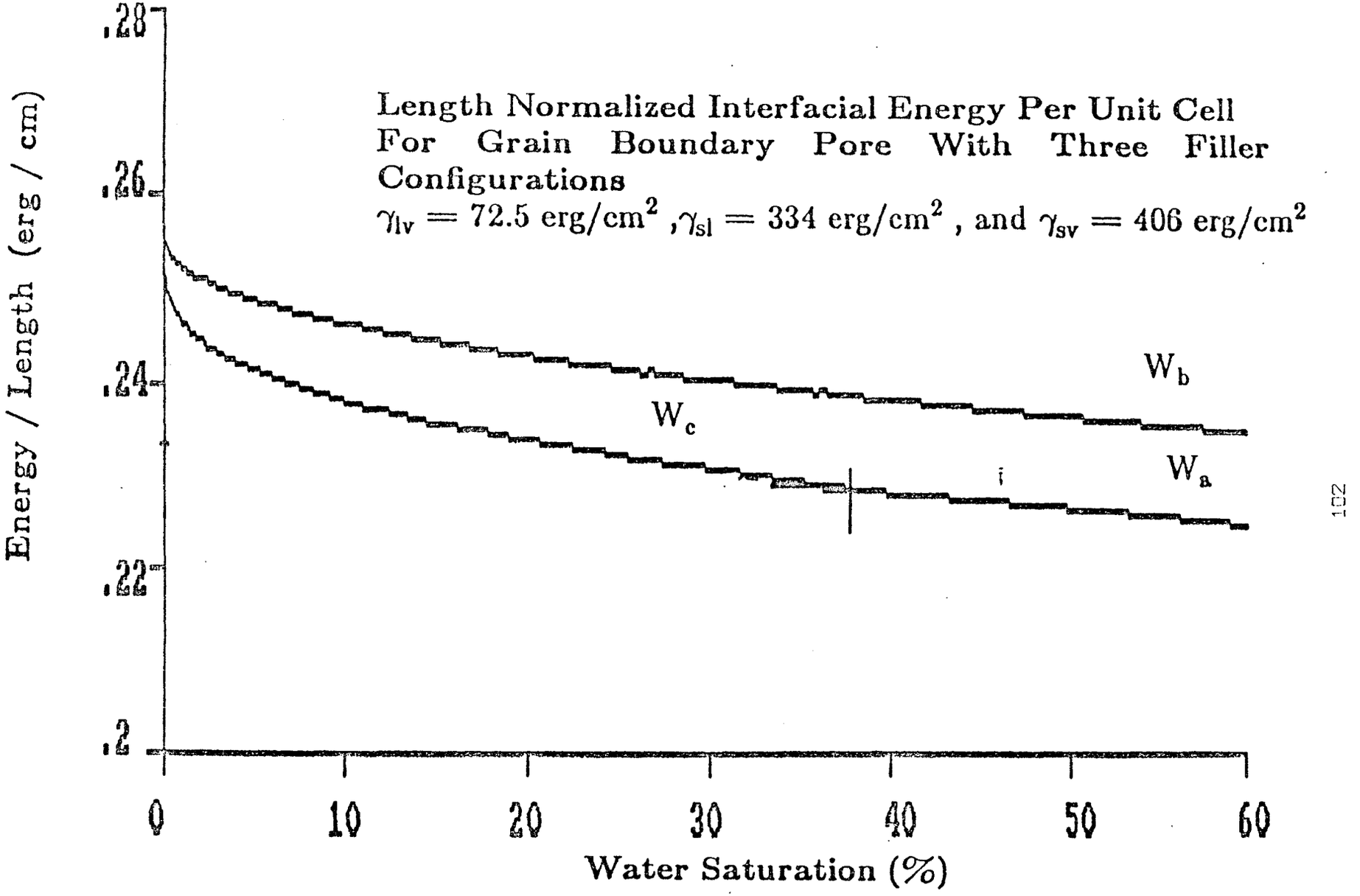

FIG. 10. Unit cell interfacial energy per unit length as a function of water saturation for a 1 *micron* radius grain for the three geometries defined in figure 9.

WIDEBAND ACOUSTIC RESPONSE OF FLUID SATURATED POROUS ROCKS: THEORY AND PRELIMINARY RESULTS USING WAVEGUIDED SAMPLES

Ehud J. Schmidt and Amos M. Nur

Stanford Rock Physics Project, Geophysics Department, Stanford University, Stanford, CA 94305

Abstract

The complex compressional and shear frequency-dependent elastic constants of non-porous and porous solids are measured in a frequency range 5 kHz to 1 MHz. The measurements are performed in a continuous wave acoustic transmission bridge using cylindrical samples. Use of waveguided samples prevents problems of diffraction and wavefront spreading, which are difficult to correct over broad frequency ranges. The theory of waveguided elastic wave propagation in isotropic media with complex elastic constants (generalization of the Pochammer-Cree solution) is presented. The resulting dispersion relations are utilized in the interpretation of the experimental results from solids with real frequency-independent elastic constants, solids with real frequency-dependent elastic constants and rocks with complex frequency-dependent effctive elastic constants. For solids with frequency-independent complex elastic constants (constant Q) theoretical results reveal the appearance of specific dissipation peaks associated with waveguide geometry. An algorithm is formulated to invert the extensional and torsional shear experimental results, utilizing the theoretical dispersion relations, to obtain the complex frequency-dependent elastic constants. Constant Q is found to be inadequate for describing the frequency dependent properties of most materials studied. Evidence of the effects of pore scattering and the reduction of matrix moduli due to water adsorption is shown for porous glass.

PACS numbers: 43.20.B, 43.20.H, 43.20.M

Introduction

The frequency dependence of the elastic moduli of solids [1], liquids [2,3], and porous solids [4–12] has been the subject of numerous experimental and theoretical [9,13–21] investigations. The motivation of these studies has been the possible utilization of the frequency dependence as an additional parameter to the more classical temperature and pressure dependence for the better understanding of material physical and chemical properties. Possibilities exist for the applicability of this frequency dependence for the creation of acoustic spectroscopy, which could reveal valuable information on molecular composition and motion for single phase materials, as well as boundary interactions and phases geometry for multiphase materials.

Measurement of material elastic properties over a broad frequency interval requires the overcoming of two major problems, the first of theoretical nature and the second of an experimental nature.

The theoretical question is that of properly interpreting experimental results obtained on a single sample over a frequency interval where the ratio of the wave's wavelength to sample dimensions varies greatly. This problem is particularly acute in measurements which span frequency ranges where the wavelength goes from being greater than the sample size to being smaller than sample size, as the theoretical corrections for diffraction and sample size effects are generally relevant on asymptotic sides of this critical wavelength [6,22]. In order to minimize the interpretive problems the experiments here are conducted in cylindrical acoustic waveguides where the elastic wave particle motion throughout the sample is described fully by solution of the appropriate wave equations. As solids with complex (lossy) elastic moduli were studied, the Pochammer-Chree solution for the propagation of elastic waves in lossless isotropic cylinders was extended to the case of propagation in media with complex elastic moduli. The importance of this solution is evident in the appearance of new specific loss peaks associated with the coupling of the loss mechanisms with waveguide geometry.

Experimentaly, construction of broadband elastic wave sources and receivers for operation in the desired frequency band is a complicated task, due to the highly dispersive frequency dependence of both the mechanical and the electromagnetic impedances of most acoustic devices [23,24]. The problem is complicated when these devices are constructed for the study of lossy media, as the various methods of damping which involve significant loss of acoustic output power may not be used. For this purpose sets of broadband compressional and torsional shear piezoelectric (PZT) tranducers were designed and built with a smoothly varying frequency response over the frequency interval 5 kHz to 1 MHz. These transducers were used for the study of non-porous solids with frequency independent elastic constants, solids with frequency dependent elastic constants and porous solids with frequency dependent elastic constants. An algorithm has been devised for the inversion of the the wave frequency dependent velocity and attenuation for the complex frequency dependent dilatational elastic modulus $C12^*$ and the shear modulus $C44^*$. Preliminary physical interpretation is provided for the inverted elastic moduli of plexiglass and porous glass.

Theory of Wave Propagation in Cylindrical Waveguides With Complex Elastic Constants.

The approach to calculating the dispersion relations for wave propagation in cylindrical waveguides with complex elastic moduli is illustrated by first examining the complex one dimensional scalar wave equation

$$\nabla^2 \psi - \frac{\rho}{M^*} \cdot \frac{\partial^2}{\partial t^2} \psi = 0 \tag{1}$$

where ρ is the density , $M^* = M' + i\, M''$ is the complex elastic modulus with M' its real part and M'' its imaginary part and ψ is the scalar potential.

A wave solution is assumed for ψ

$$\psi \approx e^{-i\,(k^* r - \omega t)} \tag{2}$$

where $k^* = k' - i\,\alpha$ is the complex wavenumber and ω is the angular frequency. Inserting

this solution into the wave equation we obtain

$$(- k^{*2} + \frac{\rho \omega^2}{M^*}) \psi = 0 \tag{3}$$

or separating into real and imaginary parts

$$k'^2 - \alpha^2 = \rho \omega^2 \frac{M'}{M'^2 + M''^2} \tag{4}$$

$$2 i k' \alpha = i \rho \omega^2 \frac{M''}{M'^2 + M''^2}$$

Equation (3) provides the dispersion relation between the complex elastic modulus and the wave's wavenumber and frequency. This relation must be satisfied at each point in the wave's path and in particular at every interfacial boundary.

If we specialize to the small loss case $k'^2 >> \alpha^2$ and $M'^2 >> M''^2$ then we get

$$\frac{\omega^2}{V^2} = k'^2 \approx \frac{\rho \omega^2}{M'} \tag{5}$$

and

$$\frac{1}{Q} = \frac{2 \alpha}{k'} \approx \frac{M''}{M'}$$

where V is the wave phase velocity and $\frac{1}{Q}$ the specific (per wavelength) dissipation factor.

For three dimensional wave propagation in isotropic media with a vector wavefield, two wave equations must be satisfied [25]

$$\nabla^2 \vec{\Psi} - \frac{\rho}{C_{44}^*} \frac{\partial^2}{\partial t^2} \vec{\Psi} = 0 \tag{6a}$$

for the shear motion, where $C_{44}^* = C_{44}' + i C_{44}''$ is the complex shear modulus and

$$\nabla^2 \Phi - \frac{\rho}{C_{11}^*} \frac{\partial^2}{\partial t^2} \Phi = 0 \tag{6b}$$

for the compressional motion, where $C_{11}^* = C_{11}' + i C_{11}''$ is the complex compressional modulus ($C_{11}^* = C_{12}^* + 2 C_{44}^*$).

In the case of a cylindrical rod, these equations are written in the cylindrical coordinates ($\hat{r}$, $\hat{\phi}$, $\hat{z}$) as

$$\hat{r}\ (\ \nabla^2\ \Psi_r - \frac{2}{r}\ \frac{\partial \Psi_\phi}{\partial \phi} - \frac{\Psi_r}{r^2}\ ) + \hat{\phi}\ (\ \nabla^2\ \Psi_\phi + \frac{2}{r^2}\ \frac{\partial \Psi_r}{\partial \phi} - \frac{\Psi_\phi}{r^2}\ ) + \hat{z}\ \nabla^2\ \vec{\Psi} \qquad (7a)$$

$$= - \frac{\rho\ \omega^2}{C_{44}^{*}}\ \vec{\Psi}$$

for the shear wavefield and

$$\frac{1}{r}\ \frac{\partial}{\partial r}\ (\ r\ \frac{\partial \Phi}{\partial r}\ ) + \frac{1}{r^2}\ \frac{\partial^2\ \Phi}{\partial \phi^2} + \frac{\partial^2 \Phi}{\partial z^2} = - \frac{\rho\ \omega^2}{C_{11}^{*}}\ \Phi \qquad (7b)$$

for the compressional wavefield.

For equation (7b) a solution can be written in terms of the cylindrical Bessel functions of the first kind of order p, J_p ;

$$\Phi = A\ J_p\ (\ k_{tl}^{\ *}\ r\ )\ \begin{matrix}\sin p\ \phi \\ \cos p\ \phi\end{matrix}\ e^{-i\ \beta^{*}\ z} \qquad (8b)$$

where $\beta^{*} = \beta^{'} - i\ \beta^{''}$ is the $\hat{z}$ component of the complex wavenumber and $k_{tl}^{\ *} = k_{tl}^{\ '} - i\ k_{tl}^{\ ''}$ is the transverse component of the complex longitudinal wavenumber. When this solution is inserted into equation (7b) we get

$$k_{tl}^{\ *2} + \beta^{*2} = \frac{\rho\ \omega^2}{C_{11}^{*}} \qquad (9b)$$

which is the dispersion relation for the compressional waves. The analogue of equation (4), it states that the sum of the squares of the directional components of the momentum is a preserved quantity, equal to the quantity on the right.

Examining equation (7a), we find that there are two possible solutions

$$\vec{\Psi} = B \cdot \vec{M} + C \cdot \vec{N}$$

where

$$\vec{M} = \vec{\nabla} \times \hat{z}\ \Psi \quad ,\text{"'} \quad \vec{\nabla} \cdot \vec{M} = 0$$

and

$$\vec{N} = \frac{C_{44}^{*\ 2}}{\omega \rho} \cdot \vec{\nabla} \times \vec{M} \quad , \quad \vec{\nabla} \cdot \vec{N} = 0$$

each of which satisfy the scalar shear wave equation

$$\nabla^2\ \Psi + \frac{\rho\ \omega^2}{C_{44}^{*}} \cdot \Psi = 0 \qquad (8a)$$

This equation has a solution in terms of the cylindrical Bessel functions of the first kind

$$\Psi = J_p \left(k_{ts}^{*} \, r \right) \begin{matrix} \sin p\,\phi \\ \cos p\,\phi \end{matrix} e^{-i\,\beta^{*} z}$$

where $k_{ts}^{*} = k_{ts}^{\prime} - i\, k_{ts}^{\prime\prime}$ is the transverse component of the shear wavenumber.

If we insert the solution into equation (8a) we obtain

$$k_{ts}^{*2} + \beta^{*2} = \frac{\rho\,\omega^2}{C_{44}^{*}} \tag{9a}$$

which is the dispersion relation for the shear waves.

The sound particle velocity which is obtained from the two potentials is

$$\vec{v} = \frac{\partial \vec{u}}{\partial t} = \nabla\,\Phi + \vec{\nabla} \times \vec{\Psi} \tag{10}$$

whose components are

$$v_r = \left[A k_{tl}^{*}\, J_p^{\prime} \left(k_{tl}^{*}\, r \right) + i\,\beta^{*}\, B J_p^{\prime} \left(k_{ts}^{*}\, r \right) + \frac{p}{r}\, C J_p \left(k_{ts}^{*}\, r \right) \right] \begin{matrix} \cos p\,\phi \\ \sin p\,\phi \end{matrix} e^{-i\,\beta^{*} z}$$

$$v_\phi = \left[\frac{p}{r}\, A J_p \left(k_{tl}^{*}\, r \right) + i\, \frac{\beta^{*}\, p}{k_{ts}^{*}\, r}\, B J_p \left(k_{ts}^{*}\, r \right) + k_{ts}^{*}\, C J_p^{\prime} \left(k_{ts}^{*}\, r \right) \right] \begin{matrix} -\sin p\,\phi \\ \cos p\,\phi \end{matrix} e^{-i\,\beta^{*} z}$$

and

$$v_z = \left[-i\,\beta^{*}\, A J_p \left(k_{tl}^{*}\, r \right) - k_{ts}^{*}\, B J_p \left(k_{ts}^{*}\, r \right) \right] \begin{matrix} \cos p\,\phi \\ \sin p\,\phi \end{matrix} e^{-i\,\beta^{*} z}$$

where $J_p \left(x \right)^{\prime} = \dfrac{\partial J_p \left(x \right)}{\partial x}$.

In cases where the cylinder is surrounded by air the solution must satisfy stress-free boundary conditions at $r = a$, where a is the cylinder radius. This requires that

$$0 = T_{rr} = \frac{1}{i\,\omega} \cdot \left[C_{11}^{*}\, \frac{\partial v_r}{\partial r} + C_{12}^{*} \left(\frac{v_r}{r} + \frac{1}{r}\, \frac{\partial v_\phi}{\partial \phi} \right) + C_{12}^{*}\, \frac{\partial v_z}{\partial z} \right] \tag{11}$$

$$0 = T_{rz} = \frac{1}{i\,\omega} \cdot \left[C_{44}^{*} \left(\frac{\partial v_r}{\partial z} + \frac{\partial v_z}{\partial r} \right) \right]$$

and

$$0 = T_{r\phi} = \frac{1}{i\,\omega} \cdot \left[C_{44}^{*} \left(\frac{1}{r}\, \frac{\partial v_r}{\partial \phi} + \frac{\partial v_\phi}{\partial r} - \frac{v_\phi}{r} \right) \right]$$

at $r = a$, where T_{ij} are the ij stress components.

If the particle velocity components are inserted into these boundary conditions we obtain the following matrix equation

$$\begin{bmatrix} A_{11} & A_{12} & A_{13} \\ A_{21} & A_{22} & A_{23} \\ A_{31} & A_{32} & A_{33} \end{bmatrix} \begin{bmatrix} A \\ B \\ C \end{bmatrix} = \begin{bmatrix} 0 \\ 0 \\ 0 \end{bmatrix} \tag{12}$$

where A_{ij} are matrix elements, given by

$$A_{11} = -C_{12}^{*} \left(k_{tl}^{*2} + \beta^{*2} \right) J_p \left(k_{tl}^{*} a \right) + 2 C_{44}^{*} k_{tl}^{*2} J_p'' \left(k_{tl}^{*} a \right)$$

$$A_{12} = 2 C_{44}^{*} i \beta^{*} k_{ts}^{*} J_p'' \left(k_{ts}^{*} a \right)$$

$$A_{13} = 2 C_{44}^{*} p \left[k_{ts}^{*} J_p' \left(k_{ts}^{*} a \right) - \frac{1}{a} J_p \left(k_{ts}^{*} a \right) \right] + \frac{2 C_{12}^{*}}{a} p k_{ts}^{*} J_p' \left(k_{ts}^{*} a \right)$$

$$A_{21} = 2 i \beta^{*} k_{tl}^{*} J_p' \left(k_{tl}^{*} a \right)$$

$$A_{22} = \left(k_{ts}^{*2} - \beta^{*2} \right) J_p' \left(k_{ts}^{*} a \right)$$

$$A_{23} = \frac{i \beta^{*} p}{a} J_p \left(k_{ts}^{*} a \right)$$

$$A_{31} = \frac{2p}{a} \left[k_{tl}^{*} J_p' \left(k_{tl}^{*} a \right) - \frac{1}{a} J_p \left(k_{tl}^{*} a \right) \right]$$

$$A_{32} = \frac{2 i \beta^{*} p}{k_{ts}^{*} a} \left[k_{ts}^{*} J_p' \left(k_{ts}^{*} a \right) - \frac{1}{a} J_p \left(k_{ts}^{*} a \right) \right]$$

$$A_{33} = k_{ts}^{*2} J_p \left(k_{ts}^{*} a \right) + \frac{2 k_{ts}^{*}}{a} J_p' \left(k_{ts}^{*} a \right) \quad .$$

The solution to this matrix equation is complicated. But if we specialize to the lowest order modes, $p = 0$, then it is possible to decouple the last row from the top two. We obtain a solution for which $C = 0$, $A, B \neq 0$ from the top two rows, and a solution for which $A, B = 0$, $C \neq 0$ from the third row.

The matrix equation for the $C = 0$, irrotational motion, is formed by requiring that

$$\begin{bmatrix} A_{11} & A_{12} \\ A_{21} & A_{22} \end{bmatrix} \begin{bmatrix} A \\ B \end{bmatrix} = \begin{bmatrix} 0 \\ 0 \end{bmatrix} \tag{13}$$

The solution of which requires that the matrix determinant be equal to 0.

After rearranging, using some relations among Bessel functions, and requiring that $C_{44}^{*} \neq 0$, we obtain the following equation for the determinant

$$\left(k_{ts}^{*2} - \beta^{*2} \right) \left(\frac{C_{12}^{*}}{C_{44}^{*}} \right) \left(k_{tl}^{*2} + \beta^{*2} \right) J_0 \left(k_{tl}^{*} a \right) J_1 \left(k_{ts}^{*} a \right) \tag{14}$$

$$- (k_{ts}^{*2} - \beta^{*2})\, k_{tl}^{*2}\, J_1(k_{ts}^{*}\, a)\, [\, J_2(k_{tl}^{*}\, a) - J_0(k_{tl}^{*}\, a)\,]$$
$$- 2\,\beta^{*2}\, k_{tl}^{*}\, k_{ts}^{*}\, J_1(k_{tl}^{*}\, a)\, [\, J_2(k_{ts}^{*}\, a) - J_0(k_{ts}^{*}\, a)\,] = 0$$

The axial wavenumbers β^{*} which satisfy equation (14), a trancendental equation, together with equations (9a) and (9b), for given material properties ρ, C_{44}^{*} and C_{12}^{*}, are the complex wavevectors of the extensional mode, a wave with combined axial and radial particle motion which propagates along $\hat{z}$, the axis of the cylinder.

The rotational solution formed from the decoupled last row of the A_{ij} matrix requires that $A_{33} = 0$. This is satisfied if $k_{ts}^{*} = 0$ or using equation (9a)

$$\beta^{*2} = \frac{\rho\,\omega^2}{C_{44}^{*}} \tag{15}$$

which is a torsional wave whose wavevector is influenced only by the shear characteristics of the media.

It is important to recognize that the theory introduced here does not account for spatial inhomogenuity of the density and elastic constants in a given material. This is because equations (6a) and (6b) originate from the homogeneous wave equation, rather than the more general inhomogeneous wave equation. Theories utilizing the inhomogeneous wave equation for ordered [17] and disorderd [18] composite media predict strong dispersion of the collective vibrational modes close to the Brillouin zone, $\beta x \geq 0.1$, where x is the typical length scale for the inhomogenuity. At lower frequencies the homogeneous wave equation becomes valid with the effective elastic constants utilized in the equation being the lowest wavenumber ($\beta = 0$) average of the material density and elastic constants [17]. $\beta x = 0.1$ may be taken as the upper limit for the applicability of the theory, without further modifications.

Having obtained the dispersion relations for the propagation of the extensional and torsional modes through media with complex elastic constants, some particular forms of these moduli will be explored, with a view to obtaining some previously known results for simple cases and understanding the implications of this theory for more general cases.

a. The Case of Real Frequency Independent Elastic Constants

The first case to be considered is the solution of equation (14), the extensional wave dispersion relation, for lossless media, with real frequency independent elastic constants. This requires setting

$$C_{11}^{*} = C_{11}' \quad , \quad C_{44}^{*} = C_{44}' \quad , \quad C_{12}^{*} = C_{12}' \quad , \quad \beta^{*} = \beta' \tag{16}$$

but $k_{ts}^{\ *}$ and $k_{tl}^{\ *}$ remain complex since the dispersion relations, equations (9b) and (9a), which are now

$$k_{tl}^{\ *2} + \beta'^{\,2} = \frac{\rho\,\omega^2}{C_{11}'} \tag{17b}$$

and

$$k_{ts}^{\ *2} + \beta'^{\,2} = \frac{\rho\,\omega^2}{C_{44}'} \tag{17a}$$

show that if $\beta'^{\,2}$ is greater than the parameter on the right side of one of these equations, then $k_{tl}^{\ *}$ or $k_{ts}^{\ *}$, respectively, will be forced to be pure imaginary.

The determinant equation for the extensional mode required by the boundary conditions, equation (14), can now be written as

$$\begin{aligned} &\left[\left(\frac{\omega}{V_s}\right)^2 - 2\beta'^{\,2}\right]\left(\frac{\omega}{V_P}\right)^2\left(\frac{C_{12}'}{C_{44}'}\right) J_1\left(k_{ts}^{\ *}\,a\right) J_0\left(k_{tl}^{\ *}\,a\right) \\ &- \left[\left(\frac{\omega}{V_s}\right)^2 - 2\beta'^{\,2}\right]\left[\left(\frac{\omega}{V_P}\right)^2 - \beta'^{\,2}\right]\left[J_2\left(k_{tl}^{\ *}\,a\right) - J_0\left(k_{tl}^{\ *}\,a\right)\right] \\ &- 2\beta'^{\,2}\,k_{tl}^{\ *}\,k_{ts}^{\ *}\,J_1\left(k_{tl}^{\ *}\,a\right)\left[J_2\left(k_{ts}^{\ *}\,a\right) - J_0\left(k_{ts}^{\ *}\,a\right)\right] = 0 \end{aligned} \tag{18}$$

where $V_P = \left(\frac{C_{11}'}{\rho}\right)^{1/2}$ is the compressional wave velocity and $V_s = \left(\frac{C_{44}'}{\rho}\right)^{1/2}$ is the shear wave velocity.

This equation was first derived by Pochammer [26], its low frequency asymptotes were studied by Lord Rayleigh [27], but the full solution was first obtained in 1941 by Bancroft [28-31]. This transcendental equation has been solved using the method of Dubbelday [32], where trial values of β' are inserted into the determinant, equation (18). The trial values are increased,

until a sign change occurs in them. This value of β' being close to the solution, this region is expanded and new trial values inserted. This iterative sequence is terminated when the variation of the solution is less than 10^{-5} relative to the previous iterative solution. Bessel functions are calculated using a series expansion [33], taking 25 terms in the series. The format of solutions of this equation is shown as the line in figure 1. The material constants used in calculating the extensional velocity dispersion are $C'_{12} = 10.152 \cdot 10^{10}\ Dyne/cm^2$, $C'_{44} = 8.748 \cdot 10^{10}\ Dyne/cm^2$, and $\rho = 2.7\ g/cm^3$. The effective velocities are $V_P = 3.2\ km/s$ and $V_s = 1.8\ km/s$. These elastic moduli are representative of the effective elastic moduli of a typical sandstone. For cgs to mks conversion note $1.0 \cdot 10^{10}\ Dyne/cm^2 = 1.0\ GPa$, $1.0 \cdot 10^5\ cm/s = 1.0\ km/s$. Sample radius is 0.4 cm and will be taken as such in all the following theoretical discussion, unless otherwise indicated. The propagational (axial) phase velocity versus frequency shown in the figure is obtained from the determined β', using the relation

$$\beta'(\omega) = \frac{\omega}{V(\omega)} .$$

The low frequency asymptote, valid when the shear wavelength is much greater than the sample diameter, $2a$, is the bar velocity, V_y, governed by Young's modulus

$$E = \frac{C'_{44}\ (3\ C'_{12} + 2\ C'_{44}\ )}{C'_{12} + C'_{44}} . \tag{19a}$$

As the frequency increases, β' increases, until k_{tl}^{*2} is forced to go negative, but k_{ts}^{*2} remains greater than zero. This indicates a decrease in the axial component of the particle displacement of the wave and the velocity decreases towards the shear wave velocity. This is the intermediate frequency regime, where $\beta'\ a \approx 1$. The bar velocity is generally somewhat smaller than the compressional velocity. In these situations there is no low frequency regime and the intermediate regime extends to zero frequency.

At higher frequencies k_{ts}^{*2} goes negative as well. The wave velocity continues to decrease, passes the shear wave velocity and approaches the Rayleigh wave velocity, V_r, given

by [34]

$$V_r = V_s \cdot \left(\frac{0.87 + 1.12\,\sigma}{1.0 + \sigma} \right) \tag{19b}$$

where σ is the Poisson ratio, the particle motion becoming increasingly localized along the sample surface.

b. The Case of Real Frequency-Dependent Elastic Constants

Any variation of the real part of the elastic constants with frequency requires a variation of the imaginary parts of the elastic constants with frequency, since the real and imaginary parts are related to each other by the Kramer-Kronig relations. However, it is still possible to examine separately the effects of a frequency-dependent real part of the elastic constants on the wave velocity in the waveguided system if the loss is very small.

The following examination observes how frequency-dependent intrinsic elastic constants combine with the waveguide boundary conditions in providing the total dispersion of velocity with frequency. The study is intended to clarify the sensitivity of the extensional mode at various points along it's geometricaly induced dispersion curve to the dilatational modulus C'_{12} vis-a-vis the shear modulus C'_{44} .

The form of the variation of the elastic moduli with frequency which is introduced into the dispersion relations, equations (17a), (17b) and (18), is of a relaxational character, namely;

$$C'_{12}\ (\omega) = C_{12\infty}{}' + \frac{C_{120}{}' - C_{12\infty}{}'}{1 + (\omega\tau_l)^2} \tag{20}$$

and

$$C'_{44}\ (\omega) = C_{44\infty}{}' + \frac{C_{440}{}' - C_{44\infty}{}'}{1 + (\omega\tau_s)^2}$$

where M_0 and M_∞ are the values of the respective moduli at zero and infinite frequency and τ the relaxation time, when the moduli attains its average value $(M_0 + M_\infty)/2$. This variation of the elastic constants is phenomenological for the present study, although there are numerous physical processes in composite materials which exhibit this type of behavior [2,3,10].

Dotted lines and points in figure 1 show the theoretical extensional phase velocity of the hypotetical sample which now has frequency dependent elastic constants. Dotted lines represent a +40% dispersion in $C_{12}^{'}$, the + signifying that the high frequency value, $C_{12\infty}^{'}$, is greater than the low frequency value, $C_{120}^{'}$, with the relaxation time being $\tau_l = 10^{-4}\ s$. Note that the changes induced by the frequency variation of $C_{12}^{'}$ are quite minor. The high frequency compressional velocity is only 3.43 km/s , due to the relatively low Poisson ratio (.267) of this material so that shear deformation is a larger component of the extensional motion. After $C_{12}^{'}$ reaches its maximum value, at about 20 kHz, the dispersion curve is smooth and runs parallel to the dispersionless case. This is typical of relaxation processes which have no memory at higher frequencies of what occured at lower frequencies. The points in figure 1 represent the case of a +40% dispersion in $C_{12}^{'}$, the relaxation time now being $10^{-6}\ s$. The displacement of the dilatational relaxation to high frequencies brings it into the domain where the mode behavior is mostly influenced by the shear properties, so that it is almost impossible to distinguish the dispersive case from the nondispersive case. The effect of a dispersive $C_{12}^{'}$ grows if the ratio of the dilatational to the shear elastic constants is enlarged (i.e., the Poisson ratio is enlarged).

Figure 2 shows the effect of a dispersive shear modulus $C_{44}^{'}$ on the extensional mode dispersion. The nondispersive hypothetical material (full line) has the same elastic constants as that shown in figure 1, but a +40% dispersion in the shear modulus is introduced by enlarging $C_{44\infty}^{'}$, with $\tau_s = 10^{-4}\ s$. The changes induced (dotted line) by the shear dispersion are very large, due to the shear modulus' appearance in both the compressional and shear velocities. With the dispersion, the compressional high frequency velocity is 3.58 km/s , the shear high frequency velocity going 'o 2.12 km/s . The dispersion curve therefore shows a great increase in velocity at 20 kHz, thereafter paralleling from above the dispersionless curve. Points in figure 2 show the effect of displacing the shear relaxation time to $10^{-6}\ s$. This brings the conclusion of the velocity increases at about 150 kHz. Since the effect of the dilatational com-

ponent of the cumulative extensional mode particle motion is greatly reduced at this frequency, the increases in velocity which we observe are much smaller than those seen for the 10^{-4} s relaxation time.

c. The Case of Complex Frequency Independent Elastic Constants

Understanding the propagation of waves in rods made of lossy materials, with the elastic moduli being complex, involves understanding initialy the effect of geometry on the measured losses. The coupling of geometry with intrinsic loss is a result of the presence of the losses in the boundary conditions, equation (11).

To understand this effect we will first consider the constant Q subset of attenuation variation with frequency. Constant Q , a frequency independent ratio between the real and imaginery parts of the elastic moduli, is known to be a useful approximation in charactarising many materials at frequencies well removed from occurances of strong dispersion, that is where $\omega \tau << 1$ or $\omega \tau >> 1$, τ being the charactaristic time scale for the dispersive phenomena (see equation (20)). It is also useful when dispersive behavior is smoothly distributed over extremely broad time scales due to large scale intrinsic geometric or material inhomogenuity. The form of the constant Q model which involves frequency independent complex elastic moduli is the simplest form of dissipation, which makes it instructive for the purpose of understanding the coupling of loss with the boundary conditions, as a precursor to the understanding of frequency dependent loss phenomena found in realistic materials.

The existence of complex moduli requires use of the generalized dispersion relations, equations (9a), (9b) and (14).

Figure 3 shows the theoretical extensional mode dispersion for a hypothetical sample with a 10% complex C_{12}, $C_{12} = 10.152 + i\,1.0152$ ($\cdot\, 10^{10}\ Dyne\ /cm^2$) and a purely real shear modulus $C_{44} = 8.748 + i\,0.0$ ($\cdot\, 10^{10}\ Dyne\ /cm^2$). Figure 3(a) shows the propagational phase velocity, obtained from the resolved β' , figure 3(b) shows the dissipation factor β'' ,

whose units are $1/cm$, and figure 3(c) the (dimensionless) specific dissipation factor $1/Q$, which is computed as

$$\frac{1}{Q} = \frac{2 \cdot \beta''}{\beta'}$$

in analogy with equation (5).

Comparing figure 3(a) to the dispersionless plot in figure 1 (full line), which was computed for purely real elastic constants, we can see that the introduction of even a large imaginery part into C_{12} has a negligable effect on the phase velocity. Examining figure 3(b), we observe a very dispersive $\beta''(\omega)$. Solution of the compressional wave equation (equation (6b)) in infinite media (with no boundary conditions) for the constant Q case gives $\beta''(\omega) = Cons \cdot \omega$, a linear variation of the dissipation factor with frequency, which is here observed above 300 kHz, $\beta' a > 4.2$. At low frequencies we find an increasing dissipation factor, which peaks at about 100 kHz ($\beta' a = 0.9$), and then decreases to zero at 170 kHz ($\beta' a = 1.8$). This minima in loss coencides with the lowest frequency inflection point in the phase velocity dispersion curve, figure 3(a). At higher frequencies we find a sharp increase in the dissipation factor which continues up to 250 kHz ($\beta' a = 3.2$), coencidental with the second inflection point in the phase velocity dispersion curve. Above this frequency the loss factor gradualy goes to the high frequency assypmtotic linear variation with frequency. Figure 3(c), $\frac{1}{Q}$ versus frequency, shows dispersive behavior quite different from that of figure 3(b). At low frequencies we find a decrease in specific dissipation as frequency increases. The specific dissipation goes to zero at 170 kHz, then rises sharply back to its low frequency levels at 250 kHz, and at yet higher frequencies drops gradualy to approximately half it's peak value.

This behavior of the loss and specific dissipation is caused by the increasingly shear composition of the wave as frequency increases. At low frequencies, $\beta' a < 1$, the wave is already largely shear in charactaristics, due to the low Poisson ratio, causing the specific dissipation factor, $\frac{1}{Q_y}$, is much smaller than $\frac{1}{Q} = .1$ which would have been the case for a purely dila-

tational wave (where shear effects can be neglected). As the frequency increases, the dilatational component in the wave continues to decrease, and since the shear modulus has been set to be purely real, the specific dissipation factor decreases until, at a frequency close to that at which the dispersion curve crosses the material shear velocity, it vanishs entirely. Above this frequency the loss increases, asymptoting to the Rayleigh wave attenuation coefficent, which contains dilatational components.

Figure 4 is the analogue of figure 3 for the case of a purely real C_{12} and a complex C_{44} with a 10% imaginery part, $C_{44} = 8.748 + i\,0.8748$ ($\cdot\, 10^{10}\ Dyne/cm^2$). The figure shows extensional theoretical results for two radii cylinders, 0.4 and 0.8 cm, shown as lines and points, respectively. Parts (a) and (b) of the figure also include, as dotted lines, theoretical constant Q torsional shear results.

Figure 4(a) shows the extensional velocity results for this complex C_{44}. The plot for the 0.4 cm radius cylinder (line) is identical to figures 3(a) and 1, showing the lack of sensitivety of the velocity to the imaginery part of the modulus. The 0.8 cm cylinder has a phase velocity which becomes dispersive at approximately half the frequency of the 0.4 cm cylinder, illustrating the dependence of these extensional mode effects on the product $\beta\, a$.

From figure 4(b) it can be seen that the behavior of the extensional dissipation factor β' is significantly different for a lossy shear modulus from its behavior for a lossy dilatational modulus, figure 3(b.) The dissipation factor for the lossy shear modulus is an order of magnitude larger and exhibits an entirely different dispersive behavior. At low frequencies the dissipation factor increases linearly with frequency, but is smaller than the torsional shear dissipation factor, the dotted lines in the figure. From $\beta\, a = 1$ to $\beta\, a = 2$ (100 kHz to 220 kHz for the 0.4 cm radius cylinder case), it rises rapidly, thereafter flattenning and finally increasing linearly as the constant Q solution of the shear wave equation in infinite media predicts, which can be seen from the close agreement with the torsional dissipation factor at high frequencies. By doubling the cylinder radius from 0.4 cm to 0.8 cm the strongly dispersive region

is brought to lower frequencies, illustrating the importance of understanding the geometry effects in loss measurements, since these would give different results for differing diameter cylinders measured at the same frequency.

Figure 4(c) shows the computed exensional specific dissipation factors for the two radii cylinders. The specific dissipation factor is 0.09 at low frequencies, just below the value of 0.1 expected for a purely shear wave, and with increasing frequency rises rapidly until it more than doubles at $\beta' \ a = 2.0$, where a strong $\frac{1}{Q}$ peak is observed. At yet higher frequencies the specific dissipation drops back to 0.09. The inflection point in the dissipation factor and the peak in the specific dissipation factor are due entirely to having reached the frequency where the wave traveling down the rod has a transverse component which is in essence a shear standing wave, composed of two in phase lossy shear waves. The occurance of this peak is solely geometric in origin, so that it should not be confused with an intrinsic loss peak. This can readily be seen from its occurance in the 0.8 cm radius cylinder at roughly half the frequency as in the 0.4 cm cylinder, the maximum frequencies in both cases coenciding with the frequencies where the two radii cylinders' extensional velocities cross the shear velocity (see figure 4(a)). At frequencies above the specific dissipation peak the loss returns to be that of a composite wave, with both dilatational and shear charactaristics, but since the shear character is still dominant, the specific dissipation is close to that of a purely shear wave.

Inversion of Experimental Results for Complex Elastic Moduli

Measurements of the complex extensional and torsional wavenumbers versus frequency may be inverted to obtain the complex, frequency dependent C'_{12} and C'_{44}.

The torsional shear results must first be inverted for C'_{44}, as values of the shear modulus are needed as input for inversion of the extensional mode for C'_{12}. The torsional dispersion relation, equation (15), is readily inverted for the shear modulus. Since equation (15) is identical to the one dimensional dispersion relation, equation (4), it can be written in seperated form as

$$X = \frac{1}{\rho\,\omega^2} \cdot [(\frac{\omega}{V_s})^2 - \beta'^2] = \frac{C'_{44}}{C'^2_{44} + C''^2_{44}} \tag{21a}$$

and

$$Y = \frac{1}{\rho\,\omega^2} \cdot [2\,(\frac{\omega}{V_s})\,\beta''] = \frac{C''_{44}}{C'^2_{44} + C''^2_{44}} \tag{21b}$$

where β' has been replaced by $(\frac{\omega}{V_s})$.

A simple algebraic manipulation of these equations gives

$$C'_{44} = \frac{X}{(X^2 + Y^2)} \tag{22a}$$

and

$$C''_{44} = \frac{Y}{(X^2 + Y^2)} \,. \tag{22b}$$

After $C^*_{44}\ (\omega)$ has been determined, the extensional results may be inverted to obtain $C^*_{12}\ (\omega)$. The principle used in the inversion is to use the dispersion relation, equation (14), to determine C^*_{12}. In obtaining the extensional wavenumber, the forward problem, ρ, C^*_{12}, C^*_{44}, and a were inserted into equation (14) and trial values of β^* were introduced to satisfy the dispersion relation. In the inverse problem, ρ, $C^*_{44}\ (\omega)$, $\beta^*\ (\omega)$, and a are introduced into equation (14), and trial values of $C^*_{12}\ (\omega)$ are iteratively attempted to satisfy the dispersion relation. The iterative process may be started close to the desired solution, which increases the rate of convergence, by recalling that the low frequency asymptotic value of the extensional mode is the bar wave, governed by Young's modulus E (equation (19a)). The complex form of equation (19a) may be solved for C^*_{12}, giving

$$C^*_{12} = C^*_{44} \cdot [\frac{2 - U}{U - 3}] \tag{23}$$

$$U = \frac{E^*}{C^*_{44}} = \frac{1}{C^*_{44}} \cdot [\rho\,(\frac{\omega}{\beta^*})^2] \,,$$

where E^* is the complex Young's modulus. The lowest frequency value of β^* and C^*_{44} may be used to obtain an estimate of C^*_{12}. After convergence is attained at this frequency, the resolved value of C^*_{12} is used as the initial value for iterations at the next frequency, and so

on. The root finding algorithm utilized is the same as that used in obtaining the forward solution [14]. An advantage of this method with respect to non-linear least squares approachs is that in the absence of noise the inverse is exact. Its disadvantage is a larger sensitivety to noise, since beyond smoothing the data before insertion into the inversion program, no other noise reduction method is used.

Figure 5 shows the application of the inversion algorithm to artificial data. The artificial torsional shear velocity and dissipation factor used as input to the inverse are those shown in figure 4(a) and (b) as dotted lines, generated from a non-dispersive $C'_{44} = 8.748 + i\,0.8748 \cdot (\ 10^{10}\ Dyne\ /cm^2\ )$. The extensional velocity and dissipation factor used as input to the program are those shown as lines, for the 0.4 cm radius cylinder case, in figure 4, generated from a non-dispersive $C'_{12} = 10.152 + i\,0.0 \cdot (\ 10^{10}\ Dyne\ /cm^2\ )$. Figure 5(a) shows the real part of the input (points) and inverted (lines) moduli C_{12} (1), and C_{44} (2). Figure 5(b) shows the complementary imaginery part of the moduli. It is clear from the figure that both the real and imaginery parts of the input moduli have been recovered nicely by the inverse. The relative error between the input and inverted moduli is 10^{-5}, allowing for two iterations of the inverse at each frequency point. The imaginery part of C_{12}, which is zero in the input data, requires a great number of iterations to recover exactly. In practical cases, in order to expidite the inversion process, the assumption is made that for Q s greater than 10^5 (measured as the ratio between the real and imaginery part of the respective modulus), the modulus is taken as being purely real.

Experiment

The swept frequency measurements of the complex elastic moduli are obtained with an acoustic transmission bridge of a similar design to the microwave electromagnetic transmission bridges used in dielectric measurements.

Figure 6 displays the transmission bridge. The sources and the receivers of the transmis-

sion bridge are supplied by an Hewlett Packard 3577A network analyzer, but for explanation purposes these are separated in the figure. Power is supplied via the variable frequency oscillator output of the network analyzer, which provides a monochromatic sine wave of fixed amplitude at each frequency. To increase this output level, which is necessary for high loss samples, an Electronic Navigation Industries (Rochester, NY) 240L 40 watt power amplifier is used in series with the network analyzer output. A power splitter divides the power between the measurement and the reference branches.

The reference branch is merely an electric cable joining the power splitter directly to the network analyzer reference (R) port. This branch provides the amplitude and phase of the signal going into the acoustic system, thus providing a reference needed for calibration of the results obtained in the measurement branch.

The measurement branch consists of directional couplers and electrical impedance matching networks on both sides of the acoustic section. The acoustic system consists of wideband PZT-5A extensional and torsional shear transducers which are epoxy bonded to a cylindrical sample of known length l and known radius a, whose elastic properties are to be measured. The input transducers convert electric voltage into elastic strain and launch an elastic wave of extensional (axial) or torsional nature, depending upon the transducer used in the measurement, along the sample axis. After propagating a length l through the sample the elastic wave is converted back to electric voltage at the output transducers. The signal thus obtained is then channeled into the network analyzer A port for measurement of the elastic transmission properties of the sample.

The impedance matching systems, consisting of transformers and inductors, are a necessary component of the system in order to compensate for the non-equivalent transformation of electric energy to mechanical energy by the PZT transducers [23,24]. The highly capacitive, frequency-dependent, electrical impedance of the transducers causes a great deal of the power supplied by the system to be reflected back into the source. The power that is converted into

elastic waves is phase shifted. The impedance matching systems reduce these effects by reducing the mismatch between the 50 ohm electric line and the transducers utilizing the broadband transformers, and by partially compensating for their capacitance with an inductor. These matching circuits are placed at both sides of the elastic component of the measurement branch since the impedance mismatchs occur equally on both sides.

The directional couplers (Mini-Circuits PDC-15-6, Mini-Circuits, Brooklyn, New York) in the measurement branch are used to correct the transmitted signal, which is sampled at the network analyzer port A, for the electric reflections that occur at the line-transducer interface and elastic reflections at the sample-transducer interface. These reflections decrease the total energy transmitted through the sample and, since we wish to know only the transmission properties of the sample, they must be corrected for. The amount of energy reflected from the input signal is sampled by the directional coupler labeled Forward Reflection and goes into port B of the network analyzer. As there is reflection at the interface between the sample and the receiving transducer, which is generally different from the input reflection coefficent, the source and receiver directions are reversed at a later stage of the measurement and the Backward Reflection directional coupler is connected into port B of the network analyzer so it too can be compensated for.

In the network analyzer the amplitude and phase of the transmitted signal, port A, suitably corrected for the reflections, is compared to the amplitude and phase of the reference (R) branch.

From the phase difference between the branches , we obtain the sample's phase velocity using the relation

$$\Delta\phi\ (\omega) = \phi_R\ (\omega) - \phi_A\ (\omega) = \omega l\ \left(\frac{1}{V_R\ (\omega)} - \frac{1}{V_{sample}\ (\omega)} \right) \tag{24}$$

where $\Delta\phi$ is the phase difference between the branches in radians following the propagation distance l and $V_R\ (\omega)$ and $V_{sample}\ (\omega)$ are the respective phase velocities of the reference and

the sample. Since the reference velocity is of order 10^5 faster than the speed of sound in the sample it can be ignored. As the network analyzer measures only phase differences up to one cycle (2π), the number of cycles are recorded by counting the number of instrument zero crossings.

It is possible to obtain also the sample group velocity using the relation

$$\frac{l}{V_{group}\ (\omega)} = t_{group}\ (\omega) = \frac{\partial \Delta\phi\ (\omega)}{\partial\omega} \tag{25}$$

where the group velocity is related to the phase velocity, to first order in ω by

$$V_{group}\ (\omega) = V_{phase}\ (\omega) + \phi \cdot \frac{\partial V_{phase}\ (\omega)}{\partial\phi\ (\omega)}$$

By comparing the amplitudes in the two branches, after correcting for reflections, we obtain the sample dissipation factor β'', using the relation

$$-\left(\frac{Amp_A}{Amp_R}\right)_{dB} = K\ (\beta_R{}'' - \beta_{sample}{}''\ )\ l \tag{26}$$

where Amp_A and Amp_R are the amplitudes of the waves received in the two branches and $K = 4.353$ is a conversion factor from decibel to natural log. It is usually possible to ignore $\beta_R{}''$ so the expression is further simplified.

The most vital component in a broadband system are broadband sources and receivers. Ideally, these elastic wave sources will satisfy the following requirements. They should have a relatively flat acoustic response over the required frequency range, possessing a minimum of intrinsic vibrational modes. For purposes of studying attenuating media, it is desirable to maximize the acoustic output for reasonable electromagnetic excitation power. Finally, the sources should be robust, so as to lend flexibility to their use, particularly with regard to changing pressure and temperature conditions.

In practice, these various requirements conflict, requiring that the developed transducer be a compromise between the various demands. A case in point is that most acoustic wave sources are damped in order to increase their bandwidth which clearly makes them less suited

for use in attenuating media. Another example of relevance to this study is the attempt to use large PZT crystal sources for low frequency acoustic work. This optimizes the acoustic output, but the transducers tend to have a quite rugged frequency response near their resonant frequency. The large transducer size also gives these sources a strongly capacitive impedance so that they are hard to drive electrically.

Two sets of broadband transducers (one extensional and one shear) were designed and built with the assistance of Alan Selfridge (Ultrasonic Devices, Palo Alto, CA). The design is similar to that proposed by Brown and Weight [35].

The torsional shear transducer is shown face forward in figure 7(a) before insertion into a metal housing, and in figure 7(b) in a side view after insertion into its housing. Figure 7(c) shows the magnitude of the torsional, reflection corrected, transmission coefficent versus frequency for transmission through a rod of Fused Silica. The transducer is constructed from a Vernitron 56790-4 T_{zz} poled PZT-5A plate (Vernitron Piezoelectric Division, Bedford, OH) which was cut into eight isosceles triangular pies of thickness 0.113 cm, height 1.17 cm and base 0.97 cm. The central angle of each pie is 45 degrees. These triangles were ground smooth and then electroded with vapor deposited gold. An unpoled PZT-5H bar (Channel C5700, Channel Industries, Santa Barbara, CA) of rectangular crosssection 2.54 cm by 2.54 cm and length 15.24 cm is used as a matched acoustic impedance backing to the pies. It was gold electroded on one end. The triangular pies were then arranged in the circular pattern shown in figure 7(a) on the electroded face of the backing bar, care being taken that the poling of all the triangles be in the same direction (in this case anticlockwise). The pies were epoxyed under pressure to the backing bar, using insulating epoxy, so that the electrical contacts formed are pressure contacts, which preserves the smoothness of the contact surface. An electrical cable, shown in the upper right hand corner of figure 7(a), was silver epoxyed to the electroded face of the backing and served as the positive electrical connection to the transducers. Electric grounding to the transducers is provided on their top face by pressure epoxying to the metal

housing, figure 7(b). The metal housing consists of a stainless steel cylindrical shell of 2.54 cm radius outer diameter and 2.26 cm inner diameter, onto which a 0.076 cm thickness stainless steel cap had been welded . A small cap thickness is neccesary in order to prevent the occurance of half wavelength elastic wave resonances in the cap over the studied frequency range.

In early models of the transducers, the backing bar was then put in a chuck and the part of the bar opposite the metal housing was surface ground into a four sided iscoceles triangular cone shape, the triangle dimension being 7.23 cm length by 2.54 cm base. The top angle was 27.2 degrees . The lower part of the backing bar would then resemble the $\hat{z}$ face of a trigonal crystal. The part which had been removed by surface grinding was then filled with a damping material composed of a 50% volume percent mixture of tungsten powder and epoxy. The purpose of this operation is to prevent reflections from the bottom of the transducer backing, an objective which was accomplished at the considerable loss of acoustic output power.

Figure 7(c) shows the magnitude of the transmission coefficent through lossless Fused Silica. The spectra is relatively smooth over the frequency range 5 kHz to 1.005 Mhz, which is the studied frequency interval. There are two noteworthy features in the spectra, the first is the strong decrease in transducer power below 50 kHz, which prevents efficent use of the transducer at very low frequencies. The second feature is the weak power peak at 230 kHz, which is the loaded resonant frequency of the transducer. The undamped resonant frequency of the shear pies is approximately 1 Mhz, so the backing effect can readily be seen.

The construction of the extensional transducers is similar. They are made of 0.259 cm thickness, 1.27 cm radii longitudinaly poled PZT-5A disks (Vernitron 4100). These disks were epoxyed to identical PZT-5H backing bars as the torsional transducers and placed in identical steel housings.

The samples are solid or rock cylinders of length 15 to 30 cm and radius 0.4 cm. Thin samples are used to displace the geometry-controlled dispersive part of the velocity versus fre-

quency curve (as was previously shown in the theoretical section) to as high a frequency as possible and to insure that the samples are spatially homogeneous in terms of their mineral and fluid composition, at experiments at partial water saturations. The fused quartz rods were obtained from General Electric, the plexiglass (hardened acrylic resin) rods from AIN Plastics and the Vycor rods from Corning Glass (Corning 7930, Corning Glass Corp., Corning, NY), and conform to manufacterer specifications. The rock samples had quartz buffers of length 3 cm and radius 0.4 cm between them and the PZT transducers. These buffers were necessary to insure repeatable mechanical contact between the porous rocks and the PZT transducers.

To insure that water saturation and temperature conditions do not vary in the course of the experiments, the acoustic part of the measurement branch, consisting of the PZT transducers, the quartz buffers and the rock samples, is inserted into a glass housing and maintained at a constant vapor pressure and temperature. Accuracy of water saturation levels obtained is better than 0.1% saturation. To insure equlibration thoroughout the sample volume after the water saturation levels were changed by surface drying, the samples were left in the glass housing for 24 hours before measurements were made. An estimate of the time nessecary for equilibration may be made by assuming that the slowest equilibration process is diffusion through the pore fluid. The time nessecary to diffuse from the sample surface to its center, a distance a , is given by

$$\tau_D = \frac{a^2}{6D}$$

where D is the diffusion constant. Utilizing an effective diffusion constant for porous media of $3.0 \cdot 10^{-6}\ cm^2/s$ at room temperature (assuming a considerably tortuous path), we obtain a diffusion time of 3.7 hours. As this time scale characterizes the rate of exponential decay of the system to equilibrium, this time scale must be multiplied by the size of the changes induced in the equilbrium state. Since the size of these changes is not well understood, a longer equilibration time was provided to the sample.

The measurements are controlled via an IEEE-488 port by an IBM/XT microcomputer. The frequency range measured, commonly from 5 kHz to 1 MHz, is divided into 175 kHz intervals. The network analyzer is programmed to sweep over an interval at a time, measuring 400 frequency points in each interval. Each interval sweep takes 3 seconds using the instrument's $\pm$ 10 Hz bandwidth receiver filter and to improve the signal to noise ratio 64 sweeps are averaged together. After the network analyzer has completed measurements over all the frequency intervals, source and receiver are reversed and measurements of the Backward Reflection coefficent are conducted over identical intervals but with only 8 sweeps per interval. Total measurement time is approximately 30 minutes.

The theory extended here is for infinite length cylinders, and ignores the boundary conditions at the sample ends, which contribute to reflected elastic waves and thus to standing waves at frequencies where integral multiples of the shear or extensional halfwavelength are equal to the sample length. It is possible to analyse the frequency response in this fashion if the measurement at each frequency is concluded before the elastic reflected wave can reach the same end again, since this begins the process of building up the interference pattern essential to the standing wave. The full standing wave pattern is only acheived after Q cycles, so that it was found that even for the lowest Q materials, it is possible to entirely suppress the standing wave by remaining for only 10 ms at each frequency point, for samples of 15 cm length or more, this leading to the 3 second time per sweep. Figure 8(a) shows the extensional magnitude versus frequency and figure 8(b) the corresponding phase shift versus frequency of a 16.0 cm long sample of 75% water saturated Massillon Dark sandstone measured at two interval sweep times, 1.4 s (lines) and 5.0 (points). The 1.4 s interval sweep rate is faster than that nessecary to build up a standing wave, so that a smooth variation of the magnitude with frequency is seen in figure 8(a), despite the fact that the frequency interval covered corresponds to a phase shift of more than 5 wavelengths. There is evidence of transducer modes at 70 and 95 kHz, but these are broad and may be compensated for. The 5.0 s interval sweep rate plot

in figure 3(a) shows the beggining of the development of a standing wave pattern. There is a peak in magnitude at the first symmmetric mode of the sample at 10 kHz followed by sizable resonances at 25 kHz and higher frequencies. Between 45 and 70 kHz sharp transducer modes may clearly be observed. Of interest is the great difference in the transmitted power between the 1.4 s and 5.0 s sweep rates, which shows the efficient energy storage in the standing wave pattern. Figure 3(b) shows the smooth variation of the phase shift over the sample length observed in the 1.4 s interval sweep plot. In the 5.0 s plot it is possible to observe a shifting of the same phase shift spectra to lower frequencies (for points at ± 180 degree phase shift, for example, see 10 and 30 kHz). This would imply an interpretation of the sample as having a lower phase velocity if the 5.0 s sweep rate response were used, utilizing equation (24), to measure the sample velocity, compared to a utilization of the 1.4 s sweep rate results. More importantly, the 5.0 s sweep rate plot shows the appearance of new sharp oscillations in phase at 30, 50 and around 65 kHz caused by the transducer modes. If these were used to obtain a phase velocity we would observe a much lower phase velocity at frequencies above these oscillations than it is in practice (since these oscillations add many multiples of 2π to the phase shift). As Massillon Dark is among the most attenuating samples studied, it can be expected that these geometric and transducer resonances play a larger role in less attenuating materials.

Following the measurement, the reflection corrected amplitude and phase are transferred to the computer for data manipulation. The phase versus frequency results are converted to velocity versus frequency using equation (24). The amplitude response of rocks requires an initial normalization to a lossless material, as there are still acoustic-electric conversion losses to account for. For this purpose the amplitude of Fused Silica ($Q = 10^5$) is used. The normalized amplitude response may then be converted into a dissipation factor β' versus frequency format using equation (26). Relative accuracy of the phase velocity measurements is estimated at approximately 0.1% and of the dissipation factor about 10%, with the accuracy being higher the lower the attenuation in the sample.

Results

a. Solids with Real Frequency Independent Elastic Constants

Solids with real frequency independent elastic constants were studied to show the applicability of the present theory as well as to test the accuracy of the experimental system.

Figure 9 is a comparison of theory and experiment for the extensional mode in Fused Silica, over the frequency range 5 kHz to 800 kHz. The line in the figure shows the experimental points using a 0.4 cm radius rod of 59 cm length. Since Fused Silica has a quality factor Q of about 10^5, the lossless theory can be applied to it. The solution of the theory, equation (22), is presented as points, using CRC Handbook of Physics and Chemistry [36] values for Fused Silica, $V_P = 5.968\ km/s$ and $V_s = 3.764\ km/s$. The agreement between theory and results is good, considering that no effort has been made to vary the tabulated values, so as to improve their fit to experiment. This experiment confirms our ability to use infinite cylinder theory, even for a high Q material, provided the experiment is conducted at sweep rates faster than those nessecary to establish the standing wave pattern. The experiment also shows that it is possible to use only the $p = 0$ fundamental mode in data analysis. This is due to the nature of the wave emitted by our transducers, which does not couple efficiently into the particle motion required by higher modes ($p > 0$), whose wave field is nonuniform with respect to the circumferental angle ϕ (see equations (8b) and (9b)) .

Figure 10 shows the torsional shear experimental results for the same sample of Fused Silica. Theoreticaly, this mode is nondispersive (equation (16)) propagating at the shear velocity at all frequencies and the experimental results bear this out. The velocity measured experimentaly is 3.78 km/s, which is slightly higher than the CRC [36] value for this material. This demonstrates the utility of the infinite cylinder theory for the torsional modes, while showing that we only couple into the fundamental mode, others being highly dispersive.

b. Solids with Complex Elastic Moduli- Plexiglass

The conclusions of the complex elastic modulus theory presented here have been examined utilizing two rods of plexiglass (acrylic plastic) of radius 0.476 and 0.63 cm. Plexiglass is known to have a shear relaxation at approximately 8 Hz [10], and was assumed to have a mostly flat elastic response above this frequency range. The quality factor of plexiglass is about 40, close to that found in many fluid saturated rocks, and it's density is 1.18 g/cm^3.

Figure 11 shows the experimental results (lines) for the extensional mode (a) velocity, and (b) dissipation factor, respectively, for the 0.476 and 0.63 cm radius samples. Also shown (as points) are theoretical results using constant Q, frequency independent complex elastic moduli, with $C_{12} = 1.58 + i\,0.0$, $C_{44} = 1.81 + i\,0.039$ ($\cdot 10^{10}$ $Dyne/cm^2$) for the two radii cases. The 0.476 cm theoretical and experimental results in 11(b) have been translated upward by 0.2 cm^{-1} to facilitate easier viewing. Figure 12 shows the experimental (lines) and theoretical (points) (a) phase velocity, and (b) dissipation factor for the geometrically dispersionless torsional shear mode. The theoretical results are obtained using the constant Q complex C_{44} values given above for the extensional analysis.

Figure 11(a), a plot of the extensional mode phase velocity for the 0.63 and 0.476 cm radii rods, shows that plexiglass does not have frequency independent elastic moduli. In the strongly geometrically dispersive region, the behavior of the velocity is close to that predicted by constant Q , which can be seen from the agreement of the theoretical and experimental results for this region (80 through 150 kHz for the 0.63 cm cylinder, 100 through 200 kHz for the 0.476 cm cylinder) for both the slope and the absolute value of the velocity. Below this geometrically dispersive region there is a lack of agreement between the experimental and theoretical results. This is due to the intrinsic frequency dependence of the elastic constants, which is not treated by the constant Q theory utilized. Figure 12(a), a plot of the torsional shear velocity versus frequency, clearly shows the high dispersivety of the shear modulus in the region 5 kHz to 120 kHz. Comparing the experimental phase velocities of the two radii cylinders, we observe that the increases in velocity at low frequencies are found in both at the

same frequency, which shows that these results are not geometry related, since in that case they would have appeared shifted in frequency between both plots. The velocity for the 0.476 cm rod is higher at 100 kHz, since it still retains a sizeable compressional contribution at this frequency, while the 0.63 cm rod, as the theoretical plot for this radius cylinder shows, is already strongly in the geometrically dispersive zone. At frequencies above the the geometrically dispersive zone (150 kHz for the 0.63 radius cylinder, 200 kHz for the 0.476 cm radius cylinder) the results for the two samples again show differences, the 0.476 cm rod results being consistently higher, due to the greater dilatational component. The differences between the results for the two rods practically disappear at about 600 kHz, where the shear components in both rods are clearly dominant.

Figure 11(b), which shows the behavior of the extensional dissipation factor with frequency, also reflects the large departure of plexiglass from constant Q behavior. The experimental results are fit nicely by the constant Q theory in the areas where geometric effects dominate, such as at 100 kHz for the 0.63 cm sample and 120 kHz for the 0.476 cm sample, but there is a clear under estimation of the losses below this geometry controlled region, where the strongly dispersive shear losses dominate, as well as at frequencies above this region. The general trend of the geometry related effects is seen , though, with the dissipation factor for the 0.63 cm rod being consistently higher than for the 0.476 cm cylinder, at all frequencies up to 550 kHz. This is a result of the largely shear character of the attenuation (see remarks associated with figure 4). The fluctuations in the dissipation factor plots are partially the result of transducer modal effects which could not be completely corrected for, and partially the result of material inhomogenuity which create phase interference effects. These effects will be examined in more detail in future work, as they may contain information about material spacial correlation functions.

Figure 12 examines the variation of the torsional shear velocity and dissipation factor for plexiglass with frequency. This mode is not geometrically dispersive so it affords a view of the

variation of the shear charactaristics of plexiglass with frequency. Figure 12(a) shows the strongly dispersive behavior of the shear velocity below 100 kHz, which was previously discussed in connection with the extensional mode, as well as a slight decrease in velocity above 400 kHz. Figure 12(b,) which shows the shear dissipation factor versus frequency, also exhibits a flattening of the slope of dissipation versus frequency at about this frequency. This suggests a specific dissipation factor peak in plexiglass at about this frequency. Since the shear dissipation factor is greater than the extensional dissipation factors, figure 11(b), it is clear that shear attenuation mechanisms are dominant in plexiglass, which is consistent with its polymeric nature.

Recent articles [15,16] have attempted to explain the specific dissipation peaks observed by Spencer [10], Murphy [11], Tittmann [12] and coworkers in the kHz range in cylindrical samples of fluid saturated rocks utilizing the Biot [13,14] solid-fluid coupling mechanism and its interaction with the cylinder boundary conditions. The results obtained here show that specific dissipation peaks may be obtained in cylindrical samples with complex elastic constants, in esssence through a coupling into various dissipative modes, the Biot mechanism being only a specific case of these. The results shown here for plexiglass show that these effects may be seen in nonporous solids as well. The theoretical treatment mentioned above has ignored the fact that the experiments of Murphy [11] and Tittmann [12] were resonant bar experiments performed on finite length cylinders. It is well known [37-39] that in finite length cylinders the end boundary conditions require a coupling of the orthogonal infinite cylinder extensional and flexural modes. The ensuing resonant frequencies depend on the length to radius ratios of the finite cylinders. Velocities determined from the frequencies of these resonances are, therefore, not generally interpretable as the extensional or flexural wave velocities. The 5.0 s interval sweep rate spectra shown in figure 8(b) illustrates this fact clearly. A corresponding treatment of the dissipation factor of finite size cylinders will show, no doubt, that the the dissipation factors are sensitive to this length to radius ratio in a fashion related to the velocity dependence. Preliminary

results of resonant bar experiments on plexiglass performed in this laboratory by Z. Wang [40] tend to support this dependence.

Following the gross comparison of the plexiglass experimental results with the constant Q model, which demonstrated experimentally the coupling of the boundary conditions with complex elastic moduli to influence the resulting frequency dependent attenuation, the results may be inverted utilizing the inversion algorithm previously described. Figure 13 shows the inverted frequency-dependent C_{12} and C_{44} of plexiglass. The experimental shear (lines in figure 12) and the 0.63 cm radius experimental extensional mode (figure 11) results were used as input to the inverse. Part (a) of the figure shows the real parts of C_{12} (1) and C_{44} (2), part (b) the corresponding imaginery part. Full lines in the figure correspond to the results of this study, dashed lines to the results of Read and Dean [41], measured with several differing systems over the frequency range 0.1 Hz to 400 kHz, and points in part (a) moduli determined from group velocity measurements of Z. Wang on the same sample, C_{44} measured at 500 kHz and C_{12} (derived from C_{11} measured at 1200 kHz) at 800 kHz. Examining the inverted shear modulus C_{44} of plexiglass, the dispersive behavior below 50 kHz may clearly be seen, charactarized by a strong increase in the real part of C_{44}, and a decrease in the imaginery part, as frequency increases. A second feature in the shear results is a broad shear relaxation at approximately 400 kHz. The form of this relaxation is quite classical, consisting of a peak in the imaginery part of C_{44} and an inflection point in the real part of the modulus. The shear results of Read and Dash [41] (dashed lines) show similar behavior with frequency, the large, low frequency, increase in the real part of the shear modulus in their study ending at lower frequencies than in this study, and the imaginery part of the shear modulus being lower than those observed here.

The inverted dilatational modulus C_{12} of plexiglass shows several interesting features. The real part of C_{12} is negative below 100 kHz, accompanied by a large imaginery part. At 100 kHz the real part of C_{12} increases and goes positive, acccompanied by a strong increase in

the imaginery part, suggesting a dilatational relaxation. Above 100 kHz the real part of the dilatational modulus increases slowly, followed by a strong increase above 400 kHz. The result of the increases in C_{12} is the increasingly liquidlike behavior of plexiglass as frequency increases. The results of Read and Dash [41] show similar increases in the real part of C_{12} with frequency, although the absolute value of the modulus they obtain over most of the frequency range studied is larger and possesses a peak at approximately 40 kHz, which we do not observe. In results for the imaginery part of C_{12} the results of this study agree more closely with those of Read and Dash [41], although their peak in the imaginery part occurs at 40 kHz and ours at 120 kHz. Similar dispersive properties of plastics has been shown by Sacshe and Pao [22]. Despite centroid smoothing of the data before its insertion into the inversion, the large degree of noise, particularly in the imaginery part of C_{12}, prevents further physical interpretation.

c. Porous Solids With Complex Elastic Moduli-Vycor

Vycor porous glass is a high porosity (30.96%) [42,43] porous glass with pores approximately 25 A° in radius. Its dry density is 1.52 g/cm^3. It affords insight into attenuation in a porous material where grain and pore scattering are small, since the effects of scattering will be important at frequencies higher than those studied here. As the pore space of vycor is created through a leaching process the pore space is well interconnected and surface wetting effects are smaller than those found in most sedimentary rocks despite an extremely high surface area (nitrogen BET method surface /volume ratio $= 1.2 \cdot 10^7\ cm^{-1}$). The solid matrix is also well connected, with a lack of sharp intergranular boundries. Material composition is 96.0% amorphous Silica, 3% B_2O_3 with the remaining fraction volatiles.

Figure 14 shows the experimental extensional (1) and shear (2); (a) phase velocity versus frequency, and (b) dissipation factor versus frequency of a room dry (10% water saturated) 0.72 cm radius vycor sample. In figure 14(b) the extensional results have been translated upward by 0.1 cm^{-1}. Figure 15 shows the inverted elastic moduli of vycor C_{12} (1), and C_{44} (2). Part (a) shows the real part of the moduli and part (b) the imaginery part. In figure 15(a) the

low frequency dispersion of the real part of C_{44} is apparent. This dispersion in the shear modulus is accompanied by a large imaginery part, figure 15(b), suggesting a low frequency shear relaxation which is concluded by 100 kHz. Above 100 kHz the shear modulus is relatively nondispersive, the imaginery part of the shear modulus slightly decreasing as the frequency increases. C_{12} of vycor shows a dispersive region at low frequencies, where the real part is negative and the imaginery part is quite large. By 200 kHz the real part of C_{12} has become positive and the imaginery part of the modulus has decreaed and gone negative, so that there is essentially no attenuation of th dilatational mode. Between 200 and 350 kHz C_{12} is nondispersive. Above 350 kHz the real part of C_{12} decreases and the imaginery part of C_{12} increases, suggesting the onset of the scattering mechanism. This high frequency negative dispersion of the real part of the elastic moduli in dry porous materials, previously observed by other investigators [4–6], correlates well with the recent applications of multiple scattering theory to spatialy correlated porous materials [20,21].

The low poisson's ratic of vycor throughout the frequency range studied together with the low frequency relaxations seen in the results suggest to the role of the adsorbed water films in decreasing the real part of the moduli and increasing the imaginery part of the moduli. A way to measure the effect of the wetting process is to compare the material elastic modulus with those derived from effective media computations, as these are based on a purely mechanical interaction between the various components in the porous solid. Taking mean velocities for vycor over the measured frequency range, $V_P = 3.4\ km/s$ and $V_s = 2.2\ km/s$, and computing effective material velocities using the self consistent results of Berryman [19], utilizing Fused Silica values $C_{11} = 7.83 \cdot 10^{11}\ Dyne/cm^2$, $C_{44} = 3.11 \cdot 10^{11}\ Dyne/cm^2$, and $\rho = 2.2g/cm^3$ for the matrix, we find that the velocities may be matched only by using as pore shapes the oblate spheroid shape with a one to five minor to major axis ratio. For the spherical pore shape which is closer to reality for vycor (as shown in transmission electron microscope pictures shown in reference 42), the estimated velocities using the self consistent ap-

proach are $V_P = 4.49\ km/s$ and $V_s = 2.76\ km/s$. This discrepancy between the self consistent (SCS) estimate for the actual pore shape and the actual measured effective values (EF), previously observed for porous materials [9,10], may be used to estimate the wetting effects using the equation

$$C_{11\,SCS} - C_{11\,EF} = \left(\frac{S}{V}\right) \cdot \gamma_{11} \tag{27}$$

$$C_{44\,SCS} - C_{44\,EF} = \left(\frac{S}{V}\right) \cdot \gamma_{66}$$

where S/V is the surface to volume ratio and γ_{11} and γ_{66} are the effective normal and tangential elements of the surface elasticity tensor [44], averages over the surface elasticity tensor over all the internal surfaces of the porous material. The numbers obtained by such analysis for the surface elasticity are of the order of those expected from the decrease in the silica-vacuum surface tension upon wetting ($\approx 10^3\ Dyne/cm$).

Conclusions

The theory of waveguided wave propagation in cylinders with complex elastic constants has been presented. The consequences of the theory to the fundamental extensional and torsional shear modes is shown and extended to frequency dependent complex elastic constants. For the case of a constant Q variation of the elastic constants with frequency, a specific dissipation peak is predicted for waveguided extensional mode experiments.

The results of experiments performed in a continuous wave acoustic transmission bridge are compared to theory and confirm the specific dissipation peak. An algorithm is implimented to invert the experimental measurements for the complex elastic moduli utilizing the derived dispersion relations. Large deviations are found between the predictions of constant Q and velocity and attenuation of the materials studied. Experimental results on vycor porous glass suggest the large effect of surface wetting on the elastic properties.

Acknowledgements

The authors thank Bertram Auld of the Stanford University Applied Physics department, Dale Morgan of the Texas Agriculture and Mining Geophysics department, and Jorge Mendoza and Charles West of the Stanford University Geophysics department for helpful critical discussions. We are grateful to Zhijing Wang of the Stanford Geophysics department for comparitive ultrasonic pulse transmission measurements on plexiglass.

The study was supported by the Office of Naval Research contract # N00014- 84-K-0560, and by the Stanford Rock Physics industrial consortium.

References

[1]W. P. Mason, Internal friction at low frequencies due to dislocations: applications to metals and rock mechanics, *In Physical acoustics (Edit. W. Mason), Vol. 8, 347 (1971)*

[2]K. Herzfeld, Absorption and dispersion of ultrasonic waves, *Academic, New York (1959)*

[3]J. Litovitz, Structural and shear relaxation in liquids, *In Physical acoustics (Edit. W. Mason), Vol. 2A, 282, Academic,* New York (1965)

[4]W. P. Mason and J. T. Kuo, Internal friction of pennslvania slate, *J. Geophys. Res. 76, 2084 (1971)*

[5]W. P. Mason, D. N. Beshers, and J. T. Kuo, Internal friction in westerly granite: relation to dislocation theory, *J. Appl. Phys. 41, 5206 (1971)*

[6]K. W. Winkler, Frequency dependent ultrasonic properties of high porosity sandstones, *J. Geophys. Res. 88 (B11), 9493 (1983)*

[7]P. R. Ogushwitz, Applicability of the Biot theory: I. low porosity materials, *J. Acoust. Soc. Am. 77 (2), 429 (1985)*

[8]P. R. Ogushwitz, Applicability of the Biot theory: II. suspensions, *J. Acoust. Soc. Am. 77 (2), 441 (1985)*

[9]P. R. Ogushwitz, Applicability of the Biot theory: III. wave speeds versus depth in marine sediments, *J. Acoust. Soc. Am. 77 (2), 453 (1985)*

[10]J. Spencer, Stress relaxations at low frequencies in fluid saturated rocks: attenuation and modulus dispersion, *J. Geophys. Res. 68 (B3), 1803 (1981)*

[11]W. F. Murphy, Effects of partial water saturation on attenuation in massillon sandstone and vycor porous glass, *J. Acoust. Soc. Am. 71 (6), 1458 (1982)*

[12]B. Tittmann, J. R. Bulau, and M. Abdel-Gawad, Dissipation of elastic waves in fluid saturated rocks, *In Physics and chemistry of porous media (Edit. D. L. Johnson and P. N.* Sen), AIP Conf. Proc. 107, 131, Amer. Inst. Phys., New York (1984)

[13]M. A. Biot, Theory of propagation of elastic waves in a fluid saturated porous solid (part I),

J. Acoust. Soc. Am. 28, 168 (1956)

[14]J. G. Berryman, Dispersion of extensional waves in fluid saturated porous cylinders at ultrasonic frequencies, *J. Acoust. Soc. Am. 74 (6), 1805 (1983)*

[15]J. E. White, Biot-Gardner theory of extensional waves in porous rocks, *Geophysics 51 (9), 742 (1986)*

[16]K. Dunn, Acoustic attenuation in fluid saturated porous cylinders at low frequencies, *J. Acoust. Soc. Am. 79 (6), 1709 (1986)*

[17]R. Tau and P. Sheng, First-principle approach to the calculation of the elastic moduli of arbitrary periodic composites, *J. Acoust. Soc. Am. 77 (5), 1651 (1985)*

[18]L. M. Schwartz, Acoustic properties of porous systems: II. microscopic description, *In Physics and chemistry of porous media (Edit. D. L. Johnson and P. N.* Sen), AIP Conf. Proc. 107, 105, Amer. Inst. Phys., New York (1984)

[19]J. G. Berryman, Long-wavelength propagation in composite elastic media; II. ellipsoidal inclusions, *J. Acoust. Soc. Am. 68 (6), 1820 (1980)*

[20]V. K. Varadan, Y. Ma, and V. V. Varadan, A multiple scattering theory for elastic wave propagation in discrete random media, *J. Acoust. Soc. Am. 77 (2), 375 (1985)*

[21]V. K. Varadan, Y. Ma, and V. V. Varadan, Multiple scattering of compressional and shear waves by fiber reinforced composite materials, *J. Acoust. Soc. Am. 80 (1), 335 (1986)*

[22]W. Sachse and Y. Pao, On the determination of phase and group velocities of dispersive waves in solids, *J. Appl. Phys. 44 (8), 4320 (1978)*

[23]D. Bolef, High frequency continuous wave ultrasonics, *In Physical acoustics (Edit. W. Mason), Vol. 8, 95, Academic, New York (1971)*

[24]W. Smith, Circuit model analysis and design of interdigital transducers for surface wave devices, *In Physical acoustics (Edit. W. Mason), Vol. 15, 100, Academic, New York* (1981)

[25]B. Auld, Acoustic fields and waves in solids, *Vol. 2, 104, John Wiley, New York (1972)*

[26]L. Pochammmer, Uber die fortpflanzungsgeschwnidigkeiten kleiner schwingungen in einem

unbegrenzten isotropen kreiszylinder, *J. f. Math. (Crelle), Bd. 81, 324 (1876)*

[27]A. Love, A treatise on the mathematical theory of elasticity, *4th edition, 287, Dover, New York (1944)*

[28]D. Bancroft, The velocity of longitudinal waves in cylindrical bars, *Phys. Rev. 59 , 588 (1941)*

[29]T. Meeker, Guided wave propagation in elongated cylinders and plates, *In Physical acoustics (Edit. W. Mason), Vol. 1A, 112, Academic, New York* (1964)

[30]R. Thurston, Elastic waves in rods and clad rods, *J. Acoust. Soc. Am. 64 (1), 1 (1978)*

[31]J. Zemanek, Attenuation and dispersion of elastic waves in a cylindrical rod, *J. Acoust. Soc. Am. 33, 1283 (1961)*

[32]P. S. Dubbelday, Application of a new complex root finding method to the dispersion relation for elastic waves in a fluid loaded plate, *SIAM J. Appl. Math. 43 (5), 1127 (1983)*

[33]I. S. Gradshteyn and I. M. Ryzhik, Table of integrals, series and products, corrected and enlarged version, *959, Academic, New York (1980)*

[34]D. Ellis, A simple shallow water propagation model including shear wave effects, *J. Acoust. Soc. Am. 78 (6), 2087 (1985)*

[35]A. F. Brown and J. P. Weight, Generation and reception of wideband ultrasound, *Ultrasonics 12, 161 (1974)*

[36]CRC Handbook of chemistry and physics, *62nd Edition, E45, Chemical Rubber Company, Boca Raton (1981)*

[37]H. D. McNiven and D. C. Perry, Axially symmetric waves in finite elastic rods, *J. Acoust. Soc. Am. 34 (4), 433 (1962)*

[38]R.D. Mindlin and H. D. McNiven, Axially symmetric waves in elastic rods, *AIME J. Appl. Mech. 27 , 145 (1960)*

[39]J. R. Hutchinson, Axisymmetric Vibration of a free finite length rod, *J. Acoust. Soc. Am. 51 (1), 234 (1972)*

[40]Z. Wang, The effects of sample size on wave attenuations and velocities in the resonant bar technique, *Stanford rock physics project report 25, 211, Stanford, California (1985)*

[41]B. E. Read and G. D. Dean, The determination of the dynamic properties of polymers and composites, *181, John Wiley, New York (1978)*

[42]T. H. Elmer, M. E. Nordberg, G. B. Carrier, and E. J. Korda, Phase separation in borosilicate glasses as seen by electron microscopy and scanning electron microscopy, *J. Am. Ceram. Soc. 53 (4), 171 (1970)*

[43]T. H. Elmer, Sintering of porous glass, *Am. Ceram. Soc. Bull. 62 (4), 513 (1983)*

[44]E. H. Luccassen-Reynders, Surface elasticity and viscosity in compression/dilation, *In Surfactant science series (Edit. M. J. Schick and F. M. Fowkes), Vol. 11,* 173, Marcel Dekker Inc., New York (1981)

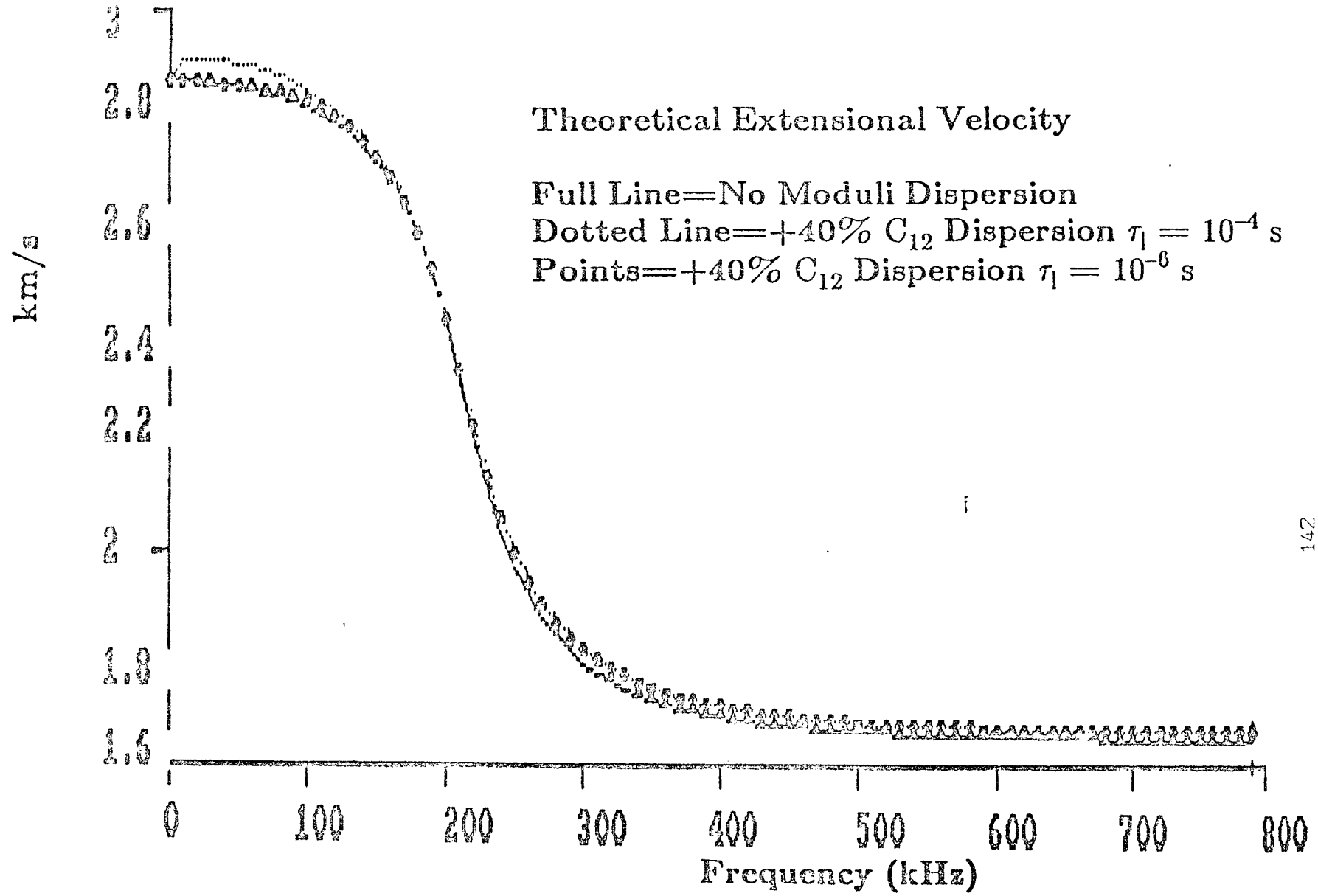

FIG. 1. Theoretical extensional velocity for real frequency dependent C'_{12}. Full line shows dispersionless moduli case, dotted line shows +40% C'_{12} dispersion with $\tau_l = 10^{-4}$ s, and points are +40% C'_{12} dispersion with $\tau_l = 10^{-6}$ s.

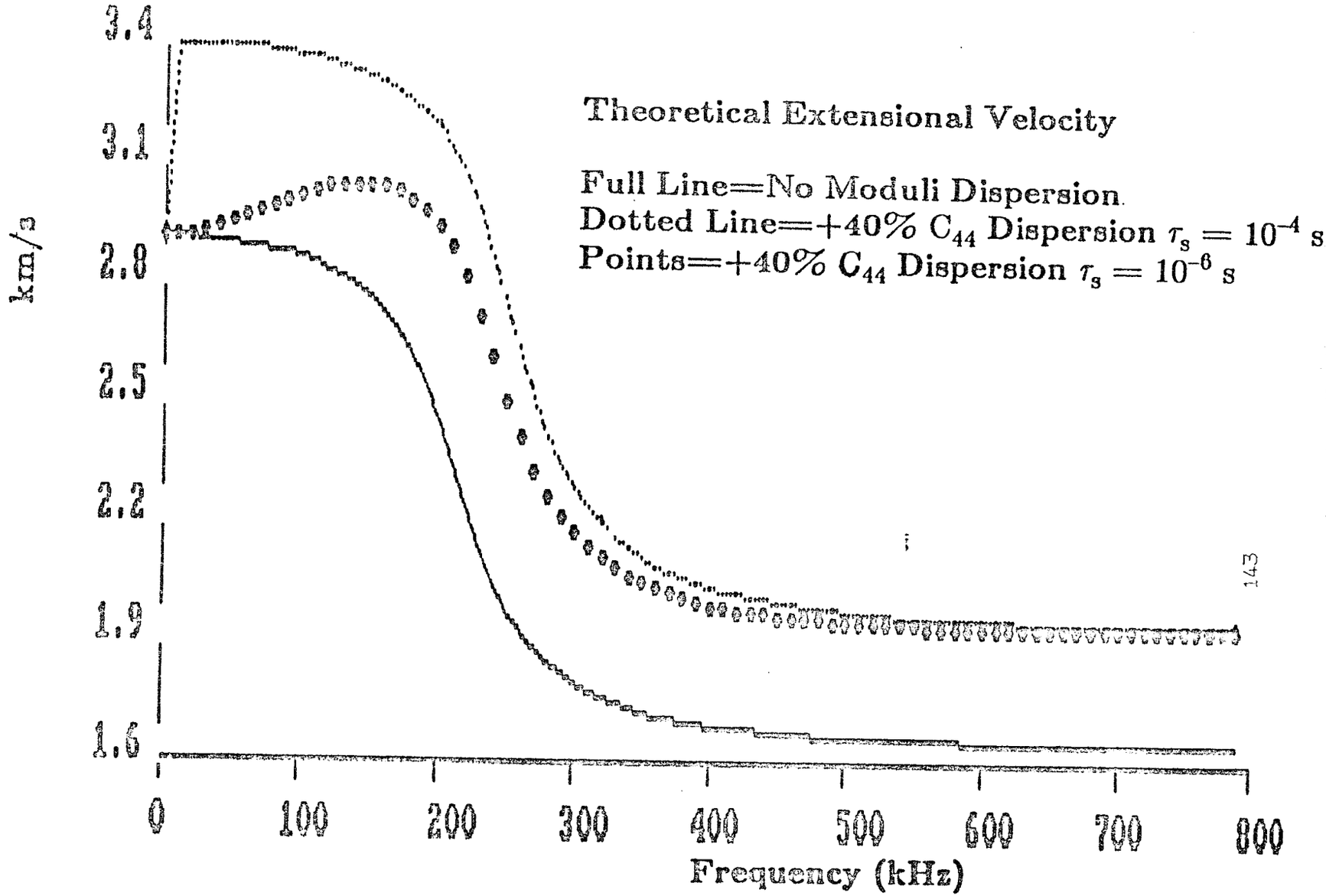

FIG. 2. Theoretical extensional velocity for real frequency dependent C'_{44}. Full line shows dispersionless moduli case, dotted line shows +40% C'_{44} dispersion with $\tau_s = 10^{-4}$ s, and points are +40% C'_{44} dispersion with $\tau_s = 10^{-6}$ sec.

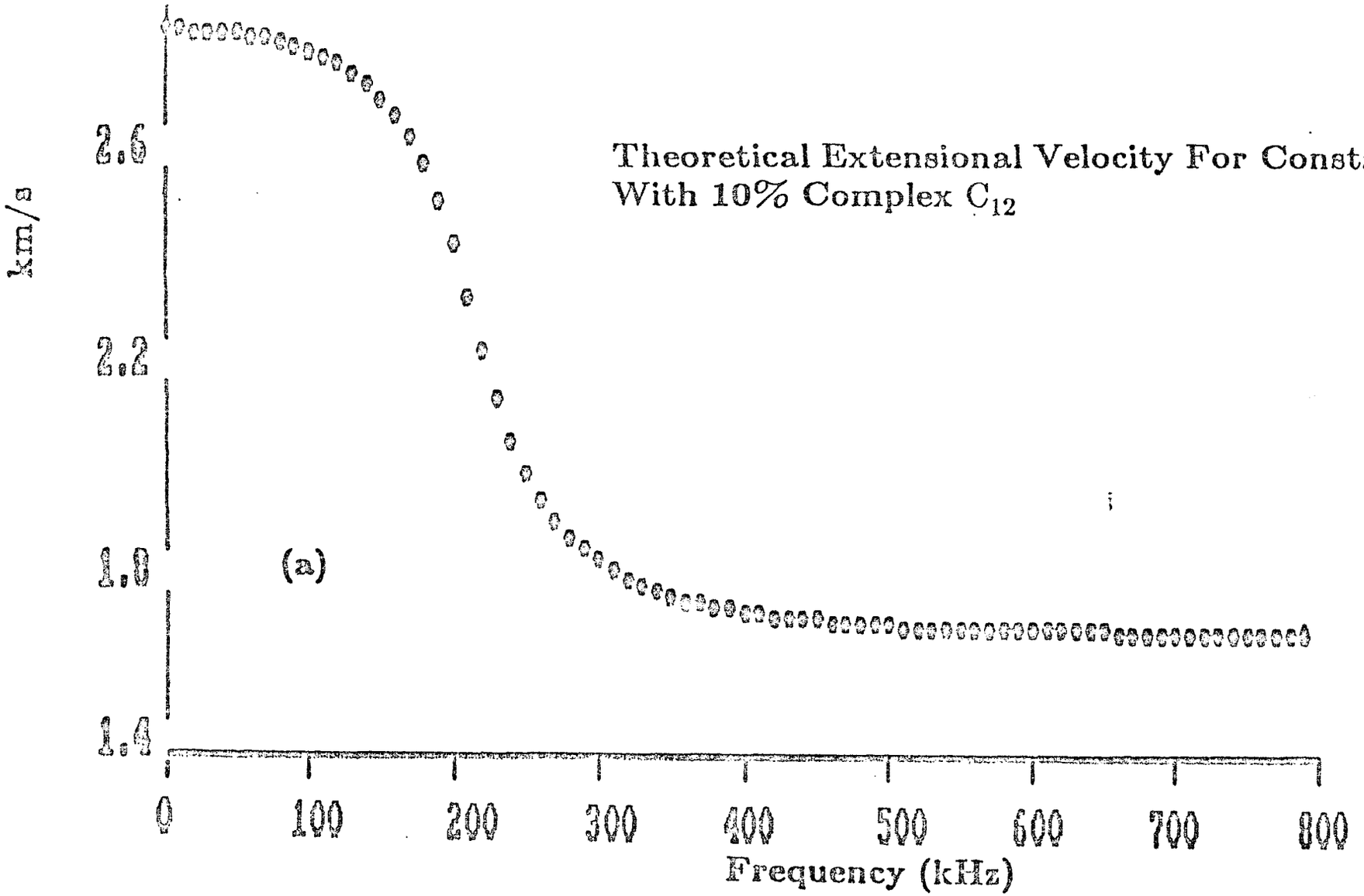

FIG. 3(a). Theoretical extensional mode for constant Q with a 10% complex C_{12}, phase velocity versus frequency.

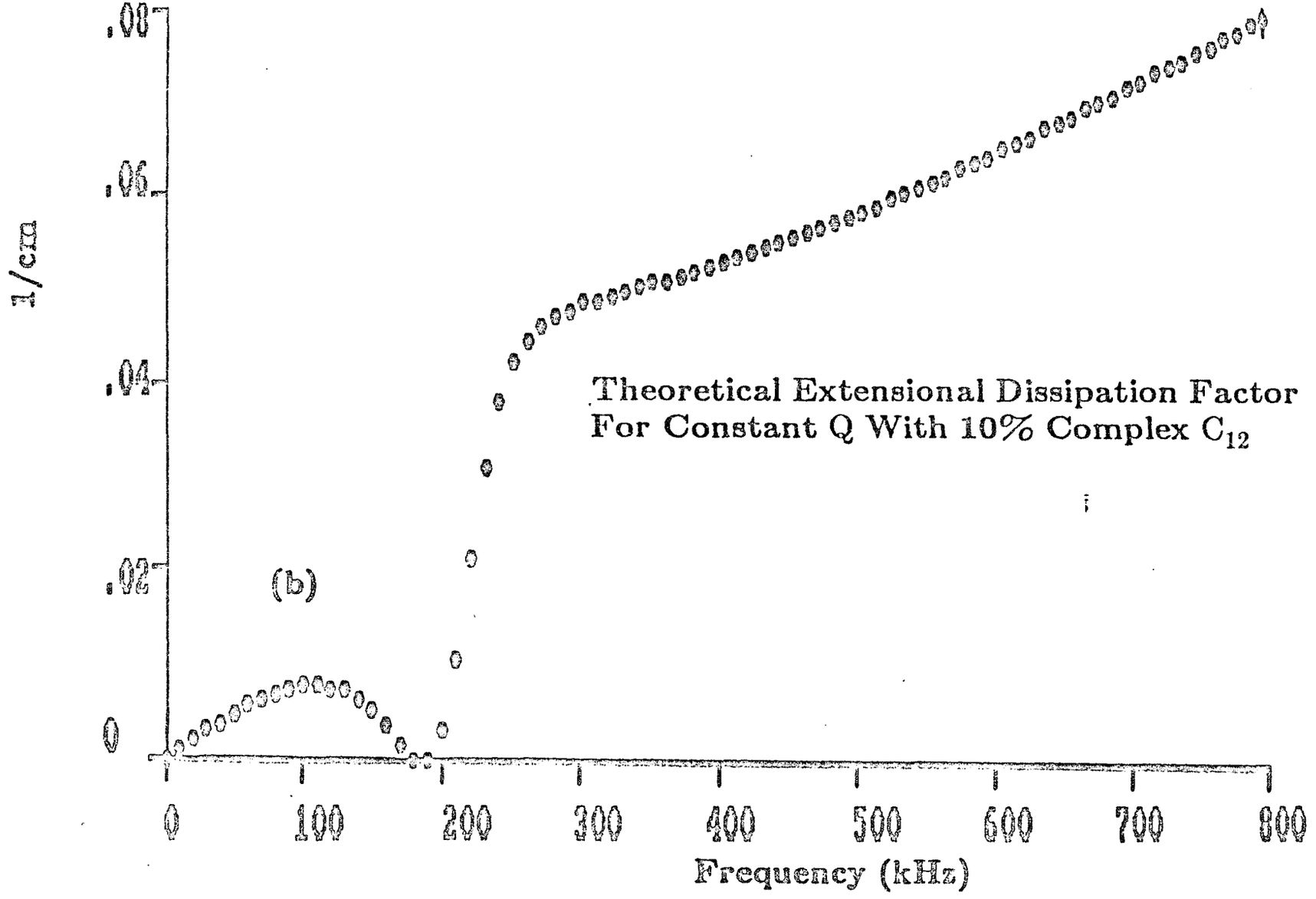

FIG. 3(b). Theoretical extensional mode for constant Q with a 10% complex C_{12}, dissipation factor versus frequency.

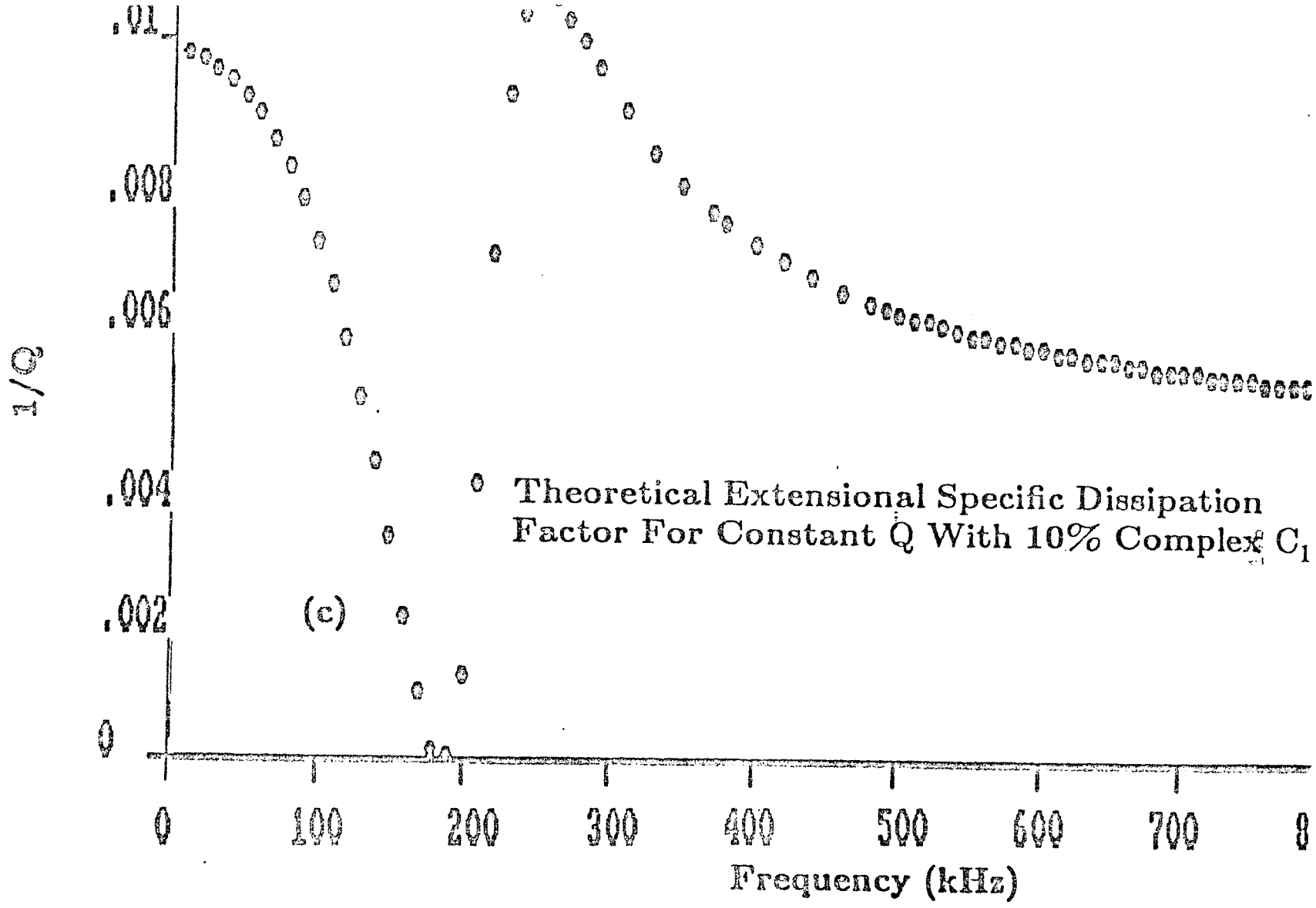

FIG. 3(c). Theoretical extensional mode for constant Q with a 10% complex C_{12}, specific dissipation factor versus frequency.

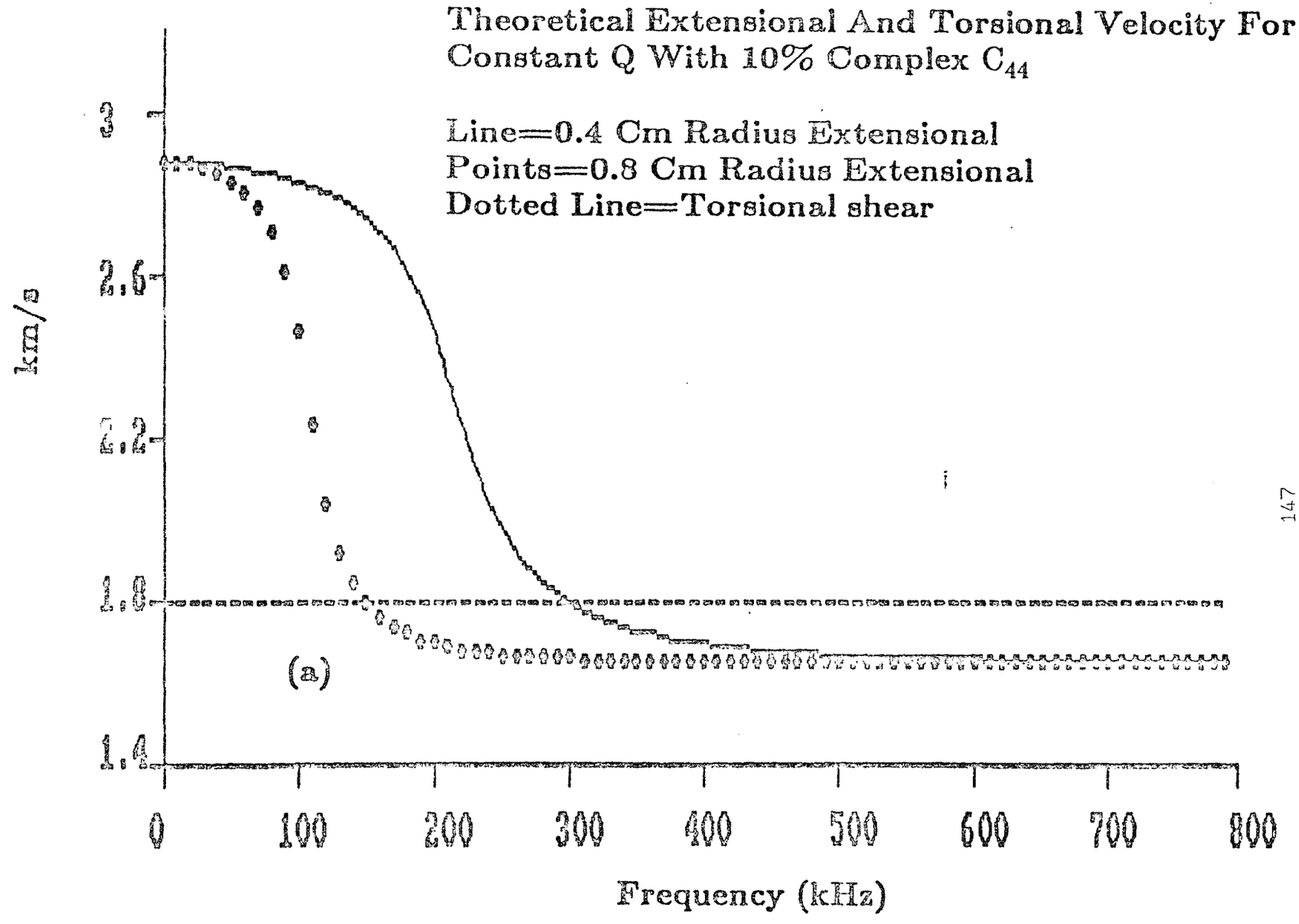

FIG. 4(a). Theoretical extensional mode for constant Q with a 10% complex C_{44} for 0.4 (line) and 0.8 cm (points) radius cylinders, phase velocity versus frequency. Dotted line shows the theoretical torsional shear phase velocity.

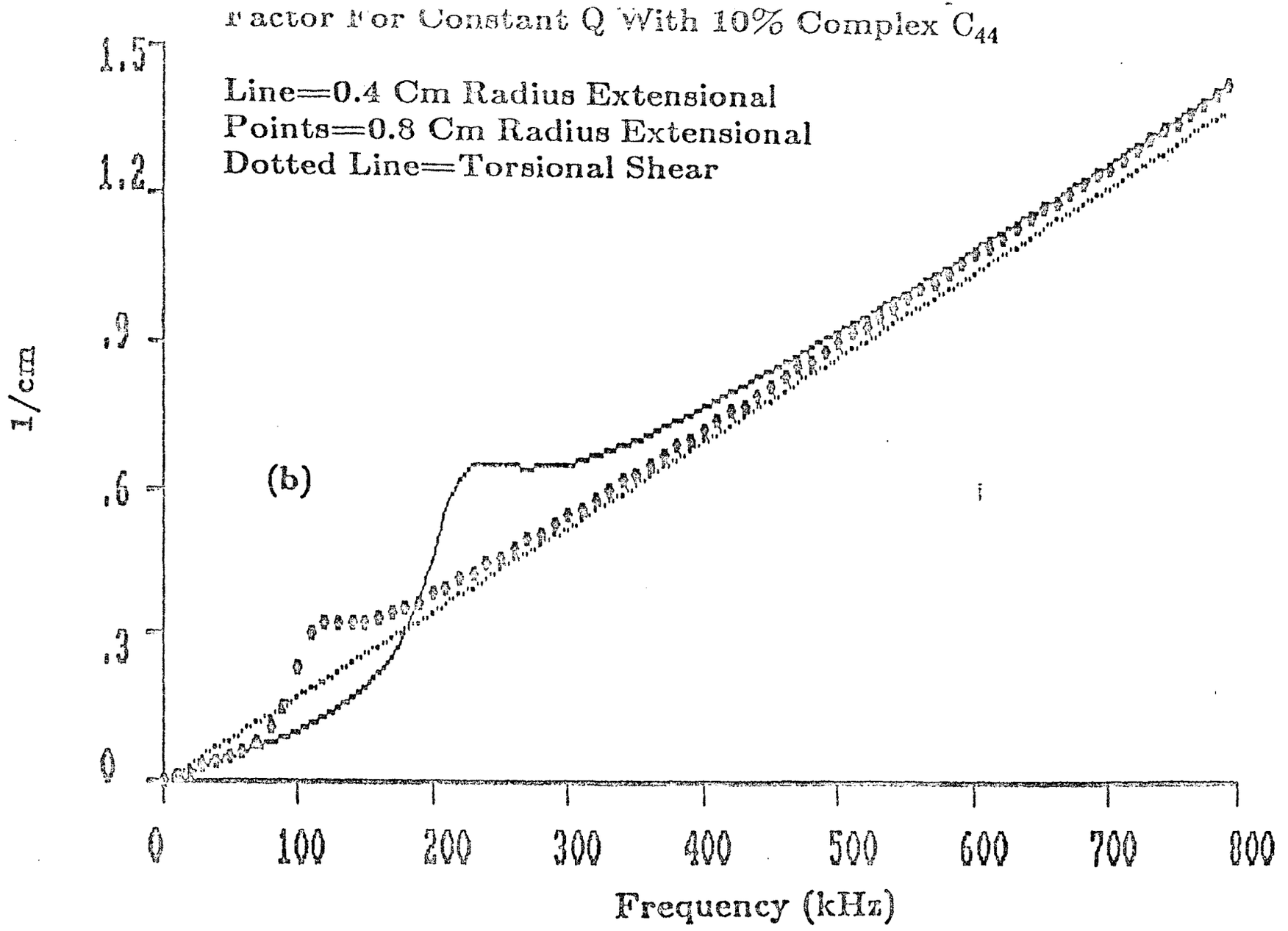

FIG. 4(b). Theoretical extensional mode for constant Q with a 10% complex C_{44} for 0.4 (line) and 0.8 cm (points) radius cylinders, dissipation factor versus frequency. Dotted line shows the theoretical torsional shear dissipation factor.

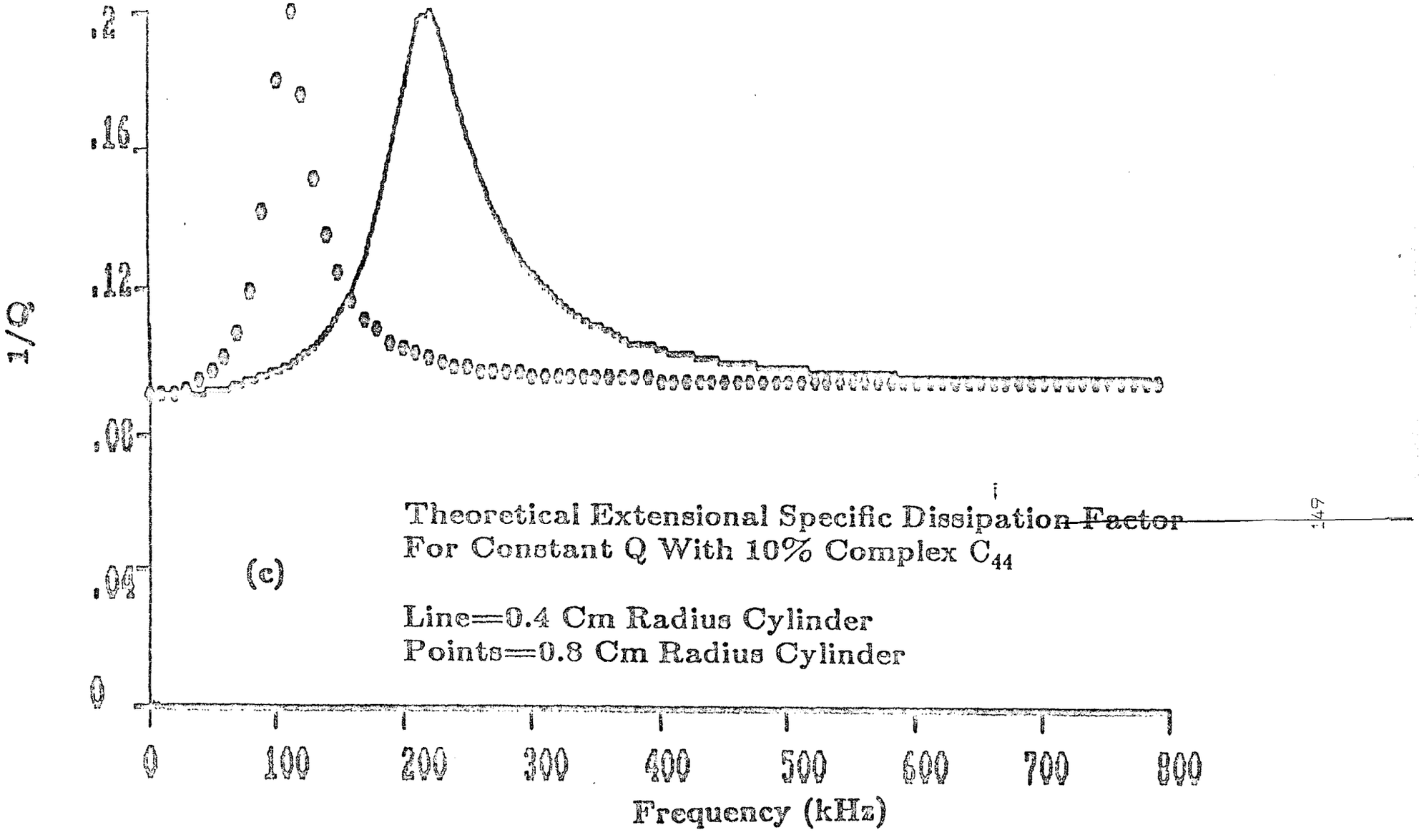

FIG. 4(c). Theoretical extensional mode for constant Q with a 10% complex C_{44} for a 0.4 (line) and 0.8 cm (points) radius cylinders, specific dissipation factor versus frequency.

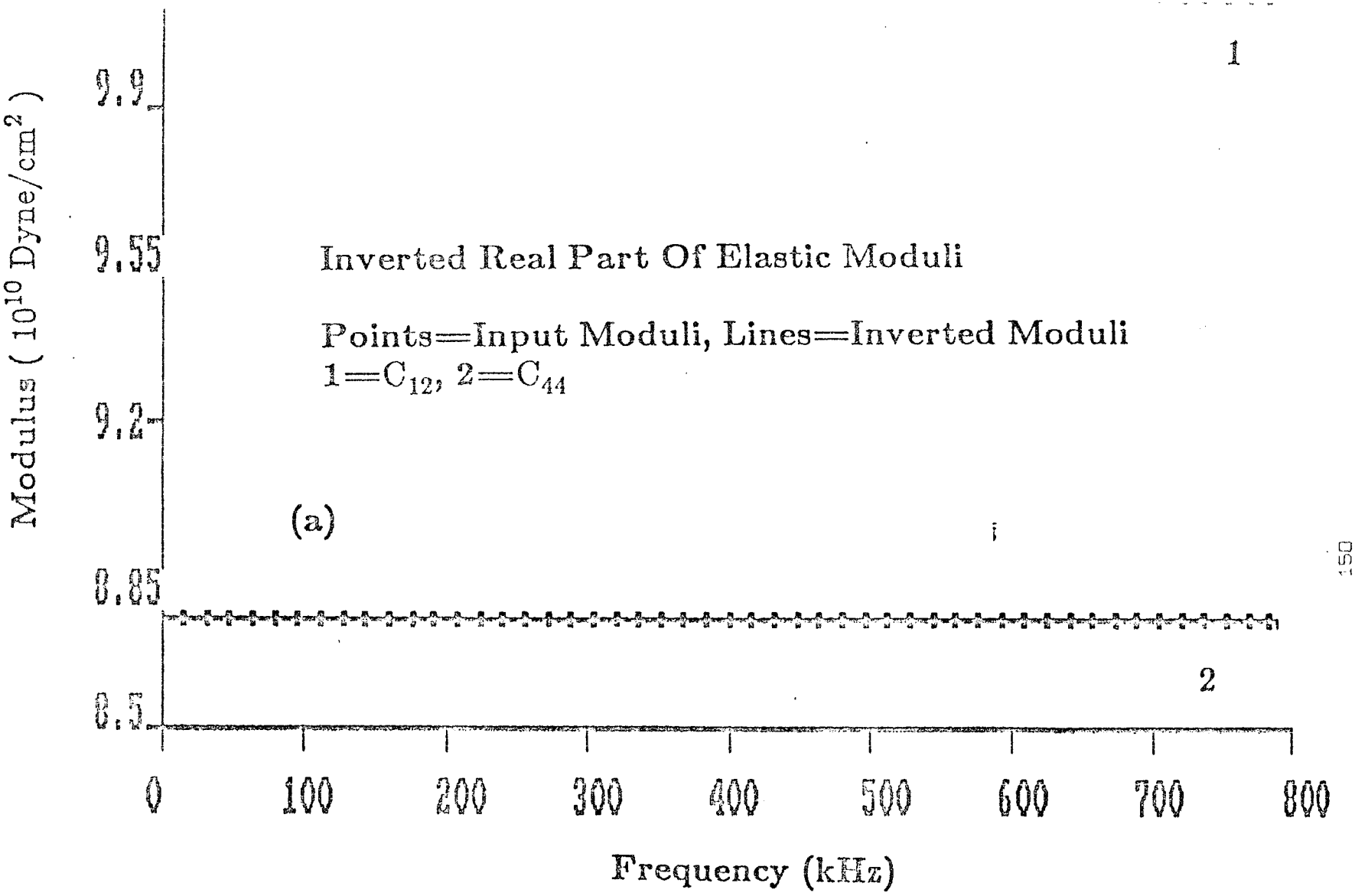

FIG. 5(a). Application of inversion to artificial data. Input (points) and inverted (line) real part of complex C_{12} (1) and C_{44} (2).

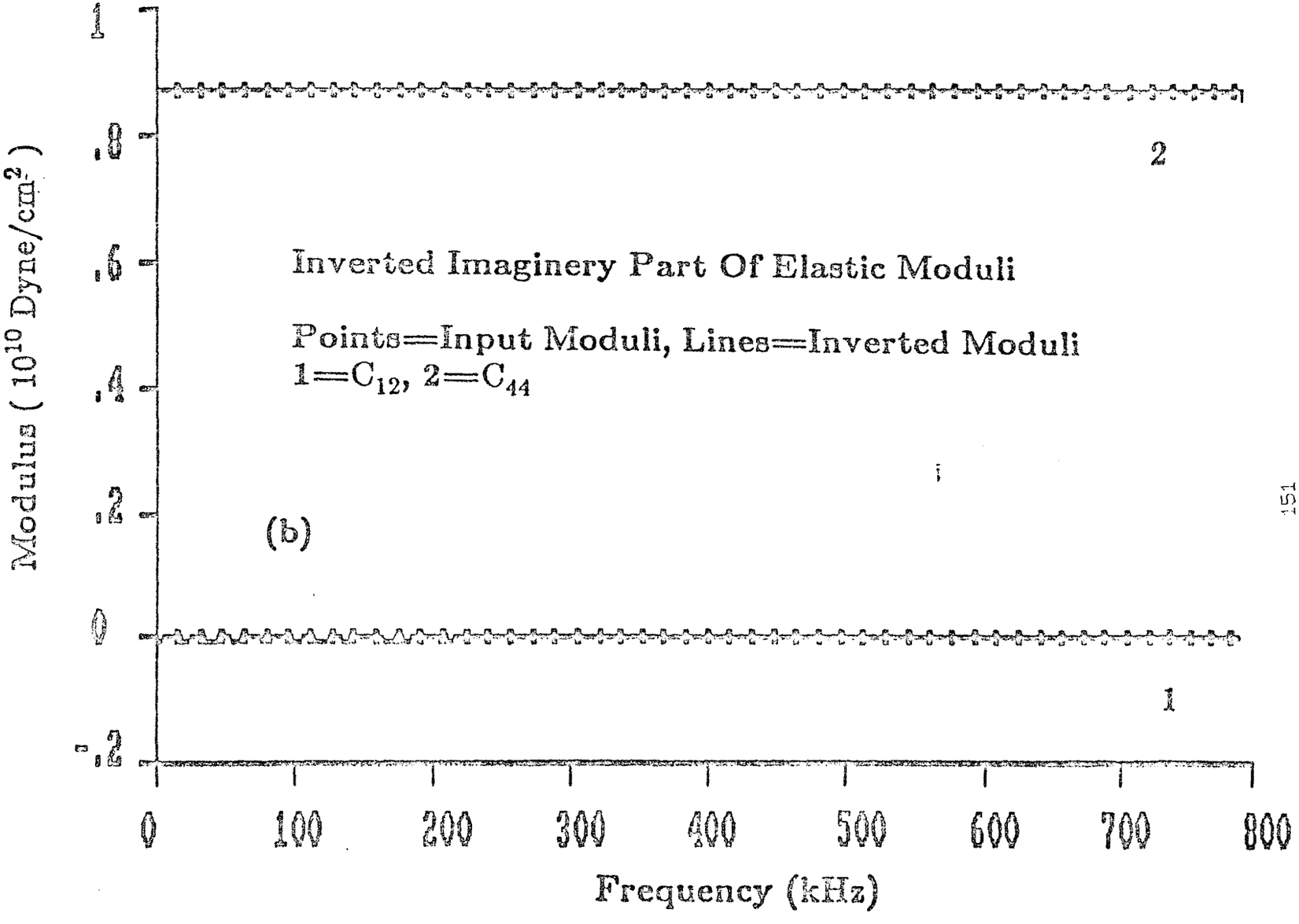

FIG. 5(b). Application of inversion to artificial data. Input (points) and inverted (line) imaginery part of complex C_{12} (1) and C_{44} (2).

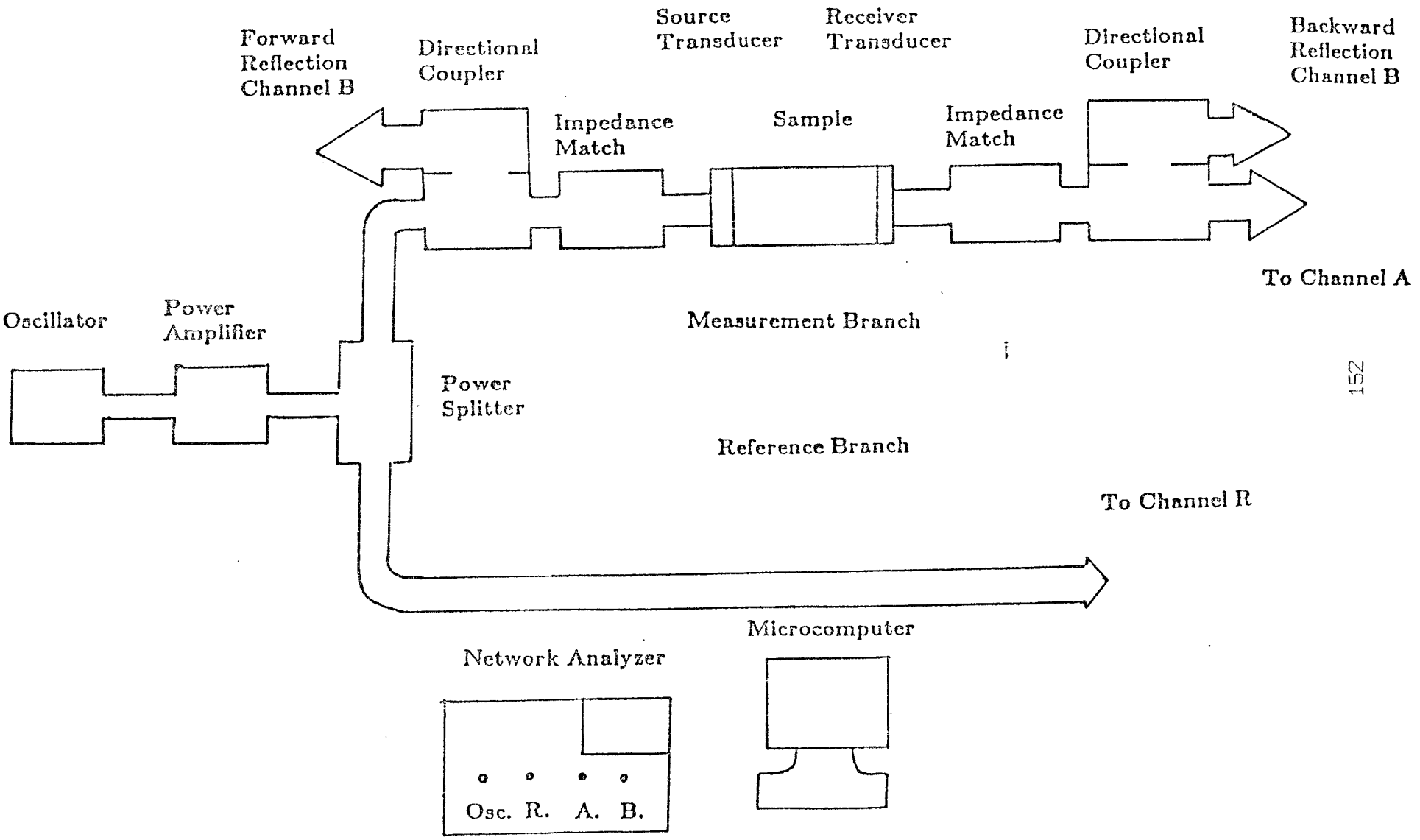

FIG. 6. Acoustic Transmission Bridge.

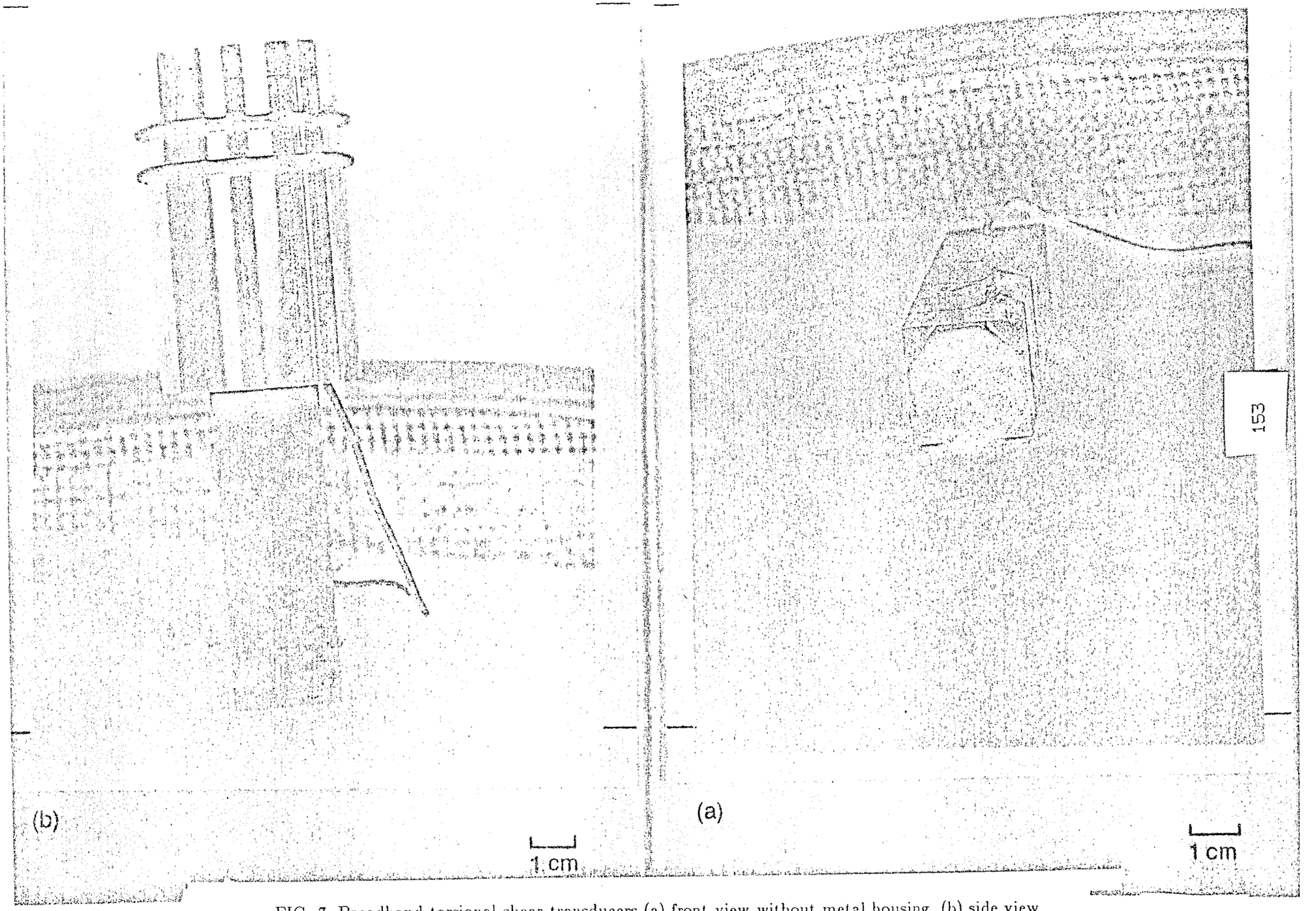

FIG. 7. Broadband torsional shear transducers (a) front view without metal housing, (b) side view

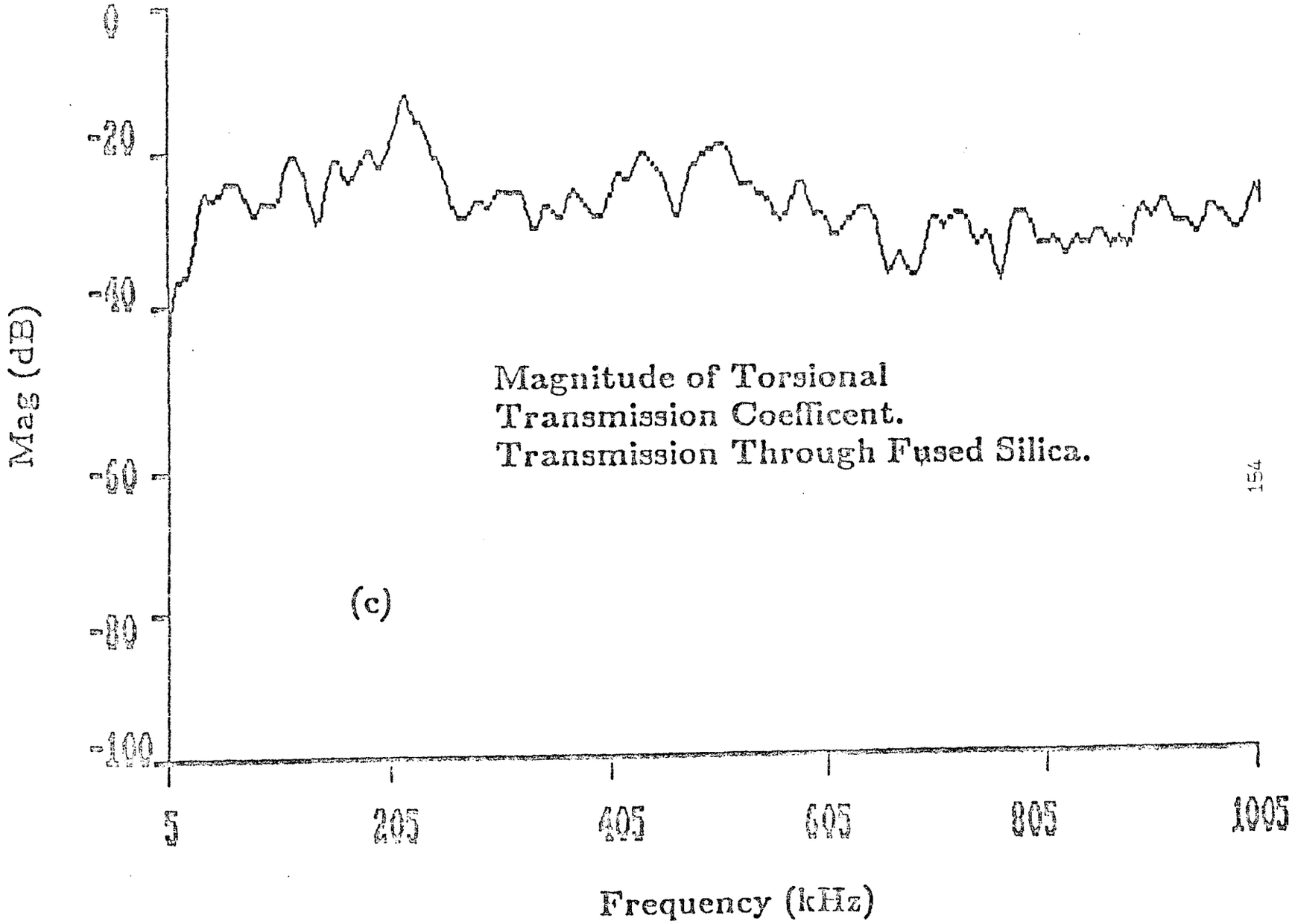

FIG. 7(c). Broadband torsional shear transducers magnitude versus frequency for transmission through Fused Silica.

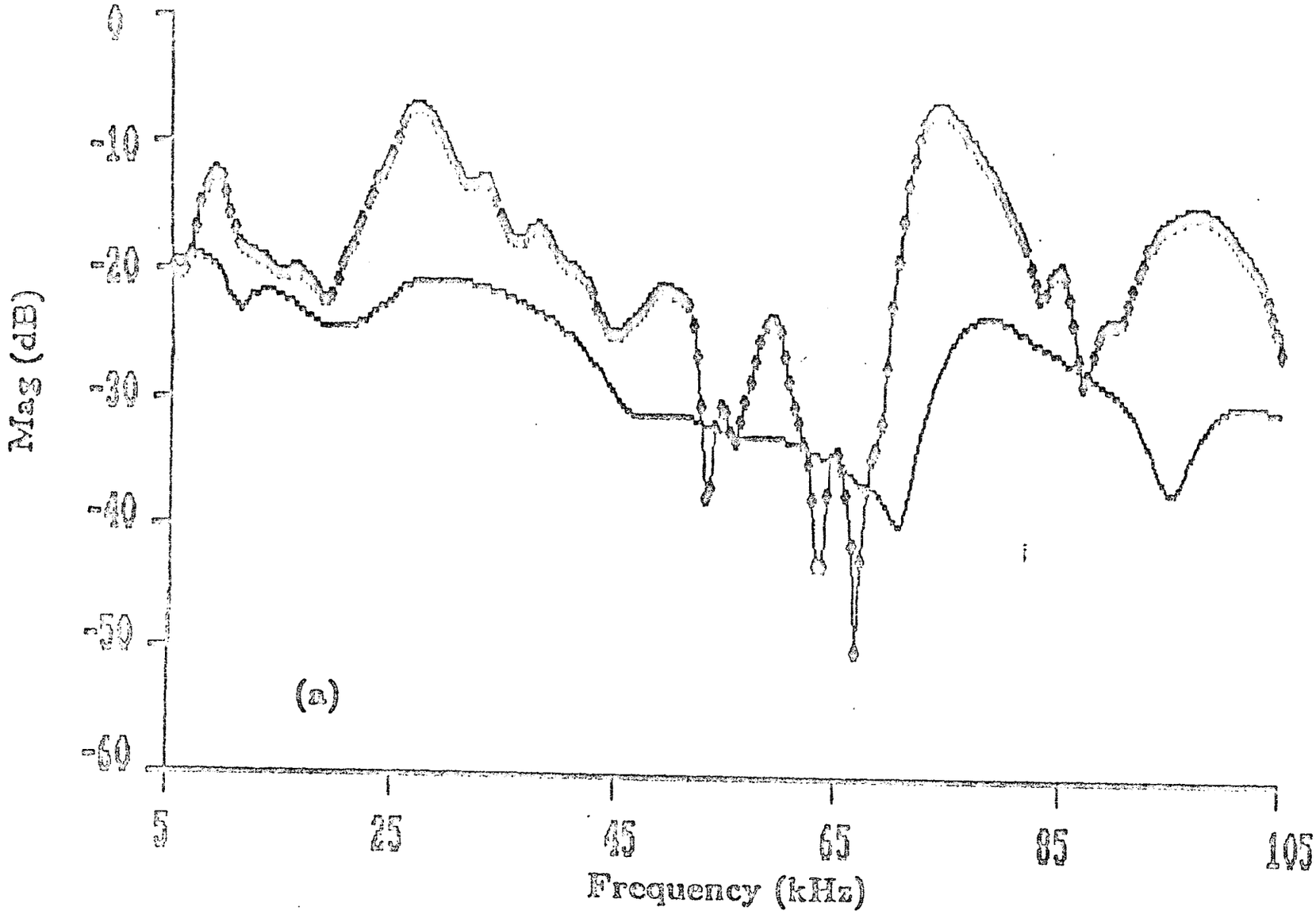

FIG. 8(a). 75% water saturated Massillon Dark extensional magnitude versus frequency for 1.4 (line) and 5.0 s (points) interval sweep times.

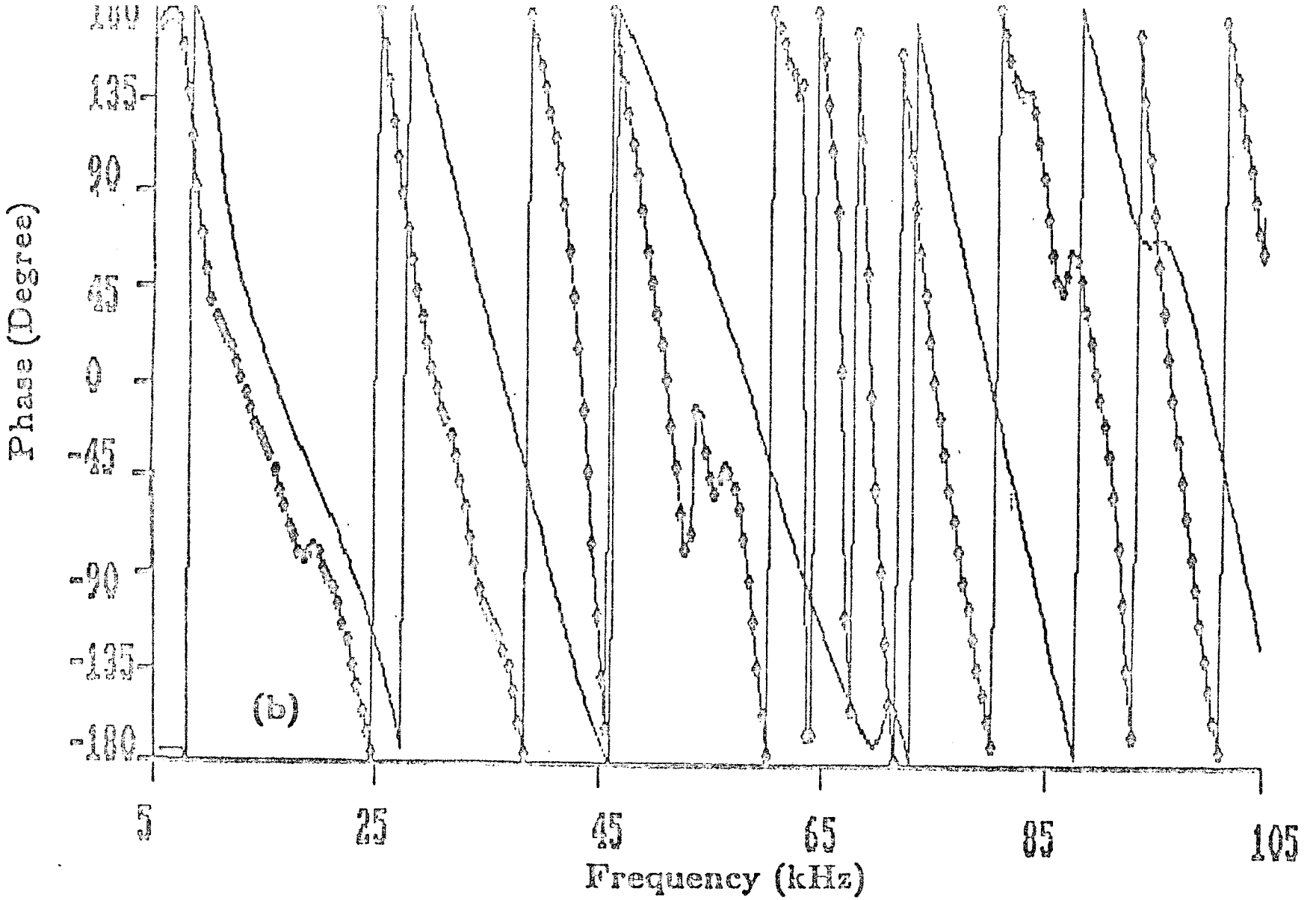

FIG. 8(b). 75% water saturated Massillon Dark extensional phase versus frequency for 1.4 (line) and 5.0 s (points) interval sweep times.

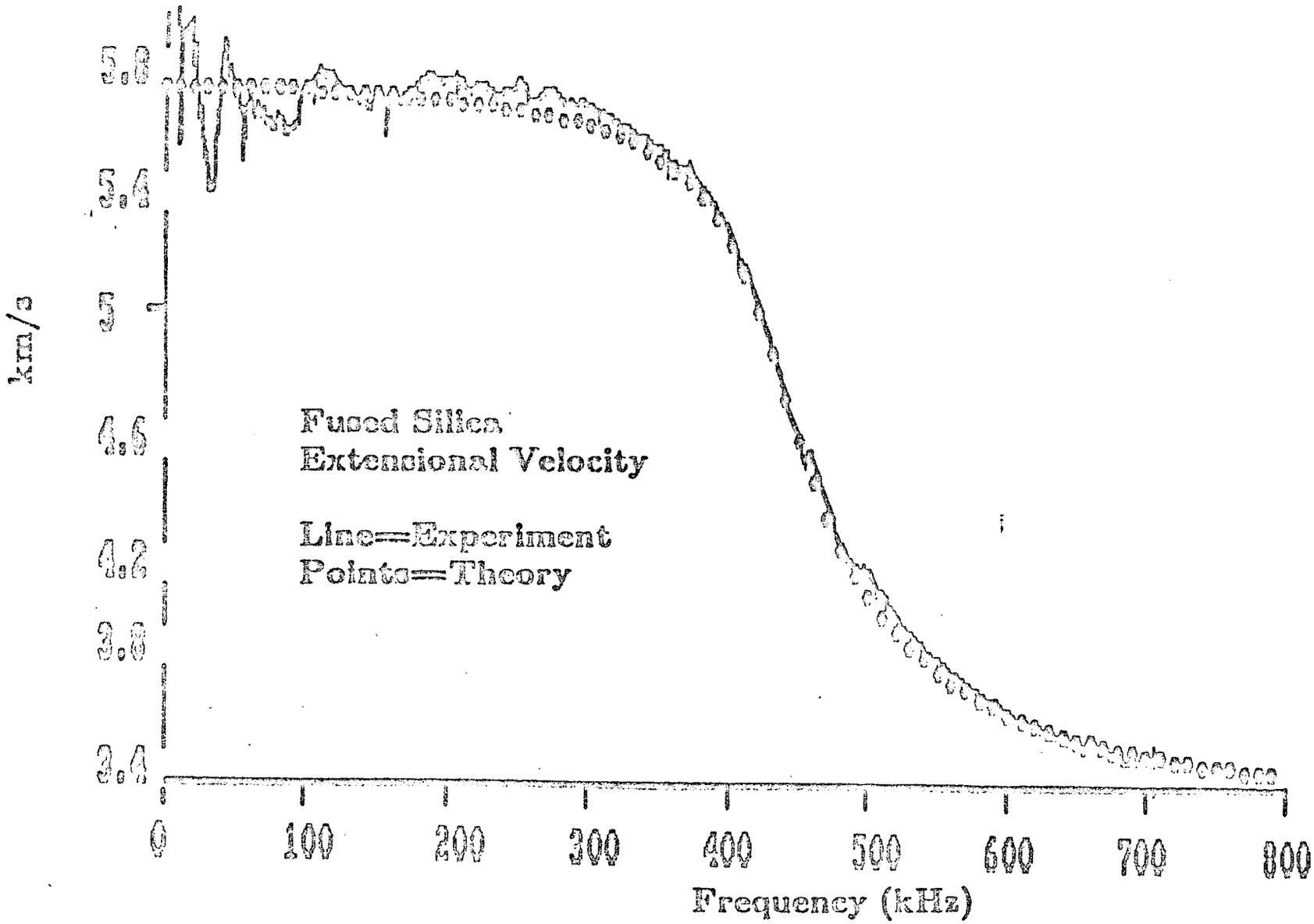

FIG. 9. Fused Silica extensional phase velocity versus frequency. Line is experiment, points are theory.

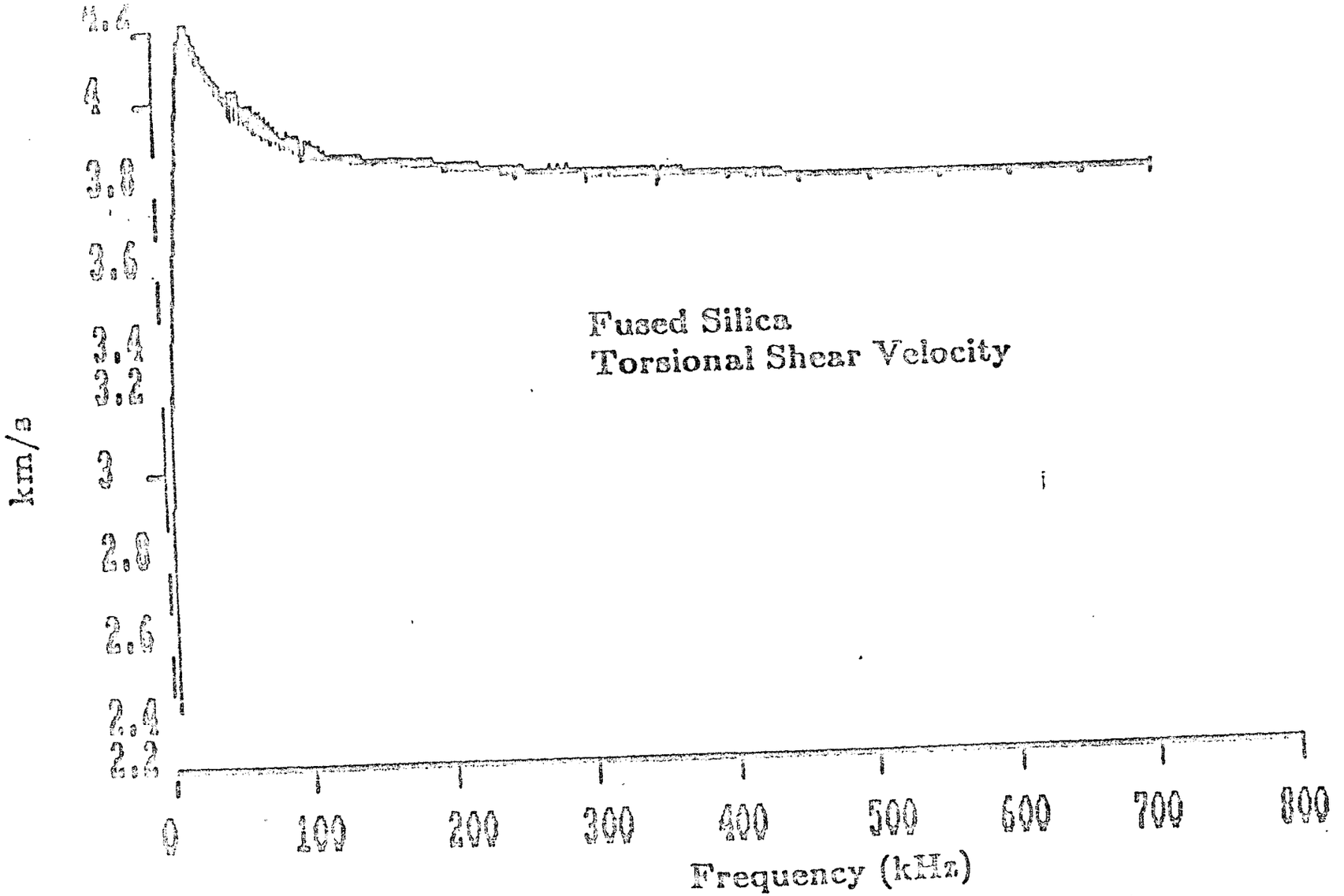

FIG. 10. Fused Silica torsional phase velocity versus frequency.

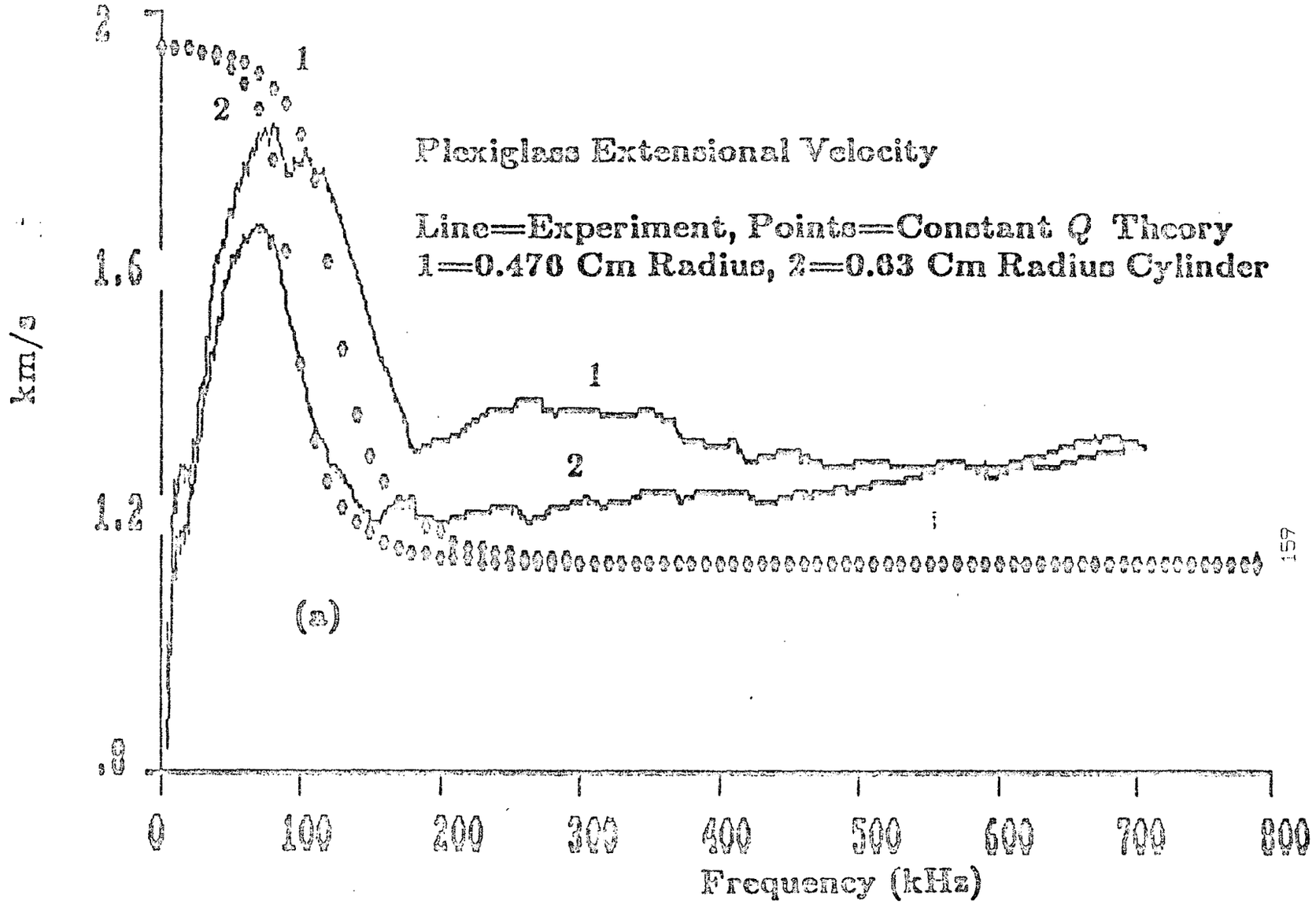

FIG. 11(a). 0.476 (1) and 0.63 cm (2) radii plexiglass extensional experimental (line) and theoretical constant Q (points) results, phase velocity versus frequency.

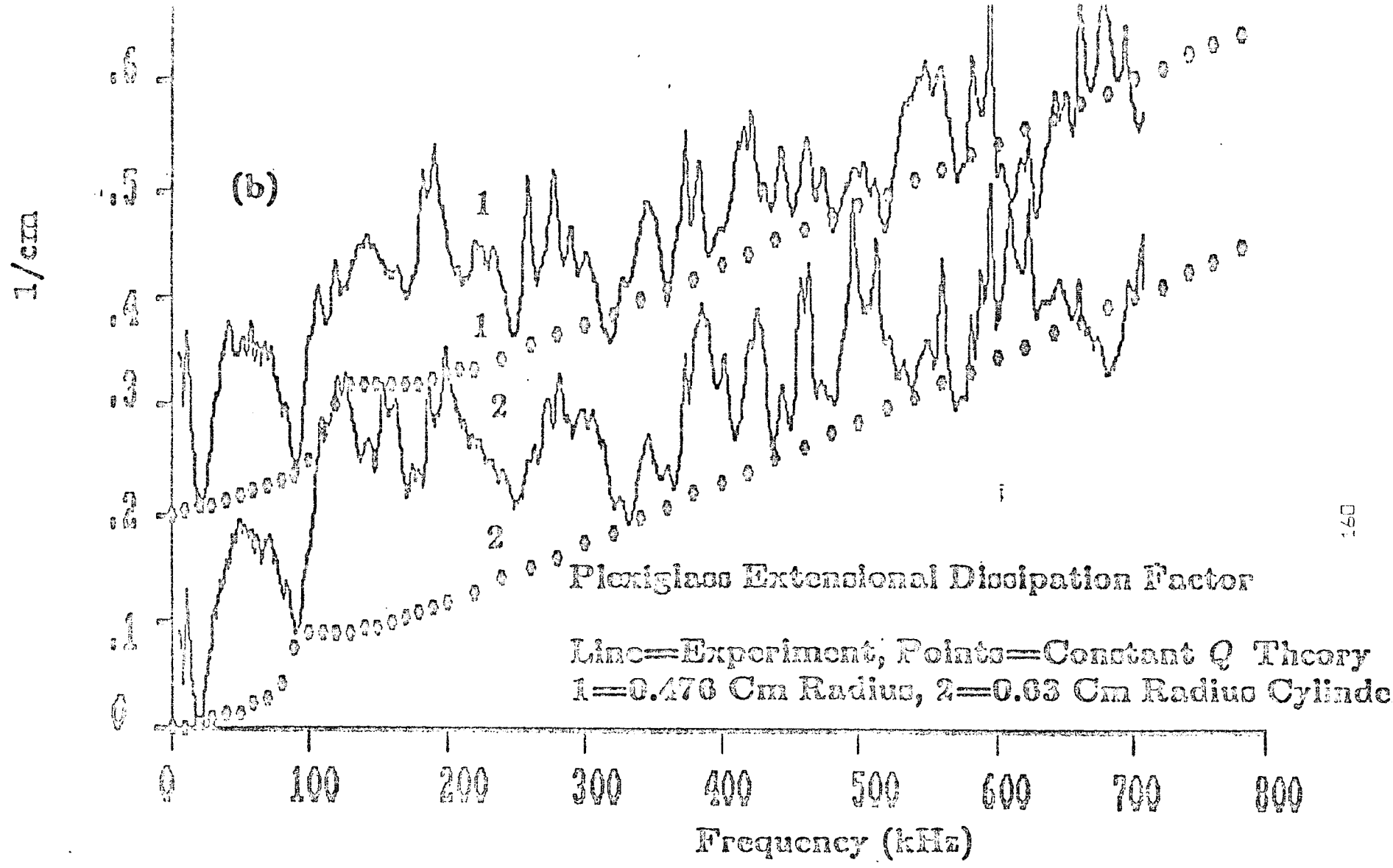

FIG. 11(b). 0.476 (1) and 0.63 cm (2) radii plexiglass extensional experimental (line) and theoretical constant Q (points) results, dissipation factor versus frequency. The 0.476 cm results have an added 0.2 cm^{-1}.

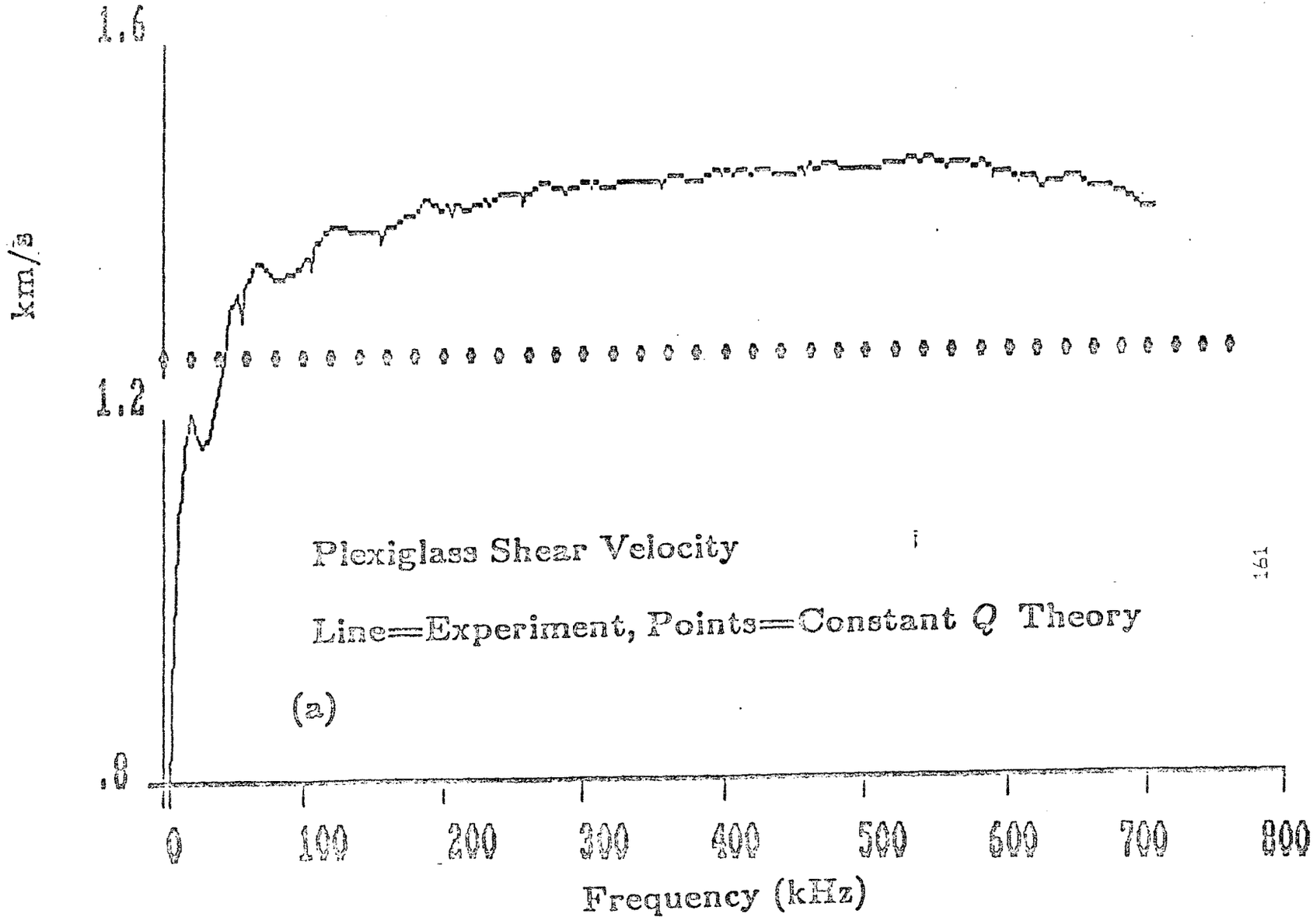

FIG. 12(a). Plexiglass torsional shear experimental (line) and theoretical constant Q (points) results, phase velocity versus frequency.

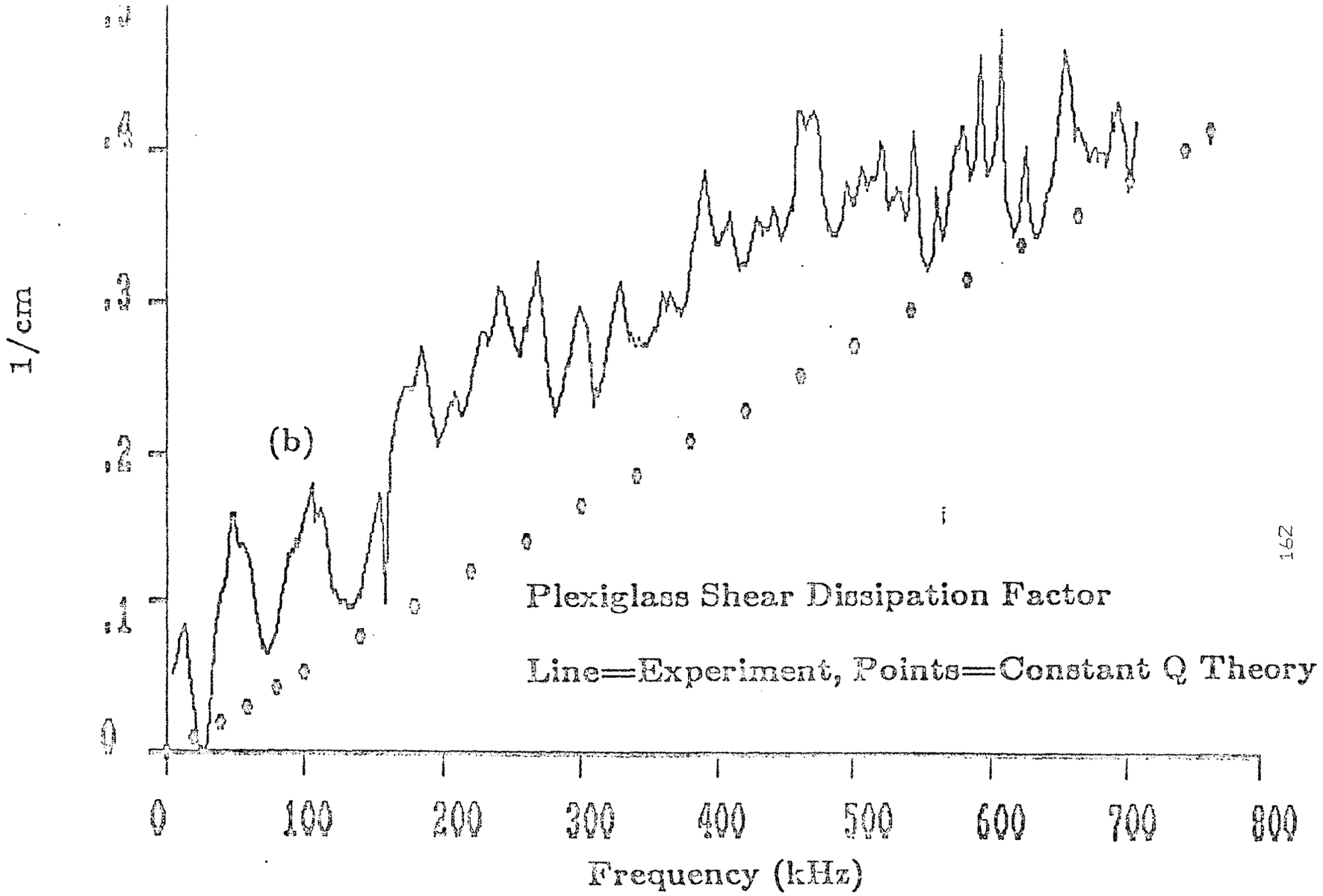

FIG. 12(b). Plexiglass torsional shear experimental (line) and theoretical constant Q (points) results, dissipation factor versus frequency.

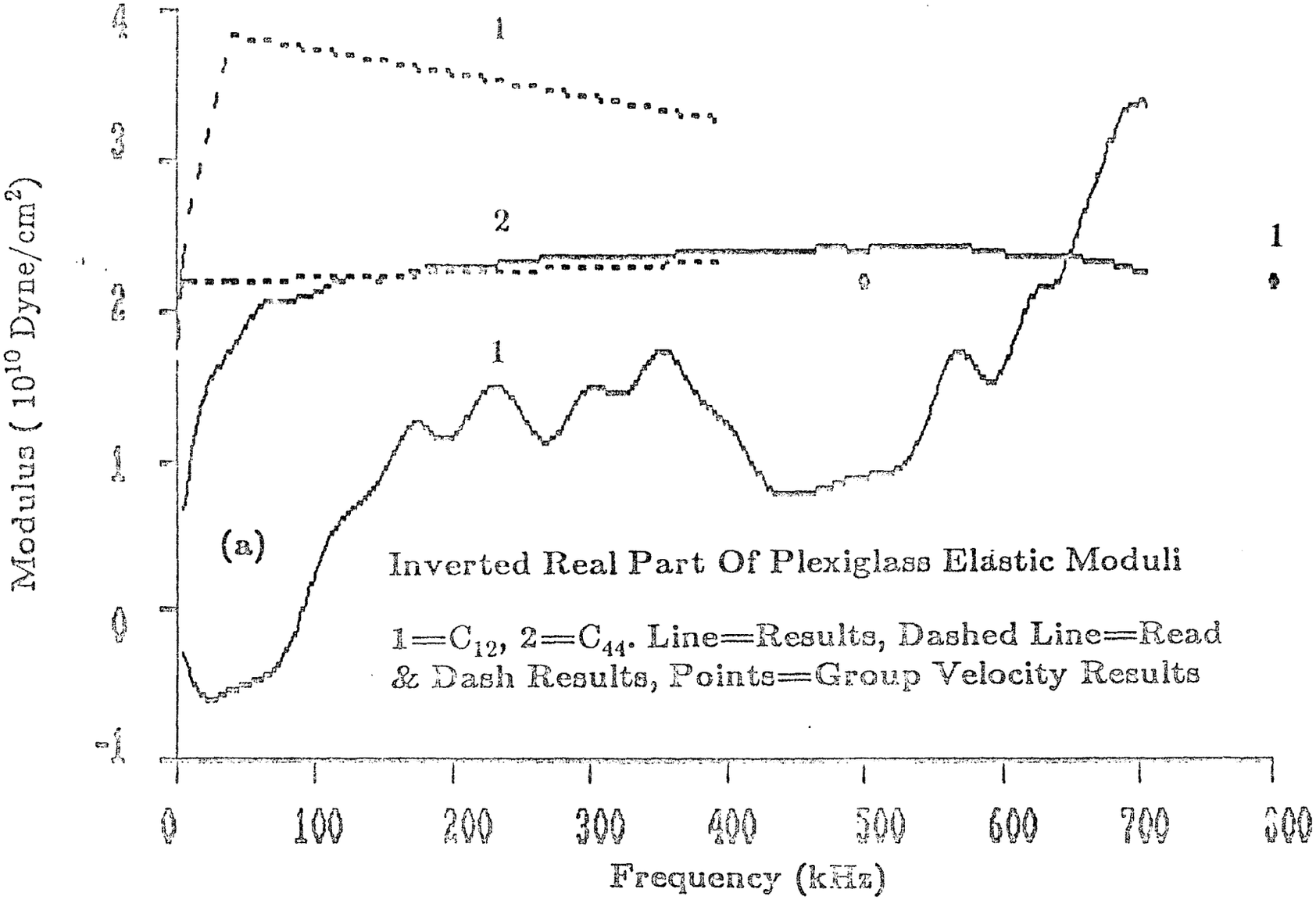

FIG. 13(a). Inverted real part of plexiglass elastic moduli C_{12} (1) and C_{44} (2). Lines in the figure are results of this study, dashed lines are results of Dash and Read [41], and points are moduli determined from group velocity measurements of Z. Wang, C_{44} at 500 kHz, C_{12} at 800 kHz.

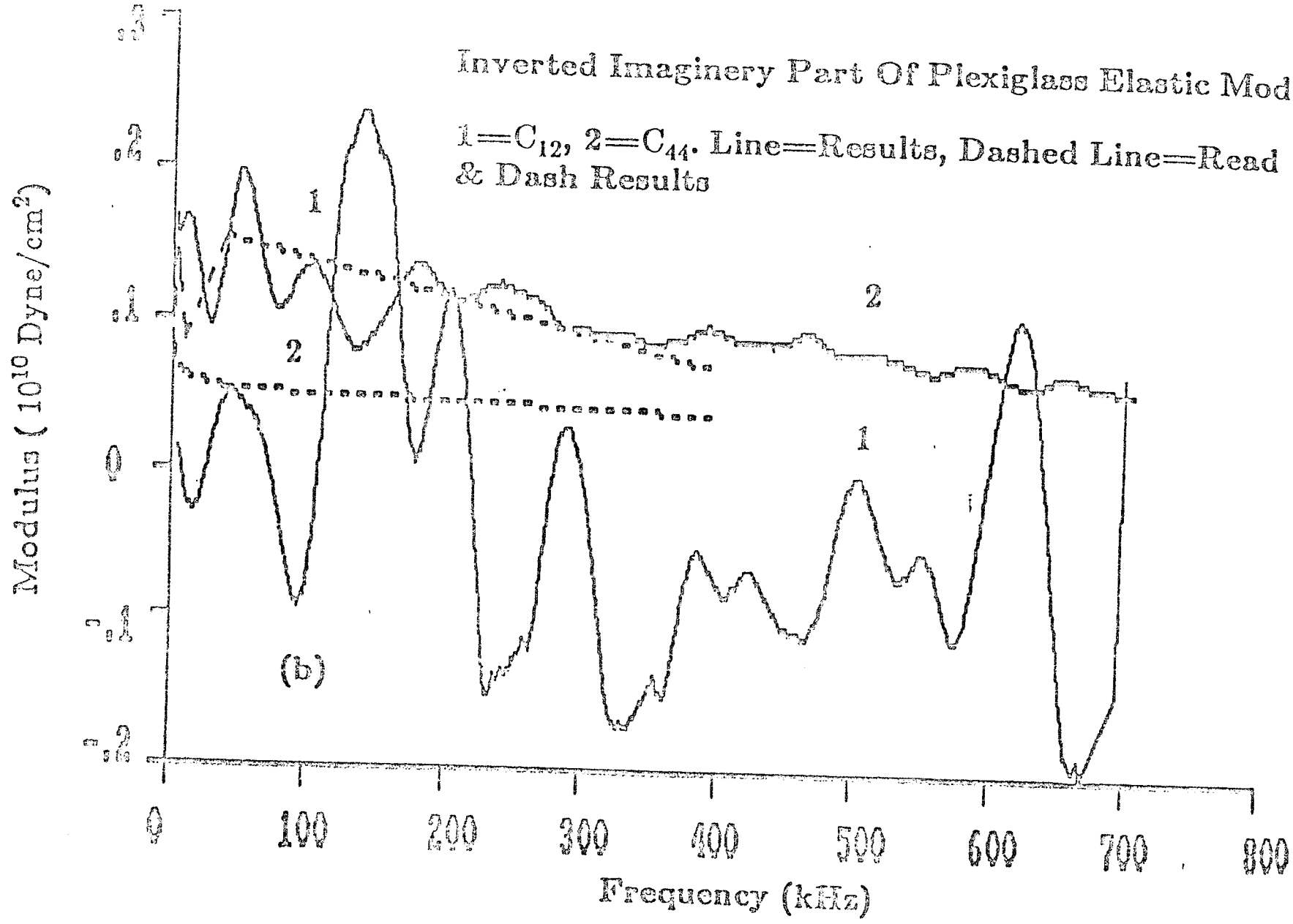

FIG. 13(b). Inverted imaginery part of plexiglass elastic moduli C_{12} (1) and C_{44} (2). Lines in the figure are results of this study, dashed lines are results of Dash and Read [41].

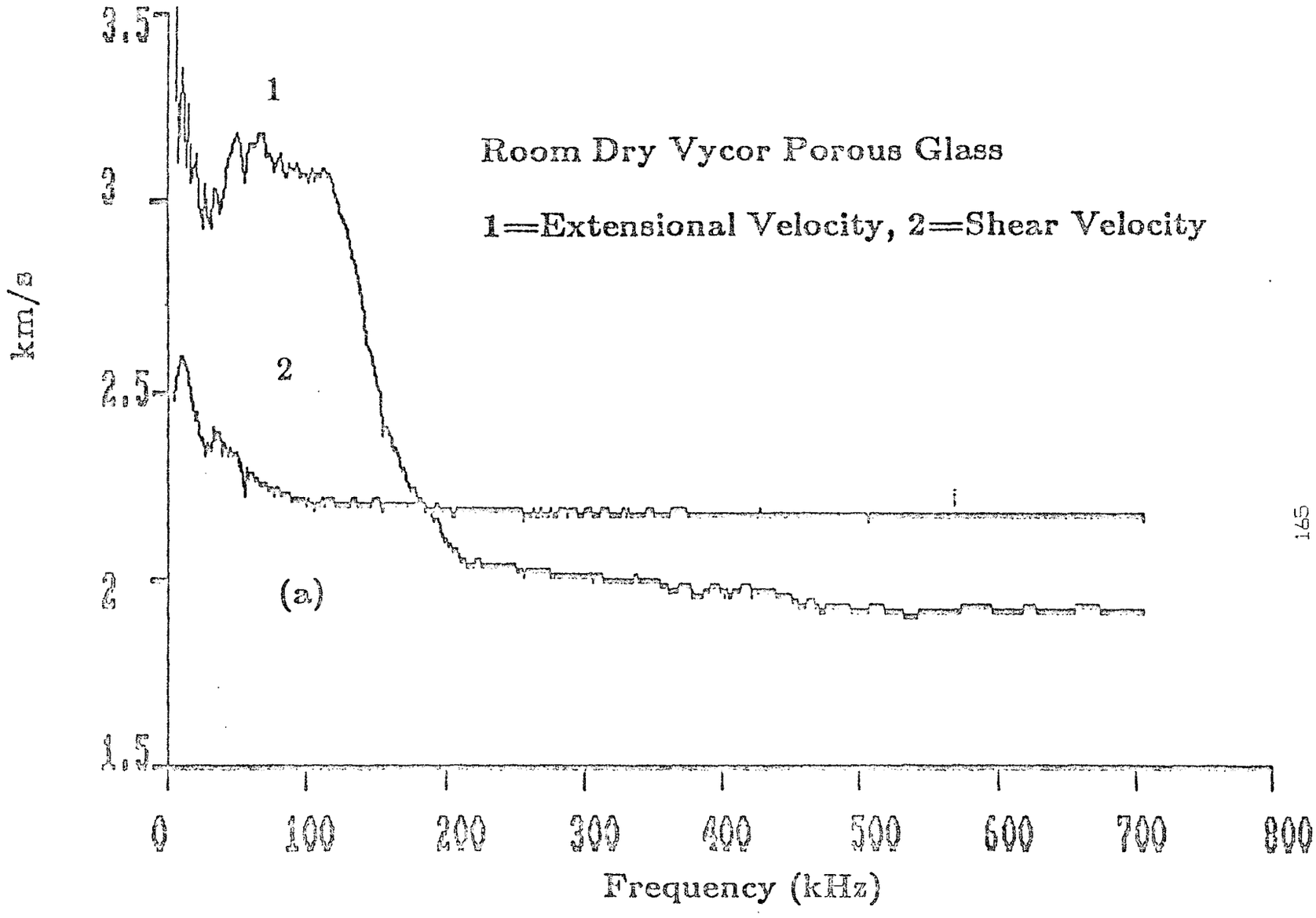

FIG. 14(a). Room dry vycor porous glass extensional (1) and shear (2) experimental results, phase velocity versus frequency.

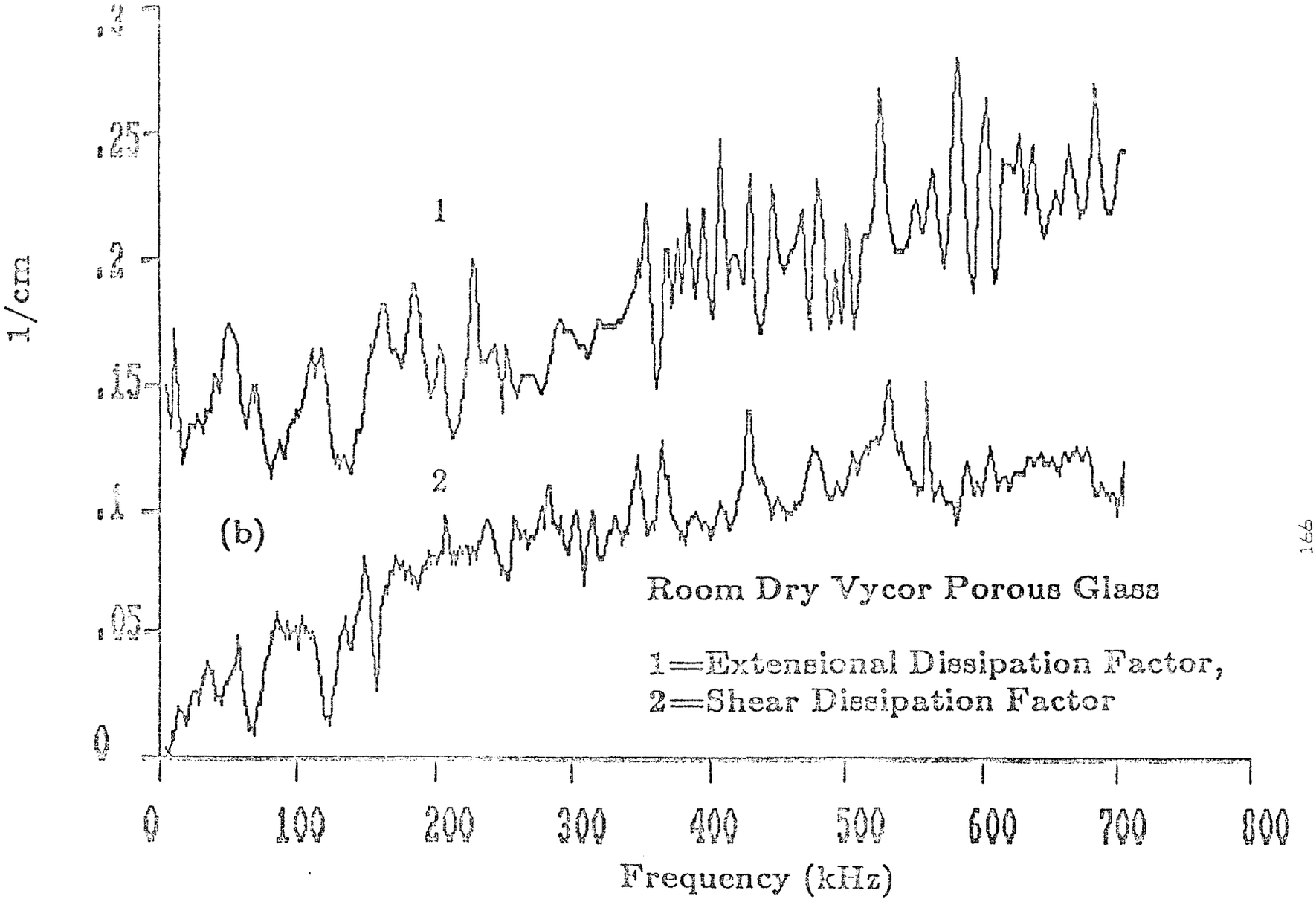

FIG. 14(b). Room dry vycor porous glass extensional (1) and shear (2) experimental results, dissipation factor versus frequency. The extensional results have an added 0.1 cm^{-1}.

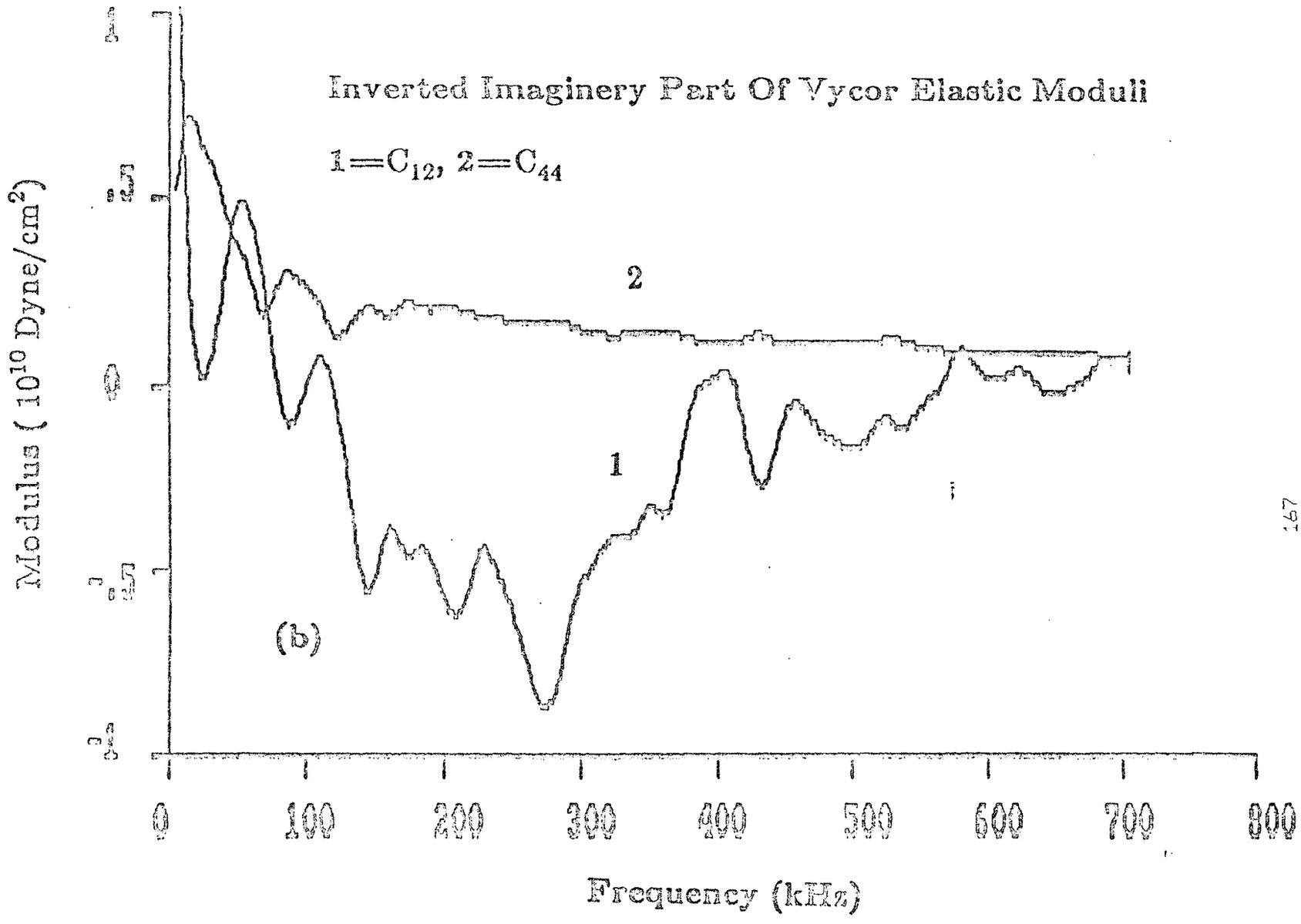

FIG. 15(b). Imaginery part of inverted vycor elastic moduli C_{12} (1) and C_{44} (2).

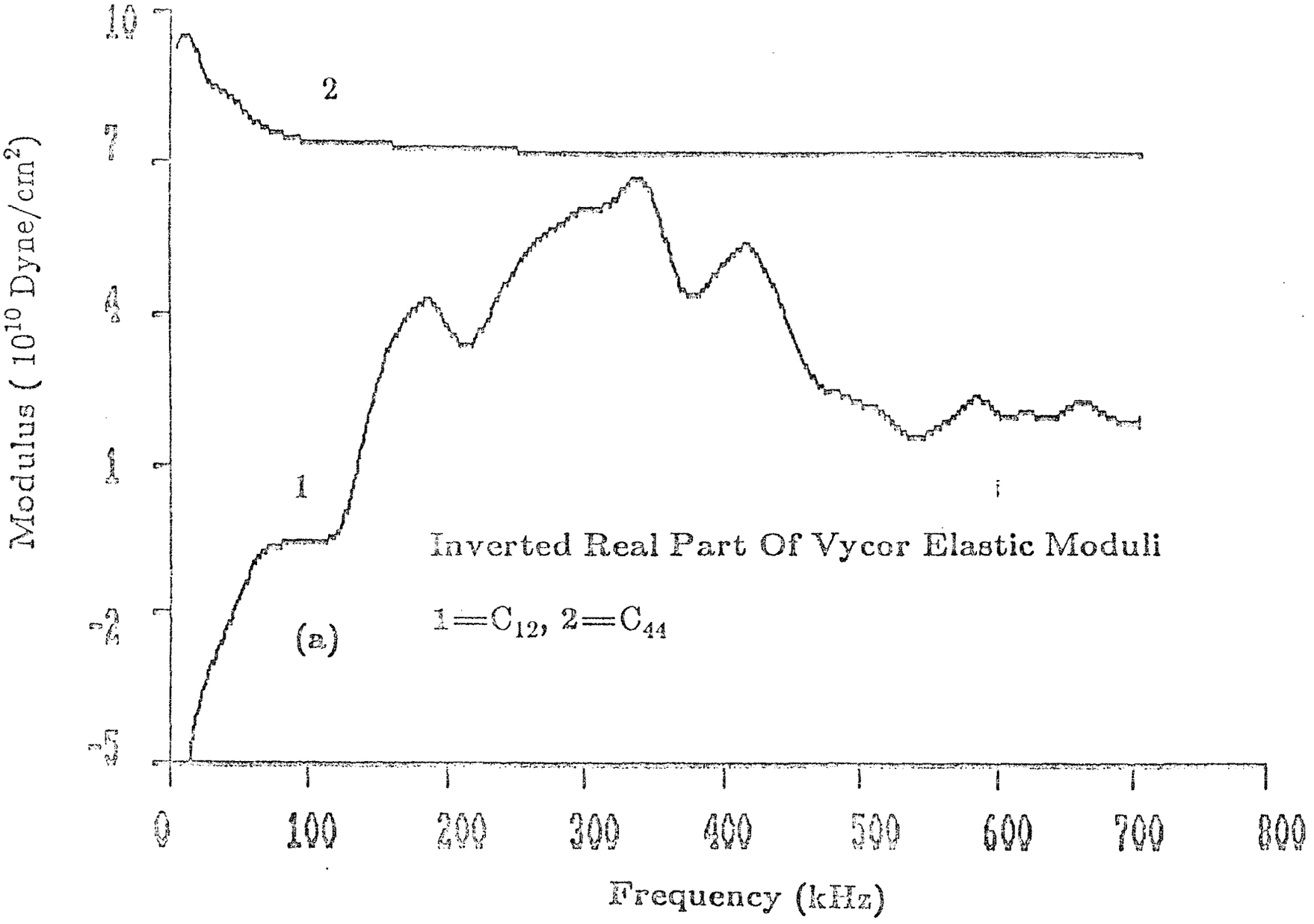

FIG. 15(a). Real part of inverted vycor elastic moduli C_{12} (1) and C_{44} (2).

Appendix A- Forward Program to Compute Extensional Dispersion

The program CDISPC.FOR is a FORTRAN 77 program to compute the velocity and attenuation of the extensional mode as a function of frequency for given complex elastic moduli C_{12} and C_{44}, density ρ, and cylinder radius a. The complex wavenumbers are computed using the complex Pochammer-Chree relations.

The present form of the program is written for frequency-independent complex elastic moduli (constant Q) although it may be enlargened to include any variety of frequency-dependent moduli. The program reads the moduli and the density and prints out the material compressional velocity , shear velocity, bar velocity, Poisson ratio, and Rayleigh wave velocities. It then asks for the frequency interval over which the dispersion relation should be evaluated and the frequency spacing within this interval. Final prompts are for the accuracy of the determination of the solution and for the filename to store the resolved velocity and dissipation factor. The program uses the method of Dubbleday [32] to determine the zeros of the dispersion relation in the complex plane. The method uses trial values of the desired wavenumbers (from which velocity and dissipation factor are computed) iteratively and moves in the complex wavenumber plane so as to box in the desired solution in a square box of dimension $2DB$ (parallel to the real axis) by $2DB$ (parallel to the imaginery axis), where DB is the size of the interval in wavenumber space for the particular iteration. The box is created by a pair of values $BT1$ and $BT2$, which have the same real part but whose imaginery part is displaced $-DB$ and $+DB$, respectively, from the trial solution. When the values of the dispersion relation for $BT1$ and $BT2$ are calculated, the sign of their difference indicates whether the real part of the solution lies at greater or smaller values than those of the trial solution. Once this is determined, a new trial solution is picked whose real part is more towards the desired solution by a factor of DB. $BT1$, $BT2$ and the value of the dispersion relations at them are recomputed and the process is repeated. The motion along the real axis ends when the sign of the

dispersion relation between $BT\,1$ and $BT\,2$ reverses sign. At this point the interim solution is set as the average of $BT\,1$ and $BT\,2$ and a vertical pair $BT\,3$ and $BT\,4$ are picked which have the same imaginery part but whose real part is displaced $-DB$ and $+DB$, respectively, from the interim value. This pair is used for motion parralel to the the imaginery axis in a fashion identical to that described for $BT\,1$ and $BT\,2$, the imaginery part of the trial value being changed by DB at each iteration. Depending upon the desired accuracy of the determination of the root, differing amounts of iterations must be made on the horizontal and vertical pairs at each frequency point, each iteration shrinking the size of the bounding box by a factor of ten.

To increase the rate of convergence, the program utilizes the low frequency assymptote of the extensional mode, the bar velocity, as the starting point for iteration at the lowest frequency point desired. The iterative process at higher frequencies begins by using as a trial value the result of the previous frequency point, the wavenumber at the new frequency ω_i being adjusted to the frequency shift from the previous frequency ω_{i-1} using the equation

$$\beta\,(\omega_i\,) = \beta(\omega_{i-1}\,) \cdot \frac{\omega_i}{\omega_{i-1}} \quad .$$

An important problem which the program overcomes is the fact that higher order solutions to the dispersion relation become possible at frequencies above $\beta a = 2.0$ (which is the cutoff frequency for the first higher order mode). These higher order modes propagate at a faster phase velocity, so the program uses the parameter JOE, which is determined by the Poisson's ratio of the material and the relative change of the propagational velocity between successive frequency points, to start the iterative process at slightly higher wavenumbers in this critical frequency region. Lack of this feature in early versions of the program made solutions oscillate between the various order solutions. It may be that these oscillations lead some investigators [14,16] to consider the existence of stop bands

(zero group velocity regions) in this frequency range. Of importance for convergence is also the usage of many orders in the series approximation of the Bessel functions, which influences the dispersion relation highly in a region where the functions are close to their zeros.

The program results are printed to a user defined program in an unformatted format, so that they may be read by BASIC language plotting programs, or by an unformatted read in FORTRAN. The configuration of the printing is as follows:

Line 1: HF, V_P, V_s

Line 2: FP

Lines 3 through (FP+2): F_i, V_i, β_i'' $\qquad i = 1,2,...FP$,

where HF is the maximum value of the frequency in kHz, V_P is the material compressional velocity, and V_s the material shear velocity, the latter two values given in km/s. FP is the number of frequency points. Lines 3 through (FP+2) each contain three values; the frequency point (in kHz), the extensional mode velocity at that point (in km/s), and the imaginery part of the wavenumber at that point (in $1/cm$). The imaginery part of the wavenumber appears with a negative sign before it since the absolute value of the (negative) imaginery part corresponds to the value of the (positive) attenuation.

The main program is followed by a Bessel function subroutine. This function is computed from a series expansion [33]. To increase the computation rate, the value of the factorials of numbers from one through fourty are included in the body of the program, which prevents having to compute them anew at each entry into the subroutine. If more than fourty terms of the series expansion of the Bessel function are needed, the value of more factorials must be included in the subroutine.

```
C       CDISPC.FOR- THE FORWARD PROGRAM
C       MAIN PROGRAM TO COMPUTE COMPLEX DISPERSION RELATION
C       FOR EXTENSIONAL WAVES IN A CYLINRICAL ROD
C       USING COMPLEX POCHAMMER-CHROE RELATIONS
C       THIS VERSION IS FOR INPUT COMPLEX ELASTIC CONSTANTS
C       AND COMPUTES IMAGINERY PART OF WAVENUMBER TOO.
C       USES ALGORITHM OF DUBBLEDAY, SIAM J. OF APPLIED MATH.
C       VOL 83 (5), 1127, 1983
C       VARIABLE DECLERATION SECTION BEGINS*****************
        INTEGER*4 N,M,I,SF,FP,FLAGL,FLAGS
        REAL*8 X,COMF,XMIN,XMAX,DX,CMIN,CMAX,CR,XX,C12R,C12I,C44R,C44I
        REAL*8 VF,VS,VE,F,W,KL,KS,A,XL,XS,CI
        REAL*8 PI,LF,HF,DF,JOE
        REAL*8 ANSM,ANSMO,DLTA,VY,KY,VSS,KSS,VR,CHS
        REAL*8 POI,RHO,SANSHO,SANSH,SANSVO,SANSV,SH,SV,DB,DLTAI
        COMPLEX*16 ZL,ZS,ZL0,ZL1,ZL2,ZS0,ZS1,ZS2
        COMPLEX*16 KTL,KTS,ANS,BTO,BTMAX,BTMINO,BTMIN
        COMPLEX*16 C11,C12,C44,KL2,KS2,R,BT
        COMPLEX*16 BT1,BT2,BT3,BT4,BTOO,BTMAXO
        COMPLEX*16 ANS1,ANS2,ANS3,ANS4
        CHARACTER*64 FNAME
        DIMENSION CR(500),XX(500),CI(500)
C       VARIABLE DECLARATION SECTION ENDS*******************
C       ************************************************
C       ******PARAMETERS USED ARE:
C       RHO=DENSITY OF MATERIAL (G/CM**3)
C       C12=LONG. COMPLEX MODULUS OF MATERIAL (DYNE/(CM**2))
C          (ALSO TERMED LAMBDA)
C       C44=SHEAR COMPLEX MODULUS OF MATERIAL (DYNE/(CM**2))
C          (ALSO TERMED MU)
C       VP=COMPRESSIONAL VELOCITY OF MATERIAL (CM/S)
C       VS=SHEAR VELOCITY OF MATERIAL (CM/S)
C       VY=BAR VELOCITY OF MATERIAL (CM/S)
C       VR=RAYLEIGH VELOCITY OF MATERIAL (CM/S)
C       POI=POISSON'S RATIO OF MATERIAL (DIMENSIONLESS)
C       R=(C12)/(C44) (DIMENSIONLESS)
C       VE=VELOCITY OF WAVE PROPAGATION IN MATERIAL (CM/S)
C       F=FREQ (CYCLES/S)
C       W=ANGULAR FREQUENCY =2*PI*F      (1/S)
C       K=WAVENUMBER (1/CM)
C       KL=LONGITUDINAL WAVENUMBER  =(W/VP)    (1/CM)
C       KS=SHEAR WAVENUMBER  =(W/VS)  (1/CM)
C       KY=BAR VELOCITY WAVENUMBER =(W/VY) (1/CM)
C       KL2=SQUARE OF COMPLEX TRANSVERSE COMPONENT OF LONG. WAVENUMBER
C       KS2=SQUARE OF COMPLEX TRANSVERSE COMONENT OF SHEAR WAVENUMBER
C       BT=Z COMPONENT OF PROPAGATIONAL WAVENUMBER  =(W/VE)  (1/CM)
C       KTL=TRANSVERSE COMPONENT OF LONG. WAVENUMBER
C          =SQRT(KL**2-BT**2)     (1/CM)
C       KTS=TRANSVERSE COMPONENT OF SHEAR WAVENUMBER
C          =SQRT(KS**2-BT**2)     (1/CM)
C       A=RADIUS OF CYLINDER (CM)
C       ZL=KTL*A (DIMENSIONLESS)
C       ZS=KTS*A (DIMENSIONLESS)
C       ZL0=J0(ZL) :ZL1=J1(ZL) : ZL2=J2(ZL)
```

```
C       ZS0=J0(ZS) :ZS1=J1(ZS) : ZS2=J2(ZS)
C       END OF PARAMETERS FOR PROGRAM ********************
        PI=3.141592654D0
        WRITE (*,250) ' PROGRAM TO CALCULATE VELOCITY AND ATTENUATION'
        WRITE (*,250) ' OF EXTENSIONAL WAVES IN A LOSSY CYLINDER'
        WRITE (*,250) ' COPYRIGHT STANFORD ROCK PHYSICS 1985,1986'
 250    FORMAT (10X,A)
C       READ IN VALUES OF COMPLEX ELASTIC CONSTANTS AND THE DENSITY
        WRITE (*,' (A\)') ' INPUT MTL. C12R,C12I (1.0D10 DYNE/(CM**2)) '
        READ (*,6) C12R,C12I
  6     FORMAT (D15.7,D15.7)
        C12R=C12R*1.0D10
        C12I=C12I*1.0D10
        C12=DCMPLX(C12R,C12I)
        WRITE (*,' (A\)') ' INPUT MTL. C44R,C44I (1.0D10 DYNE/(CM**2)) '
        READ (*,6) C44R,C44I
        C44R=C44R*1.0D10
        C44I=C44I*1.0D10
        C44=DCMPLX(C44R,C44I)
        C11=C12+2.0D0*C44
        WRITE (*,' (A\)') ' INPUT MTL. DENSITY (G/CM**3) '
        READ (*,4) RHO
  4     FORMAT (D15.7)
        VP=DSQRT(CDABS(C11/RHO))
        VS=DSQRT(CDABS(C44/RHO))
        WRITE (*,11) ' VP(KM/S)=',VP/1.0D05,'VS(KM/S)=',VS/1.0D05
 11     FORMAT (A,3X,D15.7,3X,A,3X,D15.7)
C       NEXT TWO (VY AND VSS) ARE USED TO LIMIT RANGE OF BT
        VY=DSQRT(VS**2*(3.0D0*VP**2-4.0D0*VS**2)/(VP**2-VS**2))
        VSS=VS
        R=C12/C44
        POI=0.5D0-0.5D0*(VS**2)/(VP**2-VS**2)
        WRITE (*,9) ' VY(KM/S)=',VY/1.0D05,'POI=',POI
  9     FORMAT (A,3X,D15.7,3X,A,3X,D12.5)
        VR=VS*((0.87D0+1.12D0*POI)/(1.0D0+POI))
        WRITE (*,15) ' VR=',VR/1.0D05
 15     FORMAT(A,3X,D15.7)
        WRITE (*,' (A\)') ' INPUT CYLINDER RADIUS (CM) '
        READ (*,8) A
        WRITE (*,' (A\)') ' INPUT FREQ. RANGE-IN HERTZ  (LF,HF) '
        READ (*,7) LF,HF
  7     FORMAT (D15.7,D15.7)
        WRITE (*,' (A\)') ' INPUT FREQ. SPACING-IN HERTZ  (DF) '
        READ (*,8) DF
  8     FORMAT (D15.7)
        CHS=1.0D-05
        WRITE (*,' (A\)') ' INPUT ACCURACY (DEFAULT=1.0D-05) '
        READ (*,8) CHS
        WRITE (*,' (A\)') ' INPUT FILENAME TO STORE DATA '
        READ (*,' (A\)')  FNAME
C       ******************PARAMETER READING COMPLETED
        CMIN=1.0D13
        CMAX=-1.0D-13
        FP=IDINT((HF-LF)/DF)
```

```
      FP=FP+1
C     FREQUENCY LOOP
      DO 10 I=1,FP
      F=LF+DF*(I-1)
      W=2.0D0*PI*F
C     CALL BESSEL(N,X,M,COMP)
      KL=(2.0D0*PI*F)/VP
      KS=(2.0D0*PI*F)/VS
      KY=(2.0D0*PI*F)/VY
      KSS=(2.0D0*PI*F)/VSS
      KL2=DCMPLX(RHO*W**2,0.0D0)/C11
      KS2=DCMPLX(RHO*W**2,0.0D0)/C44
      WRITE (*,64) '  F(Hz)=',F,'KLA=',KL*A,'KSA=',KS*A
 64   FORMAT (A,3X,D15.7,3X,A,3X,D15.7,3X,A,3X,D15.7)
C     NOW RUN BETTA LOOP
      ANSM=1.0D+13
      ANSM0=1.0D+13
      BT0=DCMPLX(0.99D0*KY,0.0)
      BTMAX=DCMPLX(0.99D0*KSS,0.)
      IF (I.GT.1) BT0=BT00*W
      IF (I.GT.1) BTMAX=BTMAX0*W
      BTMIN0=BTMAX
 35   DB=REAL(BTMAX-BT0)/100.D0
      IF (KS*A.GT.2.0D0) DB=DB/1.5D0
      IF (KS*A.GT.4.0D0) DB=DB/2.0D0
      IF (KS*A.GT.6.0D0) DB=DB/1.5D0
C     BEGINNING OF LOOPS ON BETA
C     FIRST COMES HORIZONTAL PAIR BT1 AND BT2
      J=1
      BT=BT0
C     BEGINNING OF HORIZONTAL LOOPS FOR J>1 OR HIGHER ITERATIONS
 36   CONTINUE
      BT1=BT-DCMPLX(0.0D0,DB)
      KTL=CSQRT(KL2-BT1**2)
      KTS=CSQRT(KS2-BT1**2)
      ZL=KTL*A
      ZS=KTS*A
         CALL BESSEL (0,ZL,30,ZL0)
         CALL BESSEL (1,ZL,30,ZL1)
         CALL BESSEL (2,ZL,30,ZL2)
         CALL BESSEL (0,ZS,30,ZS0)
         CALL BESSEL (1,ZS,30,ZS1)
         CALL BESSEL (2,ZS,30,ZS2)
C     NOW CALCULATE THE DISPERSION FUNCTION FOR BT1
      ANS1=(KS2-2.0D0*BT1**2)*ZS1*R*(KL2)*ZL0
      ANS1=ANS1-(KS2-2.0D0*BT1**2)*ZS1*(KL2-BT1**2)*(ZL2-ZL0)
      ANS1=ANS1-(2.0D0*BT1**2)*KTL*KTS*ZL1*(ZS2-ZS0)
C     WRITE (*,65) '  F=',F,'BT1=',REAL(BT1),AIMAG(BT1),'ANS1='
C    1  ,REAL(ANS1),AIMAG(ANS1)
C 65  FORMAT (A,2X,D15.7,2X,A,2X,D15.7,2X,D15.7,2X,A,2X,D15.7,2X
C    1  ,D15.7)
C     NOW DO THE SAME FOR BT2
      BT2=BT+DCMPLX(0.0D0,DB)
      KTL=CSQRT(KL2-BT2**2)
```

```
      KTS=CSQRT(KS2-BT2**2)
      ZL=KTL*A
      ZS=KTS*A
         CALL BESSEL (0,ZL,30,ZL0)
         CALL BESSEL (1,ZL,30,ZL1)
         CALL BESSEL (2,ZL,30,ZL2)
         CALL BESSEL (0,ZS,30,ZS0)
         CALL BESSEL (1,ZS,30,ZS1)
         CALL BESSEL (2,ZS,30,ZS2)
C     NOW CALCULATE THE DISPERSION FUNCTION FOR BT2
      ANS2=(KS2-2.0D0*BT2**2)*ZS1*R*(KL2)*ZL0
      ANS2=ANS2-(KS2-2.0D0*BT2**2)*ZS1*(KL2-BT2**2)*(ZL2-ZL0)
      ANS2=ANS2-(2.0D0*BT2**2)*KTL*KTS*ZL1*(ZS2-ZS0)
C     WRITE (*,65) '  F=',F,'BT2=',REAL(BT2),AIMAG(BT2),'ANS2='
C    1  ,REAL(ANS2),AIMAG(ANS2)
C     NOW WE OBTAIN HORIZONTAL SIGN
      SH=AIMAG(ANS1)*REAL(ANS2)-AIMAG(ANS2)*REAL(ANS1)
      SANSH=DSIGN(1.0D0,SH)
      IF (J.EQ.1) SANSH0=SANSH
      IF (SANSH.NE.SANSH0) THEN
C          WE HAVE FOUND OUR ROOT-SIGN HAS REVERSED
C          WE SET PARAMETERS AND GOTO VERTICAL PART
             GOTO 37
      ENDIF
C     NOW WE MAKE NEW HORIZONTAL PAIR (SIGN HAS NOT REVERSED)
C     FIXING THE DIRECTION OF MOTION BY THE SIGN SANSH
      BT=BT+SANSH*DCMPLX(DB,0.0D0)
      J=J+1
      GOTO 36
C     ****************************************************************
C     NOW COME VERTICAL PAIR BT3 AND BT4
 37   J=1
      BT=(BT1+BT2)/2.0D0
C     BEGINNING OF VERTICAL LOOPS FOR J>1 OR HIGHER ITERATIONS
 38   CONTINUE
      BT3=BT-DCMPLX(DB,0.0D0)
      KTL=CSQRT(KL2-BT3**2)
      KTS=CSQRT(KS2-BT3**2)
      ZL=KTL*A
      ZS=KTS*A
         CALL BESSEL (0,ZL,30,ZL0)
         CALL BESSEL (1,ZL,30,ZL1)
         CALL BESSEL (2,ZL,30,ZL2)
         CALL BESSEL (0,ZS,30,ZS0)
         CALL BESSEL (1,ZS,30,ZS1)
         CALL BESSEL (2,ZS,30,ZS2)
C     NOW CALCULATE THE DISPERSION FUNCTION FOR BT3
      ANS3=(KS2-2.0D0*BT3**2)*ZS1*R*(KL2)*ZL0
      ANS3=ANS3-(KS2-2.0D0*BT3**2)*ZS1*(KL2-BT3**2)*(ZL2-ZL0)
      ANS3=ANS3-(2.0D0*BT3**2)*KTL*KTS*ZL1*(ZS2-ZS0)
C     WRITE (*,65) '  F=',F,'BT3=',REAL(BT3),AIMAG(BT3),'ANS3='
C    1  ,REAL(ANS3),AIMAG(ANS3)
C     NOW DO THE SAME FOR BT4
      BT4=BT+DCMPLX(DB,0.0D0)
```

```
      KTL=CSQRT(KL2-BT4**2)
      KTS=CSQRT(KS2-BT4**2)
      ZL=KTL*A
      ZS=KTS*A
         CALL BESSEL (0,ZL,30,ZL0)
         CALL BESSEL (1,ZL,30,ZL1)
         CALL BESSEL (2,ZL,30,ZL2)
         CALL BESSEL (0,ZS,30,ZS0)
         CALL BESSEL (1,ZS,30,ZS1)
         CALL BESSEL (2,ZS,30,ZS2)
C        NOW CALCULATE THE DISPERSION FUNCTION FOR BT4
      ANS4=(KS2-2.0D0*BT4**2)*ZS1*R*(KL2)*ZL0
      ANS4=ANS4-(KS2-2.0D0*BT4**2)*ZS1*(KL2-BT4**2)*(ZL2-ZL0)
      ANS4=ANS4-(2.0D0*BT4**2)*KTL*KTS*ZL1*(ZS2-ZS0)
C        WRITE (*,65) '  F=',F,'BT4=',REAL(BT4),AIMAG(BT4),'ANS4='
C     1  ,REAL(ANS4),AIMAG(ANS4)
C        NOW WE OBTAIN VERTICAL SIGN
      SV=AIMAG(ANS3)*REAL(ANS4)-AIMAG(ANS4)*REAL(ANS3)
      SANSV=DSIGN(1.0D0,SV)
      IF (J.EQ.1) SANSV0=SANSV
      IF (SANSV.NE.SANSV0) THEN
C          WE HAVE FOUND VERTICAL ROOT-SIGN HAS REVERSED
C          WE EITHER GOTO HORIZONTAL FOR NEW ITERATION
C          OR WE TERMINATE
           ANS=(ANS3+ANS4)/2.0D0
           BT=(BT3+BT4)/2.0D0
           BTMIN=BT
           WRITE (*,84) ' BTMIN=',REAL(BTMIN),AIMAG(BTMIN)
 84     FORMAT(A,2X,D15.7,2X,D15.7)
           DLTA=CDABS((BTMIN-BTMIN0)/BTMIN0)
           DLTAI=DABS(AIMAG(BTMIN-BTMIN0)/(AIMAG(BTMIN0)+1.0D-32))
        IF (DABS(AIMAG(BTMIN)/REAL(BTMIN)).LT.1.0D-10) DLTAI=CHS
                     IF (DLTA.GT.CHS.OR.DLTAI.GT.CHS) THEN
                       BTMIN0=BTMIN
C        CONDITION FOR IMAG(BT)>0
              IF (AIMAG(BT).GT.0.0D0)  BT=DCMPLX(REAL(BT),0.0D0)
                       DB=DB/10.D0
                       J=1
                       GOTO 36
                       ELSE
                        XX(I)=F/(1.0D03)
                        CR(I)=(2.0D0*PI*F)/REAL(BTMIN*1.0D05)
                        CI(I)=AIMAG(BTMIN)
         WRITE (*,85) ' BTMIN=',REAL(BTMIN),AIMAG(BTMIN),'VE=',CR(I)
     1    ,'ANS=',REAL(ANS),AIMAG(ANS)
 85      FORMAT (A,2X,D15.7,2X,D15.7,2X,A,2X,D15.7,2X,A,2X,D15.7,2X
     1    ,D15.7)
                          BT00=BTMIN*1.00D0/W
C        JOE= CONDITION TO MAKE PROGRAM LOOK FOR HIGHEST BETTA SOLUTION
C        SO AS TO AVOID HIGHER MODE SOLUTIONS
                JOE=ABS(REAL(BT0-BTMIN)/REAL(BTMIN))*8.5D01
          IF (I.GT.1) JOE=ABS((CR(I)-CR(I-1))/CR(I-1))*2.8D0/(PDI**4/3)
                IF (KS*A.GT.6.0D0) JOE=1.0D0
              IF (JOE.GT.1.01D0) BT00=BT00*1.10D0
```

```
                              BTMAX0=BTMIN*1.20D0/W
                              GOTO 10
                            ENDIF
          ENDIF
C         NOW WE MAKE NEW VERTICAL PAIR (SIGN HAS NOT REVERSED)
C         FIXING THE DIRECTION OF MOTION BY THE SIGN SANSV
          BT=BT-SANSV*DCMPLX(0.0D0,DB)
          J=J+1
          GOTO 38
 10       CONTINUE
C         STOP
C         RESULTS PRINTING SECTION BEGINS*****************
          OPEN(8,FILE=FNAME,STATUS='NEW',ACCESS='SEQUENTIAL')
C         FREQUENCY-IN kHz,CR(I)-IN km/s,CI(I)-IN 1/cm
C         SIGN OF CI(I) IS REVERSED TO MAKE IT NEGATIVE
          WRITE (8,*) HF/(1.0D03),VP/1.0D05,VS/1.0D05
          WRITE (8,*) FP
          DO 20 I=1,FP
          WRITE (8,*) REAL(XX(I)),REAL(CR(I)),-1.0*REAL(CI(I))
 20       CONTINUE
          CLOSE (8)
          END
C         ***********************************************
C         ***********************************************
C         ***********************************************
          SUBROUTINE BESSEL (N,Z,M,COMPZ)
C         N=ORDER OF BESSEL FUNCTION OF FIRST KIND (Jn(Z))
C         Z=COMPLEX ARGUMENT
C         M=AMOUNT OF TERMS TO TAKE IN SERIES EXPANSION
C         COMPZ=COMPLEX ANSWER-OUTPUT OF THE SUBROUTINE
C         VARIABLE DECLARATION SECTION BEGINS HERE
          INTEGER*4 N,M,I,J,K
          REAL*8 X,JF,JNF,Y,FA(40)
          COMPLEX*16 Z,COMPZ
C         NEXT LINES ARE FACTORIALS OF 1 TO 40
          DATA FA/1.,2.,6.,24.,120.,720.,5040.,40320.
     1    ,362880.,3628800.,39916800.,4.790016D+08,6.227021D+09
     1    ,8.71783D+10,1.30767D+12,2.09227D+13,3.5568D+14,6.40237D+15
     1    ,1.2164D+17,2.4329D+18,5.10909D+19,1.124D+21,2.585D+22
     1    ,6.2044D+23,1.55112D+25,4.0329D+26,1.0888D+28,3.04888D+29
     1    ,8.8417D+30,2.6525D+32,8.2228D+33,2.6313D+35,8.6833D+36
     1    ,2.9523D+38,1.0333D+40,3.7199D+41,1.3763D+43
     1    ,5.2302D+44,2.0398D+46,8.1591D+47/
          COMPZ=(0.0D0,0.0D0)
          DO 10 I=1,M
          J=I-1
C         HAVE TO COMPUTE FACTORIALS HERE
C         COMPUTING J FACTORIAL
          JF=1.0D0
          IF (J.EQ.0) GOTO 25
          JF=FA(J)
C         NOW COMPUTING (N+J) FACTORIAL
 25       JNF=1.0D0
          IF ((N+J).EQ.0) GOTO 30
```

```
      JNF=FA((N+J))
C     END OF FACTORIAL COMPUTATION
 30   IF (J.EQ.0) THEN
                COMPZ=COMPZ+DCMPLX((1.0D0)/(JF*JNF))
                GOTO 31
                ENDIF
      COMPZ=COMPZ+DCMPLX(((-1.0D0)**J)/(JF*JNF))*(Z/2.0D0)**(2*J)
 31   CONTINUE
 10   CONTINUE
      IF (N.EQ.0) GOTO 18
      COMPZ=COMPZ*(Z/2.0D0)**N
 18   CONTINUE
C     X=REAL(COMPZ)
C     Y=AIMAG(COMPZ)
C     WRITE (*,19) REAL(Z),AIMAG(Z),X,Y
C 19  FORMAT (3X,D15.7,3X,D15.7,3X,D15.7,3X,D15.7)
      RETURN
      END
C     ************************************************
C     ************************************************
C     ************************************************
```

Appendix B- Inverse Program to Compute Elastic Moduli

The program DISPI.FOR is a FORTRAN 77 program to compute the frequency-dependent elastic moduli C_{44} and C_{12} from the experimentaly determined dependence of the torsional shear and extensional (velocity and attenuation) results on frequency. The material density and the cylinder radius must also be provided.

The program requests the names of the files containing the torsional and the extensional results. It is important that both files contain results taken at the same frequencies. The format of these files is identical to the output files of CDISPC.FOR, the forward program discussed in Appendix A. The program will then request the material density and the cylinder radius. The program then requests names for the C_{12} versus frequency and the C_{44} versus frequency files, which are the final output of the program. Finally, the user may chose to have centroid smoothing for a selected number of cycles, which is important for noisy data, and the user selects the accuracy of the inversion. In practice 15 smoothing cycles and an accuracy of 10^{-2} gives non-oscillatory results with fast convergence (1 minute per frequency point) even for very noisy data.

The program initially reads the torsional data file and computes the complex C_{44}. Optional smoothing of the shear modulus follows, the shear results being later sent to the selected file. The arrangement of the printed shear results is as follows;

Line 1: FF(N), REAL(MX4), REAL(MN4)

Line 2: N

Lines 3 through (N+2): F_i , Real (C_{44i}), Imag (C_{44i}) $\qquad i = 1,2,.....N$,

where FF(N) is the maximum frequency in kHz, and REAL(MX4) and REAL(MN4) are the maximum and minimum values, respectively, of the real part of the shear modulus in units of $1.0 \cdot 10^{10}\ Dyne/cm^2$. N is the number of frequency points. In lines 3 through (N+2) there are each three values; the frequency in kHz, the real part of the shear modulus, and the imaginary part of the shear modulus at that frequency, the latter two in

units of $1.0 \cdot 10^{10}\ Dyne/cm^2$.

The program then reads the extensional file, changes the velocity and attenuation values at each frequency to a complex wavenumber, and then (optionaly) smooths these results. The first step in the actual inversion of the extensional results is a calculation of the complex Young's modulus, which is used as the starting point for the iteration process at the lowest frequency value. Following this step the iteration process begins for the lowest frequency point. The iterative process uses two pairs of trial values, C_{121} and C_{122} being the horizontal pair, and C_{123} and C_{124} being the vertical pair. The horizontal pair has an imaginary part displaced $-DC$ and $+DC$ from the trial value, where DC is the iteration interval size in the elastic modulus plane. The horizontal pair are used to move parallel to the real C_{12} axis. The vertical pair have a real part displaced $-DC$ and $-DC$ from the trial value and are used to move parrelel to the imaginary C_{12} axis. More complete details of the iteration process may be found in Appendix A, the mechanism of the iterative determination of the zeros of the dispersion elation being entirely analogous for the forward problem as for the inverse.

After C_{12} has been determined to the desired accuracy at all the frequency points, an optional smoothing may be applied to the data. The last step of the program is the printing to the desired data file of the C_{12} results. The printing format is identical to that used for the shear modulus.

```
C       DISPI.FOR -THE INVERSION PROGRAM
C       MAIN PROGRAM TO COMPUTE COMPLEX ELASTIC MODULI
C       FROM DISPERSION RELATIONS FOR TORSIONAL AND
C       FOR EXTENSIONAL WAVES IN A CYLINDRICAL ROD
C       USING COMPLEX POCHAMMER-CHROE RELATIONS.
C       USES ALGORITHIM OF DUBBLEDAY, SIAM J. OF APPLIED MATH.
C       VOL 83 (5), 1127, 1983
C       VARIABLE DECLARATION SECTION BEGINS*****************
        INTEGER*4 N,M,I,SP,FP,FLAGL,FLAGS,MM
        REAL*4 MAXX,MAXY,MINY,U1,U2,FF
        REAL*8 X,COMP,XMIN,XMAX,DX,CMIN,CMAX,C12R,C12I,C44R,C44I
        REAL*8 VP,VS,VE,F,W,KL,KS,A,XL,XS
        REAL*8 PI,LF,HF,DF,JOE,XY,W1,W2,W3
        REAL*8 ANSM,ANSMO,DLTA,VY,KY,VSS,KSS,VR,AA,BB
        REAL*8 POI,RHO,SANSHO,SANSH,SANSVO,SANSV,SH,SV,DC,DLTAI,DLT
        COMPLEX*8 C44,BT,C12,XC,XYC,XXC,MX2,MN2,MX4,MN4
        COMPLEX*16 ZL,ZS,ZL0,ZL1,ZL2,ZS0,ZS1,ZS2
        COMPLEX*16 KTL,KTS,ANS,C120,C12MAX,C12MIN0
        COMPLEX*16 C12MN,C12MX0,E,EE
        COMPLEX*16 C11,KL2,KS2,R
        COMPLEX*16 C121,C122,C123,C124,C1200
        COMPLEX*16 ANS1,ANS2,ANS3,ANS4
        CHARACTER*64 FNAME,FNC441,FNC442,FNBT,FNAMES,OPT
$LARGE  U1,U2,FF,C44,BT,C12
        DIMENSION U1(2810),U2(2810),FF(2810)
        DIMENSION C44(2810),BT(2810),C12(2810)
C       VARIABLE DECLARATION SECTION ENDS*******************
C       ************************************************
C       ******PARAMETERS USED ARE:
C       RHO=DENSITY OF MATERIAL (G/CM**3)
C       C12=LONG. COMPLEX MODULUS OF MATERIAL (DYNE/(CM**2))
C          (ALSO TERMED LAMBDA)
C       C44=SHEAR COMPLEX MODULUS OF MATERIAL (DYNE/(CM**2))
C          (ALSO TERMED MU)
C       VP=COMPRESSIONAL VELOCITY OF MATERIAL (CM/S)
C       VS=SHEAR VELOCITY OF MATERIAL (CM/S)
C       VY=BAR VELOCITY OF MATERIAL (CM/S)
C       VR=RAYLEIGH VELOCITY OF MATERIAL (CM/S)
C       POI=POISSON'S RATIO OF MATERIAL (DIMENSIONLESS)
C       R=(C12)/(C44) (DIMENSIONLESS)
C       VE=VELOCITY OF WAVE PROPAGATION IN MATERIAL (CM/S)
C       F=FREQ (CYCLES/S)
C       W=ANGULAR FREQUENCY =2*PI*F  -- (1/S)
C       K=WAVENUMBER (1/CM)
C       KL=LONGITUDINAL WAVENUMBER  =(W/VP)    (1/CM)
C       KS=SHEAR WAVENUMBER  =(W/VS)  (1/CM)
C       KY=BAR VELOCITY WAVENUMBER =(W/VY) (1/CM)
C       KL2=SQUARE OF COMPLEX TRANSVERSE COMPONENT OF LONG. WAVENUMBER
C       KS2=SQUARE OF COMPLEX TRANSVERSE COMONENT OF SHEAR WAVENUMBER
C       BT=Z COMPONENT OF PROPAGATIONAL WAVENUMBER  =(W/VE)  (1/CM)
C       KTL=TRANSVERSE COMPONENT OF LONG. WAVENUMBER
C          =SQRT(KL**2-BT**2)     (1/CM)
C       KTS=TRANSVERSE COMPONENT OF SHEAR WAVENUMBER
C          =SQRT(KS**2-BT**2)     (1/CM)
```

```
C       A=RADIUS OF CYLINDER (CM)
C       ZL=KTL*A (DIMENSIONLESS)
C       ZS=KTS*A (DIMENSIONLESS)
C       ZL0=J0(ZL) :ZL1=J1(ZL) : ZL2=J2(ZL)
C       ZS0=J0(ZS) :ZS1=J1(ZS) : ZS2=J2(ZS)
C       END OF PARAMETERS FOR PROGRAM ********************
        PI=3.141592654D0
        WRITE (*,102) ' PROGRAM TO INVERT TORSIONAL AND EXTENSIONAL'
        WRITE (*,102) '  VELOCITY AND ATTENUATION FOR COMPLEX C44,C12'
        WRITE (*,102) ' COPYRIGHT STANFORD ROCK PHYSICS 1986'
  102   FORMAT (10X,A)
C       ************************************************
C       READ IN ALL PROGRAM INPUTS
        WRITE (*,' (A\)') ' INPUT  TORS. SHEAR FILENAME '
        READ (*,101) FNC441
  101   FORMAT (A)
        WRITE (*,' (A\)') ' INPUT EXTENSIONAL FILENAME? '
        READ (*,101) FNBT
        WRITE (*,' (A\)') ' INPUT MTL. DENSITY (G/CM**3) '
        READ (*,4) RHO
  4     FORMAT (D15.7)
        WRITE (*,' (A\)') ' INPUT CYLINDER RADIUS (CM) '
        READ (*,8) A
  8     FORMAT (D15.7)
        WRITE (*,' (A\)') ' INPUT FILENAME TO STORE C44 '
        READ (*,187) FNAMES
        WRITE (*,' (A\)') ' INPUT FILENAME TO STORE C12  '
        READ (*,187) FNAME
  187   FORMAT (A)
        WRITE (*,' (A\)') ' DO YOU WANT SMOOTHING (Y/N) '
        READ (*,187) OPT
        IF (OPT.EQ.'N'.OR.OPT.EQ.'n') GOTO 191
        WRITE (*,' (A\)') ' NUMBER OF SMOOTHING CYCLES '
        READ (*,189) MM
  189   FORMAT (I4)
  191   DLT=1.0D-04
        WRITE (*,' (A\)') ' INVERSION ACCURACY (DEFAULT=1.0D-04)? '
        READ (*,4) DLT
C       ************************************************
C       SUB-PROGRAM TO COMPUTE C44 FROM TORSIONAL SHEAR RESULTS
C       TORSIONAL SHEAR MODE IS GEOMETRICALLY NON-DISPERSIVE
C       FIRST READING IN DATA FILES
        OPEN (7,FILE=FNC441,STATUS='OLD',ACCESS='SEQUENTIAL')
        REWIND 7
        READ (7,*) MAXX,MAXY,MINY
        READ (7,*) N
        DO 99 I=1,N
        READ (7,*) FF(I),U1(I),U2(I)
C       ASSUMPTION MADE IS THAT U2(I)>=0
        FF(I)=FF(I)*1.0E03
  99    U1(I)=U1(I)*1.0E05
        CLOSE (7)
        WRITE (*,*) ' READ TORSIONAL SHEAR FILE'
C       ******
```

```
C       NOW MAKING C44 CALCULATIONS
        MX4=DCMPLX(-1.0D13,0.0D0)
        MN4=DCMPLX(1.0D13,0.0D0)
        DO 201 I=1,N
        W=2.0D0*PI*FF(I)
C       ADD DAMPER TO U2(I) TO PREVENT DIVISION BY ZERO
        U2(I)=U2(I)+1.0E-10
        AA=1.0D0/(RHO*W**2)
        BB=AA
        AA=AA*((W/U1(I))**2-U2(I)**2)
        BB=BB*(2.0D0*(W/U1(I))*U2(I))
        C44I=1.0D0/(BB*((AA/BB)**2+1.0D0))
        C44R=C44I*(AA/BB)
        C44(I)=DCMPLX(C44R,C44I)
        IF (REAL(C44(I)).GT.REAL(MX4)) MX4=C44(I)
        IF (REAL(C44(I)).LT.REAL(MN4)) MN4=C44(I)
C       WRITE (*,202) ' FREQ=',FF(I),'C44R=',C44R,'C44I=',C44I
C 202   FORMAT (A,2X,E15.7,2X,A,2X,D15.7,2X,A,2X,D15.7)
 201    CONTINUE
C       OPTIONAL THREE POINT SMOOTHING OF C44 FOLLOWS
        IF (OPT.EQ.'N'.OR.OPT.EQ.'n') GOTO 212
        DO 211 J=1,MM
        XC=C44(1)
        DO 209 I=2,(N-1)
        XYC=C44(I)
        C44(I)=(0.25D0*XC+0.5*XYC+0.25D0*C44(I+1))
 209    XC=XYC
 211    CONTINUE
C       PRINTING SHEAR RESULTS
 212    OPEN(8,FILE=FNAMES,STATUS='NEW',ACCESS='SEQUENTIAL')
C       FREQUENCY=kHz, MODULI=(1.0D10 DYNE/(CM**2))=1.GPa
        WRITE (8,*) FF(N)/1.0E03,REAL(MX4)/1.0E10,REAL(MN4)/1.E10
        WRITE (8,*) N
        DO 21 I=1,N
        WRITE (8,*) FF(I)/1.E03,REAL(C44(I))/1.E10,AIMAG(C44(I))/1.E10
 21     CONTINUE
        CLOSE (8)
        WRITE (*,*) ' FINISHED C44 DETERMINATION'
C       END OF C44 DETERMINATION************************
C       READ IN EXPERIMENTAL EXTENSIONAL WAVENUMBER FILE************
        OPEN (7,FILE=FNBT,STATUS='OLD',ACCESS='SEQUENTIAL')
        REWIND 7
        READ (7,*) MAXX,MAXY,MINY
        READ (7,*) N
        DO 299 I=1,N
C       ASSUMPTION MADE IS THAT ALPHA=XY>=0
        READ (7,*) FF(I),X,XY
        W=2.0D0*PI*FF(I)*1.0D03
        X=X*1.0D05
        XY=-1.0D0*XY
 299    BT(I)=DCMPLX((W/X),XY)
        CLOSE (7)
C       DO 225 I=1,N
C       WRITE (*,226) ' BT(I)=', REAL(BT(I)),AIMAG(BT(I))
```

```
C  226  FORMAT (A,3X,D15.7,3X,D15.7)
C  225  CONTINUE
C       OPTIONAL THREE POINT WEIGHTED SMOOTHING OF EXTENSIONAL DATA
C       XC=KEEPS X(I-1), XYC=KEEPS X(I)
        IF (OPT.EQ.'N'.OR.OPT.EQ.'n') GOTO 235
        DO 228 J=1,MM
        XC=BT(1)
        DO 227 I=2,(N-1)
        XYC=BT(I)
        W1=0.25D0*FF(I-1)
        W2=0.5D0*FF(I)
        W3=0.25D0*FF(I+1)
        BT(I)=(W1*XC+W2*XYC+W3*BT(I+1))/(W1+W2+W3)
 227    XC=XYC
 228    CONTINUE
 235    WRITE (*,*) ' FINISHED READING EXTENSIONAL DATA FILE'
C       ************************************
C       NOW ESTIMATE YOUNG'S MODULUS (E) USING BT(3)
C       FOR INPUT TO STARTING POINT OF EXTENSIONAL INVERSION
        W=2.0D0*PI*FF(3)*1.0D03
        E=DCMPLX(RHO*W**2,0.0D0)/REAL(BT(3)**2)
        EE=E/REAL(C44(3))
        C120=REAL(C44(3))*(2.0D0-EE)/(EE-3.0D0)
        WRITE (*,95) ' E=',REAL(E),'C120=',REAL(C120),AIMAG(C120)
  95    FORMAT (A,3X,D15.7,3X,A,3X,D15.7,3X,D15.7)
C       ************************************
        CMIN=1.0D13
        CMAX=-1.0D-13
C       FREQUENCY LOOP ************************
        MX2=DCMPLX(-1.0D13,0.0D0)
        MN2=DCMPLX(1.0D13,0.0D0)
        DO 10 I=1,N
        W=2.0D0*PI*FF(I)*1.0D03
C       CALL BESSEL(N,X,M,COMP)
C       SHEAR VALUES ARE CALCULATED ONCE FOR EVERY FREQUENCY
        KS=W/SQRT(CABS((C44(I)/RHO)))
        KS2=DCMPLX(RHO*W**2,0.0D0)/C44(I)
        KTS=CSQRT(KS2-BT(I)**2)
        ZS=KTS*A
           CALL BESSEL (0,ZS,25,ZS0)
           CALL BESSEL (1,ZS,25,ZS1)
           CALL BESSEL (2,ZS,25,ZS2)
        WRITE (*,64) '  F(Hz)=',FF(I)*1.0D03,'KS*A=',KS*A
 64     FORMAT (A,3X,D15.7,3X,A,3X,D15.7)
C       NOW RUN C12 LOOP
        ANSM=1.0D+13
        ANSM0=1.0D+13
        C12MAX=C120*1.5D0
        IF (I.GT.1) C120=C1200
        IF (I.GT.1) C12MAX=C12MX0
        C12MIN0=C12MAX
 35     DC=ABS(REAL(C12MAX-C120))/50.D0
        IF (KS*A.GT.2.0D0) DC=DC/2.0D0
        IF (KS*A.GT.6.0D0) DC=DC/1.5D0
```

```
C       NOW MAKING C44 CALCULATIONS
        MX4=DCMPLX(-1.0D13,0.0D0)
        MN4=DCMPLX(1.0D13,0.0D0)
        DO 201 I=1,N
        W=2.0D0*PI*FF(I)
C       ADD DAMPER TO U2(I) TO PREVENT DIVISION BY ZERO
        U2(I)=U2(I)+1.0E-10
        AA=1.0D0/(RHO*W**2)
        BB=AA
        AA=AA*((W/U1(I))**2-U2(I)**2)
        BB=BB*(2.0D0*(W/U1(I))*U2(I))
        C44I=1.0D0/(BB*((AA/BB)**2+1.0D0))
        C44R=C44I*(AA/BB)
        C44(I)=DCMPLX(C44R,C44I)
        IF (REAL(C44(I)).GT.REAL(MX4)) MX4=C44(I)
        IF (REAL(C44(I)).LT.REAL(MN4)) MN4=C44(I)
C       WRITE (*,202) ' FREQ=',FF(I),'C44R=',C44R,'C44I=',C44I
C 202   FORMAT (A,2X,E15.7,2X,A,2X,D15.7,2X,A,2X,D15.7)
 201    CONTINUE
C       OPTIONAL THREE POINT SMOOTHING OF C44 FOLLOWS
        IF (OPT.EQ.'N'.OR.OPT.EQ.'n') GOTO 212
        DO 211 J=1,MM
        XC=C44(1)
        DO 209 I=2,(N-1)
        XYC=C44(I)
        C44(I)=(0.25D0*XC+0.5*XYC+0.25D0*C44(I+1))
 209    XC=XYC
 211    CONTINUE
C       PRINTING SHEAR RESULTS
 212    OPEN(8,FILE=FNAMES,STATUS='NEW',ACCESS='SEQUENTIAL')
C       FREQUENCY=kHz, MODULI=(1.0D10 DYNE/(CM**2))=1.GPa
        WRITE (8,*) FF(N)/1.0E03,REAL(MX4)/1.0E10,REAL(MN4)/1.E10
        WRITE (8,*) N
        DO 21 I=1,N
        WRITE (8,*) FF(I)/1.E03,REAL(C44(I))/1.E10,AIMAG(C44(I))/1.E10
 21     CONTINUE
        CLOSE (8)
        WRITE (*,*) ' FINISHED C44 DETERMINATION'
C       END OF C44 DETERMINATION************************
C       READ IN EXPERIMENTAL EXTENSIONAL WAVENUMBER FILE*************
        OPEN (7,FILE=FNBT,STATUS='OLD',ACCESS='SEQUENTIAL')
        REWIND 7
        READ (7,*) MAXX,MAXY,MINY
        READ (7,*) N
        DO 299 I=1,N
C       ASSUMPTION MADE IS THAT ALPHA=XY>=0
        READ (7,*) FF(I),X,XY
        W=2.0D0*PI*FF(I)*1.0D03
        X=X*1.0D05
        XY=-1.0D0*XY
 299    BT(I)=DCMPLX((W/X),XY)
        CLOSE (7)
C       DO 225 I=1,N
C       WRITE (*,226) ' BT(I)=', REAL(BT(I)),AIMAG(BT(I))
```

```
C  226  FORMAT (A,3X,D15.7,3X,D15.7)
C  225  CONTINUE
C       OPTIONAL THREE POINT WEIGHTED SMOOTHING OF EXTENSIONAL DATA
C       XC=KEEPS X(I-1), XYC=KEEPS X(I)
        IF (OPT.EQ.'N'.OR.OPT.EQ.'n') GOTO 235
        DO 228 J=1,MM
        XC=BT(1)
        DO 227 I=2,(N-1)
        XYC=BT(I)
        W1=0.25D0*FF(I-1)
        W2=0.5D0*FF(I)
        W3=0.25D0*FF(I+1)
        BT(I)=(W1*XC+W2*XYC+W3*BT(I+1))/(W1+W2+W3)
 227    XC=XYC
 228    CONTINUE
 235    WRITE (*,*) ' FINISHED READING EXTENSIONAL DATA FILE'
C       ************************************
C       NOW ESTIMATE YOUNG'S MODULUS (E) USING BT(3)
C       FOR INPUT TO STARTING POINT OF EXTENSIONAL INVERSION
        W=2.0D0*PI*FF(3)*1.0D03
        E=DCMPLX(RHO*W**2,0.0D0)/REAL(BT(3)**2)
        EE=E/REAL(C44(3))
        C120=REAL(C44(3))*(2.0D0-EE)/(EE-3.0D0)
        WRITE (*,95) ' E=',REAL(E),'C120=',REAL(C120),AIMAG(C120)
  95    FORMAT (A,3X,D15.7,3X,A,3X,D15.7,3X,D15.7)
C       ************************************
        CMIN=1.0D13
        CMAX=-1.0D-13
C       FREQUENCY LOOP ************************
        MX2=DCMPLX(-1.0D13,0.0D0)
        MN2=DCMPLX(1.0D13,0.0D0)
        DO 10 I=1,N
        W=2.0D0*PI*FF(I)*1.0D03
C       CALL BESSEL(N,X,M,COMP)
C       SHEAR VALUES ARE CALCULATED ONCE FOR EVERY FREQUENCY
        KS=W/SQRT(CABS((C44(I)/RHO)))
        KS2=DCMPLX(RHO*W**2,0.0D0)/C44(I)
        KTS=CSQRT(KS2-BT(I)**2)
        ZS=KTS*A
           CALL BESSEL (0,ZS,25,ZS0)
           CALL BESSEL (1,ZS,25,ZS1)
           CALL BESSEL (2,ZS,25,ZS2)
        WRITE (*,64) '  F(Hz)=',FF(I)*1.0D03,'KS*A=',KS*A
 64     FORMAT (A,3X,D15.7,3X,A,3X,D15.7)
C       NOW RUN C12 LOOP
        ANSM=1.0D+13
        ANSM0=1.0D+13
        C12MAX=C120*1.5D0
        IF (I.GT.1) C120=C1200
        IF (I.GT.1) C12MAX=C12MX0
        C12MIN0=C12MAX
 35     DC=ABS(REAL(C12MAX-C120))/50.D0
        IF (KS*A.GT.2.0D0) DC=DC/2.0D0
        IF (KS*A.GT.6.0D0) DC=DC/1.5D0
```

```
C       BEGINNING OF LOOPS ON C12***************
C       FIRST COMES HORIZONTAL PAIR C121 AND C122
        J=1
        C12(I)=C120
C       BEGINNING OF HORIZONTAL LOOPS FOR J>1 OR HIGHER ITERATIONS
  36    CONTINUE
        C121=C12(I)-DCMPLX(0.0D0,DC)
        C11=C121+2.0D0*C44(I)
        R=C121/C44(I)
        KL2=DCMPLX(RHO*W**2,0.0D0)/C11
        KTL=CSQRT(KL2-BT(I)**2)
        ZL=KTL*A
           CALL BESSEL (0,ZL,25,ZL0)
           CALL BESSEL (1,ZL,25;ZL1)
           CALL BESSEL (2,ZL,25,ZL2)
C       NOW CALCULATE THE DISPERSION FUNCTION FOR C121
        ANS1=(KS2-2.0D0*BT(I)**2)*ZS1*R*(KL2)*ZL0
        ANS1=ANS1-(KS2-2.0D0*BT(I)**2)*ZS1*(KL2-BT(I)**2)*(ZL2-ZL0)
        ANS1=ANS1-(2.0D0*BT(I)**2)*KTL*KTS*ZL1*(ZS2-ZS0)
C       WRITE (*,65) ' F=',FF(I),'C121=',REAL(C121),AIMAG(C121),'ANS1='
C     1 ,REAL(ANS1),AIMAG(ANS1)
C 65    FORMAT (A,2X,D15.7,2X,A,2X,D15.7,2X,D15.7,2X,A,2X,D15.7,2X
C     1 ,D15.7)
C       NOW DO THE SAME FOR C122
        C122=C12(I)+DCMPLX(0.0D0,DC)
        C11=C122+2.0D0*C44(I)
        R=C122/C44(I)
        KL2=DCMPLX(RHO*W**2,0.0D0)/C11
        KTL=CSQRT(KL2-BT(I)**2)
        ZL=KTL*A
           CALL BESSEL (0,ZL,25,ZL0)
           CALL BESSEL (1,ZL,25,ZL1)
           CALL BESSEL (2,ZL,25,ZL2)
C       NOW CALCULATE THE DISPERSION FUNCTION FOR C122
        ANS2=(KS2-2.0D0*BT(I)**2)*ZS1*R*(KL2)*ZL0
        ANS2=ANS2-(KS2-2.0D0*BT(I)**2)*ZS1*(KL2-BT(I)**2)*(ZL2-ZL0)
        ANS2=ANS2-(2.0D0*BT(I)**2)*KTL*KTS*ZL1*(ZS2-ZS0)
C       WRITE (*,65) '  F=',F,'C122=',REAL(C122),AIMAG(C122),'ANS2='
C     1 ,REAL(ANS2),AIMAG(ANS2)
C       NOW WE OBTAIN HORIZONTAL SIGN
        SH=AIMAG(ANS1)*REAL(ANS2)-AIMAG(ANS2)*REAL(ANS1)
        SANSH=DSIGN(1.0D0,SH)
        IF (J.EQ.1) SANSH0=SANSH
        IF (SANSH.NE.SANSH0) THEN
C           WE HAVE FOUND OUR ROOT-SIGN HAS REVERSED
C           WE SET PARAMETERS AND GOTO VERTICAL PART
              GOTO 37
        ENDIF
C       NOW WE MAKE NEW HORIZONTAL PAIR (SIGN HAS NOT REVERSED)
C       FIXING THE DIRECTION OF MOTION BY THE SIGN SANSH
        C12(I)=C12(I)+SANSH*DCMPLX(DC,0.0D0)
        J=J+1
        GOTO 36
C       ************************************************************
```

```
C       NOW COME VERTICAL PAIR C123 AND C124
 37     J=1
        C12(I)=(C121+C122)/2.0D0
C       BEGINNING OF VERTICAL LOOPS FOR J>1 OR HIGHER ITERATIONS
  38    CONTINUE
        C123=C12(I)-DCMPLX(DC,0.0D0)
        C11=C123+2.0D0*C44(I)
        R=C123/C44(I)
        KL2=DCMPLX(RHO*W**2,0.0D0)/C11
        KTL=CSQRT(KL2-BT(I)**2)
        ZL=KTL*A
           CALL BESSEL (0,ZL,25,ZL0)
           CALL BESSEL (1,ZL,25,ZL1)
           CALL BESSEL (2,ZL,25,ZL2)
C       NOW CALCULATE THE DISPERSION FUNCTION FOR C123
        ANS3=(KS2-2.0D0*BT(I)**2)*ZS1*R*(KL2)*ZL0
        ANS3=ANS3-(KS2-2.0D0*BT(I)**2)*ZS1*(KL2-BT(I)**2)*(ZL2-ZL0)
        ANS3=ANS3-(2.0D0*BT(I)**2)*KTL*KTS*ZL1*(ZS2-ZS0)
C       WRITE (*,65) '  F=',F,'C123=',REAL(C123),AIMAG(C123),'ANS3='
C     1 ,REAL(ANS3),AIMAG(ANS3)
C       NOW DO THE SAME FOR C124
        C124=C12(I)+DCMPLX(DC,0.0D0)
        C11=C124+2.0D0*C44(I)
        R=C124/C44(I)
        KL2=DCMPLX(RHO*W**2,0.0D0)/C11
        KTL=CSQRT(KL2-BT(I)**2)
        ZL=KTL*A
           CALL BESSEL (0,ZL,25,ZL0)
           CALL BESSEL (1,ZL,25,ZL1)
           CALL BESSEL (2,ZL,25,ZL2)
C       NOW CALCULATE THE DISPERSION FUNCTION FOR C124
        ANS4=(KS2-2.0D0*BT(I)**2)*ZS1*R*(KL2)*ZL0
        ANS4=ANS4-(KS2-2.0D0*BT(I)**2)*ZS1*(KL2-BT(I)**2)*(ZL2-ZL0)
        ANS4=ANS4-(2.0D0*BT(I)**2)*KTL*KTS*ZL1*(ZS2-ZS0)
C       WRITE (*,65) '  F=',F,'C124=',REAL(C124),AIMAG(C124),'ANS4='
C     1 ,REAL(ANS4),AIMAG(ANS4)
C       NOW WE OBTAIN VERTICAL SIGN
        SV=AIMAG(ANS3)*REAL(ANS4)-AIMAG(ANS4)*REAL(ANS3)
        SANSV=DSIGN(1.0D0,SV)
        IF (J.EQ.1) SANSV0=SANSV
        IF (SANSV.NE.SANSV0) THEN
C           WE HAVE FOUND VERTICAL ROOT-SIGN HAS REVERSED
C           WE EITHER GOTO HORIZONTAL FOR NEW ITERATION
C           OR WE TERMINATE
            ANS=(ANS3+ANS4)/2.0D0
            C12(I)=(C123+C124)/2.0D0
            C12MN=C12(I)
           WRITE (*,84) ' C12MIN=',REAL(C12MN),AIMAG(C12MN),'DC=',DC
 84       FORMAT (A,2X,D15.7,2X,D15.7,2X,A,2X,D15.7)
            DLTA=CDABS((C12MN-C12MIN0)/C12MIN0)
            DLTAI=DABS(AIMAG(C12MN-C12MIN0)/(AIMAG(C12MIN0)+1.0D-32))
        IF (DABS(AIMAG(C12MN)/(REAL(C12MN)+1.D07)).LT.1.D-04) DLTAI=DLT
                      IF (DLTA.GT.DLT.OR.DLTAI.GT.DLT) THEN
C             ERROR IS NOT YET TO STANDARDS,REDUCE DC AND ITERATE AGAIN
```

```
                              C12MIN0=C12MN
                              DC=DC/10.D0
                              J=1
                              GOTO 36
                              ELSE
C                   ERROR IS TO STANDARDS,SET START POINT FOR NEXT FREQUENCY
            WRITE (*,85) ' C12MIN=',REAL(C12MN),AIMAG(C12MN)
     1       ,'ANS=',REAL(ANS),AIMAG(ANS)
 85         FORMAT (A,2X,D15.7,2X,D15.7,A,2X,D15.7,2X
     1       ,D15.7)
C           MAXIMUM-MINIMUM DETERMINATION FOLLOWS
            IF (REAL(C12(I)).GT.REAL(MX2)) MX2=C12(I)
            IF (REAL(C12(I)).LT.REAL(MN2)) MN2=C12(I)
                              C1200=C12MN*1.0D0
                              C12MX0=C1200*1.40D0
                              GOTO 10
                              ENDIF
            ENDIF
C           NOW WE MAKE NEW VERTICAL PAIR (SIGN HAS NOT REVERSED)
C           FIXING THE DIRECTION OF MOTION BY THE SIGN SANSV
            C12(I)=C12(I)-SANSV*DCMPLX(0.0D0,DC)
            J=J+1
            GOTO 38
 10         CONTINUE
C           ***********************************************
C           OPTIONAL SMOOTHING OF C12**************
            IF (OPT.EQ.'N'.OR.OPT.EQ.'n') GOTO 359
            DO 351 J=1,MM
            XC=C12(1)
            DO 353 I=2,(N-1)
            XYC=C12(I)
            C12(I)=(0.25D0*XC+0.5*XYC+0.25D0*C12(I+1))
 353        XC=XYC
 351        CONTINUE
C           C12 PRINTING SECTION BEGINS******************
 359        OPEN(8,FILE=FNAME,STATUS='NEW',ACCESS='SEQUENTIAL')
C           FREQUENCY=kHz,MODULI=1.0D10 DYNE/(CM**2)=1.0GPa
            WRITE (8,*) FF(N),REAL(MX2)/1.E10,REAL(MN2)/1.E10
            WRITE (8,*) N
            DO 20 I=1,N
            WRITE (8,*) FF(I),REAL(C12(I))/1.E10,AIMAG(C12(I))/1.E10
 20         CONTINUE
            CLOSE (8)
            END
C           ***********************************************
C           ***********************************************
C           ***********************************************
            SUBROUTINE BESSEL (N,Z,M,COMPZ)
C           N=ORDER OF BESSEL FUNCTION OF FIRST KIND (Jn(Z))
C           Z=COMPLEX ARGUMENT
C           M=AMOUNT OF TERMS TO TAKE IN SERIES EXPANSION
C           COMPZ=COMPLEX ANSWER-OUTPUT OF THE SUBROUTINE
C           VARIABLE DECLARATION SECTION BEGINS HERE
            INTEGER*4 N,M,I,J,K
```

```
      REAL*8 X,JF,JNF,Y,FA(40)
      COMPLEX*16 Z,COMPZ
C     NEXT LINES ARE FACTORIALS OF 1 TO 40
      DATA FA/1.,2.,6.,24.,120.,720.,5040.,40320.
     1  ,362880.,3628800.,39916800.,4.790016D+08,6.227021D+09
     1  ,8.71783D+10,1.30767D+12,2.09227D+13,3.5568D+14,6.40237D+15
     1  ,1.21645D+17,2.4329D+18,5.10909D+19,1.124D+21,2.585D+22
     1  ,6.2044D+23,1.55112D+25,4.0329D+26,1.0888D+28,3.04888D+29
     1  ,8.8417D+30,2.6525D+32,8.2228D+33,2.6313D+35,8.6833D+36
     1  ,2.9523D+38,1.0333D+40,3.7199D+41,1.3763D+43
     1  ,5.2302D+44,2.0398D+46,8.1591D+47/
      COMPZ=(0.0D0,0.0D0)
      DO 10 I=1,M
      J=I-1
C     HAVE TO COMPUTE FACTORIALS HERE
C     COMPUTING J FACTORIAL (JF)
      JF=1.0D0
      IF (J.EQ.0) GOTO 25
      JF=FA(J)
C     NOW COMPUTING (N+J) FACTORIAL (JNF)
 25   JNF=1.0D0
      IF ((N+J).EQ.0) GOTO 30
      JNF=FA((N+J))
C     END OF FACTORIAL COMPUTATION
 30   IF (J.EQ.0) THEN
             COMPZ=COMPZ+DCMPLX((1.0D0)/(JF*JNF))
             GOTO 31
             ENDIF
      COMPZ=COMPZ+DCMPLX(((-1.0D0)**J)/(JF*JNF))*(Z/2.0D0)**(2*J)
 31   CONTINUE
 10   CONTINUE
      IF (N.EQ.0) GOTO 18
      COMPZ=COMPZ*(Z/2.0D0)**N
 18   CONTINUE
      RETURN
      END
C     ************************************************
C     ************************************************
C     ************************************************
```

Appendix C-Surface Influence On Effective Elastic Constants

In this section proof will be provided for equation (27) of the text, the equation which provides an estimate of the effect of surface elastic constants on the elastic moduli of composite materials. The static strain energy of a solid of volume V and area S is given by

$$W = \int_V C_{ijkl}(r)\,\epsilon_{ij}(r)\,\epsilon_{kl}(r)\,dV + \int_S \gamma_{ijkl}(r)\,\epsilon_{ij}(r)\,\epsilon_{kl}(r)\,dS \qquad \text{(C1)}$$

where C_{ijkl} are the position dependent bulk elastic moduli and γ_{ijkl} are the surface elastic moduli. For the bulk case indexs i,j,k,l range from 1 to 3, while for the surface moduli these range from 1 to 2 (only in the plane of the surface which will be taken as the xy plane).

We now define some spatialy averaged strain quadratics, denoted by $< >$

$$<\epsilon_{ij}\ \epsilon_{kl}>_S = \frac{1}{S}\int_S \epsilon_{ij}(r)\,\epsilon_{kl}(r)\,dS$$

$$<\epsilon_{ij}\ \epsilon_{kl}>_V = \frac{1}{V}\int_V \epsilon_{ij}(r)\,\epsilon_{kl}(r)\,dV$$

and

$$<\epsilon_{ij}\ \epsilon_{kl}>_T = (1-\frac{Sl}{V})\cdot<\epsilon_{ij}\ \epsilon_{kl}>_V + (\frac{Sl}{V})\cdot<\epsilon_{ij}\ \epsilon_{kl}>_S$$

where T signifies total and l is the effective thickness of the surface layer.

Having defined thse averages equation (C1) can be written as

$$V\ C_{ijklEF}\cdot<\epsilon_{ij}\ \epsilon_{kl}>_T = V\ C_{ijklSCS}\cdot<\epsilon_{ij}\ \epsilon_{kl}>_V + S\ \gamma_{ijkl}\cdot<\epsilon_{ij}\ \epsilon_{kl}>_S \qquad \text{(C2)}$$

where the effective moduli (EF) are those taking into account both bulk and surface interactions, the self-consistent (SCS) those using only bulk interactions, and the surface elastic moduli tensor component γ_{ijkl} now corresponding to an effective surface elastic moduli, an average over the possibly heterogeneous surfaces.

Equation (C2) can be written as

$$C_{ijklEF} = C_{ijklSCS}\cdot\frac{<\epsilon_{ij}\ \epsilon_{kl}>_V}{<\epsilon_{ij}\ \epsilon_{kl}>_T} + (\frac{S}{V})\cdot\gamma_{ijkl}\cdot\frac{<\epsilon_{ij}\ \epsilon_{kl}>_S}{<\epsilon_{ij}\ \epsilon_{kl}>_T} \qquad \text{(C3)}$$

which is a general expression for the effective elastic moduli. For a prescribed strain and

moduli distribution within the volume and on the surfaces, a unique solution may be given for these effective moduli.

The expression may be simplified by using some intuition regarding the sign of the strain quadratics and an assumption regarding the absence of strong strain deviations. If the surfaces are joined to the bulk then

$$- <\epsilon_{ij}\ \epsilon_{kl}>_S \approx <\epsilon_{ij}\ \epsilon_{kl}>_V$$

since otherwise the surfaces would detach. Absence of strong strain concentrations would imply that

$$<\epsilon_{ij}\ \epsilon_{kl}>_V \approx <\epsilon_{ij}\ \epsilon_{kl}>_T$$

so that one finally obtains

$$C_{ijklEF} = C_{ijklSCS} - (\frac{S}{V}) \cdot \gamma_{ijkl} \tag{C4}$$

which is identical to equation (27).